

AFRL-AFOSR-VA-TR-2023-0124

Using Cyber-Physical systems to study the dynamics of unsteady leading edge vortices with cross-stream flows

Breuer, Kenneth
BROWN UNIVERSITY
1 PROSPECT ST
PROVIDENCE, RI, 02912
USA

10/31/2022
Final Technical Report

DISTRIBUTION A: Distribution approved for public release.

Air Force Research Laboratory
Air Force Office of Scientific Research
Arlington, Virginia 22203
Air Force Materiel Command

REPORT DOCUMENTATION PAGE

PLEASE DO NOT RETURN YOUR FORM TO THE ABOVE ORGANIZATION.

1. REPORT DATE	2. REPORT TYPE	3. DATES COVERED	
20221031	Final	START DATE 20180615	END DATE 20220614

4. TITLE AND SUBTITLE
Using Cyber-Physical systems to study the dynamics of unsteady leading edge vortices with cross-stream flows

5a. CONTRACT NUMBER	5b. GRANT NUMBER	5c. PROGRAM ELEMENT NUMBER
	FA9550-18-1-0322	61102F

5d. PROJECT NUMBER	5e. TASK NUMBER	5f. WORK UNIT NUMBER

6. AUTHOR(S)
Kenneth Breuer

7. PERFORMING ORGANIZATION NAME(S) AND ADDRESS(ES)
BROWN UNIVERSITY
1 PROSPECT ST
PROVIDENCE, RI 02912
USA

8. PERFORMING ORGANIZATION REPORT NUMBER

9. SPONSORING/MONITORING AGENCY NAME(S) AND ADDRESS(ES)	10. SPONSOR/MONITOR'S ACRONYM(S)	11. SPONSOR/MONITOR'S REPORT NUMBER(S)
Air Force Office of Scientific Research 875 N. Randolph St. Room 3112 Arlington, VA 22203	AFRL/AFOSR RTA1	AFRL-AFOSR-VA-TR-2023-0124

12. DISTRIBUTION/AVAILABILITY STATEMENT
A Distribution Unlimited: PB Public Release

13. SUPPLEMENTARY NOTES

14. ABSTRACT
The focus of the research was to characterize the LEV dynamics and aeroelastic instabilities associated with swept wings — wings in which there is a significant cross flow velocity. The effort was a combined experimental (at both Brown and USAFA) and computational (at the USAFA). The experiments at Brown were conducted in the 0.6 x 0.8 meter water tunnel, while experiments at USAFA were conducted in the 3 foot by 3 foot wind tunnel. Key accomplishments include the development and refinement of cyber-physical experimental aparatus at Brown and USAFA, characterization of stability maps and energy maps for both unswept and swept wings, and the measurement and computation of key flow structures associated with high amplitude pitching wings.

15. SUBJECT TERMS

16. SECURITY CLASSIFICATION OF:			17. LIMITATION OF ABSTRACT	18. NUMBER OF PAGES
a. REPORT U	b. ABSTRACT U	c. THIS PAGE U	UU	143

19a. NAME OF RESPONSIBLE PERSON	19b. PHONE NUMBER *(Include area code)*
GREGG ABATE	425-1779

Using Cyber-Physical systems to study the dynamics of unsteady leading edge vortices with cross-stream flows

Final report: AFOSR Grant FA9550-18-1-0322

Kenny Breuer, Brown University
Casey Fagley and Jurgen Seidel, USAFA
September 2022

1 Introduction

This report covers the joint research program conducted under AFSOR support by researchers at Brown University (Kenneth Breuer) and United States Air Force Academy (Jurgen Seidel and Casey Fagley). The report is organized as follows. In the following two sections we summarize the accomplishments and impacts of each partner in the research team. Appendices at the end of the report include journal and conference papers.

2 Accomplishments

2.1 Research objectives

The focus of the research was to characterize the LEV dynamics and aeroelastic instabilities associated with swept wings — wings in which there is a significant cross flow velocity. The effort was a combined experimental (at both Brown and USAFA) and computational (at the USAFA). The experiments at Brown were conducted in the 0.6 x 0.8 meter water tunnel, while experiments at USAFA were conducted in the 3 foot by 3 foot wind tunnel.

2.2 Accomplishments

2.2.1 Brown University

The key scientific accomplishments are summarized in the papers attached in Appendix A. Briefly summarizing:

Cyber-Physical experimental apparatus Much of the work under this program was based on the Cyber-Physical system that has been under development and refinement for the past several years [5, 3, 4, 6]. This system, based on a high-bandwidth real-time control of the wing motion, allows us to mount a rigid wing in the testing facility on a flexible mount that allows for pitching, to "dial in" the torsional stiffness, k, and damping, b, and more importantly, to assign an (almost) arbitrary wing inertia, I. This digital control of the structural flexibility allows us to rapidly span a wide range of parameter space, $[k, b, I]$. in non-dimensional terms, this allows us to control the non-dimensional stiffness, $k/0.5\rho U^2 c^2 s$ (where c is the wing chord and s is the wing span) and damping, $b/0.5\rho U c^3 s$ and the mass ratio, $M = I/0.5\rho c^4 s$. The ability to control the mass ratio has an incredibly useful consequence for experimentalists - we can conduct experiments in a *water* tunnel (with fluid high density), that exactly match the aeroelastic instability characteristics of a wing in *air* (i.e. a low density fluid). Note that the Reynolds number between water ($\sim 30,000$) and air ($\sim 200,000$) facilities is not identical, although both are high enough such that Re-effects are minimal.

Aeroelastic instability boundaries on unswept and swept wings Although analysis and experiments on the "classic" aeroelastic instability - static divergence and the onset of low amplitide limit cycle oscillations (LCO) - have been known for decades, here we expand the range of analysis substantially using our cyber-physical facility and explore the full dynamical system including the onset of static divergence, LCOs and, new to the overall analysis - very large amplitude pitching instabilities characterized by shedding of leading edge vorticies. We completed this for unswept wings (NACA0012) [10] and for wings with sweep angles $\Lambda = [10, 15, 20, 25, 30]$ degrees [9].

Fluid damping associated with leading edge vorticies Leading edge vorticies, shed from a pitching wing in a quiescent fluid exert a force and moment on the wing. If the wing is not continuously forced, the pitching wing will "ring down" in a manner described by a damped second order differential equation. However, the fluid damping due to the vorticies is not, typically linear (the damping, which results from the inertial motion of the vortices typically scales with the square of the velocity, while linear damping scales linearly with the velocity). We have conducted a series of measurements characterizing this vortex induced damping and developed a simple scaling which collapses all of the measured damping coefficients, b, for all values of pitching amplitude, θ, pitching axis, x_p/c, and wing sweep, Λ [12].

Ongoing work We have initiated work on two more aspects of these problems - the vortex dynamics associated with the pitching wings (measured using a detailed set of PIV measurements) and we have started to explore machine learning approaches to describe the dynamic systems of the aeroelastic instabilities. These have not yet been completed, and are continued in the follow-on AFOSR research program that started in 2021.

2.2.2 USAFA

The scientific progress is detailed in the attached Appendix A. The key technological improvements throughout the duration of the project are summarized below:

Cyber-Physical wind-tunnel integration A single degree of freedom Cyber-Physical system was developed and integrated into the USAFA Subsonic Wind Tunnel. The system consists of a motor and torque cell mounted beneath the test section. Control laws were developed to control the angular twist or pitch of a cantilever shaft to follow a 2^{nd} order linear system. The system was designed such that the mounting mechanism could be hinged and locked into 5° increments in downstream direction to incorporate wing sweep. The arrangement of the axis of rotation was different from Brown's experimental setup. The axis of rotation was parallel to the leading edge; thus, angular velocity of the leading edge and trailing edge where constant across sweep angle increments. Instability boundaries were identified and the influence of the wing swepp on the LEV formation and separation were developed.

Flow similarity between driven and responding motion Studies were done to understand and differentiate the prescribed motion discretized by sinusoidal function and responding aero-elastic motion. Particular cases indicated the presence of a 3^{rd} harmonic due to the development of a trailing edge vortex and/or secondary leading edge vortices. While the aero-elastic instabilities lied along the $C_p = 0$ contour line, similar to the Brown University results, slight differences in the motion definitively augmented LEV size/strength. A non-dimensional relationship of maximum angular rate ($\alpha_1 F^\star$) was developed which scaled the development and shedding of primary and secondary LEV structures. Finally the scaling also showed a collapse of each of the power coefficient trends for each permutation of frequency and amplitude tested.

Fully coupled computational simulations A similar assessment was carried out computationally. Both prescribed motions (rigid body rotation in this case) and responding motion given a structural dynamic model were implemented in CREATE-AV-Kestrel. Similarities between computations and experiments were made. High fidelity simulation results showed the size/strength of the primary LEV and supported experimental results that the presence of spanwise flow reduced the overall circulation of the LEV. Full details of the computational framework and resulting flow features are detailed in Fagley et al. [1].

Ongoing work We have developed a 3-DoF system to characterize dynamic stability derivatives for realistic planforms with multiple leading edge sweep angles. Angles of sweep are dramatically increased in comparison to the work attached to this report which augment the flow physics by reducing the effect of the spanwise flow and behaving like a pure vortex generator. Vortex-Vortex interactions (braiding, merging, entrainment) in high angle of attack regime of these multi-swept wing configurations contribute dramatically to the vortex breakdown progression. It is anticipated to begin testing on the dynamic response and interactions thereof.

2.3 Dissemination of results

The results of this work have been published in archival journal publications [6, 2, 10, 12, 1] and presented at conferences [11, 7–9]. Copies of these manuscripts are attached at the end of this report. Research seminars and presentations at conferences without extended abstracts or papers (such as the APS/DFD conference) are not listed.

2.4 Plans for next reporting period

Not Applicable. This is the final report.

3 Impacts

Key impacts of this work are the further development of the cyber-physical experimental platform in which we are able to simulate elastic mounting systems with arbitrary stiffness, damping and mass. Using this we can rapidly vary the aeroelastic properties of the fluid structure interaction and explore with great precision and range the aeroelastic instabilities of both unswept and swept wings.

The ability to control the virtual mass of the system is of particular importance. In this was not only can the elastic stiffness and damping of the wing be controlled, but the mass ratio - the ratio between the wing mass and the virtual mass of the surrounding fluid - can also be controlled. In particular this allows the experiments of a wing in air (with a low mass ratio) to be simulated in a water tunnel testing facility. This is an invaluable experimental feature.

A second key scientific impact of the work is the detailed characterization of fluid damping forces that this work has outlined. This has not been characterized within the framework of a dynamical systems description (e.g. a damping coefficient, b), and our results, which are

With respect to human resource development, The program provided support to train a PhD student, as well as several undergraduate students, all of whom will go on to productive scientific careers. The PhD students, Yunxing Su and Yunhang Zhu, are in postdoctoral research positions (at Brown, with Monica Martinez Wilhelmus) and U. Virginia (with Dan Quinn). Undergraduate students who worked on this project have moved onto graduate programs or industrial positions: Howon Lee as a PhD student in Aerospace at GaTech, Nicholas Simone as an engineer at Dell/EMC. Varghese Mathai, a post doc who was not supported by this project, but collaborated with the graduate student researchers has assumed a faculty position at U. Mass Amherst.

A critical achievement of this project was the establishment of a strong collaborative relationship between the PIs at Brown University and the US Air Force Academy. Although our specific research foci did not overlap explicity, the common theme of our effort was enhanced by monthly virtual team meetings and by in-person visits and meetings at USAFA and AIAA conferences. That connection has endured (e.g. Kenny Breuer visited USAFA in October 2022) and we plan to develop continued collaborations in the future.

4 Changes

Not Applicable. This is the final report.

References

[1] C. Fagley, A. Jirasek, and J. Seidel. Leading edge vortex dynamics on finite aspect ratio swept wings exhibiting large amplitude oscillations. *Journal of Fluids and Structures*, In review, 2022.

[2] H. Lee, N. Simone, Y. Su, Y. Zhu, B. L. R. Ribeiro, J. A. Franck, and K. Breuer. Leading edge vortex formation and wake trajectory: Synthesizing measurements, analysis, and machine learning. *Phys. Rev. Fluids*, 7(7):074704, July 2022. doi: 10.1103/PhysRevFluids.7.074704.

[3] K. Onoue and K. S. Breuer. Vortex formation and shedding from a cyber-physical pitching plate. *J. Fluid Mech.*, 793:229–247, Apr. 2016. doi: 10.1017/jfm.2016.134.

[4] K. Onoue and K. S. Breuer. A scaling for vortex formation on swept and unswept pitching wings. *J. Fluid Mech.*, 832:697–720, Dec. 2017. doi: 10.1017/jfm.2017.710.

[5] K. Onoue, A. Song, B. Strom, and K. S. Breuer. Large amplitude flow-induced oscillations and energy harvesting using a cyber-physical pitching plate. *Journal of Fluids and Structures*, 55:262–275, May 2015. doi: 10.1016/j.jfluidstructs.2015.03.004.

[6] Y. Su and K. Breuer. Resonant response and optimal energy harvesting of an elastically mounted pitching and heaving hydrofoil. *Phys. Rev. Fluids*, 4(6):064701, June 2019. doi: 10.1103/PhysRevFluids.4.064701.

[7] Y. Zhu and K. Breuer. Nonlinear aeroelastic instabilities on swept wings. In *AIAA Scitech 2021 Forum*, 2021.

[8] Y. Zhu and K. Breuer. Nonlinear aeroelastic instabilities on swept wings. In *Proc. 2021 ICTAM*, Milan, 2021.

[9] Y. Zhu and K. Breuer. Aeroelastic Instability Boundaries of Pitching Swept Wings. In *AIAA Scitech 2022*, page 12, San Diego, CA, Jan. 2022. doi: 10.2514/6.2022-2328.

[10] Y. Zhu, Y. Su, and K. Breuer. Nonlinear flow-induced instability of an elastically mounted pitching wing. *J. Fluid Mech.*, 899:A35, Sept. 2020. doi: 10.1017/jfm.2020.481.

[11] Y. Zhu, Y. Su, and K. Breuer. Non-linear stability boundaries of an elastically-mounted pitching wing. In *AIAA Scitech 2020 Forum*, Orlando, FL, Jan. 2020. American Institute of Aeronautics and Astronautics. doi: 10.2514/6.2020-1052.

[12] Y. Zhu, V. Mathai, and K. Breuer. Nonlinear fluid damping of elastically mounted pitching wings in quiescent water. *J. Fluid Mech.*, 923:R2, Sept. 2021. doi: 10.1017/jfm.2021.578.

A Journal and conference papers

Resonant response and optimal energy harvesting of an elastically mounted pitching and heaving hydrofoil

Yunxing Su* and Kenneth Breuer
School of Engineering, Brown University, Providence, Rhode Island 02912, USA

(Received 19 February 2019; published 20 June 2019)

The aeroelastic response and energy harvesting performance of an elastically mounted hydrofoil subject to a prescribed pitching motion are experimentally studied using a cyber-physical force-feedback control system in a uniform flow. By taking advantage of this cyber-physical system, we systematically sweep through the parameter space of the elastic support (stiffness, damping, and mass) for various frequencies of the prescribed pitching motion. It is found that the flow-induced heave amplitude and the energy harvesting performance are both strongly affected by the frequency ratio between the prescribed pitching frequency and the natural frequency of the system and the damping coefficient. In particular, for a fixed damping coefficient, the maximum flow-induced heave amplitude is achieved at the resonant condition (frequency ratio of 1), which also gives rise to the highest energy harvesting performance. At this resonance condition, though a smaller damping produces a larger heave amplitude, the optimal energy harvesting performance is obtained consistently at an intermediate damping coefficient of 1.5. In addition, at the resonance condition, the heave amplitude, or Strouhal number, and the hydrodynamic forces on the foil are both found to collapse well for different reduced frequencies, suggesting a similarity in the vortex dynamics generated by the elastically mounted system. A low-order model based on classical vibration theory is formulated to reproduce the power coefficient using the damping coefficient and Strouhal number, and we find that the power coefficient predicted by the model agrees well with that measured in the experiment over the range of reduced frequency explored.

DOI: 10.1103/PhysRevFluids.4.064701

I. INTRODUCTION

Hydrokinetic energy is gaining importance these years as it is clean and renewable compared to the conventional fossil fuels and also due to its large amount of resources available in the oceans and rivers. Instead of the widely used conventional rotatory turbines, oscillating hydrofoils are reported to offer an alternative solution to extracting the hydrokinetic energy owing to its high efficiency, shallow water feasibility, and aquatic life friendliness [1]. Thus far, most of the studies of oscillating foils in literature have focused on investigating the energy harvesting performance with prescribed foil kinematics. Hydrofoils in these studies are driven through prescribed trajectories and then the forces and moment of torques are measured to calculate the power extracted by the system. A wide-spread parameter space has been explored to optimize the power extraction performance by a sinusoidal heaving and pitching foil, including the pitch and heave amplitudes, reduced frequency, phase difference between pitching and heaving motions, pitching axis location, aspect ratio, and the geometry of the leading edge [2,3]. Particularly, researchers [2,4] numerically conducted a parametric sweep over the motion frequency and the pitch amplitude and reported

*Yunxing_Su@brown.edu

 ©2019 American Physical Society

an optimal efficiency of 0.34 at a reduced frequency of 0.15, pitch amplitude of 75°, and heave amplitude of one chord length. As discussed by the authors, the lift force and the synchronization between the force and the corresponding velocity play primary roles in the energy extraction performance. A phase difference of 90° between the heaving and the pitching motions was shown [1,4] to produce the maximum power extraction output owing to the optimal force-velocity synchronization.

The lift force on an oscillating hydrofoil can be decomposed into two components: the noncirculatory component from the inertial reaction of the fluid, which is closely related to the foil's acceleration; and the circulatory component associated with the vortex dynamics on the foil [5–8]. The formation and evolution of leading edge vortex (LEV) on the hydrofoil have been shown to be critical in the lift force generation [9], the force-velocity synchronization, and the power extraction [2]. Kinsey and Dumas [2] also reported that simulations with the same frequency and effective angle of attack (AOA) generated similar flow characteristics (LEV formation), resulting in similar lift force histories. By varying the reduced frequency and Strouhal number while keeping the same effective AOA of an oscillating foil, Baik *et al.* [10], with the help of flow field measurements, confirmed the importance of effective AOA and reduced frequency in determining the LEV evolution and the forces exerted on the foil.

Studies [11–15] showed that nonsinusoidal motion profiles were potentially beneficial to the power extraction performance of a flapping hydrofoil. Specifically, Xiao *et al.* [16] investigated the effects of trapezoidal pitch profiles on the energy harvesting performance with a fixed sinusoidal heaving motion. The researchers reported that the heave component of power extraction increased with the trapezoidal profiles while the pitch component demonstrated otherwise. With the help of particle image velocimetry (PIV) measurements, Rival *et al.* [17] examined the leading-edge vortex evolution for different motion profiles and reported that the lifetime of the LEV on a heaving airfoil could be noticeably extended with a delayed vortex growth and pinch-off by fine tuning the foil kinematics. By examining the LEV formation on a pitching and heaving hydrofoil with nonsinusoidal kinematics, Fenercioglu *et al.* [18] reported that a larger rotation speed at the pitch reversal led to an earlier vortex shedding but with a higher strength. For energy harvesting of an oscillating hydrofoil with trapezoidal pitch profiles, Deng *et al.* [19] and Teng *et al.* [15] pointed out that the large effective AOA maintained through most of the cycle was essential in increasing the power extraction performance.

Recently, a novel design of the oscillating energy harvester is introduced and examined with a prescribed pitch motion and a flow-induced heave motion, which is usually referred as semipassive energy harvester [20–24]. In those systems, the passivity of the heave motion is achieved by either numerical simulations or physical springs and dampers. The heave motion response and the energy harvesting performance of the energy harvesters are determined by the stiffness, damping, and mass of the passive heave system. However, the parametric volumes (stiffness, damping, and mass) of these semipassive energy harvesters are limited due to the difficulty in changing the values of the physical springs and dampers. One alternative solution to avoiding such limitations is by using a cyber-physical system, in which a force-feedback control system provides an easy access to varying the system parameters (stiffness, mass, and damping). Initialized by Hover *et al.* [25] for the investigation of marine cables, the cyber-physical system was then demonstrated in the studies of vortex-induced vibration of a circular cylinder [26–29] and the dynamics of the leading edge vortex on a flat plate [30–32].

In the current study, a force-feedback cyber-physical system is used to achieve the passive or elastically mounted heave motion, while the pitch motion is prescribed by the user. We focus on optimizing the energy harvesting performance of an elastically mounted hydrofoil via a parametric sweep across the elastic parameters (stiffness, damping, and virtual mass). Then follows the analysis on the elastic parameters effects on the response of the elastically mounted system. In addition, the nonsinusoidal pitch profile effects on energy extraction are also investigated to capture the optimal pitch kinematics for energy harvesting.

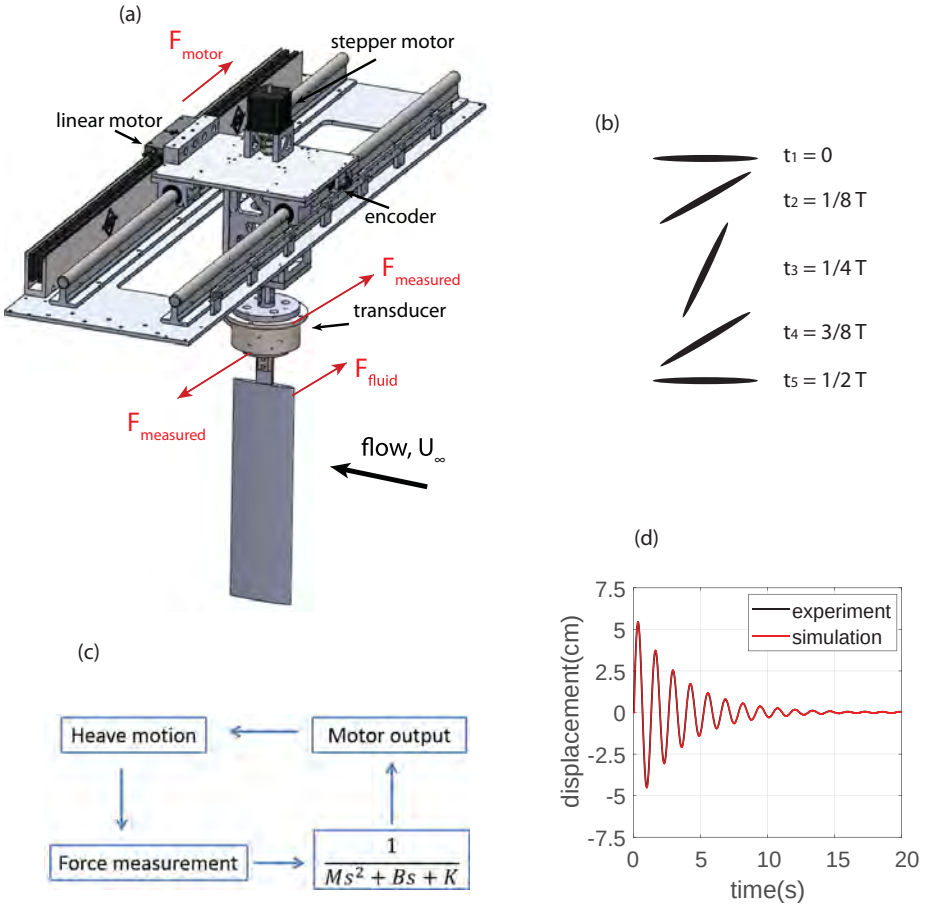


FIG. 1. (a) Experimental system with the hydrofoil, force transducer, rotary and linear motors and encoders; (b) top view of one typical kinematics of the hydrofoil ($\pi/2$ phase difference between pitch and heave) with five different positions (only the downstroke is shown here due to its stroke symmetry); (c) the force-feedback control system diagram; (d) "ring-down" experiment comparing the measured heaving position and the theoretical position.

II. EXPERIMENTAL SETUP

A. Physical apparatus

The experiments were carried out in a free-surface circulating flume at Brown University with a test section of 80 cm (wide) × 60 cm (deep) × 4 m (long). Experiments were typically conducted at a free-stream velocity, U_∞, of 0.4 m/s, measured using an Acoustic Doppler Velocimeter (Vectrino, Nortek AS), positioned upstream of the experiment area. As shown in Fig. 1(a), the hydrofoil has an elliptical profile with chord length, $c = 0.1$ m, and span, $s = 0.35$ m (aspect ratio, AR $= 3.5$). The foil is vertically suspended from a six-axis force-torque sensor (ATI IP65), which is attached to a shaft controlled by a rotary motor for pitch motion (Applied Motion Products HT23-593D) and linear motor (Aerotech BLM-142-A-AC-H-S-5000) for transverse heave motion across the flume. In these experiments, the pitching kinematics of the hydrofoil are prescribed by the user. However, in the heave direction, the hydrofoil is free to move, subject to fluid and inertial forces, and connected to a virtual spring-damper that is defined using the cyber-physical control system. Figure 1(b) demonstrates one of the typical hydrofoil motions, in this case with a phase difference of $\pi/2$ between the pitching and heaving motions. Five different hydrofoil positions are marked at different times during the downstroke of the cycle. The instantaneous heaving position, $h(t)$, and pitching position, $\theta(t)$, were measured in real time using optical encoders (U.S.

Digital E3-2500-250-IE-D-D-1) and the heaving position also served as the feedback signal for the servo motor controller. The forces (lift and torque) on the hydrofoil were directly measured by a six-axis force-torque sensor and sampled at 2000 Hz using an analog-to-digital converter (National Instruments). The nondimensional lift and torque coefficients are defined as

$$C_L = \frac{F}{0.5\rho U_\infty^2 sc} \quad \text{and} \quad C_\tau = \frac{\tau}{0.5\rho U_\infty^2 sc^2}. \tag{1}$$

As discussed in Refs. [2,3], the power extraction can be divided into contributions from the heave component and the pitch component. The cycle-averaged power coefficient and energy harvesting efficiency are then given as

$$\text{heave power:} \quad C_h = \frac{< F(t)\dot{h}(t) >}{0.5\rho U_\infty^3 cs}, \quad \text{pitch power:} \quad C_p = \frac{< \tau(t)\dot{\theta}(t) >}{0.5\rho U_\infty^3 cs}, \tag{2}$$

$$\text{heave efficiency:} \quad \eta_h = \frac{< F(t)\dot{h}(t) >}{0.5\rho U_\infty^3 A_s}, \quad \text{pitch efficiency:} \quad \eta_p = \frac{< \tau(t)\dot{\theta}(t) >}{0.5\rho U_\infty^3 A_s}, \tag{3}$$

where $\dot{h}(t)$ and $\dot{\theta}(t)$ are the heaving velocity and pitching velocity, respectively, and A_s is the swept area of the foil defined as the foil's maximum transverse excursion multiplied by the span [3,33].

B. Cyber-physical system

The elastically mounted hydrofoil can be treated as a spring-mass-damper system forced by a fluid force, F_{fluid}:

$$m\ddot{y} + b\dot{y} + ky = F_{\text{fluid}}, \tag{4}$$

where y is the displacement in the heave direction, m is the hydrofoil mass, and b and k are the damping and spring stiffness of the mounting system. At a Reynolds number of $\mathcal{O}(10^4)$, the inertial force from the fluid, $0.5\rho U_\infty^2 sc$, is assumed to be the dominant scaling force [30] and based on this assumption, we nondimensionalize the governing Eq. (4):

$$m^*\ddot{y}^* + b^*\dot{y}^* + k^* y^* = C_F, \tag{5}$$

where $y^* = y/c$ is the scaled heave amplitude, $C_F = F_{\text{fluid}}/(0.5\rho U_\infty^2 sc)$ is the coefficient of the fluid forcing, and the nondimensional parameters are given by

$$b^* = \frac{b}{0.5\rho U_\infty sc}, \tag{6}$$

$$k^* = \frac{k}{0.5\rho U_\infty^2 s}, \quad \text{and} \tag{7}$$

$$m^* = \frac{m}{0.5\rho c^2 s}. \tag{8}$$

Instead of using physical springs and dampers to achieve the elastic mounting in the heave direction, we employed a cyber-physical system that simulates the properties of the springs and dampers by implementing a force-feedback control system [25,26,28,30,34]. The cyber-physical system is schematically illustrated in Fig. 1(c). The fluid forces on the hydrofoil are measured and used as input to the feedback control system. The target heaving position output is determined by the integrated contribution of both the fluid forces and the structural forces (forces due to the springs, dampers and mass). Similar to the CPFD control system presented by Mackowski and Williamson [26], we start the force analysis with the Newton's law, $F = ma$, where F is the force that determines the motion of interest, and includes both the measured fluid force and the virtual elastic force computed in the control system:

$$F_{\text{fluid}} + F_{\text{virtual}} = ma, \tag{9}$$

where $F_{\text{virtual}} = -m\ddot{y} - b\dot{y} - ky$ is the structural forces, simulating a spring-mass-damper system. In contrast to Mackowski and Williamson's implementation, however, we integrate Eq. (9) twice to obtain the target discreet position output, Δy, for the flow-induced heave motion:

$$\iint_{t_0}^{t_0+\Delta t} F_{\text{fluid}} + F_{\text{virtual}}\, dt = m\Delta y. \tag{10}$$

One benefit of this approach is that noise in the measured force can be reduced significantly by the integration, thus avoiding the use of filters and the filter-related phase delay. Another benefit is that the system becomes more robust and less sensitive to disturbance after the use of twice integration.

Similar to the studies of elastically mounted cylinders [25,35], the fluid force in Eq. (4) can be decomposed into two components: one in phase with the foil velocity ($\dot{y}$) and the other in phase with the foil acceleration ($\ddot{y}$). For illustrative purposes, we can assume a sinusoidal flow-induced displacement and fluid force, $y(t) = H_0 \cos(\omega t)$ and $F_{\text{fluid}} = F_0 \cos(\omega t + \phi)$, where ϕ is the phase difference between the fluid force and the displacement. Then the fluid force can be rewritten as the following:

$$F_{\text{fluid}} = \frac{F_0 \sin\phi}{H_0\omega}\dot{y} - \frac{F_0 \cos\phi}{H_0\omega^2}\ddot{y}. \tag{11}$$

The first term is related to the fluid damping effect (in phase with the velocity) while the second term contributes to the added mass effect (in phase with the acceleration). Substituting this into the equations of motion [Eq. (4)], rearranging the terms and nondimensionalizing as described above, we obtain

$$\left(m^* + \frac{H_0^* C_{F_0}\cos\phi}{\pi^2 St^2}\right)\ddot{y}^* + \left(b^* - \frac{C_{F_0}\sin\phi}{\pi St}\right)\dot{y}^* + k^* y^* = 0, \tag{12}$$

where $St = 2fH_0/U_\infty$ is the Strouhal number, $C_{F_0} = F_0/0.5\rho U_\infty^2 sc$ and $H_0^* = H_0/c$. From this we can see that both the fluid damping and the added mass terms are related to the phase difference between the heaving motion and the fluid forcing, ϕ. It should be noted that when the system reaches a steady state motion, Eq. (12) inherently requires the damping term to vanish (the fluid damping cancels out the physical damping b). From the perspective of energy budget, it is clear to see that a steady state motion indicates that the energy extracted from the fluid (through negative fluid damping) is completely dissipated by the physical damping so that the total energy in the system remains unchanged. This will become important later in the discussion of the energy harvesting performance with respect to phase.

Equation (12) also highlights the role of added (fluid) mass to the dynamics of the system. At steady state, when the effective damping is zero, the natural frequency of oscillation is determined from the combination of stiffness and both the physical and added mass. The current experiments were conducted with a relatively large mass ratio, $m^* \sim 5$, and we therefore expect the physical mass to dominate over the added mass and the resonant frequency of the system to be close to the structural frequency, $2\pi f_n = \sqrt{k/m}$. However, it is also worth noting that even for low mass ratios, the role of added mass can change dramatically with the phase between the hydrofoil motion and the fluid forcing due to the $\cos\phi$ dependency in Eq. (12).

Validation

"Ring-down" experiments, using different elastic parameters (mass, stiffness, and damping), were performed to validate the system behavior. As an example, Fig. 1(d) shows the ring-down response with a fixed set of elastic parameters (stiffness $k = 200$ N/m, damping $b = 5$ kg/s and mass $m = 8.5$ kg), performed in the air. Due to the cyber-physical mass, stiffness and damping, the foil exhibits a damped oscillatory decay back to its neutral position. The measured heave position in the "ring-down" experiment is then compared with the theoretical position outputs using the same elastic parameters [Fig. 1(d)]. The results from the ring-down experiments show that the

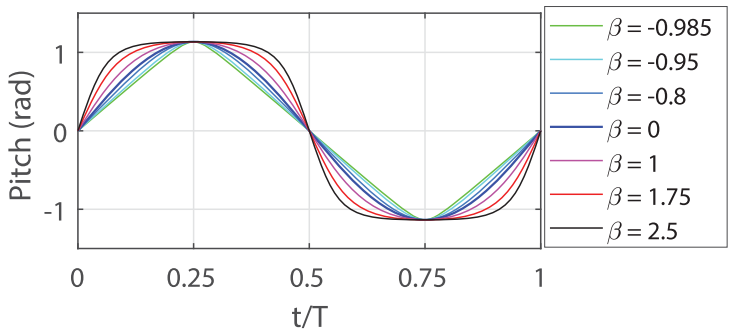


FIG. 2. Nonsinusoidal pitch profiles: $-1 < \beta < 0$ for triangular profiles; $\beta = 0$ for sinusoidal and $\beta > 0$ for trapezoidal profiles.

experimental measurement matches the theoretical position well (phase lag less than 5 degrees), even when the motion amplitude is small. As reported by Mackowski and Williamson [26], a phase lag of five degrees at the system's natural frequency generates no significant change in the experimental vibration response.

C. Nonsinusoidal pitch profiles

Several researchers [e.g., 3,11,12] have reported on the energy harvesting performance of a hydrofoil with a fully prescribed sinusoidal and nonsinusoidal motion. In these experiments we also explored both sinusoidal and nonsinusoidal pitch profile effects on the power extraction performance of an elastically mounted hydrofoil. Adopting the definition from Lu *et al.* [14], the nonsinusoidal pitch profiles are defined as

$$\theta(t) = \begin{cases} \frac{\theta_0 \sin^{-1}[-\beta \sin(2\pi f t)]}{\sin^{-1}(-\beta)}, & -1 \leqslant \beta < 0, \\ \theta_0 \sin(2\pi f t), & \beta = 0, \\ \frac{\theta_0 \tanh[\beta \sin(2\pi f t)]}{\tanh(\beta)}, & \beta > 0, \end{cases}$$

where β is a parameter characterizing the shape of the pitch profile: triangular ($-1 < \beta < 0$), sinusoidal ($\beta = 0$) and trapezoidal ($\beta > 0$) as shown in Fig. 2. As discussed by Lu *et al.* [36], β serves as a measure of the rate of change in pitch reversal; a larger β suggests a faster pitching rate and a larger pitching acceleration. This will be revisited later in the discussion of nonsinusoidal profile effects on energy harvesting performance.

D. Parametric variations

In the current manuscript, we first present results from a parametric sweep over a large range of stiffness (from 0 to 450 N/m) and damping (from 3.5 to 30 kg/s) for a fixed mass ratio and using a sinusoidal pitch profile ($\beta = 0$). By varying the actuated pitch frequency and damping, the effects of reduced frequency and damping coefficient are discussed in detail to understand the optimal parameters for energy harvesting performance. In the last part of the paper, the effects of different prescribed pitch profiles on energy harvesting are discussed on the energy harvesting performance.

III. RESULTS AND DISCUSSION

A. Parametric sweep of frequency ratio and damping coefficient

With a fixed sinusoidal pitch motion profile and a constant mass ratio of 4.9, a parametric sweep with respect to the stiffness, k, and the damping, b, were carried out to investigate the response of the flow-induced heaving motion and the resulting power extraction performance of the elastically

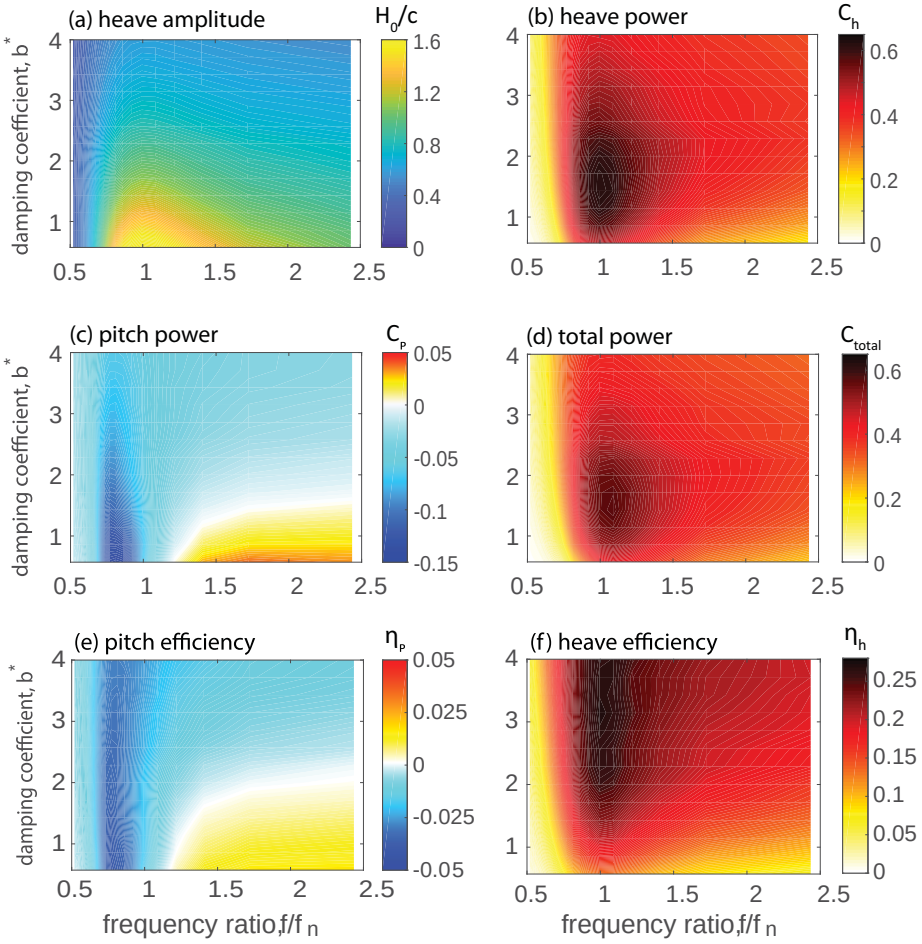


FIG. 3. Contour plots of (a) induced heave amplitude, H_0, (b) heave power coefficient, C_h, (c) pitch power coefficient, C_p, and (d) total power coefficient, C_{total}, (e) pitch efficiency, η_p, (f) heave efficiency, η_h, with respect to frequency ratio, f/f_n, and damping coefficient, b^*; parameters: prescribed sinusoidal pitch profile with pitch amplitude, $\theta_0 = 65^\circ$.

mounted hydrofoil. Results of the parametric sweep (Fig. 3) illustrate (a) the flow-induced heave amplitude, H_0, (b) the heave power coefficient, C_h, (c) the pitch power coefficient, C_p, (d) the total power coefficient, C_{total} (sum of the heave and pitch components), (e) the pitch efficiency, η_p, and (f) the heave efficiency, η_h.

First, for a fixed value of the frequency ratio, the induced heave amplitude is shown to decrease with damping coefficient. When varying the frequency ratio at a fixed damping coefficient, the maximum induced heave amplitude was observed around frequency ratio $f/f_n = 1$, which is usually referred as the resonant phenomenon [35]. This resonance suggests that, at this frequency, the preferred vortex shedding frequency is identical to the natural frequency of the energy harvester. A precipitous drop in the heave amplitude and the heave power is observed at $f/f_n < 1$, while the decrease is more smooth for $f/f_n > 1$ [Figs. 3(a) and 3(b)].

Second, when comparing the heave and pitch power coefficients [Figs. 3(b) and 3(c)], one can see that the heave power component is generally much larger than the pitch power component, particularly when the frequency ratio is close to 1. Therefore, the power extracted from the heave motion dominates the energy harvesting process, a result consistent with the results in literature using a prescribed oscillating hydrofoil [2,3,33]. For the most part, the pitch power is slightly negative except for a small region with small damping coefficient and high frequency ratio.

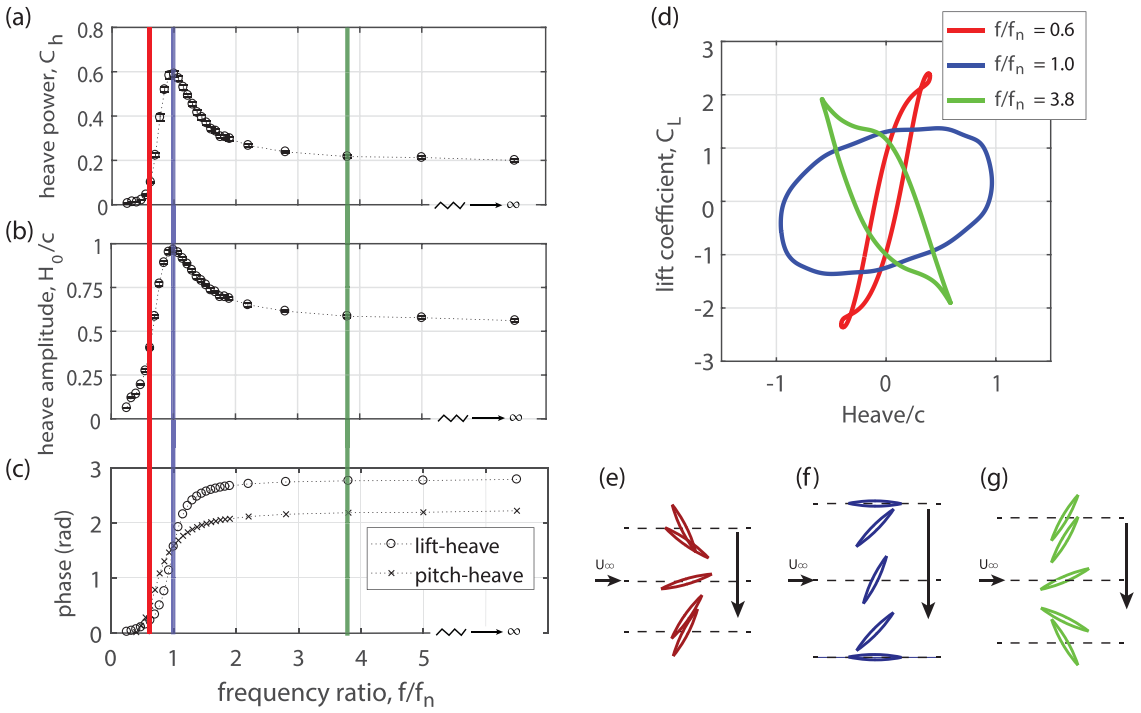


FIG. 4. Response of (a) heave power coefficient, (b) flow-induced heave amplitude, and (c) phase difference between the lift force and the flow-induced heave motion (circles ○) and phase difference between the prescribed pitch motion and the flow-induced heave motion (cross ×) at a fixed damping coefficient of 1.5; (d) lift-heave portraits for three different frequency ratios: $f/f_n = 0.6$ (red), $f/f_n = 1.0$ (blue), $f/f_n = 3.8$ (green). Foil kinematics in half a cycle: (e) $f/f_n = 0.6$ (red), (f) $f/f_n = 1.0$ (blue), (g) $f/f_n = 3.8$ (green).

Thirdly, a clearly defined peak in the heave power coefficient is observed at the frequency ratio around 1, and the damping coefficient around 1.5 [Fig. 3(b)]. However, the maximum power loss due to pitch appears around frequency ratio of 0.8 [Fig. 3(c)], which is likely due to the high torque required to rotate the hydrofoil in the presence of a strong leading edge vortex (LEV) that forms as the blade reaches its peak heave amplitude. This conjecture is supported by the PIV measurements from Kim *et al.* [3], which showed that a poorly positioned LEV on the hydrofoil resulted in energy loss in the pitch performance. Thus, in general a high net power extraction output is achieved, as shown in Fig. 3(d), with the frequency ratio for peak performance slightly larger than 1. Since the heave power component contributes most of the power extracted from the flow, in the rest of the paper, we will focus on the energy harvesting performance of the flow-induced heaving motion.

Last, the pitch efficiency [Fig. 3(e)] is small and slightly negative for most part, while the heave efficiency [Fig. 3(f)] is positive, reaching a maximum at the frequency ratio around 1 and, in general, much larger than the pitch component. However, instead of a clearly defined peak in the heave power coefficient [Fig. 3(b)], the heave efficiency [Fig. 3(f)] shows a flat peak at damping coefficient $b^* > 2$. This is not surprising considering that the flow-induced heave amplitude (which appears in the denominator of the efficiency definition) decreases with increasing damping coefficient, thus compensating the drop in the power extraction and resulting in a high efficiency performance [Eq. (3)].

B. Frequency ratio effects

In this section, a specific case with a fixed damping coefficient of $b^* = 1.5$ is examined in more detail to better understand the effect of the frequency ratio on the flow-induced heaving motion and the power extraction performance. Figure 4 shows the response of (a) the heave power coefficient,

C_h, (b) the heave amplitude, H_0, and (c) the phase difference between the lift force and the flow-induced heave and the phase difference between the prescribed pitch motion and the flow-induced heave motion. The force portrait in Fig. 4(d) shows the lift-heave relation, in which the area enclosed by the curve denotes the work done by the lift force during a cycle.

Echoing the results from the full parameter sweep (Fig. 3) we see a sharp rise in both heave amplitude and heave power as the frequency ratio approaches one, while a more gentle decay is observed for frequencies above the resonance [Figs. 4(a) and 4(b)]. The broad resonant peaks in Figs. 4(a) and 4(b) signify strong damping in the system which is, of course, advantageous for energy harvesting since "damping" represents energy extracted from the flow. Consistent with classical second-order linear system theories, a phase jump around π is observed as the system passes through resonance [Fig. 4(c)].

Figure 4(d) shows the lift force portrait for three different frequency ratios, with the curve-enclosed area representing the energy extracted by the foil in a cycle. When the frequency ratio is smaller than one (the red color scheme in Fig. 4), the phase difference between pitch and heave is close to 0, away from the optimal phase of $\pi/2$ [Fig. 4(c)]. In this case, the lift force reaches its maximum value at the end of the heave stroke, where the angle of attack (AOA) is large but the heave velocity is at its minimum [Fig. 4(e)], resulting in low energy extraction performance [Fig. 4(d)]. Similar results are observed when the frequency ratio is much larger than 1 (the green color scheme) when the lift force leads the heave motion. In both cases the peak hydrodynamic lift force is produced at the pitch reversal points where the heave velocity is low due to the poor phase synchronization. In these suboptimal cases, the phase portraits of power extraction are compressed [the red and green curves in Fig. 4(d)] and the amplitude of the flow-induced heave motion is small since not enough power is extracted from the fluid to sustain the passive heave motion.

In contrast to these cases, when the frequency ratio is close to one (the blue color scheme), a phase difference of $\pi/2$ is produced between the lift and the flow-induced heave motion and also between the prescribed pitch motion and the flow-induced heave motion [Fig. 4(c)], and with this phase synchronization, a peak power coefficient is achieved together with the maximum flow-induced heave amplitude [Figs. 4(a) and 4(b)]. This is also reflected in the phase portrait which exhibits a maximum enclosed area [blue, Fig. 4(d)], indicating maximum energy harvesting per cycle. This optimal phase synchronization is in agreement with other published results [1,4,37]. Using a hydrofoil with both prescribed heaving and pitching motions, those researchers report that a phase difference of $\pi/2$ ensures a good force-velocity synchronization for energy extraction. Here we achieve peak performance with only prescribed pitching motion.

As discussed by Hover *et al.* [25,38] and also shown in Eqs. (11) and (12), the lift force can be divided into two components: $C_{Lv} = C_L \sin\phi$, in phase with the heave velocity and serving as a damping factor, and $C_{La} = -C_L \cos\phi$, which is in phase with the acceleration and serves as an added mass factor. As before, ϕ is the phase difference between the lift force and the heave motion. Since the power is calculated from the product of the lift force and the heave velocity [Eq. (2)], positive values of C_{Lv} are associated with energy extraction from the flow. One can see from the above two components that C_{Lv} reaches its maximum value at $\phi = \pi/2$, producing the largest excitation (heave amplitude) and highest performance of energy extraction, in agreement with the current observations [Fig. 4(a) and 4(b)]. At the same time, and as previously highlighted in Eq. (12), when $\phi = \pi/2$, we see that the added-mass factor (C_{La}) vanishes, confirming that the added mass effect is small at this resonant condition. This is further validated in our experimental observation that the maximum flow-induced heave amplitude and heave power are achieved at frequency ratio $f/f_n \sim 1$ (Fig. 4), where the natural frequency, f_n is based solely on the structural support of the hydrofoil.

In particular, as the frequency ratio becomes very large (stiffness $k \sim 0$), the energy harvesting performance is far from the optimum [Fig. 4(a)], which contradicts the numerical results that zero stiffness produces the optimal performance of energy extraction [21]. This discrepancy may be due to the fact that the linear model in Zhu's simulation [21] does not include the mass and inertial of the foil, and hence does not exhibit a natural frequency. The above analysis of the frequency

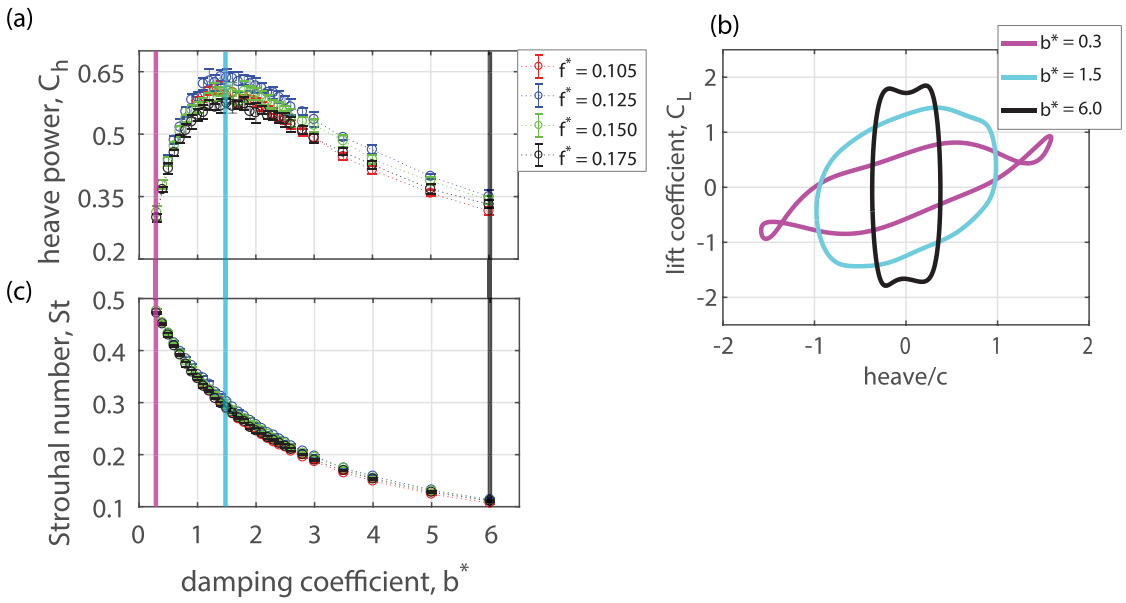


FIG. 5. At a fixed frequency ratio ($f/f_n = 1$), (a) the heave power coefficient, C_h, is plotted with respect to damping coefficient; (b) the lift-heave portrait demonstrates the work done by the lift force for different damping coefficient, $b^* = 0.3$, 1.5, and 6.0, at a reduced frequency $f^* = 0.150$; (c) the Strouhal number, $\mathrm{St} = 2fH_0/U_\infty$, is plotted with respect to damping coefficient, b^*, for different reduced frequency, $f^* = fc/U_\infty$.

ratio effects on the energy harvesting performance is based on a mass ratio around 5 ($m^* = \frac{m}{0.5\rho c^2 s}$). Further experiments with different mass ratio (m^* varying from 3 to 15) confirm that the optimal frequency ratio for energy harvesting is $f/f_n = 1$ (results not shown here).

C. Damping coefficient effects

As discussed earlier, in Sec. III A, the damping coefficient plays an important role in determining the amplitude of the flow-induced heave motion and the related energy harvesting performance. To further understand the damping effects, in this section, we discuss experiments conducted at different reduced frequencies but varying the stiffness of the heave mounting so that the frequency ratio was held constant at a value of 1. Figure 5(a) shows the heave power coefficient, C_h, as a function of damping coefficient, b^*, at four different reduced frequencies. For each reduced frequency tested, the peak performance of energy harvesting is achieved at the damping coefficient of 1.5, confirming the observation of the optimal damping coefficient in Sec. III A. The results also indicate that the peak in the heave power coefficient has a weak, nonmonotonic dependence on the reduced frequency, f^*, rising to a maximum near $f^* = 0.125$ and then decreasing at large reduced frequencies. This agrees well with the experimental results from Kim *et al.* [3]. This f^*-dependence will become important in Sec. III C 1, where we present a model for the power coefficient.

Lift-heave phase portraits for three representative damping coefficients are presented in Fig. 5(b), with the extracted energy per cycle represented by the area enclosed by the curves. For small damping (the pink color scheme), the induced heave amplitude is large (more than 1.5 chord lengths), but the lift force throughout the energy harvesting cycle is small, resulting in a low power extraction coefficient [Fig. 5(a)]. In addition, a negative hysteresis is observed near the maximum heave positions, which puts energy back into the flow, similar to the negative hysteresis observed by Onoue *et al.* [30] for a pitching flat plate. As indicated by Onoue and Breuer's PIV results [31], the negative hysteresis in the current study suggests that the LEV detaches from the foil, causing the lift force to drop. However, a second LEV starts to form before the heave cycle is complete, causing

the lift force to rise again near the top of the stroke. That second LEV impedes the return motion of the foil, transferring energy back into the flow.

By contrast, for a large damping coefficient (the black color scheme), the induced heave amplitude is small (less than 0.5 chord lengths), and although a high lift force is generated, the overall power coefficient is again small, this time due to the low heave velocity. At the optimal damping coefficient of 1.5 (the cyan color scheme), the largest enclosed area is produced by a modest lift force and a heave amplitude about one chord length [Fig. 5(b)]. This optimal heave amplitude (about one chord length) is in agreement with the results found using a prescribed pitching and heaving hydrofoil [2–4].

Scaling of the Strouhal number

In addition to the power extraction performance, another output from the semipassive energy harvester is the Strouhal number, $\mathrm{St} = 2fH_0/U_\infty$, where H_0 is the flow-induced heave amplitude. As shown in Fig. 5(c), the Strouhal number exhibits a monotonic dependence on damping but collapses extremely well over a range of reduced frequencies between 0.105 and 0.175. Not only does the response of the power and Strouhal number scale with damping, but at the optimal damping coefficient ($b^* = 1.5$), the elastically mounted system produces and maintains a Strouhal number of 0.3, which is also observed as the optimal value in literature [2,4]. We can fit this Strouhal number data with an empirical equation:

$$\mathrm{St} = 0.27e^{-0.94b^*} + 0.28e^{-0.16b^*}, \tag{13}$$

which will be used in the development of a theoretical model later in this section. To understand the collapse of the Strouhal number, we define the nominal effective angle of attack (AOA) of the foil to the flow,

$$\theta_{e0} = \theta_0 - \arctan(V_{h0}/U_\infty), \tag{14}$$

which accounts for the contributions from the pitch amplitude, θ_0, and the maximum heave velocity, V_{h0}. As the flow-induced heave motion is quasiharmonic (the first Fourier mode accounts for 95% of the observed heave kinematics), we can approximate the heave motion as sinusoidal, thus the maximum heave velocity can be estimated as $V_{h0} = 2\pi fH_0$. Considering the definition of the Strouhal number, the nominal effective AOA can be rewritten as $\theta_{e0} = \theta_0 - \arctan(\pi\,\mathrm{St})$, which indicates that, at a fixed frequency ratio of 1 and for a fixed damping coefficient, the time history of the effective angle of attack is also fixed over a wide range of physical parameters. This result finds its counterpart in the experimental results of Baik *et al.* [10]. By varying the reduced frequency and heave amplitude while keeping the same effective AOA of the foil to the flow, Baik *et al.* [10], using PIV measurements, found that the trajectories of the LEV were identical for the range of parameters explored, suggesting that, in the current study, the LEV trajectories should also be identical for different reduced frequencies (but the same Strouhal number). This conjecture will be tested in future experiments that measure the flow fields.

The same dynamic similarity should also be observed in the hydrodynamic forces acting on the foil, and this assertion is confirmed in Fig. 6, which shows an excellent collapse in both the lift coefficient [Fig. 6(a)] and the torque coefficient [Fig. 6(b)], especially during the first part of the cycle, $t/T = 0 - 0.25$. We do see minor differences in the hydrodynamic forces at different frequencies during the latter part of the cycle, $t/T = 0.25$–0.5, but they are small and do not appear to follow any consistent trend. However, during $t/T = 0.25$–0.5, one can see [Fig. 6(b)] that the peaks in the torque coefficient are higher and appear later in the cycle for larger reduced frequencies. This higher peak in torque can be attributed to the increased added-mass effect at larger pitching reduced frequencies, which is supported by Rival *et al.* [17] and Eldredge and Jones [8], who reported that the noncirculatory (added-mass) contribution to the hydrodynamic forces was related to the inertial reaction of the fluid and thus increased with the reduced frequency. This reduced frequency dependency is also observed by Baik *et al.* [10], who demonstrated that, with

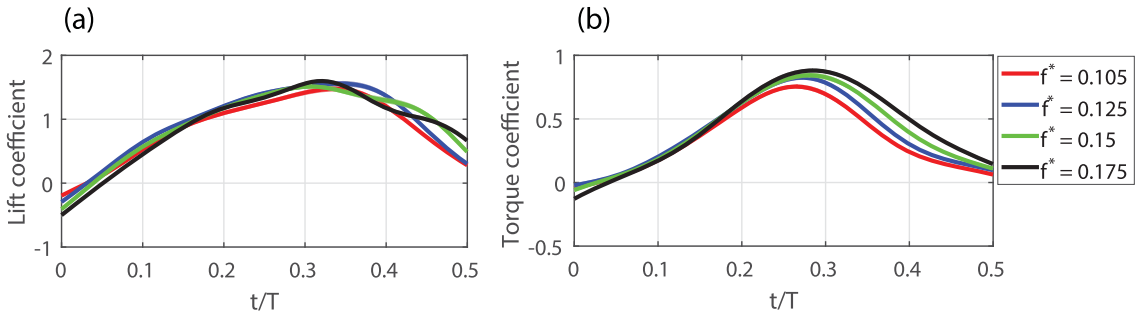


FIG. 6. Temporal evolution of (a) lift coefficient and (b) torque coefficient for different reduced frequencies, at a fixed frequency ratio of 1 and a fixed damping coefficient of 1.5. Data of half a cycle are shown for simplicity due to the dynamic symmetry.

the same effective AOA history, the observable trend of the force histories was strongly associated to the Strouhal number, with small modifications due to reduced frequency—similar to the present observations of forces in Fig. 6. In addition, Onoue *et al.* [32] reported that an increase in reduced frequency helped to mitigate the drift of the LEV core toward the trailing edge, thus delaying the vortex separation from the hydrofoil. This delayed movement of the LEV core due to the reduced frequency explains the late peaks in the torque coefficient for high reduced frequencies [Fig. 6(b)] in the current study.

D. Comparisons with a reduced-order model

The insights discussed in the previous sections can be incorporated into a simple model that helps to understand the behavior of this energy-harvesting system. From classical vibration theory, power dissipated by the damper in a forced oscillator is given by $b\dot{h}^2(t)$ [39]. Normalizing the damper dissipation by the kinetic energy flux in the oncoming flow, $0.5\rho U_\infty^3 sc$, we can write the power extraction coefficient for the heave motion as

$$C_h = \frac{< b\dot{h}^2(t) >}{0.5\rho U_\infty^3 sc}. \tag{15}$$

Considering the definition of damping coefficient [Eq. (6)] and assuming a sinusoidal flow-induced heave motion, $h(t) = H_0 \sin(2\pi ft)$, where f and H_0 are the heave motion frequency and amplitude, respectively, the power coefficient [Eq. (15)] can be rewritten as

$$\begin{aligned} C_h &= \frac{b}{0.5\rho U_\infty sc}\left(\frac{2\pi fH_0}{U_\infty}\right)^2 < \cos^2(2\pi ft) > \\ &= 0.5b^*(\pi \mathrm{St})^2, \end{aligned} \tag{16}$$

where $\mathrm{St} = 2fH_0/U_\infty$ is the Strouhal number.

Since the Strouhal number is a universal function of the damping coefficient (Fig. 5), we can substitute the empirically determined equation for the Strouhal number [Eq. (13)] into the equation for the power coefficient and express the heave power coefficient C_h solely as a function of the damping coefficient, b^*. Doing so, and taking the derivative of that function with respect to b^*, we find that the maximum heave power coefficient is achieved at $b^* = 1.46$, which agrees very well with the observation ($b^* \sim 1.5$) in the experiments (Fig. 3, Sec. III A.)

The equation for the power coefficient [Eq. (16)] also suggests a linear scaling with damping coefficient, a prediction confirmed by the experimental data over all frequencies tested (Fig. 7). The slope of the experimental data, though linear, is slightly smaller than that predicted by the theoretical model, a discrepancy probably due to the breakdown of the assumption of a sinusoidal heave motion, which is observed to be less accurate as the damping coefficient becomes large.

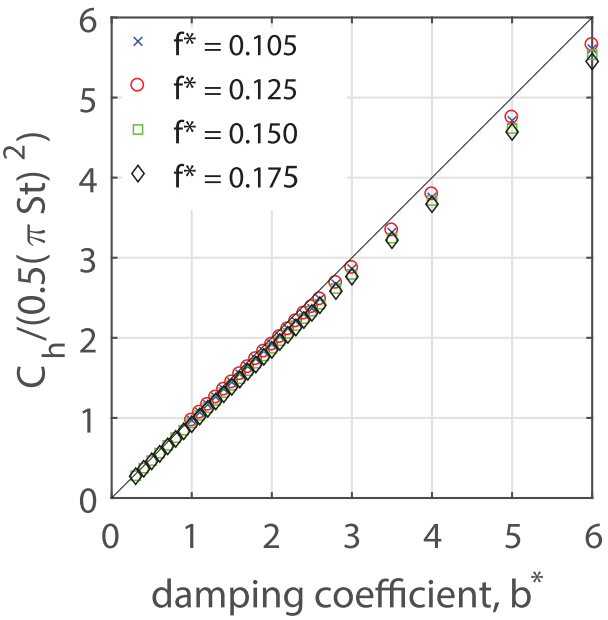


FIG. 7. Relationship between heave power coefficient, scaled by the Strouhal number squared, and the damping coefficient. Solid line: theoretical prediction [Eq. (16)]; symbols: experimental results at several frequencies, all at a fixed frequency ratio of 1.

E. Nonsinusoidal pitching profiles effects on energy harvesting

It has been reported that nonsinusoidal motion profiles can potentially increase the energy harvesting performance of a flapping hydrofoil by changing the effective angle of attack of the foil and the resulting vortex dynamics and hydrodynamic forces [11–15]. In the current study, we will focus on the nonsinusoidal pitch kinematics since the pitch motion is prescribed while the the heave motion is flow-induced (elastically mounted). In addressing the effects of the pitching kinematics, we first revisit the effect of frequency ratio, f/f_n, and damping coefficient, b^*, and expand on our earlier observation (Fig. 3) that the optimal performance of energy extraction is achieved at the frequency ratio of 1 and damping coefficient of 1.5. We now see that this result is maintained for different pitching profiles (Fig. 8). However, the pitch profile has a significant effect, particularly near the optimal performance region ($f/f_n = 1$ and $b^* = 1.5$). Comparing the energy harvesting performance between different pitching profiles, we see from Fig. 8 that the triangular pitch profiles ($-1 < \beta < 0$) reduce the power extraction performance, compared to the sinusoidal pitch profile, while the trapezoidal profiles ($\beta > 0$) increase the power coefficient.

If we look into this with finer resolution, then we can vary the profile parameter β at a fixed frequency and damping ($f/f_n = 1$ and $b^* = 1.5$), and we see (Fig. 9) that the heave power performance is improved by the trapezoidal pitch profiles ($\beta > 0$) compared with the sinusoidal profile ($\beta = 0$), which is in agreement with the numerical results of Xiao *et al.* [16]. The power coefficient reaches 0.9 at $\beta \sim 2$—a 50% improvement over the sinusoidal performance—before levelling off. In contrast, the triangular pitch profiles ($-1 < \beta < 0$) reduce the heave power output especially with a precipitous drop observed at $-1 < \beta < -0.75$. The heave power coefficient predicted using our simple theoretical model [Eq. (16)] is also presented and compared with the measured heave power coefficient [Fig. 9(a)]. The good agreement between the two curves validates the utility of the model, even for different pitch profiles, ranging from triangular to trapezoidal profiles. It is not surprising that the prediction lies slightly above the experimental values, considering that the measured flow-induced heave profile is not purely sinusoidal, which is assumed by the model.

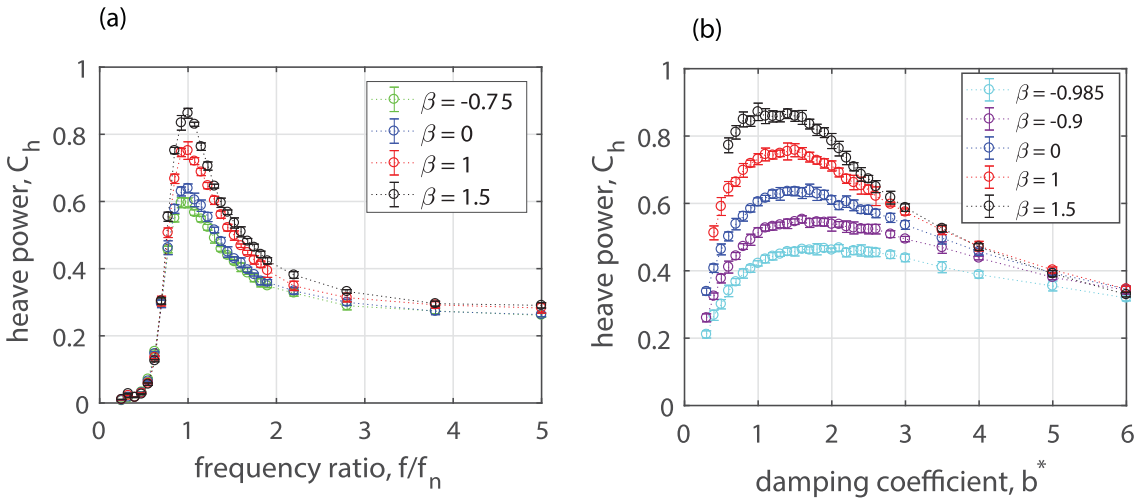


FIG. 8. (a) Heave power coefficient as a function of frequency ratio, f/f_n, at different pitch profiles (β); (b) heave power coefficient as a function of damping coefficient, b^*, at different pitch profiles (β).

It is perhaps unsurprising that the pitch power loss increases with β [Fig. 9(b)] since more power is required to initiate the faster pitch reversal in the trapezoidal pitch profiles [11]. However, such power loss (for example, -0.08 at $\beta = 2.5$) is much smaller than the improvement in the heave power (0.30 at $\beta = 2.5$), resulting in a net improvement in the total power output in trapezoidal pitch profiles [the cyan line in Fig. 9(a)]. This loss-gain tradeoff is eventually lost at large values of β, and by $\beta = 2.25$, the cost associated with the increased negative pitching power is greater than the benefit associated with the improved positive heave power, resulting in a levelling off and eventual decline in the total power coefficient [the cyan line in Fig. 9(a)].

Figure 9(c) shows the lift-heave phase portrait for three different pitching profiles as identified in Fig. 9(a). With the extracted energy per cycle represented by the enclosed area, Fig. 9(c) confirms the previous result that the trapezoidal pitch profile (the green curve) extracts much more energy in a cycle than the sinusoidal (the blue curve) and triangular (the red curve) profiles, consistent with the power coefficient [Fig. 9(a)]. In addition, we can see from Fig. 9(c) that the increment of power

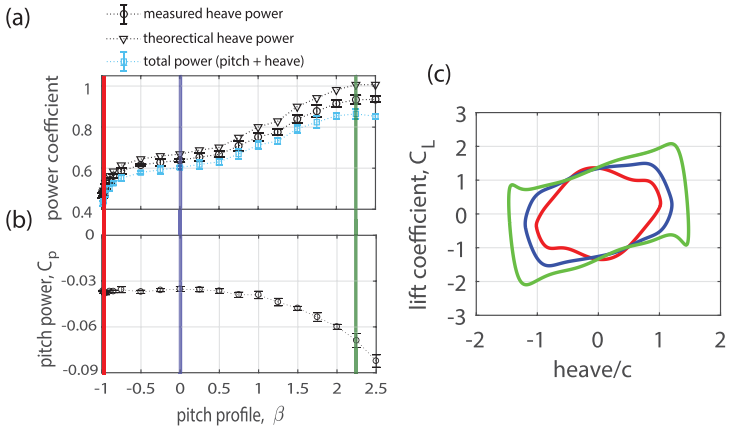


FIG. 9. (a) Heave power coefficient measured in the experiment and predicted by the theoretical model [Eq. (16)] and total power coefficient measured in the experiment, (b) pitch power coefficient, and (c) lift-heave phase portrait. Parameters: reduced frequency $f^* = 0.125$, frequency ratio, $f/f_n = 1$, damping coefficient, $b^* = 1.5$.

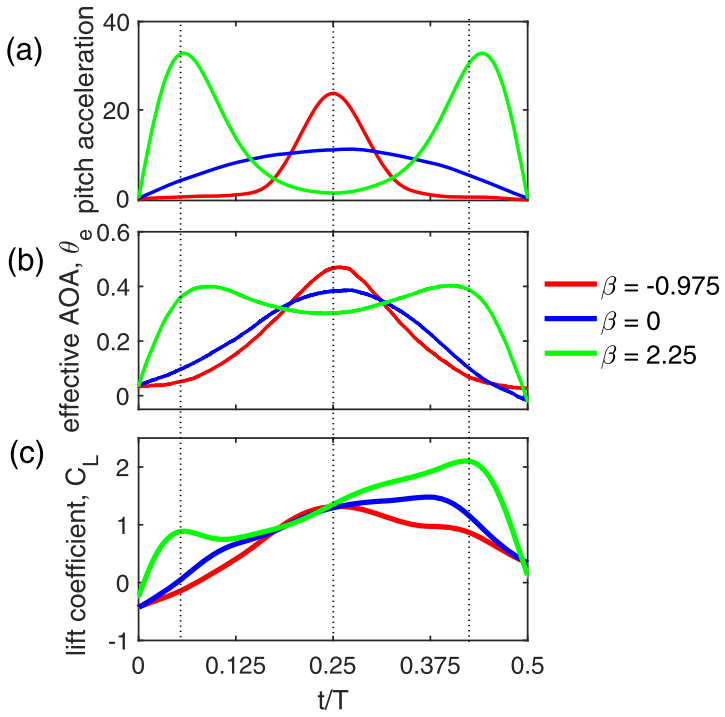


FIG. 10. Instantaneous (a) pitch acceleration (rad/s^2), (b) effective AOA, and (c) lift coefficient are shown for three pitch profiles ($\beta = -0.975$ (triangular), 0 (sinusoidal), and 2.25 (trapezoidal), for half cycle). The instantaneous effective AOA is given by $\theta_e(t) = \theta(t) - \arctan(V_h(t)/U_\infty)$, where $V_h(t)$ is the instantaneous heave velocity. Parameters: reduced frequency, $f^* = 0.125$, frequency ratio, $f/f_n = 1$, damping coefficient, $b^* = 1.5$.

output comes from two parts: the increase in the flow-induced heave amplitude and the enhancement of lift force, which will be discussed in detail later in this section.

As seen in Sec. III C 1, the effective angle of attack (AOA) plays an important role in the hydrodynamic force production and similar effective AOA histories are accompanied by similar hydrodynamic forces on an oscillating hydrofoil. To understand the hydrodynamic origins of the lift force enhancement associated with the different pitch profiles, time histories of the pitch acceleration, lift coefficient, and the associated instantaneous effective AOA are shown in Fig. 10. For all three pitch profiles, we see two peaks in the lift coefficient, one early in the half-cycle, the second towards the end of the half-cycle. This is similar to the trends observed by Deng *et al.* [19] and Teng *et al.* [15].

Early in the cycle, $t/T < 0.18$, the LEV is weak, and we expect that it does not contribute very much to the lift force. Here, we see that the the triangular profile ($\beta = -0.975$, red line) is almost completely in phase with the effective AOA, θ_e, and the pitch acceleration is negligible, suggesting that the dominant mechanism for lift generation is quasisteady. As β increases (corresponding to a larger pitch acceleration), the force due to the added mass ("noncirculatory lift" [6,40–42]) becomes important and the lift coefficient rises more quickly. This explanation is supported by the observation that, for the trapezoidal pitch profile (green curves), the maximum in lift occurs at the same time as the maximum in pitch acceleration ($t/T = 0.06$) and before the maximum in the effective angle of attack, θ_e ($t/T \sim 0.09$).

As time increases, the lift force continues to rise, reflecting the importance of the LEV which is growing on the upper surface of the foil and generates an unsteady circulatory lift force. The LEV strength is greatest in the case of the trapezoidal pitch profile [18,19] and this is reflected in the high C_L during this part of the cycle ($t/T > 0.25$). In the case of the triangular pitch profile, the LEV

grows more slowly, but the mid-cycle peak in the pitch acceleration contributes to an additional noncirculatory "bump" in the lift force at $t/T \sim 0.25$ which compensates for the weak circulatory lift generated by the LEV.

Finally, the lift force drops precipitously at the end of the half-cycle. Here the decrease in C_L is not consistently associated with any feature in the pitch acceleration or the effective angle of attack, confirming previous results that show that the drop in force is related to the shedding of the LEV from the foil [3,6,10], which is not easily associated with the pitch profile.

IV. CONCLUSIONS

In this paper, the power extraction performance of a semipassive energy harvester was studied using a hydrofoil with a prescribed pitch motion and an elastically mounted heave motion achieved using a cyber-physical support. The power of the cyber-physical system allowed for a broad parametric sweep over the stiffness and damping to explore the performance of the semipassive energy harvester. We found that the optimal energy harvesting performance was achieved at damping coefficient of 1.5 and at frequency ratio $f/f_n = 1$, the resonance condition, where the phase difference between the prescribed pitch and the elastically mounted heave is 90°, which agrees well with the results obtained using a fully prescribed foil [2–4,43]. In addition, at this resonance condition the Strouhal number (heaving amplitude) and the hydrodynamic forces were found to collapse remarkably well for different reduced frequency tested ($f^* = 0.105 \sim 0.175$), suggesting a similarity in the vortex dynamics maintained in the elastically mounted system.

Effects of nonsinusoidal pitch profiles on energy harvesting performance were also reported, and it is found that the triangular pitch profiles ($-1 < \beta < 0$) were not as effective as the the sinusoidal pitch profiles ($\beta = 0$), while using the trapezoidal pitch profiles extracted more energy per cycle than the with the sinusoidal pitch profile, in line with the previous results [11,14]. In addition, the optimal trapezoidal pitch profile was found at $\beta = 2.25$, with over 50% improvement in the power coefficient compared with the sinusoidal pitch profile. This improvement was attributed to the lift force enhancement from both the noncirculatory force contribution related to the large pitch acceleration at the beginning of the stroke and the circulatory force contribution associated with a stronger LEV formation due to the large effective AOA maintained through most portion of the cycle.

To establish the connection between the hydrodynamic response in the elastically mounted system and the associated power extraction performance, we found that a simple model based on classical vibration theory was able to reproduce the observed maximum in the power coefficient, relying only on the observed scaling between the Strouhal number (i.e., the heave amplitude) and the system damping (i.e., energy harvested). The model agrees well with the measured results over a range of reduced frequency ($f^* = 0.105 \sim 0.175$) for both sinusoidal and nonsinusoidal pitch profiles. Nevertheless, to gain a deeper understanding of the observed scaling of the Strouhal number, measurements of the LEV dynamics (using, for example, PIV) will be performed in the future. Effects of nonlinear structural mounting (stiffness and damping) can also be explored to further improve the hydrodynamic response and the associated power extraction performance.

ACKNOWLEDGMENTS

The authors gratefully acknowledge the financial support from Advanced Research Projects Agency-Energy (ARPA-E), Grant No. DE-AR0000318, and the Air Force Office of Scientific Research (AFOSR), Grant No. FA9550-18-1-0322. We thank our colleagues in the Leading Edge team, particularly Jen Franck, Michael Miller, and Shreyas Mandre, for their insights and assistance.

[1] W. McKinney and J. DeLaurier, The Wingmill: An oscillating-wing windmill, J. Energy **5**, 109 (1981).

[2] T. Kinsey and G. Dumas, Parametric study of an oscillating airfoil in a power-extraction regime, AIAA J. **46**, 1318 (2008).

[3] D. Kim, B. Strom, S. Mandre, and K. Breuer, Energy harvesting performance and flow structure of an oscillating hydrofoil with finite span, J. Fluids Struct. **70**, 314 (2017).
[4] Q. Zhu, Optimal frequency for flow energy harvesting of a flapping foil, J. Fluid Mech. **675**, 495 (2011).
[5] T. Theodorsen, General theory of aerodynamic instability and the mechanisms of flutter, National Advisory Committee for Aeronautics, Report No. 496, 1935.
[6] C. W. Pitt Ford and H. Babinsky, Lift and the leading-edge vortex, J. Fluid Mech. **720**, 280 (2013).
[7] E. Limacher, C. Morton, and D. Wood, Generalized derivation of the added-mass and circulatory forces for viscous flows, Phys. Rev. Fluids **3**, 014701 (2018).
[8] J. D. Eldredge and A. R. Jones, Leading-edge vortices: Mechanics and modeling, Annu. Rev. Fluid Mech., **51**, 75 (2019).
[9] W. J. McCroskey, Unsteady airfoils, Annu. Rev. Fluid Mech. **14**, 285 (1982).
[10] Y. S. Baik, L. P. Bernal, K. Granlund, and M. V. Ol, Unsteady force generation and vortex dynamics of pitching and plunging aerofoils, J. Fluid Mech. **709**, 37 (2012).
[11] M. F. Platzer, M. A. Ashraf, J. Young, and J. C. S. Lai, Development of a new oscillating-wing wind and hydropower generator, in *Proceedings of the 47th AIAA Aerospace Sciences Meeting including the New Horizons Forum and Aerospace Exposition, Aerospace Sciences Meetings* (AIAA, Orlando, FL, 2009).
[12] M. A. Ashraf, J. Young, J. C. S. Lai, and M. F. Platzer, Numerical analysis of an oscillating-wing wing and Hydropower generator, AIAA J. **49**, 1374 (2011).
[13] J. Young, M. A. Ashraf, J. C. S. Lai, and M. F. Platzer, Numerical simulation of fully passive flapping foil power generation, AIAA J. **51**, 2727 (2013).
[14] K. Lu, Y. H. Xie, and D. Zhang, Nonsinusoidal motion effects on energy extraction performance of a flapping foil, Renew. Energy **64**, 283 (2014).
[15] L. Teng, J. Deng, D. Pan, and X. Shao, Effects of nonsinusoidal pitching motion on energy extraction performance of a semiactive flapping foil, Renew. Energy **85**, 810 (2016).
[16] Q. Xiao, W. Liao, S. Yang, and Y. Peng, How motion trajectory affects energy extraction performance of a biomimic energy generator with an oscillating foil? Renew. Energy **37**, 61 (2012).
[17] D. Rival, T. Prangemeier, and C. Tropea, The influence of airfoil kinematics on the formation of leading-edge vortices in bio-inspired flight, Exp. Fluids **46**, 823 (2009).
[18] I. Fenercioglu, B. Zaloglu, J. Young, M. A. Ashraf, J. C. S. Lai, and M. F. Platzer, Flow structures around an oscillating-wing power generator, AIAA J. **53**, 3316 (2015).
[19] J. Deng, C. P. Caulfield, and X. Shao, Effect of aspect ratio on the energy extraction efficiency of three-dimensional flapping foils, Phys. Fluids **26**, 043102 (2014).
[20] E. Shimizu, K. Isogai, and S. Obayashi, Multiobjective design study of a flapping wing power generator, J. Fluids Eng. **130**, 021104 (2008).
[21] Q. Zhu, M. Haase, and C. H. Wu, Modeling the capacity of a novel flow-energy harvester, Appl. Math. Model. **33**, 2207 (2008).
[22] Q. Zhu and Z. Peng, Mode coupling and flow energy harvesting by a flapping foil, Phys. Fluids **21**, 033601 (2009).
[23] H. Abiru and A. Yoshitake, Study on a flapping wing hydroelectric power generation system, J. Environ. Eng. **6**, 178 (2011).
[24] G. H. Huxham, S. Cochard, and J. Patterson, Experimental parametric investigation of an oscillating hydrofoil tidal stream energy converter, in *Proceedings of the 18th Australasian Fluid Mechanics Conference*, AFMC, Launceston, Australia, 2012.
[25] F. S. Hover, S. N. Miller, and M. S. Triantafyllou, Vortex-induced vibration of marine cables: Experiments using force feedback, J. Fluids Struct. **11**, 307 (1997).
[26] A. W. Mackowski and C. H. K. Williamson, Developing a cyber-physical fluid dynamics facility for fluid-structure interaction studies, J. Fluids Struct. **27**, 748 (2011).
[27] A. W. Mackowski and C. H. K. Williamson, An experimental investigation of vortex-induced vibration with nonlinear restoring forces, Phys. Fluids **25**, 087101 (2013).
[28] J. H. Lee, N. Xiros, and M. M. Bernitsas, Virtual damper-spring system for VIV experiments and hydrokinetic energy conversion, Ocean Eng. **38**, 732 (2011).

[29] J. H. Lee and M. M. Bernitsas, High-damping, high-Reynolds VIV tests for energy harnessing using the VIVACE converter, Ocean Eng. **38**, 1697 (2011).
[30] K. Onoue, A. Song, B. Strom, and K. S. Breuer, Large amplitude flow-induced oscillations and energy harvesting using a cyber-physical pitching plate, J. Fluids Struct. **55**, 262 (2015).
[31] K. Onoue and K. S. Breuer, Vortex formation and shedding from a cyber-physical pitching plate, J. Fluid Mech. **793**, 229 (2016).
[32] K. Onoue and K. S. Breuer, A scaling for vortex formation on swept and unswept pitching wings, J. Fluid Mech. **832**, 697 (2017).
[33] Y. Su, M. Miller, S. Mandre, and K. Breuer, Confinement effects on energy harvesting by a heaving and pitching hydrofoil, J. Fluids Struct. **84**, 233 (2019).
[34] A. W. Mackowski and C. H. K. Williamson, Effect of pivot location and passive heave on propulsion from a pitching airfoil, Phys. Rev. Fluids **2**, 013101 (2017).
[35] R. Govardhan and C. H. K. Williamson, Modes of vortex formation and frequency response of a freely vibrating cylinder, J. Fluid Mech. **420**, 85 (2000).
[36] K. Lu, Y. H. Xie, and D. Zhang, Numerical study of large amplitude, nonsinusoidal motion and camber effects on pitching airfoil propulsion, J. Fluids Struct. **36**, 184 (2013).
[37] S. T. Davids, A computational and experimental investigation of a flutter generator, Thesis Dissertation of Naval Postgraduate School, 1999.
[38] F. S. Hover, A. H. Techet, and M. S. Triantafyllou, Forces on oscillating uniform and tapered cylinders in cross flow, J. Fluid Mech. **363**, 97 (1998).
[39] S. Rao, *Mechanical Vibrations*, 4th ed. (Pearson Prentice Hall, Upper Saddle River, NJ, 2004).
[40] J. Eldredge and C. Wang, High-fidelity simulations and low-order modeling of a rapidly pitching plate, in *Proceedings of the 40th Fluid Dynamics Conference and Exhibit, Fluid Dynamics and Co-located Conferences, Chicago, IL* (AIAA, Reston, VA, 2010).
[41] C. Hartloper, M. Kinzel, and D. E. Rival, On the competition between leading-edge and tip-vortex growth for a pitching plate, Exp. Fluids **54**, 1447 (2013).
[42] M. R. Visbal, Unsteady flow structure and loading of a pitching low-aspect-ratio wing, Phys. Rev. Fluids **2**, 024703 (2017).
[43] K. D. Jones, S. Davids, and M. F. Platzer, Oscillating-wing power generation, in *Proceedings of the 3rd ASME/JSME Joint Fluids Engineering Conference* (ASME/JSME, San Francisco, CA, 1999).

Downloaded from https://www.cambridge.org/core. Brown University Library, on 30 Jul 2020 at 14:31:36, subject to the Cambridge Core terms of use, available at https://www.cambridge.org/core/terms. https://doi.org/10.1017/jfm.2020.481

J. Fluid Mech. (2020), *vol*. 899, A35. © The Author(s), 2020.
Published by Cambridge University Press
doi:10.1017/jfm.2020.481

Nonlinear flow-induced instability of an elastically mounted pitching wing

Yuanhang Zhu[1],†, **Yunxing Su**[1] **and Kenneth Breuer**[1]

[1]Center for Fluid Mechanics, School of Engineering, Brown University, Providence, RI 02912, USA

(Received 8 February 2020; revised 21 May 2020; accepted 10 June 2020)

We experimentally study the nonlinear flow-induced instability of an elastically mounted pitching wing in a circulating water tunnel. The structural parameters of the finite-span wing are simulated and regulated using a cyber-physical control system. At a small fixed damping, we systematically vary the stiffness of the wing for different inertia values to test for the stability boundaries of the system. We observe that, for a high-inertia wing, the system dynamics bifurcates from stable fixed points to small-amplitude oscillations followed by large-amplitude limit-cycle oscillations (LCOs) via a subcritical bifurcation, which features hysteretic bistability and an abrupt amplitude jump. Under this condition, the pitching frequency of the wing locks onto its structural frequency and the oscillation is dominated by the inertial force, corresponding to a structural mode. Force and flow field measurements indicate the presence of a secondary leading-edge vortex (LEV). As the wing inertia decreases, the width of the bistable region shrinks. At a sufficiently low inertia, the pitching amplitude changes smoothly with the stiffness without any hysteresis, revealing a supercritical bifurcation. Under this condition, no lock-in phenomenon is observed and the pitching frequency remains relatively constant at a value lower than the structural frequency. Force decomposition shows dominating fluid force, indicating a hydrodynamic mode. The secondary LEV is absent. We show that the onset of large-amplitude LCOs in both the structural mode and the hydrodynamic mode scales with the Cauchy number, and the LCOs in the structural mode collapse with the non-dimensional velocity. We examine the subcritical transition in detail; we find that this transition depends on the static characteristics of the wing, and the secondary LEV starts to emerge at the early stage of the transition. Lastly, we adopt an energy approach to map out the stability of the system and explain the existence of the two distinct types of bifurcations observed for different inertia values.

Key words: flow–structure interactions, nonlinear instability, vortex dynamics

1. Introduction

Nonlinear flow-induced instability of elastically mounted wings is a classic aeroelastic problem that has been studied extensively for decades. However, our understanding of this problem still remains far from complete, due to its highly nonlinear nature, and the numerous parameters involved. In recent years, in addition to its original applications for understanding aeroelastic failures (Dowell *et al.* 1989), the nonlinear aeroelastic instability

† Email address for correspondence: yuanhang_zhu@brown.edu

has become an important subject for the development of flapping-wing micro air vehicles (MAVs) (Ho *et al.* 2003; Shyy *et al.* 2010) and flapping-foil energy harvesting devices (Xiao & Zhu 2014; Young, Lai & Platzer 2014; Su & Breuer 2019). Many flapping-wing MAVs emulate the flight of insects (e.g. Jafferis *et al.* 2019) because of the relatively simple flight kinematics, which can be primarily decomposed into prescribed flapping and passive pitching. The passive pitching of insect wings can be modelled as a flat plate attached to a torsional spring–damper system hinged at the leading edge (Wang 2005; Bergou, Xu & Wang 2007; Ishihara *et al.* 2009; Bergou *et al.* 2010; Beatus & Cohen 2015; Wu, Nowak & Breuer 2019). The locomotion of insects and other aquatic animals has also inspired the development of flapping-foil kinetic energy harvesters, among which Peng & Zhu (2009) proposed a fully passive pitch–heave configuration, where the energy-extracting heaving motion is driven by the flow-induced pitching instability instead of prescribed (Zhu & Peng 2009). Many numerical (Zhu 2011; Young *et al.* 2013; Veilleux & Dumas 2017; Wang *et al.* 2017) and experimental (Dimitriadis & Li 2009; Amandolese, Michelin & Choquel 2013; Boudreau *et al.* 2018; Duarte *et al.* 2019) studies have been carried out to explore the nonlinear pitch–heave coupling, yet the flow-induced pitching instability itself remains relatively elusive.

1.1. *Unsteady pitching wings with prescribed kinematics*

A key phenomenon associated with the nonlinear aeroelastic instability of passively pitching wings is the stall flutter, caused by the interaction between characteristics of the structural support of the wing and dynamic stall events (McCroskey 1982; Dimitriadis & Li 2009). Dynamic stall is an unsteady aerodynamic effect that occurs when a wing is pitching rapidly. It is featured by the formation, growth and shedding of a strong leading-edge vortex (LEV), which results in a transient increase, followed by a sharp drop, in lift (McCroskey 1982; Eldredge & Jones 2019). Many studies have focused on characterizing this dynamic stall phenomenon using prescribed kinematics. Baik *et al.* (2012) experimentally studied the aerodynamic force and flow dynamics of an airfoil undergoing sinusoidal pitch–plunge motion. It was shown that the unsteady aerodynamic force generation largely depends on the Strouhal number, $St \equiv 2fh_0c/U$, where f, h_0, c and U are the oscillation frequency, the plunging amplitude, the chord length and the free-stream velocity, respectively. The flow evolution and LEV dynamics were shown to be mainly controlled by the reduced frequency, $K \equiv \pi fc/U$. Their experimental results also agree reasonably well with the classic linear potential flow models proposed by Theodorsen (1935) and Garrick (1936). Using a similar set-up, Granlund, Ol & Bernal (2013) found that, when a wing is undergoing smoothed linear pitch ramps, the unsteady fluid force and the LEV development highly depend on the pitching rate, which was later reinforced by Jantzen *et al.* (2014). Granlund *et al.* (2013) also successfully generalized the unsteady force scaling proposed by Strickland & Graham (1987) to take into account the effect of pivot axis.

1.2. *Flow-induced oscillations of passively pitching wings*

Compared to the studies of prescribed pitching wings, in which the kinematics of the wing alters the flow field and thus the fluid force (i.e. one-way coupling), flow-induced oscillations of passively pitching wings is a two-way coupling problem, in which the resultant fluid force will in turn change the pitching kinematics. Once the fluid force is coupled with the structural force, self-sustained oscillations will be excited. In nonlinear dynamical systems, self-sustained (or self-excited) oscillations refer to the oscillations that

Downloaded from https://www.cambridge.org/core. Brown University Library, on 30 Jul 2020 at 14:31:36, subject to the Cambridge Core terms of use, available at https://www.cambridge.org/core/terms. https://doi.org/10.1017/jfm.2020.481

Downloaded from https://www.cambridge.org/core. Brown University Library, on 30 Jul 2020 at 14:31:36, subject to the Cambridge Core terms of use, available at https://www.cambridge.org/core/terms. https://doi.org/10.1017/jfm.2020.481

can spontaneously sustain without external periodic forcing (Strogatz 1994). For elastically mounted pitching wings, self-sustained oscillations can exist when the energy dissipated by the structural damping balances the energy input from the ambient fluid.

A relatively recent paper reporting on older wind tunnel experiments (Dugundji 2008) summarized the nonlinear instabilities of an elastically mounted flat plate pivoted about the midchord, and demonstrated the nonlinear divergence phenomenon, along with large-amplitude flow-induced oscillations. More recently, Onoue *et al.* (2015) utilized a cyber-physical control system (see § 1.3) to study a similar problem in much more detail. By fixing the free-stream velocity, the inertia and damping of the wing, and systematically varying the torsional stiffness, the authors successfully identified the onset and annihilation boundaries of small- and large-amplitude flow-induced oscillations and reported nonlinear hysteretic behaviours of the amplitude response. The effect of Reynolds number and structural damping was also briefly discussed. Onoue & Breuer (2016, 2017) conducted experiments using particle image velocimetry (PIV) to characterize the flow field of a pitching plate undergoing large-amplitude flow-induced oscillations. They successfully associated the unsteady aerodynamic torque with the dynamics of the separated flow structures. The LEV formation time and circulation were shown to depend on the characteristic feeding shear-layer velocity. Numerically, Menon & Mittal (2019) studied flow-induced pitching oscillations of an elastically supported two-dimensional NACA-0015 airfoil at a Reynolds number of 1000. The effects of several control parameters were investigated, including the spring stiffness, the equilibrium angle of attack (AOA), the structural damping and the location of the pivot axis. It was found that flow-induced oscillations occur when the structural time scale exceeds the flow time scale. Based on the fact that the flow-induced oscillations are nearly sinusoidal, the authors used prescribed sinusoidal motions to map out the energy transfer between the airfoil and the surrounding flow over a range of pitching amplitudes and frequencies. This 'energy map' was shown to be an effective tool for understanding the complex nonlinear behaviours associated with the flow-induced oscillations.

Although briefly mentioned by Dugundji (2008), the effect of wing inertia on the flow-induced instability has not been systematically explored in any of these studies. Menon & Mittal (2019) argued that changing the wing inertia (or, equivalently, the mass ratio between the wing and the surrounding fluid) is equivalent to changing the pitching frequency, which makes sense because it is well known that the natural frequency of an elastic system is determined by its stiffness and inertia (mass) (Rao 1995). However, in the context of vortex-induced vibrations (VIVs) of elastically mounted cylinders, it has been shown that different mass ratios lead to different oscillation modes (Govardhan & Williamson 2000, 2002; Williamson & Govardhan 2004; Navrose & Mittal 2017). In particular, Govardhan & Williamson (2000, 2002) showed that, when the mass ratio falls below a critical value, both the VIV amplitude and frequency jump to higher values. This suggests that the wing inertia might play an important and complex role in shaping the flow-induced instability of pitching wings, rather than only affecting the natural frequency.

1.3. *Cyber-physical systems*

Cyber-physical systems have been employed in several previous experimental studies for researching fluid–structure interactions (FSI), including VIVs (Hover, Miller & Triantafyllou 1997; Lee, Xiros & Bernitsas 2011; Mackowski & Williamson 2011) and passively pitching wings (Onoue *et al.* 2015; Fagley, Seidel & McLaughlin 2016; Su & Breuer 2019). These systems combine a cyber system and a physical system to

experimentally simulate the kinematics and dynamics of elastically mounted objects. The cyber system is a feedback control network that takes in the physically measured system kinematics – e.g. force (Hover *et al.* 1997; Mackowski & Williamson 2011; Su & Breuer 2019), velocity (Lee *et al.* 2011; Onoue *et al.* 2015) and displacement (Lee *et al.* 2011; Fagley *et al.* 2016) – and calculates in real time the corresponding system response based on the virtual structural properties defined by the user. The physical system usually consists of an actuator, which receives and executes the system response signal from the cyber system, and a sensor, which measures the system kinematics again at the next moment and sends it back to the cyber system. The cyber system and the physical system thereby form a closed control loop, which mimics a real-time structural response, if operated at sufficiently high bandwidth. Compared to a traditional physical mass–spring–damper system, cyber-physical systems enable easier systematic exploration of the parameter space. The variation range of virtual structural properties can be very large, and the incremental step can be very small, both of which are difficult to achieve using physical systems.

1.4. *Contributions of the present study*

The present work extends the study of a pitching plate by Onoue *et al.* (2015) and Onoue & Breuer (2016) to include the variation of the wing inertia, which has been shown to be critical in defining different VIV modes but has yet to be explored in the passively pitching wing literature. We take advantage of a cyber-physical system to experimentally simulate an elastically mounted pitching wing in free-stream flows, with the motivations of exploring the effect of wing inertia on the flow-induced instability, defining proper scaling parameters for the stability boundaries, and understanding the underlying flow physics associated with the instability. The present experiments are conducted in water, which slows down the time scale of the vortex dynamics associated with FSI, and thus benefits the flow visualization experiments. However, as we will discuss, since we can control the inertia of the wing, we can also simulate the behaviour of a wing in air, even though the experiments are conducted in water. In addition to providing new details and insights into the substantially studied aeroelastic problem, the present study can also be of potential value as a source of experimental data for correlation with theoretical and/or computational models (Dowell & Hall 2001; Dowell, Edwards & Strganac 2003; Zhu, Haase & Wu 2009; Zhu 2012; Young *et al.* 2013; Menon & Mittal 2019).

In the sections below, we describe our experimental set-up and introduce non-dimensional control parameters (§ 2), characterize the amplitude (§ 3.1), frequency (§ 3.2) and force response of the system and the corresponding flow dynamics (§ 3.3), discuss the transition to flow-induced instability (§ 3.4), interpret the system stability from the perspective of energy transfer (§ 3.5), and lastly summarize our key findings (§ 4).

2. Experimental set-up and non-dimensional parameters

Figure 1 shows the schematic of our experimental set-up. All the experiments are conducted in the Brown University free-surface water tunnel, which has a test section of width (W) $\times$ depth (D) $\times$ length (L) $= 0.8$ m $\times$ 0.6 m $\times$ 4.0 m. We mount a NACA-0012 wing vertically in the water tunnel, with an endplate on the top to eliminate wingtip vortices at the root. To emulate the behaviour of real-life wings, such as MAV airfoils and energy-harvesting hydrofoils, no endplate is added to the bottom tip of the wing. The wing is made of clear acrylic with a span of $s = 0.3$ m and a chord length of $c = 0.1$ m. The pivoting point (i.e. the elastic axis) of the wing is fixed at the midchord,

Downloaded from https://www.cambridge.org/core. Brown University Library, on 30 Jul 2020 at 14:31:36, subject to the Cambridge Core terms of use, available at https://www.cambridge.org/core/terms. https://doi.org/10.1017/jfm.2020.481

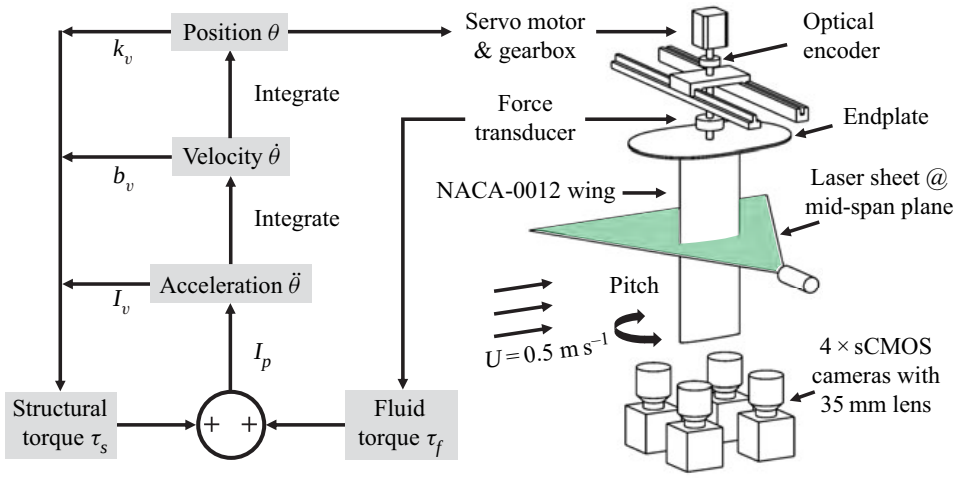


FIGURE 1. A schematic of the experimental set-up.

$c/2$, throughout all experiments. Detailed wing characteristics can be found in appendix A. To maintain a constant chord-based Reynolds number, $Re = \rho Uc/\mu = 50\,000$, where ρ and μ are water density and dynamic viscosity, respectively, we fix the free-stream velocity at $U = 0.5$ m s^{-1}. This velocity is measured by an acoustic Doppler velocimeter (ADV; Nortek Vectrino), positioned at the centre of the W–D plane, 2.5 m upstream of the wing.

2.1. *Cyber-physical system implementation*

We implement the real-time cyber-physical system (CPS) using MATLAB Simulink with an update rate of 4000 Hz. To introduce the CPS, we start with the governing equation of the system

$$I\ddot{\theta} + b\dot{\theta} + k\theta = \tau_f, \tag{2.1}$$

where I, b and k are the effective inertia, damping and stiffness of the wing, respectively, and τ_f is the fluid torque. The effective inertia, $I = I_p + I_v$, is a combination of the physical inertia of the wing, I_p, and a user assigned virtual inertia, I_v. Because no physical spring is present in the system and the frictional damping is negligible, we use virtual values to achieve the target stiffness, $k = k_v$, and the target damping, $b = b_v$. Adding up all the virtual torques, the total virtual structural torque can be calculated as

$$\tau_s = -(k_v\theta + b_v\dot{\theta} + I_v\ddot{\theta}). \tag{2.2}$$

Substituting (2.2) into (2.1), we can get

$$I_p\ddot{\theta} = \tau_f + \tau_s. \tag{2.3}$$

Now we introduce the real-time control loop depicted in figure 1. The fluid torque exerted on the wing, τ_f, measured by a six-axis force/torque transducer (ATI 9105-TIF-Delta-IP65), is fed into the loop. After adding the structural torque, τ_s (calculated from the previous time step), the total torque, $\tau_f + \tau_s$, is divided by the physical inertia of the wing, I_p, to get the pitching acceleration, $\ddot{\theta}$:

$$\ddot{\theta} = (\tau_f + \tau_s)/I_p. \tag{2.4}$$

Next, $\ddot{\theta}$ is integrated once to get the pitching velocity, $\dot{\theta}$, and again to get the pitching position, θ. The pitching position signal is used as input to a servomotor

Downloaded from https://www.cambridge.org/core. Brown University Library, on 30 Jul 2020 at 14:31:36, subject to the Cambridge Core terms of use, available at https://www.cambridge.org/core/terms. https://doi.org/10.1017/jfm.2020.481

(Parker SM233AE), coupled with a gearbox (Automation Direct PGCN23-0525), to pitch the wing. We use an optical encoder (US Digital E3-2500-250-IE-D-D-1), which is independent of the CPS, to record the actual pitching angle. At each time step, the structural torque, τ_s, is recalculated using (2.2) based on the new pitching dynamics (θ, $\dot{\theta}$ and $\ddot{\theta}$) and added to τ_f at the next time step to close the control loop. Data from the ADV, the force/torque transducer and the optical encoder are sampled using a data acquisition (DAQ) board (National Instruments PCIe-6353) at a frequency of 4000 Hz. The position signal is also output by the same DAQ board to the servomotor via a motor drive (Advanced Motion Controls DPRALTE-020B080).

Validation of the performance of this real-time cyber-physical system can be found in appendix A. Compared to the velocity loop used by Onoue *et al.* (2015), the position loop is less sensitive to noise and more robust because of the double integration. No filtering is required to get a clean and smooth position signal. For plotting purposes only, a zero-phase sixth-order low-pass Butterworth filter is applied to the raw force data so as to smooth out small oscillations. The filter cut-off frequency is set to 25 times the observed pitching frequency. It is important to emphasize that this filter is only employed for post-processing of the data; no filter is used inside the real-time control loop.

2.2. *Particle image velocimetry set-up*

The flow field around the pitching wing is measured using a time-resolved two-dimensional PIV system shown in figure 1. The laser sheet, created by a double-pulse Nd:YAG laser (200 mJ at 532 nm, Quantel Laser EverGreen 200) with LaVision sheet optics, illuminates the midspan plane of the wing. Because the wing is made of clear acrylic, the laser sheet can pass through the wing, enabling flow field measurement on both sides of the wing. It should be noted that the laser sheet plane is sufficiently far from the wingtip that the tip vortex is excluded from the measurement. The flow is seeded by 50 μm silver-coated hollow ceramic spheres. Image pairs of the flow field are acquired by four coplanar cameras (LaVision Imager sCMOS, 2560 $\times$ 2160 pixels) equipped with 35 mm lenses and mounted beneath the water tunnel. The laser and cameras are synchronized by a Programmable Timing Unit (PTU; LaVision). The PIV images are fed into the LaVision DaVis software (v.10) for image processing. Multi-pass cross-correlation (two passes at 64 $\times$ 64 pixels, two passes at 32 $\times$ 32 pixels, both with 50 % overlap) is used to calculate velocity vectors from each camera view, and the vector fields of the four cameras are stitched together to form a larger field of view ($\sim 4c \times 4c$).

2.3. *Non-dimensional parameters*

Following Onoue *et al.* (2015), we assume the fluid inertia force $0.5\rho U^2c^2s$ to be the dominating scaling force and normalize the stiffness, damping, inertia and fluid torque as

$$k^* = \frac{k}{0.5\rho U^2c^2s}, \quad b^* = \frac{b}{0.5\rho Uc^3s}, \quad I^* = \frac{I}{0.5\rho c^4s}, \quad \tau_f^* = \frac{\tau_f}{0.5\rho U^2c^2s}. \tag{2.5a–d}$$

Therefore, the non-dimensional governing equation of the system becomes

$$I^*\ddot{\theta}^* + b^*\dot{\theta}^* + k^*\theta^* = \tau_f^*, \tag{2.6}$$

where $\theta^* = \theta$, $\dot{\theta}^* = \dot{\theta}c/U$ and $\ddot{\theta}^* = \ddot{\theta}c^2/U^2$.

It is worth mentioning that the inverse of the non-dimensional stiffness is identical to the commonly used Cauchy number, $Ca = 1/k^*$, which describes the ratio between the fluid

Downloaded from https://www.cambridge.org/core. Brown University Library, on 30 Jul 2020 at 14:31:36, subject to the Cambridge Core terms of use, available at https://www.cambridge.org/core/terms. https://doi.org/10.1017/jfm.2020.481

inertia force and the elastic force (Ishihara *et al.* 2009; Jin *et al.* 2019; Wu *et al.* 2019). The non-dimensional inertia, I^*, is equivalent to the mass ratio between the wing and ambient fluid (Tzezana & Breuer 2019). The non-dimensional fluid torque, τ_f^*, is the unsteady moment coefficient of the wing. Another important non-dimensional parameter in the present study, which has appeared in many previous FSI studies (Khalak & Williamson 1996; Kim *et al.* 2013; Fagley *et al.* 2016; Menon & Mittal 2019), is the non-dimensional velocity U^*, defined as $U^* = U/(2\pi fc)$, where f is the oscillation frequency. It is important to note that U^* can have different definitions in the present study, depending on the frequency used to calculate U^*. There are several frequencies of interest in the dynamics of elastically mounted pitching wings, including: (*a*) the frequency of flow oscillations that may occur even in the absence of structural motions (e.g. the von Kármán vortex shedding frequency described in Menon & Mittal 2019); (*b*) the structural (or natural) frequency of the wing, f_s, calculated based on the spring stiffness and the wing inertia (i.e. $f_s = (\sqrt{k/I})/2\pi$); and (*c*) the pitching frequency, f_p, which arises from the dynamic coupling between the flow and the structure (in the aeroelastic literature, this frequency may be called the flutter or limit-cycle oscillation frequency). In the following sections, we will use U_s^* to denote U^* calculated using f_s (i.e. $U_s^* = U/(2\pi f_s c)$), and U_p^* to denote U^* calculated using f_p (i.e. $U_p^* = U/(2\pi f_p c)$).

3. Results and discussion

3.1. *Subcritical and supercritical bifurcations*

In the present study, we fix the structural damping of the wing at $b^* = 0.13$ and keep the initial AOA at *zero*. We want to note that different initial AOAs can introduce significant differences in bifurcation behaviours (Dugundji 2008; Razak, Andrianne & Dimitriadis 2011; Menon & Mittal 2019). In the present study, we only focus on the zero initial AOA case. At different wing inertias, we first incrementally increase the Cauchy number, Ca, by decreasing the wing stiffness, k^*, to define the onset of instability. Then we incrementally decrease Ca by increasing k^* to test for the annihilation of instability and the presence of any hysteresis. The amplitude response of the system, $|A|$, is defined using the absolute value of the peak pitching amplitude, and the divergence angle, $|\overline{A}|$, is defined as the absolute value of the mean pitching angle. We plot $|A|$ and $|\overline{A}|$ against the Cauchy number $Ca = 1/k^*$ instead of k^* because the former can better resemble typical bifurcation diagrams in dynamical systems (Strogatz 1994).

Figure 2 shows the amplitude response of the system at two different wing inertias. When the inertia is relatively high ($I^* = 10.6$, figure 2*a*), as we increase Ca, the wing first remains stable with a negligible divergence angle. Although the zero divergence angle is always an equilibrium state for an elastically mounted wing with zero initial AOA, this state may not be a stable fixed point in practice. To test for the true stability of the wing, we introduce a small external perturbation, or 'kick', into the system. This perturbation is computer-generated by superimposing a short virtual torque to the cyber-physical system. A series of perturbation tests with controlled amplitude variance were conducted to determine a proper perturbation amplitude, so that the system is not pushed into other stability regimes. If zero divergence is a stable fixed point solution, the wing will return to the zero divergence angle after the perturbation. However, if the zero-angle condition is an unstable fixed point, the wing will stay at a non-zero divergence angle at which the fluid torque is balanced by the restoring torque provided by the (virtual) spring. The direction of this angle depends on the direction of the initial perturbation, but both positive and

Downloaded from https://www.cambridge.org/core. Brown University Library, on 30 Jul 2020 at 14:31:36, subject to the Cambridge Core terms of use, available at https://www.cambridge.org/core/terms. https://doi.org/10.1017/jfm.2020.481

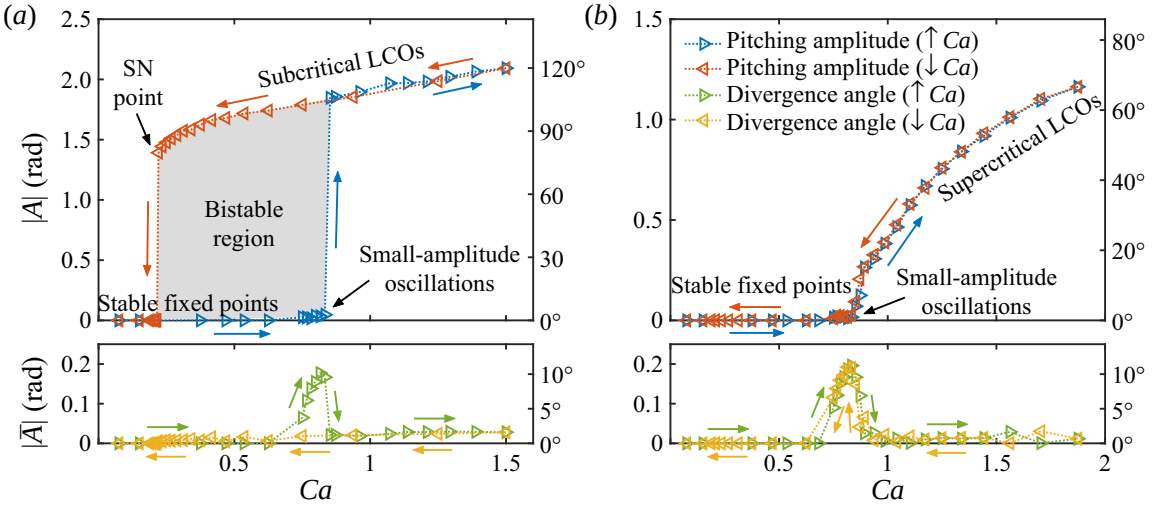


FIGURE 2. Amplitude response of the system at (*a*) $I^* = 10.60$ and (*b*) $I^* = 0.33$, presented in radians on the left y-axis, and in degrees on the right y-axis. Note that (*a*) and (*b*) share the same legend.

negative angles are possible. This static divergence phenomenon is well characterized in the literature (Dugundji 2008; Dimitriadis & Li 2009).

As we continue to increase Ca, the static divergence angle becomes larger and small-amplitude oscillations are observed. In this regime, the pitching amplitude θ, velocity θ^* and acceleration $\ddot{\theta}^*$ are all small, causing the damping torque $b^*\dot{\theta}^*$ and the inertial torque $I^*\ddot{\theta}^*$ to be negligible. As a result, these deflected small-amplitude oscillations are dominated by the balance between the fluid torque τ_f^* and the spring restoring torque $k^*\theta^*$ around the divergence angle. Although these small-amplitude oscillations are not the main focus of the present study, they should be distinguished from the laminar separation flutter reported in the literature (Poirel, Harris & Benaissa 2008; Poirel & Yuan 2010; Poirel, Metivier & Dumas 2011; Barnes & Visbal 2018), where the oscillations are both driven and limited by the aerodynamic force, and can thus sustain even without the presence a structural spring (Poirel *et al.* 2008, figure 8). Moreover, we believe that the small-amplitude oscillations observed in the present study are not strictly stall flutter (Dimitriadis & Li 2009; Bhat & Govardhan 2013), because no obvious hysteresis is observed in the force measurements, and the maximum pitching angle mostly stays below the static stall angle. Rather, we think these small-amplitude oscillations come from the interaction between the random flow disturbance and the structural dynamics (mainly the spring stiffness) of the wing.

As the Cauchy number, Ca, is further increased, we observe a critical value above which the pitching dynamics of the wing transitions from small-amplitude oscillations to large-amplitude LCOs. This transition is reflected by an abrupt jump of the pitching amplitude, $|A|$, and a drop of the divergence angle, $|\bar{A}|$ (figure 2*a*). The large-amplitude LCOs are nearly sinusoidal and feature a dominant characteristic frequency. The amplitude of these LCOs continues to increase with Ca, and the corresponding characteristic frequency decreases with Ca (see figure 4*a*). As we decrease the Cauchy number, Ca, the large-amplitude LCOs persist even when Ca is decreased below the critical value, defining a bistable, hysteretic region, before the pitching amplitude returns to the stable fixed point regime via a saddle-node (SN) point. In this bistable region, the system has two stable solutions (i.e. stable LCOs and stable fixed points) and one unstable solution

Downloaded from https://www.cambridge.org/core. Brown University Library, on 30 Jul 2020 at 14:31:36, subject to the Cambridge Core terms of use, available at https://www.cambridge.org/core/terms. https://doi.org/10.1017/jfm.2020.481

(i.e. unstable LCOs, not observable in experiments). The divergence angle $|\bar{A}|$ remains near zero for the entire decreasing path, creating a small hysteretic region near the critical *Ca*. Similar bifurcation behaviours have been reported in the wind tunnel experiments literature (Dugundji 2008; Dimitriadis & Li 2009; Amandolese *et al.* 2013; Onoue *et al.* 2015). If we ignore the static divergence angle and relax the constraint in the definition of a Hopf bifurcation that the system has to be a fixed point prior to the bifurcation (Strogatz 1994), the bifurcation observed in the present experiment possesses every feature of a subcritical Hopf bifurcation, with the critical *Ca* corresponding to the Hopf point. The large-amplitude LCOs observed in this operating condition are hence referred to as subcritical LCOs.

The amplitude response for a wing with a much lower inertia ($I^* = 0.33$) is shown in figure 2(*b*). Again, for small *Ca* values, we perturb the system to test for its true stability. Similar to the high-inertia case, as we increase *Ca*, the system experiences static divergence and small-amplitude oscillations around the divergence angle. As *Ca* is further increased, the small-amplitude oscillations become larger and the divergence angle gradually decreases to zero. At even higher values of *Ca*, the LCO amplitude continues to increase and the divergence angle remains around zero. As we decrease *Ca*, both the pitching amplitude $|A|$ and the divergence angle $|\bar{A}|$ follow exactly the same path back to the original fixed point regime. No hysteresis or amplitude jump is observed during the experiment. As before, if we ignore the static divergence angle and the initial small-amplitude oscillations, the transition appears to be a supercritical Hopf-type bifurcation. We therefore refer to the large-amplitude LCOs observed in this operating condition as supercritical LCOs. Compared to the subcritical bifurcation, which is often referred to as a hard bifurcation because of the dangerous abrupt amplitude jump and hysteresis, a supercritical bifurcation is usually denoted as a soft bifurcation, which is considered to be safer for many applications (Strogatz 1994).

We then test the stability boundaries of the system over a range of wing inertia values. In figure 3(*a*), the pitching amplitude, $|A|$, is plotted against the Cauchy number, *Ca*. We see that the width of the bistable region shrinks as the inertia decreases, evidenced by the change in the location of the SN point. When the inertia is sufficiently low, the bistable region completely disappears and the subcritical bifurcation becomes supercritical. However, regardless of the bifurcation type (supercritical or subcritical), the onset of instability (i.e. the Hopf point) seems to occur at the same Cauchy number for all wing inertia values. The underlying mechanism of this phenomenon will be discussed in § 3.4.

In figure 3(*b*), we re-plot the pitching amplitude, this time against the f_s-based non-dimensional velocity U_s^*. The connection between *Ca*, k^* and U_s^* is

$$U_s^* = \frac{U}{2\pi f_s c} = \sqrt{\frac{I^*}{k^*}} = \sqrt{Ca\, I^*}. \tag{3.1}$$

We first observe that, under this scaling, for subcritical bifurcations, the location of the Hopf point rises as the wing inertia increases. After the onset of large-amplitude LCOs, we observe that the pitching amplitude for the three subcritical LCO branches ($I^* = 10.60$, 5.30 and 2.65) almost completely overlap, and that these LCOs extinguish at roughly the same critical U_s^* (i.e. the same SN point), indicating that U_s^* is a good scaling parameter for this feature of the instability. The critical U_s^* is actually determined by a critical structural frequency f_s, because the free-stream velocity U and the chord length of the wing c remain constant in the present experiment (see (3.1)). Below this critical U_s^* (above the corresponding critical f_s), subcritical LCOs cannot sustain. The underlying mechanism

Downloaded from https://www.cambridge.org/core. Brown University Library, on 30 Jul 2020 at 14:31:36, subject to the Cambridge Core terms of use, available at https://www.cambridge.org/core/terms. https://doi.org/10.1017/jfm.2020.481

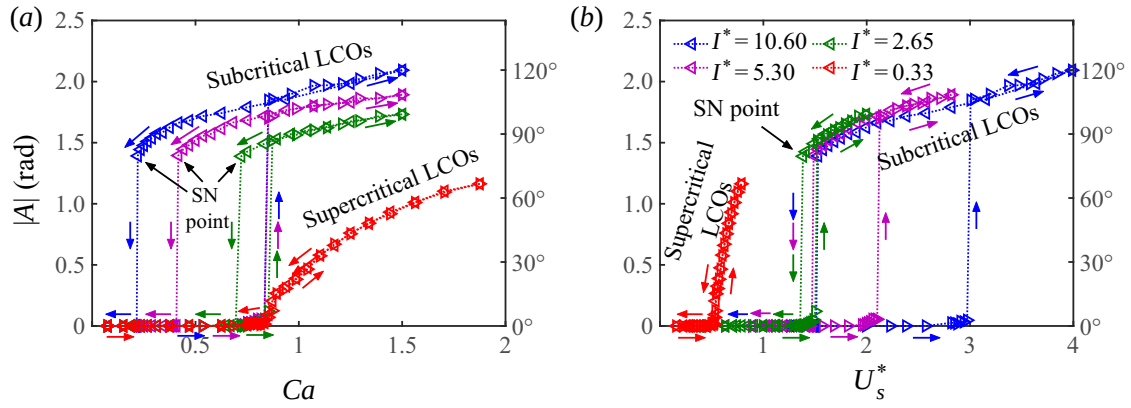


FIGURE 3. Pitching amplitude at different wing inertias, plotted against (*a*) the Cauchy number, *Ca*, and (*b*) the f_s-based non-dimensional velocity, U_s^*. Symbols: ▷, increasing *Ca*; ◁, decreasing *Ca*. Note that (*a*) and (*b*) share the same legend.

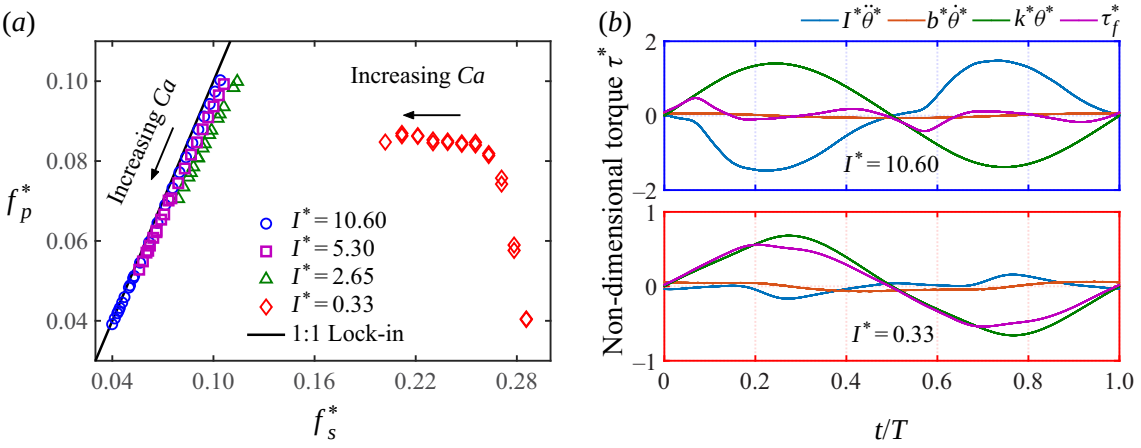


FIGURE 4. (*a*) The frequency response of the wing at four different inertia values. (*b*) Non-dimensional torques experienced by the wing at $Ca = 1.5$ over one normalized pitching cycle: $I^*\ddot{\theta}^*$, inertial torque; $b^*\dot{\theta}^*$, damping torque; $k^*\theta^*$, spring restoring torque; and τ_f^*, fluid torque. Upper panel is for $I^* = 10.60$ and lower for $I^* = 0.33$. Note the *y*-scale difference in (*b*).

for this phenomenon will be discussed in § 3.5. Moreover, the collapse of the subcritical LCO branches indicates that all these LCOs share a universal oscillation mode even though the wing inertia is different. This observation supports Menon & Mittal's (2019) argument that changing the wing inertia only affects the natural frequency of the system. However, we should note that U_s^* is only able to collapse subcritical LCOs. The behaviour of supercritical LCOs ($I^* = 0.33$) seems to be qualitatively different (i.e. the oscillations are always below the critical U_s^*), suggesting a different mode of oscillation. This is more fully characterized in the next section.

3.2. *Structural mode and hydrodynamic mode*

In figure 4(*a*), we plot the measured pitching frequency of the wing, f_p, against the calculated structural frequency, f_s, both normalized by the fluid time scale (i.e. $f^* = fc/U$). Because it is difficult to extract f_p^* for small-amplitude oscillations (see figure 2), the data shown only correspond to relatively large-amplitude LCOs (i.e. super- and subcritical

Downloaded from https://www.cambridge.org/core. Brown University Library, on 30 Jul 2020 at 14:31:36, subject to the Cambridge Core terms of use, available at https://www.cambridge.org/core/terms. https://doi.org/10.1017/jfm.2020.481

LCOs, see figure 3). To illustrate how each term in (2.6) affects the pitching dynamics over one cycle, we decompose the non-dimensional torque experienced by the wing into the inertial torque, $I^*\ddot{\theta}^*$, the damping torque, $b^*\dot{\theta}^*$, the spring restoring torque, $k^*\theta^*$, and the fluid torque, τ_f^*. The decomposition result is shown in figure 4(*b*), with the top panel corresponding to the high-inertia case ($I^* = 10.6$) and the bottom panel corresponding to the low-inertia case ($I^* = 0.33$), both at $Ca = 1.5$.

We observe that for the high-inertia case ($I^* = 10.60$), as Ca is varied, the pitching frequency, f_p^*, locks onto the structural frequency, f_s^* (figure 4*a*, blue circles). The maximum f_p^* corresponds to the SN point in the bifurcation diagram (see figure 2*a*), whereas the minimum f_p^* corresponds to the highest Ca. This lock-in phenomenon indicates that the structural force is the dominating force governing the pitching motion, which is supported by the torque decomposition in figure 4(*b*, top). In this panel, we see that the spring restoring torque, $k^*\theta^*$, is of similar amplitude, and opposite sign to the inertial torque, $I^*\ddot{\theta}^*$, while the fluid torque, τ_f^*, and the damping torque, $b^*\dot{\theta}^*$, are relatively small. A similar lock-in phenomenon was observed by Onoue *et al.* (2015) and Menon & Mittal (2019). In figure 4(*a*), we also plot the frequency response for the two moderate-inertia cases ($I^* = 5.30$ and 2.65, purple squares and green triangles). The lock-in phenomenon persists in these two cases but f_p^* is slightly lower than f_s^*, especially for the lower-inertia wing. We attribute this to the increase of effective inertia brought by the added-mass effect, which is more prominent for lower inertia values. The fact that the lock-in phenomenon is observed for all the subcritical LCOs further confirms that these LCOs feature the same oscillation mode, which we denote as the *structural* mode.

In contrast, for the low-inertia case ($I^* = 0.33$), the frequency response (figure 4(*a*), red diamonds) lies to the right of the 1 : 1 lock-in line, indicating that the pitching frequency, f_p^*, is always lower than the structural frequency, f_s^*. No lock-in phenomenon is observed. As we increase Ca, the pitching frequency stays at a relatively constant value (i.e. constant Strouhal number $St = f_p^* \approx 0.085$), indicating an intrinsic fluid time scale. This suggests that the fluid torque, τ_f^*, is driving the pitching motion, which is verified by figure 4(*b*, bottom). It is seen that the spring restoring torque, $k^*\theta^*$, mainly balances the fluid torque, τ_f^*. These two torques are in phase because they are of opposite sign in the governing equation (see (2.6)). The fluid torque, τ_f^*, has a similar magnitude, but a higher frequency, as compared to that of the high-inertia case. However, because of the low I^*, the inertial torque $I^*\ddot{\theta}^*$ stays comparatively small over the entire pitching cycle, causing the frequency of τ_f^* to override the structural frequency. The damping torque, $b^*\dot{\theta}^*$, is almost negligible in this case. Therefore, we denote the supercritical LCOs as the *hydrodynamic* mode.

3.3. *Force response and the corresponding flow field*

We plot the torque–angle phase diagram, τ_f^*–θ, for both the high-inertia case ($I^* = 10.60$) and the low-inertia case ($I^* = 0.33$) in the centre of figure 5. The static torque–angle measurement is plotted for comparison. The corresponding phase-averaged flow fields at different time instants are also plotted surrounding that diagram. Because of symmetry, we only show the vorticity fields for half of the pitching cycle. Figure 5(*a–g*) correspond to the positive half pitching cycle of the high-inertia case ($I^* = 10.60$). Figure 5(*i–v*) correspond to the negative half pitching cycle of the low-inertia case ($I^* = 0.33$).

For the high-inertia case, the force response and the corresponding vorticity field are very similar to that observed by Onoue & Breuer (2016). As the wing departs from the zero pitching angle, the fluid torque τ_f^* starts to grow. The phase diagram shows that τ_f^* is non-zero at $\theta = 0$. This positive intercept is presumably due to the pressure difference

Downloaded from https://www.cambridge.org/core. Brown University Library, on 30 Jul 2020 at 14:31:36, subject to the Cambridge Core terms of use, available at https://www.cambridge.org/core/terms. https://doi.org/10.1017/jfm.2020.481

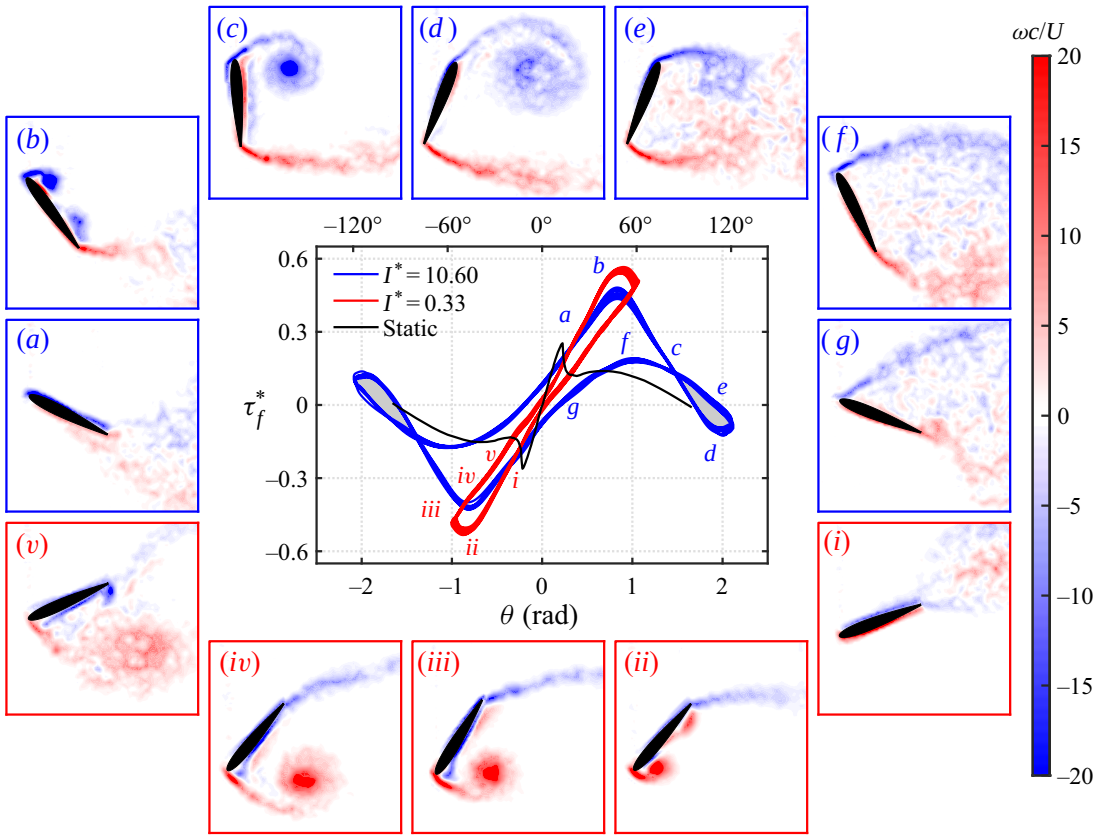


FIGURE 5. Torque–angle phase diagram (centre) for $I^* = 10.60$ (structural mode) and $I^* = 0.33$ (hydrodynamic mode) at $Ca = 1.5$ (the same operating conditions as in figure 4*b*), and the corresponding vorticity fields (flow direction is left to right): (*a–g*) $I^* = 10.60$, corresponding to the blue curve; (*i–v*) $I^* = 0.33$, corresponding to the red curve. See supplementary movies available at https://doi.org/10.1017/jfm.2020.481.

between the two sides of the wing, caused by the separated flow on the lower wing surface inherited from the previous cycle (Onoue & Breuer 2016). The PIV measurements (figure 5*a*,*b*) depict the emergence of a strong LEV, which is attached to the upper surface of the wing, in the fore section. Meanwhile, we observe a patch of vorticity on the aft part of the upper surface, which could be a shear-layer vortex caused by the rolling-up of surface vorticity (Sharma & Visbal 2019). The τ_f^* value starts to decrease after a peak around $\theta \approx 0.82$ (47°) is experienced, corresponding to the shedding of the LEV from the wing surface (figure 5*c*). Compared to the static measurement, this decrease in τ_f^* significantly exceeds the static stall angle, θ_s. The maximum value of τ_f^* is also amplified approximately by a factor of 2. This transient increase of τ_f^* (due to the transient increase of C_L) and the delay in stall evince the dynamic stall phenomenon (McCroskey 1982; Eldredge & Jones 2019). Although τ_f^* is decreasing and the spring restoring torque is increasing, the wing continues to pitch up due to its high inertia, until the maximum pitching amplitude is achieved around $\theta \approx 2.09$ (120°).

In Onoue & Breuer (2016, figure 3), the maximum θ is around 90°. This discrepancy is presumably due to differences in the wing characteristics (i.e. flat plate versus NACA-0012 wing). The τ_f^* value goes below zero at roughly the same θ as in the static measurement. At the maximum θ, the LEV reaches its maximum size while remaining relatively coherent (figure 5*d*), before it breaks into smaller-scale structures and fully detaches from the wing

Downloaded from https://www.cambridge.org/core. Brown University Library, on 30 Jul 2020 at 14:31:36, subject to the Cambridge Core terms of use, available at https://www.cambridge.org/core/terms. https://doi.org/10.1017/jfm.2020.481

surface, evidenced by the disconnection between the leading edge and the LEV feeding shear layer. After arriving at the peak θ, the pitching motion starts to reverse. Then τ_f^* increases again and experiences another peak, due to the formation, growth and shedding of a secondary LEV caused by the rolling-up of the feeding shear layer (figure 5*e*,*f*) (Jantzen *et al.* 2014; Onoue & Breuer 2016). The relatively diffusive appearance of the secondary LEV (figure 5*e*) could be an artifact due to the fact that these vorticity fields are phase-averaged, while the real LEV may exhibit some phase jitter. In the final stage, the restoring torque pulls the wing back to the zero pitching angle, while the flow on the upper wing surface is still separated (figure 5*g*). This results in the negative intercept of τ_f^* at the beginning of the second half of the pitching cycle.

For the low-inertia case, the initial behaviour of the force response and the flow field (figure 5*i*,*ii*) is very similar to that of the high-inertia case (figure 5*a*,*b*). For both cases, τ_f^* peaks at a similar angular position $\theta \approx 0.82$ (47°), agreeing well with experiments and models by Strickland & Graham (1987) and Granlund *et al.* (2013), in which the wing undergoes rapid pitching at constant angular velocities. The origin of this peak in τ_f^* for both cases is the formation and shedding of the primary LEV. The peak τ_f^* is higher for the low-inertia case, presumably due to a stronger LEV defined by a higher reduced frequency and thereby a larger feeding shear-layer velocity (Onoue & Breuer 2016, 2017).

The primary discrepancy between the high-inertia case and the low-inertia case appears right after the maximum τ_f^* is achieved. The low-inertia wing does not have enough momentum (due to the low inertia) to keep pitching up when the LEV starts to detach from the wing surface (figure 5*iii*). Therefore, θ reaches its maximum almost immediately after the peak τ_f^* has arrived. As the LEV further sheds from the wing surface, it moves towards the aft part of the wing (figure 5*iv*) and becomes less coherent (figure 5*v*). The τ_f^* value decreases monotonically and the spring restoring torque gradually brings the wing back to the zero pitching angle. At $\theta = 0$, the y-intercept of τ_f^* for the low-inertia case is smaller than that of the high-inertia case, because the flow on the suction side of the wing reattaches faster. In the low-inertia case, no secondary peak in τ_f^* is observed and the secondary LEV is absent during the pitch reversal. As a result, no negative hysteresis region (figure 5 grey shaded areas) is formed, suggesting that no energy is being transferred from the system to the wake over the pitching cycle (Onoue & Breuer 2016). However, this does not necessarily indicate that low wing inertia is more favourable for energy harvesting, as the harvesting efficiency depends on the net area of the hysteretic region.

3.4. *Transition to subcritical limit-cycle oscillations*

One key feature of the subcritical bifurcation observed for the high-inertia wing is the abrupt jump of the pitching amplitude at the critical *Ca* (see figure 2*a*). In the time domain, when *Ca* is increased above the critical value, the amplitude jump is in fact a gradual transition process, in which the pitching amplitude grows and saturates over a period of around one minute (∼12 cycles). Figure 6(*a*) shows the time trace of the pitching motion during this transition. Figure 6(*b*) shows the temporal evolution of the corresponding fluid torque, τ_f^*. Figure 6(*c*) shows the transitional τ_f^*–θ phase diagram. The static measurement is also plotted in black for comparison. In figure 6(*b*,*c*), the time dependence of τ_f^* is indicated by the colour shade. The red colour represents the starting stage of the transition, whereas the cyan colour indicates the amplitude saturation stage.

Before the transition occurs, the wing undergoes small-amplitude quasi-steady oscillations around its equilibrium divergence angle (see § 3.1). At this stage, the flow on the wing surface is mostly attached (PIV measurements not shown here). As *Ca* is

Downloaded from https://www.cambridge.org/core. Brown University Library, on 30 Jul 2020 at 14:31:36, subject to the Cambridge Core terms of use, available at https://www.cambridge.org/core/terms. https://doi.org/10.1017/jfm.2020.481

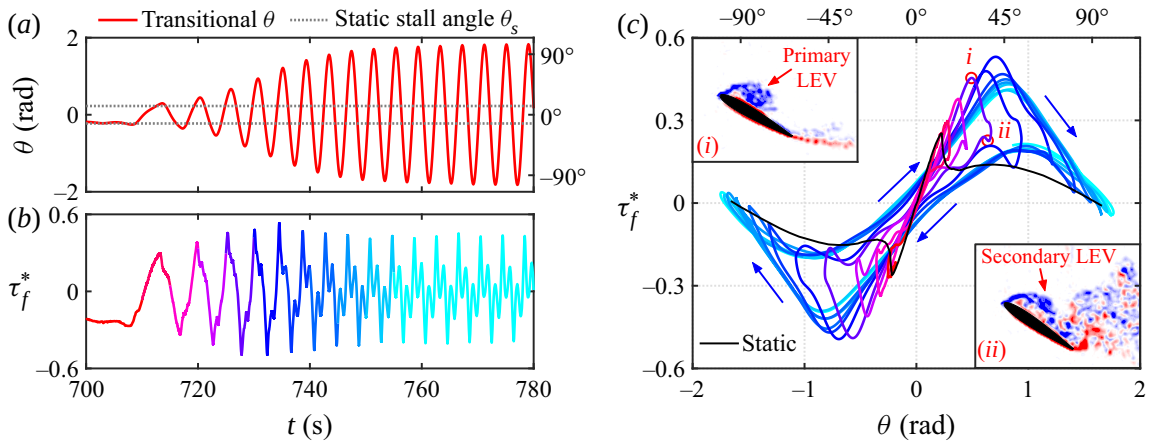


FIGURE 6. Transition to subcritical LCOs in the high-inertia case ($I^* = 10.60$) at $Ca = 0.85$. (a) Time trace of the amplitude transition (red solid line). Grey dotted lines indicate the static stall angle θ_s. (b) Temporal evolution of the fluid torque τ_f^* during the transition. (c) Transitional torque–angle phase diagram. Insets: Two representative vorticity field showing (i) a primary LEV and (ii) a secondary LEV. The angular positions of these two vorticity fields are indicated by red circles. Insets (i) and (ii) share the same colour bar with figure 5.

increased above the critical value, the spring is not stiff enough to hold the wing below the static stall angle, θ_s (i.e. the grey dotted lines in figure 6a). Once θ_s is exceeded, the flow starts to separate and the wing experiences a sudden drop in τ_f^*. The spring restoring torque loses its counterpart so that the wing is accelerated to pitch towards the opposite direction. At this very initial stage of the transition, the pitch reversal starts as soon as the separation occurs. However, at the later stage of the transition and when the oscillation saturates, the wing will continue to pitch after the flow separates (i.e. pitching 'overshoot'), on account of the high inertia. As the wing starts to gain velocity, the flow becomes unsteady and the static stall transitions to dynamic stall. As a result, the stall is delayed and the maximum τ_f^* increases because of the formation of LEVs (figure 6c, inset i). This positive feedback loop results in a further increase in the pitching amplitude. Figure 6(c) clearly depicts this transition, showing how the wing departs from the quasi-steady state to the unsteady state. The growth in pitching amplitude is finally limited by the spring restoring torque (see also figure 4b, top), which leads to the amplitude saturation. How this quasi-steady to unsteady transition shapes the stability characteristics of the system will be discussed in § 3.5.

In § 3.3, we have shown that the secondary peak in τ_f^* during the pitch reversal is associated with the presence of a secondary LEV (figure 5e). Figure 6(c) illustrates how this secondary τ_f^* peak emerges and strengthens during the transition, providing evidence for the emergence and development of the corresponding secondary LEV, which is confirmed by vorticity measurements. Figure 6(c, inset ii) shows that a secondary LEV is indeed formed during the pitch reversal, even during the very first few cycles of the transition. Moreover, figure 6(c) also shows that secondary LEVs can exist for a relatively low pitching amplitude ($|A| < 1$), which suggests that the absence of the secondary LEV in the low-inertia case (figure 5) is not due to the low pitching amplitude ($|A| \approx 1$), but could well be a result of the high pitching frequency, as compared to the high-inertia case. For a high pitching frequency, the feeding shear layer does not have sufficient time to roll up so that the secondary LEV is not able to form in the low-inertia case.

In summary, figure 6 manifests that the onset of the subcritical LCOs depends on the static characteristics (i.e. the static stall angle) of the wing. It also provides a connection

Downloaded from https://www.cambridge.org/core. Brown University Library, on 30 Jul 2020 at 14:31:36, subject to the Cambridge Core terms of use, available at https://www.cambridge.org/core/terms. https://doi.org/10.1017/jfm.2020.481

between the quasi-steady state and the unsteady state for the pitching dynamics and the fluid torque, which could benefit the modelling of the system. It is important to note that, although the main focus of this section is to reveal the underlying dynamics and flow physics of a subcritical transition, the mechanism that triggers this transition (i.e. the pitching amplitude exceeding the static stall angle) also applies to a supercritical transition. However, while the subcritical transition has a prolonged amplitude evolution (figure 6*a*), the supercritical transition is almost instantaneous, due to the low wing inertia. This explains why the onset of LCOs scales well with Ca (figure 3*a*) in spite of the different bifurcation types. The reason why the system can settle into different LCO solutions will be discussed next in § 3.5.

3.5. *System stability from the perspective of energy transfer*

Now we characterize the stability of our system from the perspective of energy transfer between the fluid and the supporting structure. Morse & Williamson (2009) were among the first to introduce the energy approach for predicting VIVs of an elastically mounted translating cylinder. In the context of passively pitching wings, this approach has been shown to be effective for predicting the stability of small-amplitude ($|A| < 6^\circ$, Bhat & Govardhan 2013) and moderate-amplitude ($|A| < 50^\circ$, Menon & Mittal 2019) flow-induced oscillations. Here we extend this approach to the large-amplitude ($50^\circ < |A| < 120^\circ$) regime.

As noted before (Onoue *et al.* 2015; Menon & Mittal 2019), the flow-induced pitching motion is well described by a sinusoidal motion. This is also true in the current measurements ($R^2 > 0.98$). Thus, if we assume that the pitching motion can be described by

$$\theta = |A| \sin(2\pi f_p t), \tag{3.2}$$

where $|A|$ is the pitching amplitude and f_p is the pitching frequency, we can prescribe the amplitude and frequency of the motion, measure the fluid torque, τ_f, and integrate the equation of motion (2.6) over n cycles to obtain the cycle-averaged energy transfer between the fluid and the structure:

$$E = \frac{1}{n} \int_{t_0}^{t_0+nT} (\tau_f \dot{\theta} - b\dot{\theta}^2)\, \mathrm{d}t. \tag{3.3}$$

For the results presented here, we have used $n = 20$ and swept f_p from 0.15 to 0.6 Hz with a step size of 0.05 and $|A|$ from 0 to 2.5 rad with a step size of 0.175. The $\tau_f\dot{\theta}$ term represents the power extracted by the wing from the ambient fluid, and the $b\dot{\theta}^2$ term represents the power dissipated by the structural damping (Menon & Mittal 2019). Following Onoue *et al.* (2015), we multiply E by the pitching frequency, f_p, and normalize the equation to get the power coefficient of the system:

$$C_p = \frac{f_p^*}{n} \int_{t_0}^{t_0+nT} (\tau_f^* \dot{\theta}^* - b^* \dot{\theta}^{*2})\, \mathrm{d}t^*. \tag{3.4}$$

The power coefficient map is shown in figure 7, with the x-axis represented by f_p^* in figure 7(*a*) and by $U_p^* = 1/(2\pi f_p^*)$ in figure 7(*b*). In both plots, red, white and blue represent regions of power extraction ($C_p > 0$), balance ($C_p = 0$) and dissipation ($C_p < 0$), respectively. The power balance ($C_p = 0$) curve is indicated by black dashed lines. The value $|A| = 0$ is also a possible solution for power balance. We wish to note that, although

Downloaded from https://www.cambridge.org/core. Brown University Library, on 30 Jul 2020 at 14:31:36, subject to the Cambridge Core terms of use, available at https://www.cambridge.org/core/terms. https://doi.org/10.1017/jfm.2020.481

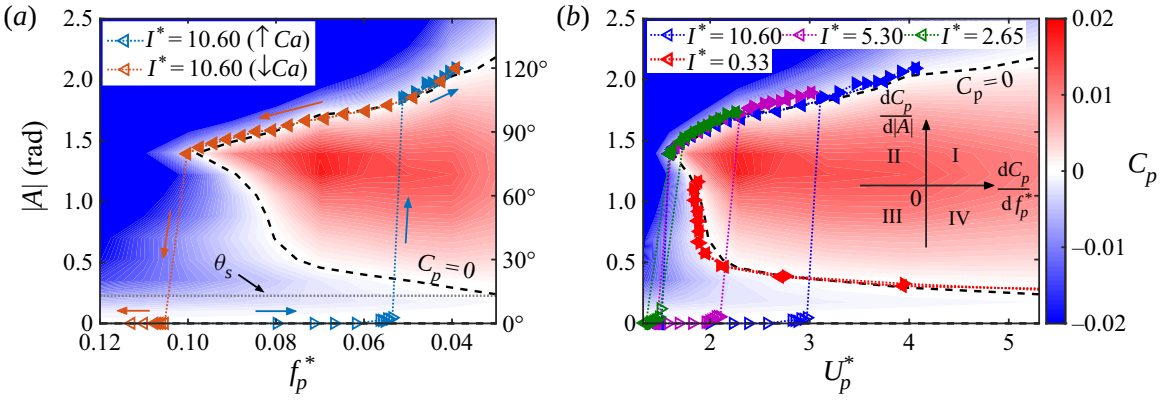


FIGURE 7. (*a*) Contour plot of the power coefficient, C_p, overlaid by the amplitude response of the system at $I^* = 10.6$. The zero power coefficient contour is indicated by black dashed lines. The static stall angle θ_s is labelled by a grey dotted line. Note the reverse scale of the x-axis. (*b*) Power coefficient map plotted against the non-dimensional velocity, overlaid by the amplitude response of the system at different inertia values. Inset: A diagram illustrating the four quadrants of the power coefficient gradient: x-axis, $\mathrm{d}C_p/\mathrm{d}f_p^*$; y-axis, $\mathrm{d}C_p/\mathrm{d}|A|$.

figure 7 reflects the power coefficient map of one particular damping value ($b^* = 0.13$), the power coefficient map of other damping values can be easily generated by simply varying b^* in (3.4). This demonstrates the universality of the energy approach for analysing systems with different structural damping values (Morse & Williamson 2009; Menon & Mittal 2019). To connect the power coefficient map with the previously discussed system stability boundaries, we re-plot the amplitude response data, from figures 2(*a*) and 3(*b*), onto figures 7(*a*) and 7(*b*), respectively. To make the connection between figures 7(*a*) and 2(*a*) more intuitive, we plot the x-axis of figure 7(*a*) *using a reverse scale*, so that the shape of the bifurcation diagram remains relatively consistent in these two plots. In both figures 7(*a*) and 7(*b*), the frequency for large-amplitude LCOs (i.e. solid markers) is the measured pitching frequency f_p^*. For the data points with zero- or small-amplitude oscillations (i.e. hollow markers), the frequency is the structural frequency f_s^* (see § 3.2).

Comparing figure 7(*a*) with the energy map of Menon & Mittal (2019, figure 13), we see that, although the frequency range of these two maps is quite different (i.e. $0.03 \leq f_p^* \leq 0.12$ versus $0.10 < f_p^* < 0.75$), the general shape looks similar for the overlapped amplitude range (i.e. $0 \leq |A| \leq 50^\circ$). Both maps show that the wing extracts more energy from the ambient fluid when the pitching frequency is low, and dissipates more energy when the pitching frequency is high (note the reverse x-axis in figure 7*a*). However, the detailed shapes of the power balance curve ($C_p = 0$) are very different in these two maps. The $C_p = 0$ curve seems to extend to $(f_p^*, |A|) = (0, 0)$ in figure 7(*a*), but stays relatively vertical and has a non-zero x-intercept in figure 13 of Menon & Mittal (2019). Moreover, $|A| = 0$ is part of the $C_p = 0$ curve in figure 7(*a*), but not in figure 13 of Menon & Mittal (2019). We believe that these differences mainly come from the different initial AOAs used in these two studies (i.e. 0° versus 15°). It has been shown by Dugundji (2008), Razak *et al.* (2011) and Menon & Mittal (2019, figure 3) that different initial AOAs can lead to significantly different stability characteristics, which suggests that the power coefficient map (or the energy map) of a zero-initial-AOA wing and a 15°-initial-AOA wing can be quite different.

Comparing the power coefficient map and the amplitude response reveals many interesting features. Figure 7(*a*) shows that, for $I^* = 10.60$, large-amplitude LCOs

Downloaded from https://www.cambridge.org/core. Brown University Library, on 30 Jul 2020 at 14:31:36, subject to the Cambridge Core terms of use, available at https://www.cambridge.org/core/terms. https://doi.org/10.1017/jfm.2020.481

fall exactly on the upper branch of the $C_p = 0$ curve. This is expected because the self-sustained flow-induced oscillations represent a condition of energy balance (Morse & Williamson 2009; Menon & Mittal 2019). We have shown in § 3.2 that the subcritical LCOs for $I^* = 10.60$ represent a structural mode, where the pitching frequency locks onto the structural frequency. This means that, for any data point representing subcritical LCOs, its x-coordinate (i.e. f_p^*) is constrained by k^* and I^*, so that it is only free to move in the y-direction (i.e. change $|A|$) under external perturbations. If $|A|$ increases (or decreases), the system will enter the blue region where $C_p < 0$ (or the red region where $C_p > 0$) and go back to the equilibrium solution ($C_p = 0$) because of power dissipation (or power extraction). Based on this analysis, we can deduce the stability criterion for the structural mode (Menon & Mittal 2019):

$$C_p = 0 \quad \text{and} \quad \frac{\mathrm{d}C_p}{\mathrm{d}|A|} < 0. \tag{3.5}$$

The upper branch of the $C_p = 0$ curve satisfies this criterion, so that it is a stable equilibrium solution for subcritical LCOs. The x-axis (i.e. $|A| = 0$) also represents a stable equilibrium for the same reason. In contrast, the lower branch of the $C_p = 0$ curve represents an unstable equilibrium solution, because its power gradient along the y-direction is positive (i.e. $\mathrm{d}C_p/\mathrm{d}|A| > 0$). The existence of multiple (stable LCO, unstable LCO and stable fixed point) solutions is an important feature of a subcritical Hopf bifurcation, which has been discussed in § 3.1. Revealing the unstable equilibrium solution, which is not possible in passive experiments, is one of the benefits for adopting the energy approach.

Figure 7(*b*) provides insights into the system stability for other wing inertia values. Because the measured pitching frequency, f_p (instead of f_s), is used to calculate U_p^* for the large-amplitude LCOs, we see that the amplitude response of the subcritical LCOs ($I^* = 10.60$, 5.30 and 2.65) collapse remarkably well, as compared to figure 3(*b*). All these subcritical LCOs, regardless of their inertia values, fall onto the upper $C_p = 0$ branch, for the reason discussed above. Moreover, the power coefficient map explains why there exists a critical U_p^*, below which the subcritical LCOs cannot sustain. This is because, below this critical U_p^* (or above the corresponding critical f_p^*), the power coefficient of the system is negative ($C_p < 0$). More power is damped by the structural damping than extracted from the fluid, so that the power of the system is insufficient to sustain large-amplitude LCOs. The underlying flow physics causing the decrease of C_p requires further investigations.

For $I^* = 0.33$, we see that supercritical LCOs fall onto the lower branch of the $C_p = 0$ curve. As discussed earlier, this lower branch is an unstable equilibrium solution for the structural mode. However, its stability has a different nature for the hydrodynamic mode. In the structural mode, the pitching frequency is constrained by the structural frequency, so that the stability of an equilibrium solution is determined by $\mathrm{d}C_p/\mathrm{d}|A|$ (see (3.5)). In contrast, for the hydrodynamic mode, because the oscillation is dictated by the fluid force (see figure 4*b*, bottom), the system is not constrained to move vertically in the energy map, but is free to move in *both* the $|A|$-direction and the f_p^*-direction. On the lower branch of the $C_p = 0$ curve, if the system is perturbed to enter the blue region where $C_p < 0$ (or the red region where $C_p > 0$), f_p^* can in turn decrease (or increase) to accommodate power dissipations (or power extractions), and the system will thus return to the equilibrium solution ($C_p = 0$) again. Therefore, the lower branch of the $C_p = 0$ curve ($\mathrm{d}C_p/\mathrm{d}f_p^* < 0$) is a stable equilibrium solution for supercritical LCOs.

It is important to note that, because the system is free to move vertically as well, $\mathrm{d}C_p/\mathrm{d}|A| < 0$ can also contribute to the stability of supercritical LCOs. Therefore, the

Downloaded from https://www.cambridge.org/core. Brown University Library, on 30 Jul 2020 at 14:31:36, subject to the Cambridge Core terms of use, available at https://www.cambridge.org/core/terms. https://doi.org/10.1017/jfm.2020.481

stability criterion for the hydrodynamic mode is

$$C_p = 0 \quad \text{and} \quad \left(\frac{\mathrm{d}C_p}{\mathrm{d}|A|} < 0 \quad \text{or} \quad \frac{\mathrm{d}C_p}{\mathrm{d}f_p^*} < 0 \right). \tag{3.6}$$

Following this criterion, the upper branch of the $C_p = 0$ curve and $|A| = 0$ are also stable equilibrium solutions for the hydrodynamic mode. However, this does not mean that the low-inertia system can have multiple equilibrium solutions at a given Ca, because Ca does not have a one-to-one correspondence with f_p^* in the hydrodynamic mode. The specific combination of $|A|$ and f_p^* depends on how much power is extracted from the fluid. The selection of different stable equilibrium solutions further confirms the intrinsic difference between the hydrodynamic mode and the structural mode.

Now we can summarize and visualize the stability criterion for the structural mode and the hydrodynamic mode. As shown by (3.5) and (3.6), the common prerequisite for stability for these two oscillation modes is $C_p = 0$. To examine the stability of the $C_p = 0$ curve, we visualize the sign of $\mathrm{d}C_p/\mathrm{d}f_p^*$ and $\mathrm{d}C_p/\mathrm{d}|A|$ using a quadrant diagram, as shown by the inset of figure 7(*b*). For the structural mode, the system is stable in quadrants III and IV (including the negative y-axis), and unstable in quadrants I and II (including the x-axis and the positive y-axis). For the hydrodynamic mode, the system is stable in quadrants II, III and IV (including the negative x- and y-axis), and unstable only in quadrant I (including the positive x- and y-axis). As discussed earlier, for the present system, the $C_p = 0$ curve has three branches. The upper branch is in quadrant III, so it is a stable solution for both oscillations modes. The lower branch is in quadrant II, so it is a stable solution for the hydrodynamic mode and an unstable solution for the structural mode. The $|A| = 0$ branch lies on the negative y-axis, so it is a stable solution for both oscillation modes again.

One critical question in the present study is why the bifurcation is subcritical for the structural mode and supercritical for the hydrodynamic mode. The power coefficient map provides us with some insights. As shown in figure 7(*b*), for all wing inertias, near the transitional U_p^* values, the stability of the system, indicated by the power coefficient map, is a stable equilibrium at $|A| = 0$. In theory, without any external perturbations, the system should stay at this stable fixed point solution for any U_p^*. However, we should note that the power coefficient map only identifies the stability of (near-) sinusoidal symmetric oscillations. The stability of the static divergence and quasi-steady small-amplitude oscillations is not accessible from this map. In our experiments, as Ca is increased, the wing first bifurcates into a static divergence angle, which brings asymmetry to the problem. Then the system develops small-amplitude oscillations around this divergence angle (§ 3.1). As shown in figure 6(*a*), after the pitching amplitude exceeds the static stall angle, θ_s, unsteady oscillations start near $(f_p^*, |A|) = (0, \theta_s)$, which presumably falls into the power extraction regime (i.e. the red region, see figure 7*a*). In this regime, the system has two possible evolution paths depending on the oscillation mode.

(i) For the structural mode, because of the constraint in the pitching frequency discussed above, f_p^* has to gradually develop into f_s^*. In this process, the system keeps gaining energy from the ambient fluid ($C_p > 0$) and finally settles to the upper $C_p = 0$ branch (3.5), which results in the abrupt jump in pitching amplitude, defining a subcritical-type bifurcation. The width of the bistable region is determined by the difference between the onset f^*, which varies with I^* because the onset k^* is fixed (§ 3.4), and the critical (saddle-node) f^*, which is unchanged for any combination of I^* and k^*. This explains the shrinking of the bistable region for different wing inertias (figure 3).

Downloaded from https://www.cambridge.org/core. Brown University Library, on 30 Jul 2020 at 14:31:36, subject to the Cambridge Core terms of use, available at https://www.cambridge.org/core/terms. https://doi.org/10.1017/jfm.2020.481

(ii) For the hydrodynamic mode, however, without the constraint in f_p^*, the system can pick up the lowest possible $|A|$ on the lower $C_p = 0$ curve as a stable solution after the transition from quasi-steady oscillations (3.6). This results in a smooth connection between the deflected small-amplitude oscillations and the symmetric large-amplitude LCOs, which creates a supercritical-type bifurcation.

For both paths, the quasi-steady to unsteady transition described in § 3.4 acts as a triggering mechanism for the onset of large-amplitude LCOs. Unveiling this triggering mechanism is of help towards creating a proper low-order model for the system.

4. Conclusion

We have performed water tunnel experiments to examine the stability boundaries of a rigid but flexibly mounted NACA-0012 wing at a Reynolds number of 50 000. We fixed the structural damping of the wing at a small value and systematically varied the torsional stiffness to explore the stability boundaries for different wing inertias. A subcritical bifurcation which features an abrupt amplitude jump and hysteretic bistability was observed for high-inertia wings, whereas a supercritical bifurcation in which the amplitude response varies smoothly with the control parameter without hysteresis was observed for a low-inertia wing. For both types of bifurcations, we showed that the onset of large-amplitude flow-induced oscillations scales with the Cauchy number, Ca. For high-inertia wings, the amplitude and the saddle-node point of subcritical LCOs were reported to scale with the non-dimensional velocity, U^*. Frequency response and force decomposition suggested that subcritical LCOs were dominated by the inertial force, corresponding to a structural mode, while supercritical LCOs were regulated by the fluid force, corresponding to a hydrodynamic mode. The force response was associated with the flow dynamics to explain the difference between the structural mode and the hydrodynamic mode. Two unique phenomena related to the structural mode, namely the frequency lock-in and the presence of a secondary LEV, were reported. We examined the transition to subcritical LCOs in detail, and it was shown that this transition depends on the static characteristics of the wing, and the emergence of the secondary LEV was an important feature of the transition. Finally, we adopted an energy approach to characterize the stability of the system. The stable equilibrium solution for the hydrodynamic mode was shown to be unstable for the structural mode because of the frequency lock-in phenomenon, which further resulted in the distinctive super- and subcritical bifurcations for these two modes.

Acknowledgments

This work is funded by the Air Force Office of Scientific Research, Grant FA9550-18-1-0322, managed by Dr G. Abate. The authors thank D. Harris and members of the Breuer Lab at Brown University, as well as J. Seidel, C. Fagley and A. Jirasek at the US Air Force Academy, for many helpful discussions and insights.

Declaration of interests

The authors report no conflict of interest.

Supplementary movies

Supplementary movies are available at https://doi.org/10.1017/jfm.2020.481.

Downloaded from https://www.cambridge.org/core. Brown University Library, on 30 Jul 2020 at 14:31:36, subject to the Cambridge Core terms of use, available at https://www.cambridge.org/core/terms. https://doi.org/10.1017/jfm.2020.481

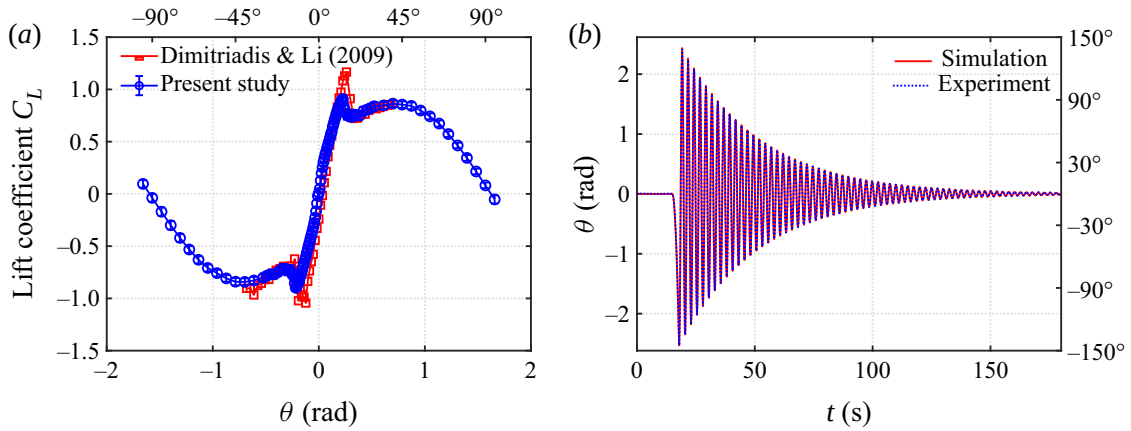


FIGURE 8. (*a*) Characterization of the wing. (*b*) Validation of the cyber-physical system.

Appendix A. System characterization

We characterize our NACA-0012 wing by measuring the static lift force L at different pitching angles. The lift coefficient, C_L, defined as $C_L = L/(0.5\rho U^2 cs)$, is plotted against the pitching angle θ in figure 8(*a*). The measured lift coefficients matches well with previous wind tunnel experiments by Dimitriadis & Li (2009).

We validate our cyber-physical system by conducting free oscillation ('ring-down') experiments. The ring-down experiments are conducted in air to exclude the nonlinear fluid damping effect. We apply a short-time constant-torque impulse to the wing using the cyber-physical system, after which we record and analyse the decay of the free damped oscillations. Figure 8(*b*) shows that the measured pitching decay agrees very well with the simulated decay, which is derived based on the virtual inertia, stiffness and damping, indicating that our cyber-physical system can accurately simulate physical structural dynamics of the system.

Appendix B. Effect of the Reynolds number

One issue of interest is whether the scaling used in explaining the flow-induced instability boundaries are appropriate(§ 3.1), and to what extent the phenomena are affected by the Reynolds number. These effects are tested by repeating the bifurcation tests for the high-inertia case ($I^* = 10.6$) at four different flow speeds $U = 0.3$–0.6 m s^{-1}. The resulting Reynolds number varies from $Re = 30\,000$ to $60\,000$. The virtual structural parameters (I_v, b_v and k_v) are varied to match the non-dimensional parameters (I^*, b^* and k^*). The results are shown in figure 9. Figure 9(*a*) shows that, as the Reynolds number is varied, the amplitude response remains almost the same, despite some subtle changes in the pitching amplitude and the critical Ca. Taking $Ca = 1.5$ and plotting the corresponding non-dimensional torque–angle phase diagram in figure 9(*b*), we observe that the phase diagrams of the four different Reynolds numbers collapse very well. These results indicate that the Reynolds number has a very minor effect on the present experimental results, which agrees with Onoue *et al.* (2015). The robustness of our non-dimensionalization is also justified by the unchanging amplitude response and phase diagram. However, we should note that the effect of Reynolds number also depends on the choice of the structural damping b^*. In the present experiments, the structural damping is fixed at a very small value $b^* = 0.13$. At a higher b^*, the Reynolds number can have a prominent effect on the flow-induced oscillations (see figure 12 in Onoue *et al.* 2015).

Downloaded from https://www.cambridge.org/core. Brown University Library, on 30 Jul 2020 at 14:31:36, subject to the Cambridge Core terms of use, available at https://www.cambridge.org/core/terms. https://doi.org/10.1017/jfm.2020.481

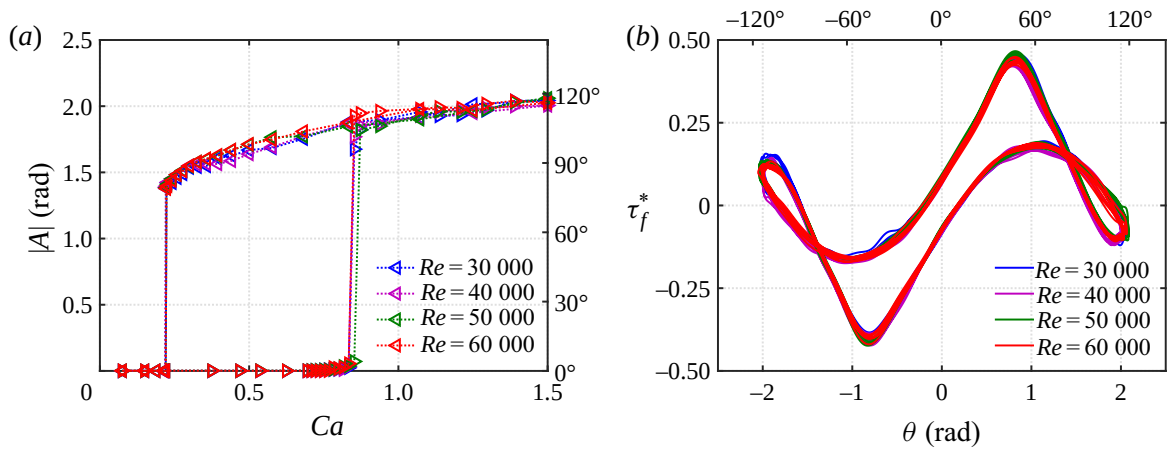


FIGURE 9. (*a*) Amplitude response of the high-inertia case ($I^* = 10.60$) at four different Reynolds numbers and (*b*) the corresponding torque–angle phase diagram at $Ca = 1.5$.

REFERENCES

AMANDOLESE, X., MICHELIN, S. & CHOQUEL, M. 2013 Low speed flutter and limit cycle oscillations of a two-degree-of-freedom flat plate in a wind tunnel. *J. Fluids Struct.* **43**, 244–255.

BAIK, Y. S., BERNAL, L. P., GRANLUND, K. & OL, M. V. 2012 Unsteady force generation and vortex dynamics of pitching and plunging aerofoils. *J. Fluid Mech.* **709**, 37–68.

BARNES, C. J. & VISBAL, M. R. 2018 On the role of flow transition in laminar separation flutter. *J. Fluids Struct.* **77**, 213–230.

BEATUS, T. & COHEN, I. 2015 Wing-pitch modulation in maneuvering fruit flies is explained by an interplay between aerodynamics and a torsional spring. *Phys. Rev.* E **92** (2), 022712.

BERGOU, A. J., RISTROPH, L., GUCKENHEIMER, J., COHEN, I. & WANG, Z. J. 2010 Fruit flies modulate passive wing pitching to generate in-flight turns. *Phys. Rev. Lett.* **104** (14), 148101.

BERGOU, A. J., XU, S. & WANG, Z. J. 2007 Passive wing pitch reversal in insect flight. *J. Fluid Mech.* **591**, 321–337.

BHAT, S. S. & GOVARDHAN, R. N. 2013 Stall flutter of NACA 0012 airfoil at low Reynolds numbers. *J. Fluids Struct.* **41**, 166–174.

BOUDREAU, M., DUMAS, G., RAHIMPOUR, M. & OSHKAI, P. 2018 Experimental investigation of the energy extraction by a fully-passive flapping-foil hydrokinetic turbine prototype. *J. Fluids Struct.* **82**, 446–472.

DIMITRIADIS, G. & LI, J. 2009 Bifurcation behavior of airfoil undergoing stall flutter oscillations in low-speed wind tunnel. *AIAA J.* **47** (11), 2577–2596.

DOWELL, E., EDWARDS, J. & STRGANAC, T. 2003 Nonlinear aeroelasticity. *J. Aircraft* **40** (5), 857–874.

DOWELL, E. H., CURTISS, H. C., SCANLAN, R. H. & SISTO, F. 1989 *A Modern Course in Aeroelasticity*. Springer.

DOWELL, E. H. & HALL, K. C. 2001 Modeling of fluid-structure interaction. *Annu. Rev. Fluid Mech.* **33** (1), 445–490.

DUARTE, L., DELLINGER, N., DELLINGER, G., GHENAIM, A. & TERFOUS, A. 2019 Experimental investigation of the dynamic behaviour of a fully passive flapping foil hydrokinetic turbine. *J. Fluids Struct.* **88**, 1–12.

DUGUNDJI, J. 2008 Some aeroelastic and nonlinear vibration problems encountered on the journey to Ithaca. *AIAA J.* **46** (1), 21–35.

ELDREDGE, J. D. & JONES, A. R. 2019 Leading-edge vortices: mechanics and modeling. *Annu. Rev. Fluid Mech.* **51**, 75–104.

FAGLEY, C., SEIDEL, J. & MCLAUGHLIN, T. 2016 Cyber-physical flexible wing for aeroelastic investigations of stall and classical flutter. *J. Fluids Struct.* **67**, 34–47.

GARRICK, I. E. 1936 Propulsion of a flapping and oscillating airfoil. *NACA Tech. Rep.* 567.

Downloaded from https://www.cambridge.org/core. Brown University Library, on 30 Jul 2020 at 14:31:36, subject to the Cambridge Core terms of use, available at https://www.cambridge.org/core/terms. https://doi.org/10.1017/jfm.2020.481

GOVARDHAN, R. & WILLIAMSON, C. H. K. 2000 Modes of vortex formation and frequency response of a freely vibrating cylinder. *J. Fluid Mech.* **420**, 85–130.

GOVARDHAN, R. & WILLIAMSON, C. H. K. 2002 Resonance forever: existence of a critical mass and an infinite regime of resonance in vortex-induced vibration. *J. Fluid Mech.* **473**, 147–166.

GRANLUND, K. O., OL, M. V. & BERNAL, L. P. 2013 Unsteady pitching flat plates. *J. Fluid Mech.* **733**, R5.

HO, S., NASSEF, H., PORNSINSIRIRAK, N., TAI, Y.-C. & HO, C.-M. 2003 Unsteady aerodynamics and flow control for flapping wing flyers. *Prog. Aerosp. Sci.* **39** (8), 635–681.

HOVER, F. S., MILLER, S. N. & TRIANTAFYLLOU, M. S. 1997 Vortex-induced vibration of marine cables: experiments using force feedback. *J. Fluids Struct.* **11** (3), 307–326.

ISHIHARA, D., YAMASHITA, Y., HORIE, T., YOSHIDA, S. & NIHO, T. 2009 Passive maintenance of high angle of attack and its lift generation during flapping translation in crane fly wing. *J. Expl Biol.* **212** (23), 3882–3891.

JAFFERIS, N. T., HELBLING, E. F., KARPELSON, M. & WOOD, R. J. 2019 Untethered flight of an insect-sized flapping-wing microscale aerial vehicle. *Nature* **570** (7762), 491–495.

JANTZEN, R. T., TAIRA, K., GRANLUND, K. O. & OL, M. V. 2014 Vortex dynamics around pitching plates. *Phys. Fluids* **26** (5), 053606.

JIN, Y., KIM, J.-T., FU, S. & CHAMORRO, L. P. 2019 Flow-induced motions of flexible plates: fluttering, twisting and orbital modes. *J. Fluid Mech.* **864**, 273–285.

KHALAK, A. & WILLIAMSON, C. H. K. 1996 Dynamics of a hydroelastic cylinder with very low mass and damping. *J. Fluids Struct.* **10** (5), 455–472.

KIM, D., COSSÉ, J., CERDEIRA, C. H. & GHARIB, M. 2013 Flapping dynamics of an inverted flag. *J. Fluid Mech.* **736**, R1.

LEE, J. H., XIROS, N. & BERNITSAS, M. M. 2011 Virtual damper-spring system for VIV experiments and hydrokinetic energy conversion. *Ocean Engng* **38** (5–6), 732–747.

MACKOWSKI, A. W. & WILLIAMSON, C. H. K. 2011 Developing a cyber-physical fluid dynamics facility for fluid-structure interaction studies. *J. Fluids Struct.* **27** (5–6), 748–757.

MCCROSKEY, W. J. 1982 Unsteady airfoils. *Annu. Rev. Fluid Mech.* **14** (1), 285–311.

MENON, K. & MITTAL, R. 2019 Flow physics and dynamics of flow-induced pitch oscillations of an airfoil. *J. Fluid Mech.* **877**, 582–613.

MORSE, T. L. & WILLIAMSON, C. H. K. 2009 Prediction of vortex-induced vibration response by employing controlled motion. *J. Fluid Mech.* **634**, 5–39.

NAVROSE & MITTAL, S. 2017 The critical mass phenomenon in vortex-induced vibration at low *Re*. *J. Fluid Mech.* **820**, 159–186.

ONOUE, K. & BREUER, K. S. 2016 Vortex formation and shedding from a cyber-physical pitching plate. *J. Fluid Mech.* **793**, 229–247.

ONOUE, K. & BREUER, K. S. 2017 A scaling for vortex formation on swept and unswept pitching wings. *J. Fluid Mech.* **832**, 697–720.

ONOUE, K., SONG, A., STROM, B. & BREUER, K. S. 2015 Large amplitude flow-induced oscillations and energy harvesting using a cyber-physical pitching plate. *J. Fluids Struct.* **55**, 262–275.

PENG, Z. & ZHU, Q. 2009 Energy harvesting through flow-induced oscillations of a foil. *Phys. Fluids* **21** (12), 123602.

POIREL, D., HARRIS, Y. & BENAISSA, A. 2008 Self-sustained aeroelastic oscillations of a NACA0012 airfoil at low-to-moderate Reynolds numbers. *J. Fluids Struct.* **24** (5), 700–719.

POIREL, D., METIVIER, V. & DUMAS, G. 2011 Computational aeroelastic simulations of self-sustained pitch oscillations of a NACA0012 at transitional Reynolds numbers. *J. Fluids Struct.* **27** (8), 1262–1277.

POIREL, D. & YUAN, W. 2010 Aerodynamics of laminar separation flutter at a transitional Reynolds number. *J. Fluids Struct.* **26** (7–8), 1174–1194.

RAO, S. S. 1995 *Mechanical Vibrations*. Addison-Wesley.

RAZAK, N. A., ANDRIANNE, T. & DIMITRIADIS, G. 2011 Flutter and stall flutter of a rectangular wing in a wind tunnel. *AIAA J.* **49** (10), 2258–2271.

SHARMA, A. & VISBAL, M. 2019 Numerical investigation of the effect of airfoil thickness on onset of dynamic stall. *J. Fluid Mech.* **870**, 870–900.

Downloaded from https://www.cambridge.org/core. Brown University Library, on 30 Jul 2020 at 14:31:36, subject to the Cambridge Core terms of use, available at https://www.cambridge.org/core/terms. https://doi.org/10.1017/jfm.2020.481

SHYY, W., AONO, H., CHIMAKURTHI, S. K., TRIZILA, P., KANG, C.-K., CESNIK, C. E. S. & LIU, H. 2010 Recent progress in flapping wing aerodynamics and aeroelasticity. *Prog. Aerosp. Sci.* **46** (7), 284–327.

STRICKLAND, J. H. & GRAHAM, G. M. 1987 Force coefficients for a NACA-0015 airfoil undergoing constant pitch rate motions. *AIAA J.* **25** (4), 622–624.

STROGATZ, S. H. 1994 *Nonlinear Dynamics and Chaos: With Applications to Physics, Biology, Chemistry, and Engineering*. Perseus Books.

SU, Y & BREUER, K. S. 2019 Resonant response and optimal energy harvesting of an elastically mounted pitching and heaving hydrofoil. *Phys. Rev. Fluids* **4** (6), 064701.

THEODORSEN, T. 1935 General theory of aerodynamic instability and the mechanism of flutter. *NACA Tech. Rep.* 496.

TZEZANA, G. A. & BREUER, K. S. 2019 Thrust, drag and wake structure in flapping compliant membrane wings. *J. Fluid Mech.* **862**, 871–888.

VEILLEUX, J.-C. & DUMAS, G. 2017 Numerical optimization of a fully-passive flapping-airfoil turbine. *J. Fluids Struct.* **70**, 102–130.

WANG, Z., DU, L., ZHAO, J. & SUN, X. 2017 Structural response and energy extraction of a fully passive flapping foil. *J. Fluids Struct.* **72**, 96–113.

WANG, Z. J. 2005 Dissecting insect flight. *Annu. Rev. Fluid Mech.* **37**, 183–210.

WILLIAMSON, C. H. K. & GOVARDHAN, R. 2004 Vortex-induced vibrations. *Annu. Rev. Fluid Mech.* **36**, 413–455.

WU, K. S., NOWAK, J. & BREUER, K. S. 2019 Scaling of the performance of insect-inspired passive-pitching flapping wings. *J. R. Soc. Interface* **16** (161), 20190609.

XIAO, Q. & ZHU, Q. 2014 A review on flow energy harvesters based on flapping foils. *J. Fluids Struct.* **46**, 174–191.

YOUNG, J., ASHRAF, M. A., LAI, J. C. S. & PLATZER, M. F. 2013 Numerical simulation of fully passive flapping foil power generation. *AIAA J.* **51** (11), 2727–2739.

YOUNG, J., LAI, J. C. S. & PLATZER, M. F. 2014 A review of progress and challenges in flapping foil power generation. *Prog. Aerosp. Sci.* **67**, 2–28.

ZHU, Q. 2011 Optimal frequency for flow energy harvesting of a flapping foil. *J. Fluid Mech.* **675**, 495–517.

ZHU, Q. 2012 Energy harvesting by a purely passive flapping foil from shear flows. *J. Fluids Struct.* **34**, 157–169.

ZHU, Q., HAASE, M. & WU, C. H. 2009 Modeling the capacity of a novel flow-energy harvester. *Appl. Math. Model.* **33** (5), 2207–2217.

ZHU, Q. & PENG, Z. 2009 Mode coupling and flow energy harvesting by a flapping foil. *Phys. Fluids* **21** (3), 033601.

Downloaded from https://www.cambridge.org/core. Brown University Library, on 30 Jul 2020 at 14:31:36, subject to the Cambridge Core terms of use, available at https://www.cambridge.org/core/terms. https://doi.org/10.1017/jfm.2020.481

Downloaded from https://www.cambridge.org/core. Brown University Library, on 30 Jul 2020 at 14:31:36, subject to the Cambridge Core terms of use, available at https://www.cambridge.org/core/terms. https://doi.org/10.1017/jfm.2020.481

J. Fluid Mech. (2020), *vol*. 899, A35. © The Author(s), 2020.
Published by Cambridge University Press
doi:10.1017/jfm.2020.481

Nonlinear flow-induced instability of an elastically mounted pitching wing

Yuanhang Zhu[1],†, **Yunxing Su**[1] **and Kenneth Breuer**[1]

[1]Center for Fluid Mechanics, School of Engineering, Brown University, Providence, RI 02912, USA

(Received 8 February 2020; revised 21 May 2020; accepted 10 June 2020)

We experimentally study the nonlinear flow-induced instability of an elastically mounted pitching wing in a circulating water tunnel. The structural parameters of the finite-span wing are simulated and regulated using a cyber-physical control system. At a small fixed damping, we systematically vary the stiffness of the wing for different inertia values to test for the stability boundaries of the system. We observe that, for a high-inertia wing, the system dynamics bifurcates from stable fixed points to small-amplitude oscillations followed by large-amplitude limit-cycle oscillations (LCOs) via a subcritical bifurcation, which features hysteretic bistability and an abrupt amplitude jump. Under this condition, the pitching frequency of the wing locks onto its structural frequency and the oscillation is dominated by the inertial force, corresponding to a structural mode. Force and flow field measurements indicate the presence of a secondary leading-edge vortex (LEV). As the wing inertia decreases, the width of the bistable region shrinks. At a sufficiently low inertia, the pitching amplitude changes smoothly with the stiffness without any hysteresis, revealing a supercritical bifurcation. Under this condition, no lock-in phenomenon is observed and the pitching frequency remains relatively constant at a value lower than the structural frequency. Force decomposition shows dominating fluid force, indicating a hydrodynamic mode. The secondary LEV is absent. We show that the onset of large-amplitude LCOs in both the structural mode and the hydrodynamic mode scales with the Cauchy number, and the LCOs in the structural mode collapse with the non-dimensional velocity. We examine the subcritical transition in detail; we find that this transition depends on the static characteristics of the wing, and the secondary LEV starts to emerge at the early stage of the transition. Lastly, we adopt an energy approach to map out the stability of the system and explain the existence of the two distinct types of bifurcations observed for different inertia values.

Key words: flow–structure interactions, nonlinear instability, vortex dynamics

1. Introduction

Nonlinear flow-induced instability of elastically mounted wings is a classic aeroelastic problem that has been studied extensively for decades. However, our understanding of this problem still remains far from complete, due to its highly nonlinear nature, and the numerous parameters involved. In recent years, in addition to its original applications for understanding aeroelastic failures (Dowell *et al.* 1989), the nonlinear aeroelastic instability

† Email address for correspondence: yuanhang_zhu@brown.edu

has become an important subject for the development of flapping-wing micro air vehicles (MAVs) (Ho *et al.* 2003; Shyy *et al.* 2010) and flapping-foil energy harvesting devices (Xiao & Zhu 2014; Young, Lai & Platzer 2014; Su & Breuer 2019). Many flapping-wing MAVs emulate the flight of insects (e.g. Jafferis *et al.* 2019) because of the relatively simple flight kinematics, which can be primarily decomposed into prescribed flapping and passive pitching. The passive pitching of insect wings can be modelled as a flat plate attached to a torsional spring–damper system hinged at the leading edge (Wang 2005; Bergou, Xu & Wang 2007; Ishihara *et al.* 2009; Bergou *et al.* 2010; Beatus & Cohen 2015; Wu, Nowak & Breuer 2019). The locomotion of insects and other aquatic animals has also inspired the development of flapping-foil kinetic energy harvesters, among which Peng & Zhu (2009) proposed a fully passive pitch–heave configuration, where the energy-extracting heaving motion is driven by the flow-induced pitching instability instead of prescribed (Zhu & Peng 2009). Many numerical (Zhu 2011; Young *et al.* 2013; Veilleux & Dumas 2017; Wang *et al.* 2017) and experimental (Dimitriadis & Li 2009; Amandolese, Michelin & Choquel 2013; Boudreau *et al.* 2018; Duarte *et al.* 2019) studies have been carried out to explore the nonlinear pitch–heave coupling, yet the flow-induced pitching instability itself remains relatively elusive.

1.1. *Unsteady pitching wings with prescribed kinematics*

A key phenomenon associated with the nonlinear aeroelastic instability of passively pitching wings is the stall flutter, caused by the interaction between characteristics of the structural support of the wing and dynamic stall events (McCroskey 1982; Dimitriadis & Li 2009). Dynamic stall is an unsteady aerodynamic effect that occurs when a wing is pitching rapidly. It is featured by the formation, growth and shedding of a strong leading-edge vortex (LEV), which results in a transient increase, followed by a sharp drop, in lift (McCroskey 1982; Eldredge & Jones 2019). Many studies have focused on characterizing this dynamic stall phenomenon using prescribed kinematics. Baik *et al.* (2012) experimentally studied the aerodynamic force and flow dynamics of an airfoil undergoing sinusoidal pitch–plunge motion. It was shown that the unsteady aerodynamic force generation largely depends on the Strouhal number, $St \equiv 2fh_0c/U$, where f, h_0, c and U are the oscillation frequency, the plunging amplitude, the chord length and the free-stream velocity, respectively. The flow evolution and LEV dynamics were shown to be mainly controlled by the reduced frequency, $K \equiv \pi fc/U$. Their experimental results also agree reasonably well with the classic linear potential flow models proposed by Theodorsen (1935) and Garrick (1936). Using a similar set-up, Granlund, Ol & Bernal (2013) found that, when a wing is undergoing smoothed linear pitch ramps, the unsteady fluid force and the LEV development highly depend on the pitching rate, which was later reinforced by Jantzen *et al.* (2014). Granlund *et al.* (2013) also successfully generalized the unsteady force scaling proposed by Strickland & Graham (1987) to take into account the effect of pivot axis.

1.2. *Flow-induced oscillations of passively pitching wings*

Compared to the studies of prescribed pitching wings, in which the kinematics of the wing alters the flow field and thus the fluid force (i.e. one-way coupling), flow-induced oscillations of passively pitching wings is a two-way coupling problem, in which the resultant fluid force will in turn change the pitching kinematics. Once the fluid force is coupled with the structural force, self-sustained oscillations will be excited. In nonlinear dynamical systems, self-sustained (or self-excited) oscillations refer to the oscillations that

Downloaded from https://www.cambridge.org/core. Brown University Library, on 30 Jul 2020 at 14:31:36, subject to the Cambridge Core terms of use, available at https://www.cambridge.org/core/terms. https://doi.org/10.1017/jfm.2020.481

Downloaded from https://www.cambridge.org/core. Brown University Library, on 30 Jul 2020 at 14:31:36, subject to the Cambridge Core terms of use, available at https://www.cambridge.org/core/terms. https://doi.org/10.1017/jfm.2020.481

can spontaneously sustain without external periodic forcing (Strogatz 1994). For elastically mounted pitching wings, self-sustained oscillations can exist when the energy dissipated by the structural damping balances the energy input from the ambient fluid.

A relatively recent paper reporting on older wind tunnel experiments (Dugundji 2008) summarized the nonlinear instabilities of an elastically mounted flat plate pivoted about the midchord, and demonstrated the nonlinear divergence phenomenon, along with large-amplitude flow-induced oscillations. More recently, Onoue *et al.* (2015) utilized a cyber-physical control system (see § 1.3) to study a similar problem in much more detail. By fixing the free-stream velocity, the inertia and damping of the wing, and systematically varying the torsional stiffness, the authors successfully identified the onset and annihilation boundaries of small- and large-amplitude flow-induced oscillations and reported nonlinear hysteretic behaviours of the amplitude response. The effect of Reynolds number and structural damping was also briefly discussed. Onoue & Breuer (2016, 2017) conducted experiments using particle image velocimetry (PIV) to characterize the flow field of a pitching plate undergoing large-amplitude flow-induced oscillations. They successfully associated the unsteady aerodynamic torque with the dynamics of the separated flow structures. The LEV formation time and circulation were shown to depend on the characteristic feeding shear-layer velocity. Numerically, Menon & Mittal (2019) studied flow-induced pitching oscillations of an elastically supported two-dimensional NACA-0015 airfoil at a Reynolds number of 1000. The effects of several control parameters were investigated, including the spring stiffness, the equilibrium angle of attack (AOA), the structural damping and the location of the pivot axis. It was found that flow-induced oscillations occur when the structural time scale exceeds the flow time scale. Based on the fact that the flow-induced oscillations are nearly sinusoidal, the authors used prescribed sinusoidal motions to map out the energy transfer between the airfoil and the surrounding flow over a range of pitching amplitudes and frequencies. This 'energy map' was shown to be an effective tool for understanding the complex nonlinear behaviours associated with the flow-induced oscillations.

Although briefly mentioned by Dugundji (2008), the effect of wing inertia on the flow-induced instability has not been systematically explored in any of these studies. Menon & Mittal (2019) argued that changing the wing inertia (or, equivalently, the mass ratio between the wing and the surrounding fluid) is equivalent to changing the pitching frequency, which makes sense because it is well known that the natural frequency of an elastic system is determined by its stiffness and inertia (mass) (Rao 1995). However, in the context of vortex-induced vibrations (VIVs) of elastically mounted cylinders, it has been shown that different mass ratios lead to different oscillation modes (Govardhan & Williamson 2000, 2002; Williamson & Govardhan 2004; Navrose & Mittal 2017). In particular, Govardhan & Williamson (2000, 2002) showed that, when the mass ratio falls below a critical value, both the VIV amplitude and frequency jump to higher values. This suggests that the wing inertia might play an important and complex role in shaping the flow-induced instability of pitching wings, rather than only affecting the natural frequency.

1.3. *Cyber-physical systems*

Cyber-physical systems have been employed in several previous experimental studies for researching fluid–structure interactions (FSI), including VIVs (Hover, Miller & Triantafyllou 1997; Lee, Xiros & Bernitsas 2011; Mackowski & Williamson 2011) and passively pitching wings (Onoue *et al.* 2015; Fagley, Seidel & McLaughlin 2016; Su & Breuer 2019). These systems combine a cyber system and a physical system to

experimentally simulate the kinematics and dynamics of elastically mounted objects. The cyber system is a feedback control network that takes in the physically measured system kinematics – e.g. force (Hover *et al.* 1997; Mackowski & Williamson 2011; Su & Breuer 2019), velocity (Lee *et al.* 2011; Onoue *et al.* 2015) and displacement (Lee *et al.* 2011; Fagley *et al.* 2016) – and calculates in real time the corresponding system response based on the virtual structural properties defined by the user. The physical system usually consists of an actuator, which receives and executes the system response signal from the cyber system, and a sensor, which measures the system kinematics again at the next moment and sends it back to the cyber system. The cyber system and the physical system thereby form a closed control loop, which mimics a real-time structural response, if operated at sufficiently high bandwidth. Compared to a traditional physical mass–spring–damper system, cyber-physical systems enable easier systematic exploration of the parameter space. The variation range of virtual structural properties can be very large, and the incremental step can be very small, both of which are difficult to achieve using physical systems.

1.4. *Contributions of the present study*

The present work extends the study of a pitching plate by Onoue *et al.* (2015) and Onoue & Breuer (2016) to include the variation of the wing inertia, which has been shown to be critical in defining different VIV modes but has yet to be explored in the passively pitching wing literature. We take advantage of a cyber-physical system to experimentally simulate an elastically mounted pitching wing in free-stream flows, with the motivations of exploring the effect of wing inertia on the flow-induced instability, defining proper scaling parameters for the stability boundaries, and understanding the underlying flow physics associated with the instability. The present experiments are conducted in water, which slows down the time scale of the vortex dynamics associated with FSI, and thus benefits the flow visualization experiments. However, as we will discuss, since we can control the inertia of the wing, we can also simulate the behaviour of a wing in air, even though the experiments are conducted in water. In addition to providing new details and insights into the substantially studied aeroelastic problem, the present study can also be of potential value as a source of experimental data for correlation with theoretical and/or computational models (Dowell & Hall 2001; Dowell, Edwards & Strganac 2003; Zhu, Haase & Wu 2009; Zhu 2012; Young *et al.* 2013; Menon & Mittal 2019).

In the sections below, we describe our experimental set-up and introduce non-dimensional control parameters (§ 2), characterize the amplitude (§ 3.1), frequency (§ 3.2) and force response of the system and the corresponding flow dynamics (§ 3.3), discuss the transition to flow-induced instability (§ 3.4), interpret the system stability from the perspective of energy transfer (§ 3.5), and lastly summarize our key findings (§ 4).

2. Experimental set-up and non-dimensional parameters

Figure 1 shows the schematic of our experimental set-up. All the experiments are conducted in the Brown University free-surface water tunnel, which has a test section of width (W) $\times$ depth (D) $\times$ length (L) $= 0.8$ m $\times$ 0.6 m $\times$ 4.0 m. We mount a NACA-0012 wing vertically in the water tunnel, with an endplate on the top to eliminate wingtip vortices at the root. To emulate the behaviour of real-life wings, such as MAV airfoils and energy-harvesting hydrofoils, no endplate is added to the bottom tip of the wing. The wing is made of clear acrylic with a span of $s = 0.3$ m and a chord length of $c = 0.1$ m. The pivoting point (i.e. the elastic axis) of the wing is fixed at the midchord,

Downloaded from https://www.cambridge.org/core. Brown University Library, on 30 Jul 2020 at 14:31:36, subject to the Cambridge Core terms of use, available at https://www.cambridge.org/core/terms. https://doi.org/10.1017/jfm.2020.481

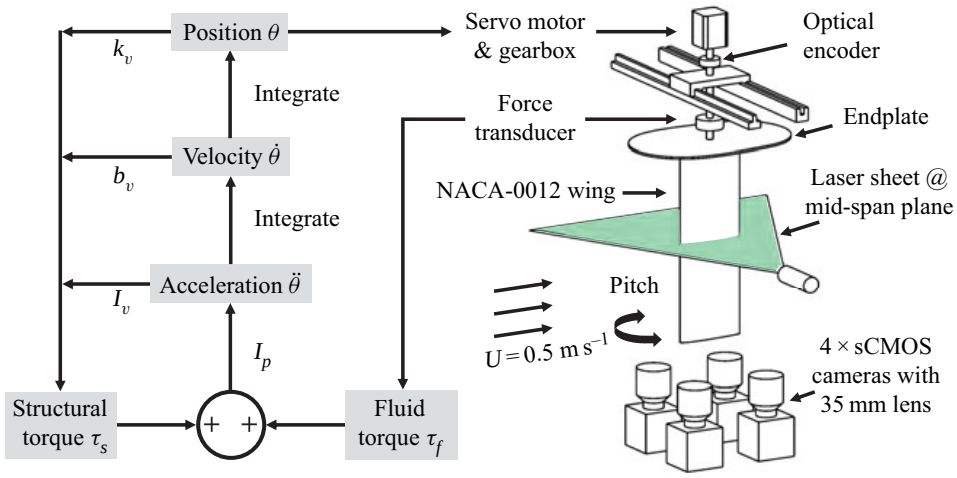


FIGURE 1. A schematic of the experimental set-up.

$c/2$, throughout all experiments. Detailed wing characteristics can be found in appendix A. To maintain a constant chord-based Reynolds number, $Re = \rho Uc/\mu = 50\,000$, where ρ and μ are water density and dynamic viscosity, respectively, we fix the free-stream velocity at $U = 0.5$ m s^{-1}. This velocity is measured by an acoustic Doppler velocimeter (ADV; Nortek Vectrino), positioned at the centre of the W–D plane, 2.5 m upstream of the wing.

2.1. *Cyber-physical system implementation*

We implement the real-time cyber-physical system (CPS) using MATLAB Simulink with an update rate of 4000 Hz. To introduce the CPS, we start with the governing equation of the system

$$I\ddot{\theta} + b\dot{\theta} + k\theta = \tau_f, \tag{2.1}$$

where I, b and k are the effective inertia, damping and stiffness of the wing, respectively, and τ_f is the fluid torque. The effective inertia, $I = I_p + I_v$, is a combination of the physical inertia of the wing, I_p, and a user assigned virtual inertia, I_v. Because no physical spring is present in the system and the frictional damping is negligible, we use virtual values to achieve the target stiffness, $k = k_v$, and the target damping, $b = b_v$. Adding up all the virtual torques, the total virtual structural torque can be calculated as

$$\tau_s = -(k_v\theta + b_v\dot{\theta} + I_v\ddot{\theta}). \tag{2.2}$$

Substituting (2.2) into (2.1), we can get

$$I_p\ddot{\theta} = \tau_f + \tau_s. \tag{2.3}$$

Now we introduce the real-time control loop depicted in figure 1. The fluid torque exerted on the wing, τ_f, measured by a six-axis force/torque transducer (ATI 9105-TIF-Delta-IP65), is fed into the loop. After adding the structural torque, τ_s (calculated from the previous time step), the total torque, $\tau_f + \tau_s$, is divided by the physical inertia of the wing, I_p, to get the pitching acceleration, $\ddot{\theta}$:

$$\ddot{\theta} = (\tau_f + \tau_s)/I_p. \tag{2.4}$$

Next, $\ddot{\theta}$ is integrated once to get the pitching velocity, $\dot{\theta}$, and again to get the pitching position, θ. The pitching position signal is used as input to a servomotor

Downloaded from https://www.cambridge.org/core. Brown University Library, on 30 Jul 2020 at 14:31:36, subject to the Cambridge Core terms of use, available at https://www.cambridge.org/core/terms. https://doi.org/10.1017/jfm.2020.481

(Parker SM233AE), coupled with a gearbox (Automation Direct PGCN23-0525), to pitch the wing. We use an optical encoder (US Digital E3-2500-250-IE-D-D-1), which is independent of the CPS, to record the actual pitching angle. At each time step, the structural torque, τ_s, is recalculated using (2.2) based on the new pitching dynamics (θ, $\dot{\theta}$ and $\ddot{\theta}$) and added to τ_f at the next time step to close the control loop. Data from the ADV, the force/torque transducer and the optical encoder are sampled using a data acquisition (DAQ) board (National Instruments PCIe-6353) at a frequency of 4000 Hz. The position signal is also output by the same DAQ board to the servomotor via a motor drive (Advanced Motion Controls DPRALTE-020B080).

Validation of the performance of this real-time cyber-physical system can be found in appendix A. Compared to the velocity loop used by Onoue *et al.* (2015), the position loop is less sensitive to noise and more robust because of the double integration. No filtering is required to get a clean and smooth position signal. For plotting purposes only, a zero-phase sixth-order low-pass Butterworth filter is applied to the raw force data so as to smooth out small oscillations. The filter cut-off frequency is set to 25 times the observed pitching frequency. It is important to emphasize that this filter is only employed for post-processing of the data; no filter is used inside the real-time control loop.

2.2. *Particle image velocimetry set-up*

The flow field around the pitching wing is measured using a time-resolved two-dimensional PIV system shown in figure 1. The laser sheet, created by a double-pulse Nd:YAG laser (200 mJ at 532 nm, Quantel Laser EverGreen 200) with LaVision sheet optics, illuminates the midspan plane of the wing. Because the wing is made of clear acrylic, the laser sheet can pass through the wing, enabling flow field measurement on both sides of the wing. It should be noted that the laser sheet plane is sufficiently far from the wingtip that the tip vortex is excluded from the measurement. The flow is seeded by 50 μm silver-coated hollow ceramic spheres. Image pairs of the flow field are acquired by four coplanar cameras (LaVision Imager sCMOS, 2560 $\times$ 2160 pixels) equipped with 35 mm lenses and mounted beneath the water tunnel. The laser and cameras are synchronized by a Programmable Timing Unit (PTU; LaVision). The PIV images are fed into the LaVision DaVis software (v.10) for image processing. Multi-pass cross-correlation (two passes at 64 $\times$ 64 pixels, two passes at 32 $\times$ 32 pixels, both with 50 % overlap) is used to calculate velocity vectors from each camera view, and the vector fields of the four cameras are stitched together to form a larger field of view ($\sim 4c \times 4c$).

2.3. *Non-dimensional parameters*

Following Onoue *et al.* (2015), we assume the fluid inertia force $0.5\rho U^2c^2s$ to be the dominating scaling force and normalize the stiffness, damping, inertia and fluid torque as

$$k^* = \frac{k}{0.5\rho U^2c^2s}, \quad b^* = \frac{b}{0.5\rho Uc^3s}, \quad I^* = \frac{I}{0.5\rho c^4s}, \quad \tau_f^* = \frac{\tau_f}{0.5\rho U^2c^2s}. \tag{2.5a–d}$$

Therefore, the non-dimensional governing equation of the system becomes

$$I^*\ddot{\theta}^* + b^*\dot{\theta}^* + k^*\theta^* = \tau_f^*, \tag{2.6}$$

where $\theta^* = \theta$, $\dot{\theta}^* = \dot{\theta}c/U$ and $\ddot{\theta}^* = \ddot{\theta}c^2/U^2$.

It is worth mentioning that the inverse of the non-dimensional stiffness is identical to the commonly used Cauchy number, $Ca = 1/k^*$, which describes the ratio between the fluid

Downloaded from https://www.cambridge.org/core. Brown University Library, on 30 Jul 2020 at 14:31:36, subject to the Cambridge Core terms of use, available at https://www.cambridge.org/core/terms. https://doi.org/10.1017/jfm.2020.481

inertia force and the elastic force (Ishihara *et al.* 2009; Jin *et al.* 2019; Wu *et al.* 2019). The non-dimensional inertia, I^*, is equivalent to the mass ratio between the wing and ambient fluid (Tzezana & Breuer 2019). The non-dimensional fluid torque, τ_f^*, is the unsteady moment coefficient of the wing. Another important non-dimensional parameter in the present study, which has appeared in many previous FSI studies (Khalak & Williamson 1996; Kim *et al.* 2013; Fagley *et al.* 2016; Menon & Mittal 2019), is the non-dimensional velocity U^*, defined as $U^* = U/(2\pi fc)$, where f is the oscillation frequency. It is important to note that U^* can have different definitions in the present study, depending on the frequency used to calculate U^*. There are several frequencies of interest in the dynamics of elastically mounted pitching wings, including: (*a*) the frequency of flow oscillations that may occur even in the absence of structural motions (e.g. the von Kármán vortex shedding frequency described in Menon & Mittal 2019); (*b*) the structural (or natural) frequency of the wing, f_s, calculated based on the spring stiffness and the wing inertia (i.e. $f_s = (\sqrt{k/I})/2\pi$); and (*c*) the pitching frequency, f_p, which arises from the dynamic coupling between the flow and the structure (in the aeroelastic literature, this frequency may be called the flutter or limit-cycle oscillation frequency). In the following sections, we will use U_s^* to denote U^* calculated using f_s (i.e. $U_s^* = U/(2\pi f_s c)$), and U_p^* to denote U^* calculated using f_p (i.e. $U_p^* = U/(2\pi f_p c)$).

3. Results and discussion

3.1. *Subcritical and supercritical bifurcations*

In the present study, we fix the structural damping of the wing at $b^* = 0.13$ and keep the initial AOA at *zero*. We want to note that different initial AOAs can introduce significant differences in bifurcation behaviours (Dugundji 2008; Razak, Andrianne & Dimitriadis 2011; Menon & Mittal 2019). In the present study, we only focus on the zero initial AOA case. At different wing inertias, we first incrementally increase the Cauchy number, Ca, by decreasing the wing stiffness, k^*, to define the onset of instability. Then we incrementally decrease Ca by increasing k^* to test for the annihilation of instability and the presence of any hysteresis. The amplitude response of the system, $|A|$, is defined using the absolute value of the peak pitching amplitude, and the divergence angle, $|\overline{A}|$, is defined as the absolute value of the mean pitching angle. We plot $|A|$ and $|\overline{A}|$ against the Cauchy number $Ca = 1/k^*$ instead of k^* because the former can better resemble typical bifurcation diagrams in dynamical systems (Strogatz 1994).

Figure 2 shows the amplitude response of the system at two different wing inertias. When the inertia is relatively high ($I^* = 10.6$, figure 2*a*), as we increase Ca, the wing first remains stable with a negligible divergence angle. Although the zero divergence angle is always an equilibrium state for an elastically mounted wing with zero initial AOA, this state may not be a stable fixed point in practice. To test for the true stability of the wing, we introduce a small external perturbation, or 'kick', into the system. This perturbation is computer-generated by superimposing a short virtual torque to the cyber-physical system. A series of perturbation tests with controlled amplitude variance were conducted to determine a proper perturbation amplitude, so that the system is not pushed into other stability regimes. If zero divergence is a stable fixed point solution, the wing will return to the zero divergence angle after the perturbation. However, if the zero-angle condition is an unstable fixed point, the wing will stay at a non-zero divergence angle at which the fluid torque is balanced by the restoring torque provided by the (virtual) spring. The direction of this angle depends on the direction of the initial perturbation, but both positive and

Downloaded from https://www.cambridge.org/core. Brown University Library, on 30 Jul 2020 at 14:31:36, subject to the Cambridge Core terms of use, available at https://www.cambridge.org/core/terms. https://doi.org/10.1017/jfm.2020.481

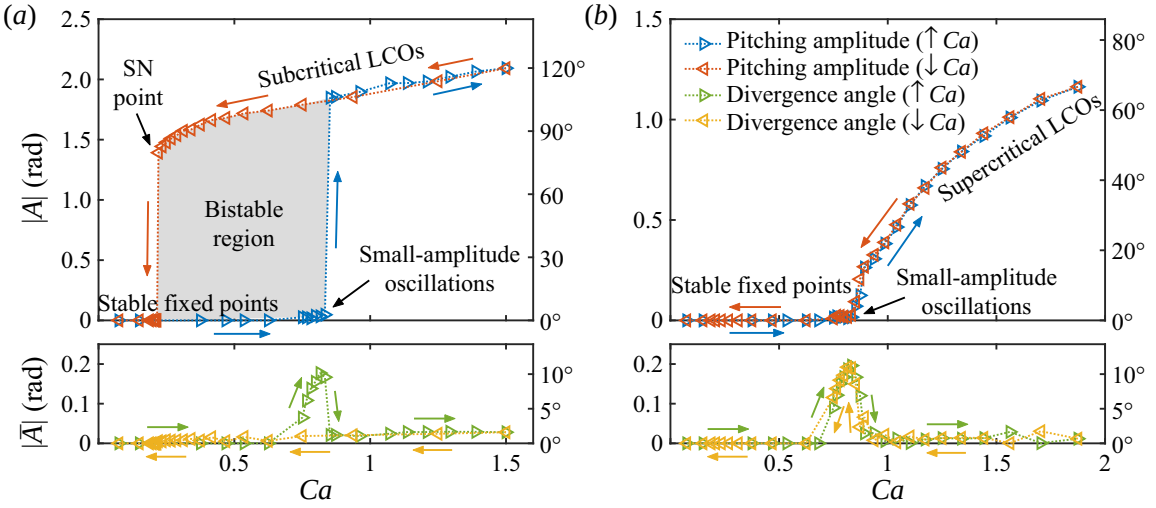


FIGURE 2. Amplitude response of the system at (*a*) $I^* = 10.60$ and (*b*) $I^* = 0.33$, presented in radians on the left y-axis, and in degrees on the right y-axis. Note that (*a*) and (*b*) share the same legend.

negative angles are possible. This static divergence phenomenon is well characterized in the literature (Dugundji 2008; Dimitriadis & Li 2009).

As we continue to increase Ca, the static divergence angle becomes larger and small-amplitude oscillations are observed. In this regime, the pitching amplitude θ, velocity θ^* and acceleration $\ddot{\theta}^*$ are all small, causing the damping torque $b^*\dot{\theta}^*$ and the inertial torque $I^*\ddot{\theta}^*$ to be negligible. As a result, these deflected small-amplitude oscillations are dominated by the balance between the fluid torque τ_f^* and the spring restoring torque $k^*\theta^*$ around the divergence angle. Although these small-amplitude oscillations are not the main focus of the present study, they should be distinguished from the laminar separation flutter reported in the literature (Poirel, Harris & Benaissa 2008; Poirel & Yuan 2010; Poirel, Metivier & Dumas 2011; Barnes & Visbal 2018), where the oscillations are both driven and limited by the aerodynamic force, and can thus sustain even without the presence a structural spring (Poirel *et al.* 2008, figure 8). Moreover, we believe that the small-amplitude oscillations observed in the present study are not strictly stall flutter (Dimitriadis & Li 2009; Bhat & Govardhan 2013), because no obvious hysteresis is observed in the force measurements, and the maximum pitching angle mostly stays below the static stall angle. Rather, we think these small-amplitude oscillations come from the interaction between the random flow disturbance and the structural dynamics (mainly the spring stiffness) of the wing.

As the Cauchy number, Ca, is further increased, we observe a critical value above which the pitching dynamics of the wing transitions from small-amplitude oscillations to large-amplitude LCOs. This transition is reflected by an abrupt jump of the pitching amplitude, $|A|$, and a drop of the divergence angle, $|\bar{A}|$ (figure 2*a*). The large-amplitude LCOs are nearly sinusoidal and feature a dominant characteristic frequency. The amplitude of these LCOs continues to increase with Ca, and the corresponding characteristic frequency decreases with Ca (see figure 4*a*). As we decrease the Cauchy number, Ca, the large-amplitude LCOs persist even when Ca is decreased below the critical value, defining a bistable, hysteretic region, before the pitching amplitude returns to the stable fixed point regime via a saddle-node (SN) point. In this bistable region, the system has two stable solutions (i.e. stable LCOs and stable fixed points) and one unstable solution

Downloaded from https://www.cambridge.org/core. Brown University Library, on 30 Jul 2020 at 14:31:36, subject to the Cambridge Core terms of use, available at https://www.cambridge.org/core/terms. https://doi.org/10.1017/jfm.2020.481

(i.e. unstable LCOs, not observable in experiments). The divergence angle $|\bar{A}|$ remains near zero for the entire decreasing path, creating a small hysteretic region near the critical *Ca*. Similar bifurcation behaviours have been reported in the wind tunnel experiments literature (Dugundji 2008; Dimitriadis & Li 2009; Amandolese *et al.* 2013; Onoue *et al.* 2015). If we ignore the static divergence angle and relax the constraint in the definition of a Hopf bifurcation that the system has to be a fixed point prior to the bifurcation (Strogatz 1994), the bifurcation observed in the present experiment possesses every feature of a subcritical Hopf bifurcation, with the critical *Ca* corresponding to the Hopf point. The large-amplitude LCOs observed in this operating condition are hence referred to as subcritical LCOs.

The amplitude response for a wing with a much lower inertia ($I^* = 0.33$) is shown in figure 2(*b*). Again, for small *Ca* values, we perturb the system to test for its true stability. Similar to the high-inertia case, as we increase *Ca*, the system experiences static divergence and small-amplitude oscillations around the divergence angle. As *Ca* is further increased, the small-amplitude oscillations become larger and the divergence angle gradually decreases to zero. At even higher values of *Ca*, the LCO amplitude continues to increase and the divergence angle remains around zero. As we decrease *Ca*, both the pitching amplitude $|A|$ and the divergence angle $|\bar{A}|$ follow exactly the same path back to the original fixed point regime. No hysteresis or amplitude jump is observed during the experiment. As before, if we ignore the static divergence angle and the initial small-amplitude oscillations, the transition appears to be a supercritical Hopf-type bifurcation. We therefore refer to the large-amplitude LCOs observed in this operating condition as supercritical LCOs. Compared to the subcritical bifurcation, which is often referred to as a hard bifurcation because of the dangerous abrupt amplitude jump and hysteresis, a supercritical bifurcation is usually denoted as a soft bifurcation, which is considered to be safer for many applications (Strogatz 1994).

We then test the stability boundaries of the system over a range of wing inertia values. In figure 3(*a*), the pitching amplitude, $|A|$, is plotted against the Cauchy number, *Ca*. We see that the width of the bistable region shrinks as the inertia decreases, evidenced by the change in the location of the SN point. When the inertia is sufficiently low, the bistable region completely disappears and the subcritical bifurcation becomes supercritical. However, regardless of the bifurcation type (supercritical or subcritical), the onset of instability (i.e. the Hopf point) seems to occur at the same Cauchy number for all wing inertia values. The underlying mechanism of this phenomenon will be discussed in § 3.4.

In figure 3(*b*), we re-plot the pitching amplitude, this time against the f_s-based non-dimensional velocity U_s^*. The connection between *Ca*, k^* and U_s^* is

$$U_s^* = \frac{U}{2\pi f_s c} = \sqrt{\frac{I^*}{k^*}} = \sqrt{Ca\, I^*}. \tag{3.1}$$

We first observe that, under this scaling, for subcritical bifurcations, the location of the Hopf point rises as the wing inertia increases. After the onset of large-amplitude LCOs, we observe that the pitching amplitude for the three subcritical LCO branches ($I^* = 10.60$, 5.30 and 2.65) almost completely overlap, and that these LCOs extinguish at roughly the same critical U_s^* (i.e. the same SN point), indicating that U_s^* is a good scaling parameter for this feature of the instability. The critical U_s^* is actually determined by a critical structural frequency f_s, because the free-stream velocity U and the chord length of the wing c remain constant in the present experiment (see (3.1)). Below this critical U_s^* (above the corresponding critical f_s), subcritical LCOs cannot sustain. The underlying mechanism

Downloaded from https://www.cambridge.org/core. Brown University Library, on 30 Jul 2020 at 14:31:36, subject to the Cambridge Core terms of use, available at https://www.cambridge.org/core/terms. https://doi.org/10.1017/jfm.2020.481

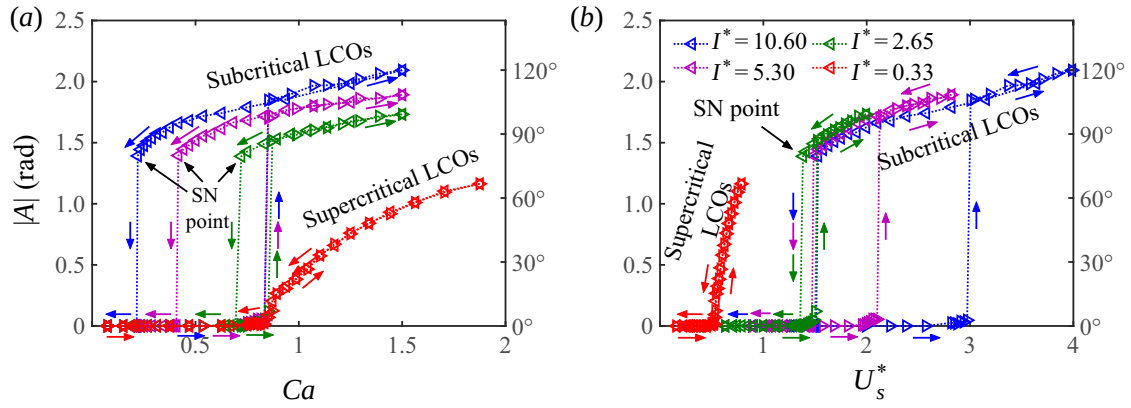


FIGURE 3. Pitching amplitude at different wing inertias, plotted against (*a*) the Cauchy number, *Ca*, and (*b*) the f_s-based non-dimensional velocity, U_s^*. Symbols: ▷, increasing *Ca*; ◁, decreasing *Ca*. Note that (*a*) and (*b*) share the same legend.

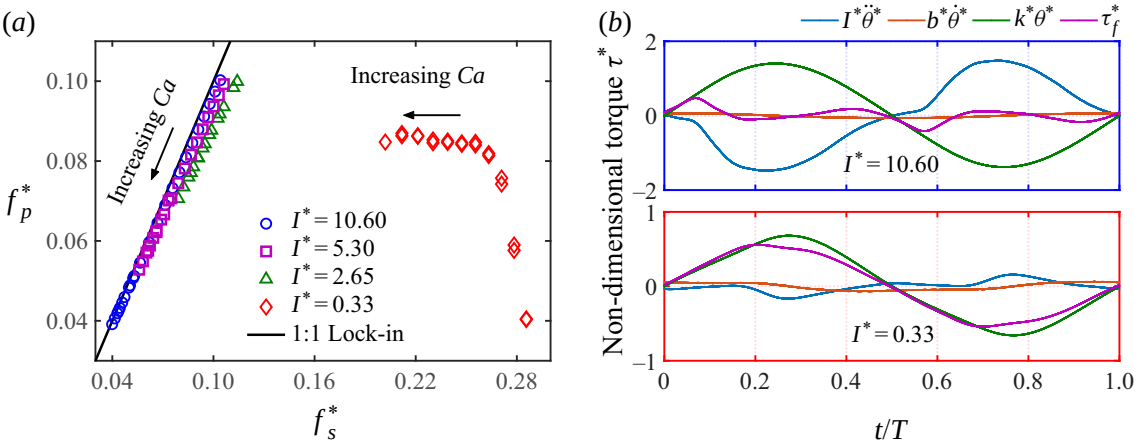


FIGURE 4. (*a*) The frequency response of the wing at four different inertia values. (*b*) Non-dimensional torques experienced by the wing at $Ca = 1.5$ over one normalized pitching cycle: $I^*\ddot{\theta}^*$, inertial torque; $b^*\dot{\theta}^*$, damping torque; $k^*\theta^*$, spring restoring torque; and τ_f^*, fluid torque. Upper panel is for $I^* = 10.60$ and lower for $I^* = 0.33$. Note the *y*-scale difference in (*b*).

for this phenomenon will be discussed in § 3.5. Moreover, the collapse of the subcritical LCO branches indicates that all these LCOs share a universal oscillation mode even though the wing inertia is different. This observation supports Menon & Mittal's (2019) argument that changing the wing inertia only affects the natural frequency of the system. However, we should note that U_s^* is only able to collapse subcritical LCOs. The behaviour of supercritical LCOs ($I^* = 0.33$) seems to be qualitatively different (i.e. the oscillations are always below the critical U_s^*), suggesting a different mode of oscillation. This is more fully characterized in the next section.

3.2. *Structural mode and hydrodynamic mode*

In figure 4(*a*), we plot the measured pitching frequency of the wing, f_p, against the calculated structural frequency, f_s, both normalized by the fluid time scale (i.e. $f^* = fc/U$). Because it is difficult to extract f_p^* for small-amplitude oscillations (see figure 2), the data shown only correspond to relatively large-amplitude LCOs (i.e. super- and subcritical

Downloaded from https://www.cambridge.org/core. Brown University Library, on 30 Jul 2020 at 14:31:36, subject to the Cambridge Core terms of use, available at https://www.cambridge.org/core/terms. https://doi.org/10.1017/jfm.2020.481

LCOs, see figure 3). To illustrate how each term in (2.6) affects the pitching dynamics over one cycle, we decompose the non-dimensional torque experienced by the wing into the inertial torque, $I^*\ddot{\theta}^*$, the damping torque, $b^*\dot{\theta}^*$, the spring restoring torque, $k^*\theta^*$, and the fluid torque, τ_f^*. The decomposition result is shown in figure 4(*b*), with the top panel corresponding to the high-inertia case ($I^* = 10.6$) and the bottom panel corresponding to the low-inertia case ($I^* = 0.33$), both at $Ca = 1.5$.

We observe that for the high-inertia case ($I^* = 10.60$), as Ca is varied, the pitching frequency, f_p^*, locks onto the structural frequency, f_s^* (figure 4*a*, blue circles). The maximum f_p^* corresponds to the SN point in the bifurcation diagram (see figure 2*a*), whereas the minimum f_p^* corresponds to the highest Ca. This lock-in phenomenon indicates that the structural force is the dominating force governing the pitching motion, which is supported by the torque decomposition in figure 4(*b*, top). In this panel, we see that the spring restoring torque, $k^*\theta^*$, is of similar amplitude, and opposite sign to the inertial torque, $I^*\ddot{\theta}^*$, while the fluid torque, τ_f^*, and the damping torque, $b^*\dot{\theta}^*$, are relatively small. A similar lock-in phenomenon was observed by Onoue *et al.* (2015) and Menon & Mittal (2019). In figure 4(*a*), we also plot the frequency response for the two moderate-inertia cases ($I^* = 5.30$ and 2.65, purple squares and green triangles). The lock-in phenomenon persists in these two cases but f_p^* is slightly lower than f_s^*, especially for the lower-inertia wing. We attribute this to the increase of effective inertia brought by the added-mass effect, which is more prominent for lower inertia values. The fact that the lock-in phenomenon is observed for all the subcritical LCOs further confirms that these LCOs feature the same oscillation mode, which we denote as the *structural* mode.

In contrast, for the low-inertia case ($I^* = 0.33$), the frequency response (figure 4(*a*), red diamonds) lies to the right of the 1 : 1 lock-in line, indicating that the pitching frequency, f_p^*, is always lower than the structural frequency, f_s^*. No lock-in phenomenon is observed. As we increase Ca, the pitching frequency stays at a relatively constant value (i.e. constant Strouhal number $St = f_p^* \approx 0.085$), indicating an intrinsic fluid time scale. This suggests that the fluid torque, τ_f^*, is driving the pitching motion, which is verified by figure 4(*b*, bottom). It is seen that the spring restoring torque, $k^*\theta^*$, mainly balances the fluid torque, τ_f^*. These two torques are in phase because they are of opposite sign in the governing equation (see (2.6)). The fluid torque, τ_f^*, has a similar magnitude, but a higher frequency, as compared to that of the high-inertia case. However, because of the low I^*, the inertial torque $I^*\ddot{\theta}^*$ stays comparatively small over the entire pitching cycle, causing the frequency of τ_f^* to override the structural frequency. The damping torque, $b^*\dot{\theta}^*$, is almost negligible in this case. Therefore, we denote the supercritical LCOs as the *hydrodynamic* mode.

3.3. *Force response and the corresponding flow field*

We plot the torque–angle phase diagram, τ_f^*–θ, for both the high-inertia case ($I^* = 10.60$) and the low-inertia case ($I^* = 0.33$) in the centre of figure 5. The static torque–angle measurement is plotted for comparison. The corresponding phase-averaged flow fields at different time instants are also plotted surrounding that diagram. Because of symmetry, we only show the vorticity fields for half of the pitching cycle. Figure 5(*a–g*) correspond to the positive half pitching cycle of the high-inertia case ($I^* = 10.60$). Figure 5(*i–v*) correspond to the negative half pitching cycle of the low-inertia case ($I^* = 0.33$).

For the high-inertia case, the force response and the corresponding vorticity field are very similar to that observed by Onoue & Breuer (2016). As the wing departs from the zero pitching angle, the fluid torque τ_f^* starts to grow. The phase diagram shows that τ_f^* is non-zero at $\theta = 0$. This positive intercept is presumably due to the pressure difference

Downloaded from https://www.cambridge.org/core. Brown University Library, on 30 Jul 2020 at 14:31:36, subject to the Cambridge Core terms of use, available at https://www.cambridge.org/core/terms. https://doi.org/10.1017/jfm.2020.481

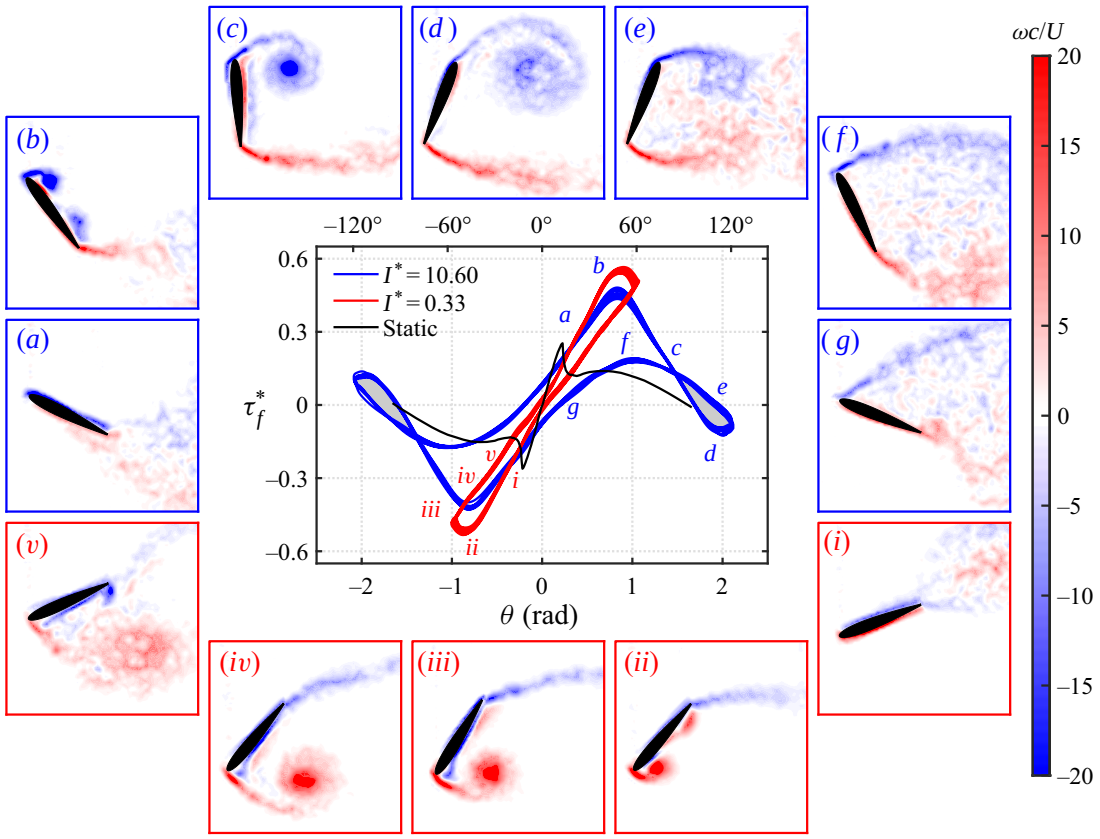


FIGURE 5. Torque–angle phase diagram (centre) for $I^* = 10.60$ (structural mode) and $I^* = 0.33$ (hydrodynamic mode) at $Ca = 1.5$ (the same operating conditions as in figure 4*b*), and the corresponding vorticity fields (flow direction is left to right): (*a–g*) $I^* = 10.60$, corresponding to the blue curve; (*i–v*) $I^* = 0.33$, corresponding to the red curve. See supplementary movies available at https://doi.org/10.1017/jfm.2020.481.

between the two sides of the wing, caused by the separated flow on the lower wing surface inherited from the previous cycle (Onoue & Breuer 2016). The PIV measurements (figure 5*a*,*b*) depict the emergence of a strong LEV, which is attached to the upper surface of the wing, in the fore section. Meanwhile, we observe a patch of vorticity on the aft part of the upper surface, which could be a shear-layer vortex caused by the rolling-up of surface vorticity (Sharma & Visbal 2019). The τ_f^* value starts to decrease after a peak around $\theta \approx 0.82$ (47°) is experienced, corresponding to the shedding of the LEV from the wing surface (figure 5*c*). Compared to the static measurement, this decrease in τ_f^* significantly exceeds the static stall angle, θ_s. The maximum value of τ_f^* is also amplified approximately by a factor of 2. This transient increase of τ_f^* (due to the transient increase of C_L) and the delay in stall evince the dynamic stall phenomenon (McCroskey 1982; Eldredge & Jones 2019). Although τ_f^* is decreasing and the spring restoring torque is increasing, the wing continues to pitch up due to its high inertia, until the maximum pitching amplitude is achieved around $\theta \approx 2.09$ (120°).

In Onoue & Breuer (2016, figure 3), the maximum θ is around 90°. This discrepancy is presumably due to differences in the wing characteristics (i.e. flat plate versus NACA-0012 wing). The τ_f^* value goes below zero at roughly the same θ as in the static measurement. At the maximum θ, the LEV reaches its maximum size while remaining relatively coherent (figure 5*d*), before it breaks into smaller-scale structures and fully detaches from the wing

Downloaded from https://www.cambridge.org/core. Brown University Library, on 30 Jul 2020 at 14:31:36, subject to the Cambridge Core terms of use, available at https://www.cambridge.org/core/terms. https://doi.org/10.1017/jfm.2020.481

surface, evidenced by the disconnection between the leading edge and the LEV feeding shear layer. After arriving at the peak θ, the pitching motion starts to reverse. Then τ_f^* increases again and experiences another peak, due to the formation, growth and shedding of a secondary LEV caused by the rolling-up of the feeding shear layer (figure 5*e*,*f*) (Jantzen *et al.* 2014; Onoue & Breuer 2016). The relatively diffusive appearance of the secondary LEV (figure 5*e*) could be an artifact due to the fact that these vorticity fields are phase-averaged, while the real LEV may exhibit some phase jitter. In the final stage, the restoring torque pulls the wing back to the zero pitching angle, while the flow on the upper wing surface is still separated (figure 5*g*). This results in the negative intercept of τ_f^* at the beginning of the second half of the pitching cycle.

For the low-inertia case, the initial behaviour of the force response and the flow field (figure 5*i*,*ii*) is very similar to that of the high-inertia case (figure 5*a*,*b*). For both cases, τ_f^* peaks at a similar angular position $\theta \approx 0.82$ (47°), agreeing well with experiments and models by Strickland & Graham (1987) and Granlund *et al.* (2013), in which the wing undergoes rapid pitching at constant angular velocities. The origin of this peak in τ_f^* for both cases is the formation and shedding of the primary LEV. The peak τ_f^* is higher for the low-inertia case, presumably due to a stronger LEV defined by a higher reduced frequency and thereby a larger feeding shear-layer velocity (Onoue & Breuer 2016, 2017).

The primary discrepancy between the high-inertia case and the low-inertia case appears right after the maximum τ_f^* is achieved. The low-inertia wing does not have enough momentum (due to the low inertia) to keep pitching up when the LEV starts to detach from the wing surface (figure 5*iii*). Therefore, θ reaches its maximum almost immediately after the peak τ_f^* has arrived. As the LEV further sheds from the wing surface, it moves towards the aft part of the wing (figure 5*iv*) and becomes less coherent (figure 5*v*). The τ_f^* value decreases monotonically and the spring restoring torque gradually brings the wing back to the zero pitching angle. At $\theta = 0$, the y-intercept of τ_f^* for the low-inertia case is smaller than that of the high-inertia case, because the flow on the suction side of the wing reattaches faster. In the low-inertia case, no secondary peak in τ_f^* is observed and the secondary LEV is absent during the pitch reversal. As a result, no negative hysteresis region (figure 5 grey shaded areas) is formed, suggesting that no energy is being transferred from the system to the wake over the pitching cycle (Onoue & Breuer 2016). However, this does not necessarily indicate that low wing inertia is more favourable for energy harvesting, as the harvesting efficiency depends on the net area of the hysteretic region.

3.4. *Transition to subcritical limit-cycle oscillations*

One key feature of the subcritical bifurcation observed for the high-inertia wing is the abrupt jump of the pitching amplitude at the critical *Ca* (see figure 2*a*). In the time domain, when *Ca* is increased above the critical value, the amplitude jump is in fact a gradual transition process, in which the pitching amplitude grows and saturates over a period of around one minute (∼12 cycles). Figure 6(*a*) shows the time trace of the pitching motion during this transition. Figure 6(*b*) shows the temporal evolution of the corresponding fluid torque, τ_f^*. Figure 6(*c*) shows the transitional τ_f^*–θ phase diagram. The static measurement is also plotted in black for comparison. In figure 6(*b*,*c*), the time dependence of τ_f^* is indicated by the colour shade. The red colour represents the starting stage of the transition, whereas the cyan colour indicates the amplitude saturation stage.

Before the transition occurs, the wing undergoes small-amplitude quasi-steady oscillations around its equilibrium divergence angle (see § 3.1). At this stage, the flow on the wing surface is mostly attached (PIV measurements not shown here). As *Ca* is

Downloaded from https://www.cambridge.org/core. Brown University Library, on 30 Jul 2020 at 14:31:36, subject to the Cambridge Core terms of use, available at https://www.cambridge.org/core/terms. https://doi.org/10.1017/jfm.2020.481

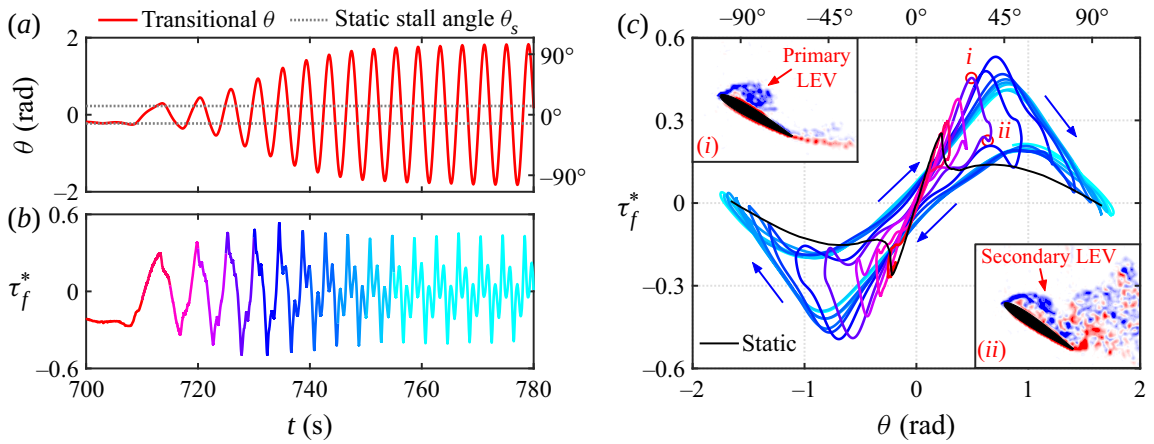


FIGURE 6. Transition to subcritical LCOs in the high-inertia case ($I^* = 10.60$) at $Ca = 0.85$. (a) Time trace of the amplitude transition (red solid line). Grey dotted lines indicate the static stall angle θ_s. (b) Temporal evolution of the fluid torque τ_f^* during the transition. (c) Transitional torque–angle phase diagram. Insets: Two representative vorticity field showing (i) a primary LEV and (ii) a secondary LEV. The angular positions of these two vorticity fields are indicated by red circles. Insets (i) and (ii) share the same colour bar with figure 5.

increased above the critical value, the spring is not stiff enough to hold the wing below the static stall angle, θ_s (i.e. the grey dotted lines in figure 6a). Once θ_s is exceeded, the flow starts to separate and the wing experiences a sudden drop in τ_f^*. The spring restoring torque loses its counterpart so that the wing is accelerated to pitch towards the opposite direction. At this very initial stage of the transition, the pitch reversal starts as soon as the separation occurs. However, at the later stage of the transition and when the oscillation saturates, the wing will continue to pitch after the flow separates (i.e. pitching 'overshoot'), on account of the high inertia. As the wing starts to gain velocity, the flow becomes unsteady and the static stall transitions to dynamic stall. As a result, the stall is delayed and the maximum τ_f^* increases because of the formation of LEVs (figure 6c, inset i). This positive feedback loop results in a further increase in the pitching amplitude. Figure 6(c) clearly depicts this transition, showing how the wing departs from the quasi-steady state to the unsteady state. The growth in pitching amplitude is finally limited by the spring restoring torque (see also figure 4b, top), which leads to the amplitude saturation. How this quasi-steady to unsteady transition shapes the stability characteristics of the system will be discussed in § 3.5.

In § 3.3, we have shown that the secondary peak in τ_f^* during the pitch reversal is associated with the presence of a secondary LEV (figure 5e). Figure 6(c) illustrates how this secondary τ_f^* peak emerges and strengthens during the transition, providing evidence for the emergence and development of the corresponding secondary LEV, which is confirmed by vorticity measurements. Figure 6(c, inset ii) shows that a secondary LEV is indeed formed during the pitch reversal, even during the very first few cycles of the transition. Moreover, figure 6(c) also shows that secondary LEVs can exist for a relatively low pitching amplitude ($|A| < 1$), which suggests that the absence of the secondary LEV in the low-inertia case (figure 5) is not due to the low pitching amplitude ($|A| \approx 1$), but could well be a result of the high pitching frequency, as compared to the high-inertia case. For a high pitching frequency, the feeding shear layer does not have sufficient time to roll up so that the secondary LEV is not able to form in the low-inertia case.

In summary, figure 6 manifests that the onset of the subcritical LCOs depends on the static characteristics (i.e. the static stall angle) of the wing. It also provides a connection

Downloaded from https://www.cambridge.org/core. Brown University Library, on 30 Jul 2020 at 14:31:36, subject to the Cambridge Core terms of use, available at https://www.cambridge.org/core/terms. https://doi.org/10.1017/jfm.2020.481

between the quasi-steady state and the unsteady state for the pitching dynamics and the fluid torque, which could benefit the modelling of the system. It is important to note that, although the main focus of this section is to reveal the underlying dynamics and flow physics of a subcritical transition, the mechanism that triggers this transition (i.e. the pitching amplitude exceeding the static stall angle) also applies to a supercritical transition. However, while the subcritical transition has a prolonged amplitude evolution (figure 6*a*), the supercritical transition is almost instantaneous, due to the low wing inertia. This explains why the onset of LCOs scales well with Ca (figure 3*a*) in spite of the different bifurcation types. The reason why the system can settle into different LCO solutions will be discussed next in § 3.5.

3.5. *System stability from the perspective of energy transfer*

Now we characterize the stability of our system from the perspective of energy transfer between the fluid and the supporting structure. Morse & Williamson (2009) were among the first to introduce the energy approach for predicting VIVs of an elastically mounted translating cylinder. In the context of passively pitching wings, this approach has been shown to be effective for predicting the stability of small-amplitude ($|A| < 6^\circ$, Bhat & Govardhan 2013) and moderate-amplitude ($|A| < 50^\circ$, Menon & Mittal 2019) flow-induced oscillations. Here we extend this approach to the large-amplitude ($50^\circ < |A| < 120^\circ$) regime.

As noted before (Onoue *et al.* 2015; Menon & Mittal 2019), the flow-induced pitching motion is well described by a sinusoidal motion. This is also true in the current measurements ($R^2 > 0.98$). Thus, if we assume that the pitching motion can be described by

$$\theta = |A| \sin(2\pi f_p t), \tag{3.2}$$

where $|A|$ is the pitching amplitude and f_p is the pitching frequency, we can prescribe the amplitude and frequency of the motion, measure the fluid torque, τ_f, and integrate the equation of motion (2.6) over n cycles to obtain the cycle-averaged energy transfer between the fluid and the structure:

$$E = \frac{1}{n} \int_{t_0}^{t_0+nT} (\tau_f \dot{\theta} - b\dot{\theta}^2)\, \mathrm{d}t. \tag{3.3}$$

For the results presented here, we have used $n = 20$ and swept f_p from 0.15 to 0.6 Hz with a step size of 0.05 and $|A|$ from 0 to 2.5 rad with a step size of 0.175. The $\tau_f\dot{\theta}$ term represents the power extracted by the wing from the ambient fluid, and the $b\dot{\theta}^2$ term represents the power dissipated by the structural damping (Menon & Mittal 2019). Following Onoue *et al.* (2015), we multiply E by the pitching frequency, f_p, and normalize the equation to get the power coefficient of the system:

$$C_p = \frac{f_p^*}{n} \int_{t_0}^{t_0+nT} (\tau_f^* \dot{\theta}^* - b^* \dot{\theta}^{*2})\, \mathrm{d}t^*. \tag{3.4}$$

The power coefficient map is shown in figure 7, with the x-axis represented by f_p^* in figure 7(*a*) and by $U_p^* = 1/(2\pi f_p^*)$ in figure 7(*b*). In both plots, red, white and blue represent regions of power extraction ($C_p > 0$), balance ($C_p = 0$) and dissipation ($C_p < 0$), respectively. The power balance ($C_p = 0$) curve is indicated by black dashed lines. The value $|A| = 0$ is also a possible solution for power balance. We wish to note that, although

Downloaded from https://www.cambridge.org/core. Brown University Library, on 30 Jul 2020 at 14:31:36, subject to the Cambridge Core terms of use, available at https://www.cambridge.org/core/terms. https://doi.org/10.1017/jfm.2020.481

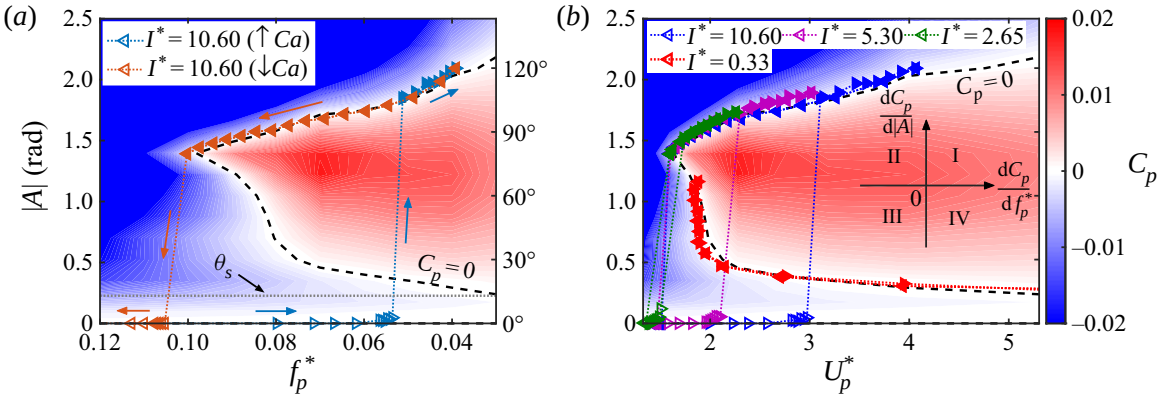


FIGURE 7. (*a*) Contour plot of the power coefficient, C_p, overlaid by the amplitude response of the system at $I^* = 10.6$. The zero power coefficient contour is indicated by black dashed lines. The static stall angle θ_s is labelled by a grey dotted line. Note the reverse scale of the x-axis. (*b*) Power coefficient map plotted against the non-dimensional velocity, overlaid by the amplitude response of the system at different inertia values. Inset: A diagram illustrating the four quadrants of the power coefficient gradient: x-axis, $\mathrm{d}C_p/\mathrm{d}f_p^*$; y-axis, $\mathrm{d}C_p/\mathrm{d}|A|$.

figure 7 reflects the power coefficient map of one particular damping value ($b^* = 0.13$), the power coefficient map of other damping values can be easily generated by simply varying b^* in (3.4). This demonstrates the universality of the energy approach for analysing systems with different structural damping values (Morse & Williamson 2009; Menon & Mittal 2019). To connect the power coefficient map with the previously discussed system stability boundaries, we re-plot the amplitude response data, from figures 2(*a*) and 3(*b*), onto figures 7(*a*) and 7(*b*), respectively. To make the connection between figures 7(*a*) and 2(*a*) more intuitive, we plot the x-axis of figure 7(*a*) *using a reverse scale*, so that the shape of the bifurcation diagram remains relatively consistent in these two plots. In both figures 7(*a*) and 7(*b*), the frequency for large-amplitude LCOs (i.e. solid markers) is the measured pitching frequency f_p^*. For the data points with zero- or small-amplitude oscillations (i.e. hollow markers), the frequency is the structural frequency f_s^* (see § 3.2).

Comparing figure 7(*a*) with the energy map of Menon & Mittal (2019, figure 13), we see that, although the frequency range of these two maps is quite different (i.e. $0.03 \leq f_p^* \leq 0.12$ versus $0.10 < f_p^* < 0.75$), the general shape looks similar for the overlapped amplitude range (i.e. $0 \leq |A| \leq 50^\circ$). Both maps show that the wing extracts more energy from the ambient fluid when the pitching frequency is low, and dissipates more energy when the pitching frequency is high (note the reverse x-axis in figure 7*a*). However, the detailed shapes of the power balance curve ($C_p = 0$) are very different in these two maps. The $C_p = 0$ curve seems to extend to $(f_p^*, |A|) = (0, 0)$ in figure 7(*a*), but stays relatively vertical and has a non-zero x-intercept in figure 13 of Menon & Mittal (2019). Moreover, $|A| = 0$ is part of the $C_p = 0$ curve in figure 7(*a*), but not in figure 13 of Menon & Mittal (2019). We believe that these differences mainly come from the different initial AOAs used in these two studies (i.e. 0° versus 15°). It has been shown by Dugundji (2008), Razak *et al.* (2011) and Menon & Mittal (2019, figure 3) that different initial AOAs can lead to significantly different stability characteristics, which suggests that the power coefficient map (or the energy map) of a zero-initial-AOA wing and a 15°-initial-AOA wing can be quite different.

Comparing the power coefficient map and the amplitude response reveals many interesting features. Figure 7(*a*) shows that, for $I^* = 10.60$, large-amplitude LCOs

Downloaded from https://www.cambridge.org/core. Brown University Library, on 30 Jul 2020 at 14:31:36, subject to the Cambridge Core terms of use, available at https://www.cambridge.org/core/terms. https://doi.org/10.1017/jfm.2020.481

fall exactly on the upper branch of the $C_p = 0$ curve. This is expected because the self-sustained flow-induced oscillations represent a condition of energy balance (Morse & Williamson 2009; Menon & Mittal 2019). We have shown in § 3.2 that the subcritical LCOs for $I^* = 10.60$ represent a structural mode, where the pitching frequency locks onto the structural frequency. This means that, for any data point representing subcritical LCOs, its x-coordinate (i.e. f_p^*) is constrained by k^* and I^*, so that it is only free to move in the y-direction (i.e. change $|A|$) under external perturbations. If $|A|$ increases (or decreases), the system will enter the blue region where $C_p < 0$ (or the red region where $C_p > 0$) and go back to the equilibrium solution ($C_p = 0$) because of power dissipation (or power extraction). Based on this analysis, we can deduce the stability criterion for the structural mode (Menon & Mittal 2019):

$$C_p = 0 \quad \text{and} \quad \frac{\mathrm{d}C_p}{\mathrm{d}|A|} < 0. \tag{3.5}$$

The upper branch of the $C_p = 0$ curve satisfies this criterion, so that it is a stable equilibrium solution for subcritical LCOs. The x-axis (i.e. $|A| = 0$) also represents a stable equilibrium for the same reason. In contrast, the lower branch of the $C_p = 0$ curve represents an unstable equilibrium solution, because its power gradient along the y-direction is positive (i.e. $\mathrm{d}C_p/\mathrm{d}|A| > 0$). The existence of multiple (stable LCO, unstable LCO and stable fixed point) solutions is an important feature of a subcritical Hopf bifurcation, which has been discussed in § 3.1. Revealing the unstable equilibrium solution, which is not possible in passive experiments, is one of the benefits for adopting the energy approach.

Figure 7(*b*) provides insights into the system stability for other wing inertia values. Because the measured pitching frequency, f_p (instead of f_s), is used to calculate U_p^* for the large-amplitude LCOs, we see that the amplitude response of the subcritical LCOs ($I^* = 10.60$, 5.30 and 2.65) collapse remarkably well, as compared to figure 3(*b*). All these subcritical LCOs, regardless of their inertia values, fall onto the upper $C_p = 0$ branch, for the reason discussed above. Moreover, the power coefficient map explains why there exists a critical U_p^*, below which the subcritical LCOs cannot sustain. This is because, below this critical U_p^* (or above the corresponding critical f_p^*), the power coefficient of the system is negative ($C_p < 0$). More power is damped by the structural damping than extracted from the fluid, so that the power of the system is insufficient to sustain large-amplitude LCOs. The underlying flow physics causing the decrease of C_p requires further investigations.

For $I^* = 0.33$, we see that supercritical LCOs fall onto the lower branch of the $C_p = 0$ curve. As discussed earlier, this lower branch is an unstable equilibrium solution for the structural mode. However, its stability has a different nature for the hydrodynamic mode. In the structural mode, the pitching frequency is constrained by the structural frequency, so that the stability of an equilibrium solution is determined by $\mathrm{d}C_p/\mathrm{d}|A|$ (see (3.5)). In contrast, for the hydrodynamic mode, because the oscillation is dictated by the fluid force (see figure 4*b*, bottom), the system is not constrained to move vertically in the energy map, but is free to move in *both* the $|A|$-direction and the f_p^*-direction. On the lower branch of the $C_p = 0$ curve, if the system is perturbed to enter the blue region where $C_p < 0$ (or the red region where $C_p > 0$), f_p^* can in turn decrease (or increase) to accommodate power dissipations (or power extractions), and the system will thus return to the equilibrium solution ($C_p = 0$) again. Therefore, the lower branch of the $C_p = 0$ curve ($\mathrm{d}C_p/\mathrm{d}f_p^* < 0$) is a stable equilibrium solution for supercritical LCOs.

It is important to note that, because the system is free to move vertically as well, $\mathrm{d}C_p/\mathrm{d}|A| < 0$ can also contribute to the stability of supercritical LCOs. Therefore, the

Downloaded from https://www.cambridge.org/core. Brown University Library, on 30 Jul 2020 at 14:31:36, subject to the Cambridge Core terms of use, available at https://www.cambridge.org/core/terms. https://doi.org/10.1017/jfm.2020.481

stability criterion for the hydrodynamic mode is

$$C_p = 0 \quad \text{and} \quad \left(\frac{\mathrm{d}C_p}{\mathrm{d}|A|} < 0 \quad \text{or} \quad \frac{\mathrm{d}C_p}{\mathrm{d}f_p^*} < 0 \right). \tag{3.6}$$

Following this criterion, the upper branch of the $C_p = 0$ curve and $|A| = 0$ are also stable equilibrium solutions for the hydrodynamic mode. However, this does not mean that the low-inertia system can have multiple equilibrium solutions at a given Ca, because Ca does not have a one-to-one correspondence with f_p^* in the hydrodynamic mode. The specific combination of $|A|$ and f_p^* depends on how much power is extracted from the fluid. The selection of different stable equilibrium solutions further confirms the intrinsic difference between the hydrodynamic mode and the structural mode.

Now we can summarize and visualize the stability criterion for the structural mode and the hydrodynamic mode. As shown by (3.5) and (3.6), the common prerequisite for stability for these two oscillation modes is $C_p = 0$. To examine the stability of the $C_p = 0$ curve, we visualize the sign of $\mathrm{d}C_p/\mathrm{d}f_p^*$ and $\mathrm{d}C_p/\mathrm{d}|A|$ using a quadrant diagram, as shown by the inset of figure 7(*b*). For the structural mode, the system is stable in quadrants III and IV (including the negative y-axis), and unstable in quadrants I and II (including the x-axis and the positive y-axis). For the hydrodynamic mode, the system is stable in quadrants II, III and IV (including the negative x- and y-axis), and unstable only in quadrant I (including the positive x- and y-axis). As discussed earlier, for the present system, the $C_p = 0$ curve has three branches. The upper branch is in quadrant III, so it is a stable solution for both oscillations modes. The lower branch is in quadrant II, so it is a stable solution for the hydrodynamic mode and an unstable solution for the structural mode. The $|A| = 0$ branch lies on the negative y-axis, so it is a stable solution for both oscillation modes again.

One critical question in the present study is why the bifurcation is subcritical for the structural mode and supercritical for the hydrodynamic mode. The power coefficient map provides us with some insights. As shown in figure 7(*b*), for all wing inertias, near the transitional U_p^* values, the stability of the system, indicated by the power coefficient map, is a stable equilibrium at $|A| = 0$. In theory, without any external perturbations, the system should stay at this stable fixed point solution for any U_p^*. However, we should note that the power coefficient map only identifies the stability of (near-) sinusoidal symmetric oscillations. The stability of the static divergence and quasi-steady small-amplitude oscillations is not accessible from this map. In our experiments, as Ca is increased, the wing first bifurcates into a static divergence angle, which brings asymmetry to the problem. Then the system develops small-amplitude oscillations around this divergence angle (§ 3.1). As shown in figure 6(*a*), after the pitching amplitude exceeds the static stall angle, θ_s, unsteady oscillations start near $(f_p^*, |A|) = (0, \theta_s)$, which presumably falls into the power extraction regime (i.e. the red region, see figure 7*a*). In this regime, the system has two possible evolution paths depending on the oscillation mode.

(i) For the structural mode, because of the constraint in the pitching frequency discussed above, f_p^* has to gradually develop into f_s^*. In this process, the system keeps gaining energy from the ambient fluid ($C_p > 0$) and finally settles to the upper $C_p = 0$ branch (3.5), which results in the abrupt jump in pitching amplitude, defining a subcritical-type bifurcation. The width of the bistable region is determined by the difference between the onset f^*, which varies with I^* because the onset k^* is fixed (§ 3.4), and the critical (saddle-node) f^*, which is unchanged for any combination of I^* and k^*. This explains the shrinking of the bistable region for different wing inertias (figure 3).

Downloaded from https://www.cambridge.org/core. Brown University Library, on 30 Jul 2020 at 14:31:36, subject to the Cambridge Core terms of use, available at https://www.cambridge.org/core/terms. https://doi.org/10.1017/jfm.2020.481

(ii) For the hydrodynamic mode, however, without the constraint in f_p^*, the system can pick up the lowest possible $|A|$ on the lower $C_p = 0$ curve as a stable solution after the transition from quasi-steady oscillations (3.6). This results in a smooth connection between the deflected small-amplitude oscillations and the symmetric large-amplitude LCOs, which creates a supercritical-type bifurcation.

For both paths, the quasi-steady to unsteady transition described in § 3.4 acts as a triggering mechanism for the onset of large-amplitude LCOs. Unveiling this triggering mechanism is of help towards creating a proper low-order model for the system.

4. Conclusion

We have performed water tunnel experiments to examine the stability boundaries of a rigid but flexibly mounted NACA-0012 wing at a Reynolds number of 50 000. We fixed the structural damping of the wing at a small value and systematically varied the torsional stiffness to explore the stability boundaries for different wing inertias. A subcritical bifurcation which features an abrupt amplitude jump and hysteretic bistability was observed for high-inertia wings, whereas a supercritical bifurcation in which the amplitude response varies smoothly with the control parameter without hysteresis was observed for a low-inertia wing. For both types of bifurcations, we showed that the onset of large-amplitude flow-induced oscillations scales with the Cauchy number, Ca. For high-inertia wings, the amplitude and the saddle-node point of subcritical LCOs were reported to scale with the non-dimensional velocity, U^*. Frequency response and force decomposition suggested that subcritical LCOs were dominated by the inertial force, corresponding to a structural mode, while supercritical LCOs were regulated by the fluid force, corresponding to a hydrodynamic mode. The force response was associated with the flow dynamics to explain the difference between the structural mode and the hydrodynamic mode. Two unique phenomena related to the structural mode, namely the frequency lock-in and the presence of a secondary LEV, were reported. We examined the transition to subcritical LCOs in detail, and it was shown that this transition depends on the static characteristics of the wing, and the emergence of the secondary LEV was an important feature of the transition. Finally, we adopted an energy approach to characterize the stability of the system. The stable equilibrium solution for the hydrodynamic mode was shown to be unstable for the structural mode because of the frequency lock-in phenomenon, which further resulted in the distinctive super- and subcritical bifurcations for these two modes.

Acknowledgments

This work is funded by the Air Force Office of Scientific Research, Grant FA9550-18-1-0322, managed by Dr G. Abate. The authors thank D. Harris and members of the Breuer Lab at Brown University, as well as J. Seidel, C. Fagley and A. Jirasek at the US Air Force Academy, for many helpful discussions and insights.

Declaration of interests

The authors report no conflict of interest.

Supplementary movies

Supplementary movies are available at https://doi.org/10.1017/jfm.2020.481.

Downloaded from https://www.cambridge.org/core. Brown University Library, on 30 Jul 2020 at 14:31:36, subject to the Cambridge Core terms of use, available at https://www.cambridge.org/core/terms. https://doi.org/10.1017/jfm.2020.481

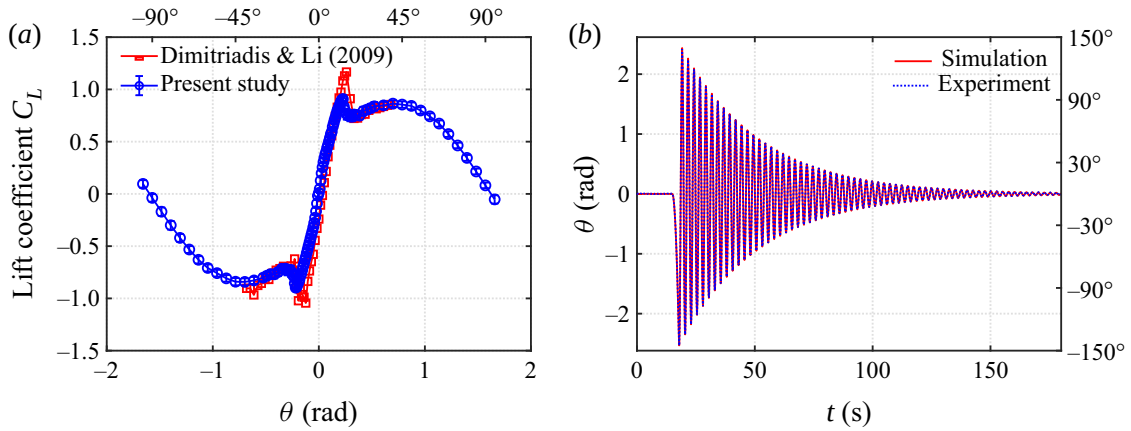


FIGURE 8. (*a*) Characterization of the wing. (*b*) Validation of the cyber-physical system.

Appendix A. System characterization

We characterize our NACA-0012 wing by measuring the static lift force L at different pitching angles. The lift coefficient, C_L, defined as $C_L = L/(0.5\rho U^2 cs)$, is plotted against the pitching angle θ in figure 8(*a*). The measured lift coefficients matches well with previous wind tunnel experiments by Dimitriadis & Li (2009).

We validate our cyber-physical system by conducting free oscillation ('ring-down') experiments. The ring-down experiments are conducted in air to exclude the nonlinear fluid damping effect. We apply a short-time constant-torque impulse to the wing using the cyber-physical system, after which we record and analyse the decay of the free damped oscillations. Figure 8(*b*) shows that the measured pitching decay agrees very well with the simulated decay, which is derived based on the virtual inertia, stiffness and damping, indicating that our cyber-physical system can accurately simulate physical structural dynamics of the system.

Appendix B. Effect of the Reynolds number

One issue of interest is whether the scaling used in explaining the flow-induced instability boundaries are appropriate(§ 3.1), and to what extent the phenomena are affected by the Reynolds number. These effects are tested by repeating the bifurcation tests for the high-inertia case ($I^* = 10.6$) at four different flow speeds $U = 0.3$–0.6 m s^{-1}. The resulting Reynolds number varies from $Re = 30\,000$ to $60\,000$. The virtual structural parameters (I_v, b_v and k_v) are varied to match the non-dimensional parameters (I^*, b^* and k^*). The results are shown in figure 9. Figure 9(*a*) shows that, as the Reynolds number is varied, the amplitude response remains almost the same, despite some subtle changes in the pitching amplitude and the critical Ca. Taking $Ca = 1.5$ and plotting the corresponding non-dimensional torque–angle phase diagram in figure 9(*b*), we observe that the phase diagrams of the four different Reynolds numbers collapse very well. These results indicate that the Reynolds number has a very minor effect on the present experimental results, which agrees with Onoue *et al.* (2015). The robustness of our non-dimensionalization is also justified by the unchanging amplitude response and phase diagram. However, we should note that the effect of Reynolds number also depends on the choice of the structural damping b^*. In the present experiments, the structural damping is fixed at a very small value $b^* = 0.13$. At a higher b^*, the Reynolds number can have a prominent effect on the flow-induced oscillations (see figure 12 in Onoue *et al.* 2015).

Downloaded from https://www.cambridge.org/core. Brown University Library, on 30 Jul 2020 at 14:31:36, subject to the Cambridge Core terms of use, available at https://www.cambridge.org/core/terms. https://doi.org/10.1017/jfm.2020.481

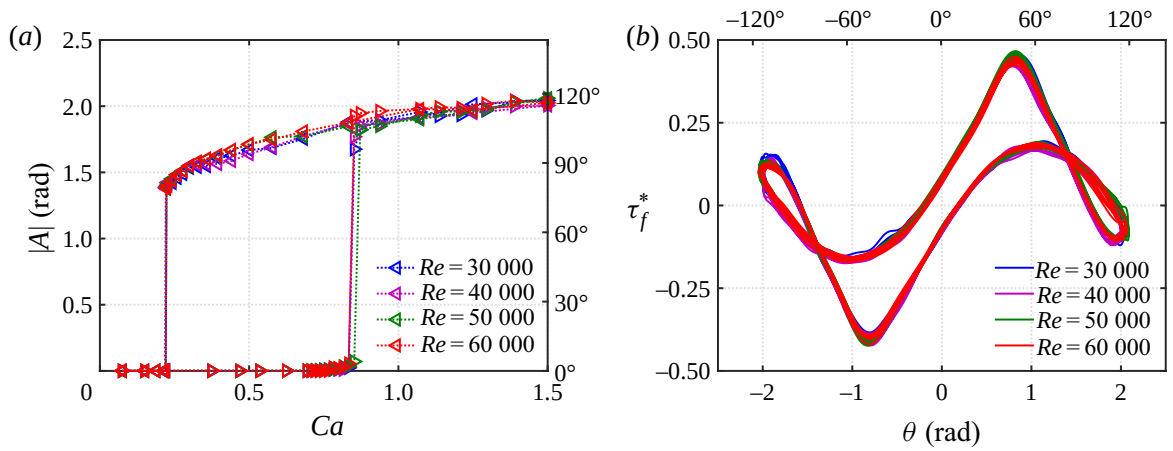


FIGURE 9. (*a*) Amplitude response of the high-inertia case ($I^* = 10.60$) at four different Reynolds numbers and (*b*) the corresponding torque–angle phase diagram at $Ca = 1.5$.

REFERENCES

AMANDOLESE, X., MICHELIN, S. & CHOQUEL, M. 2013 Low speed flutter and limit cycle oscillations of a two-degree-of-freedom flat plate in a wind tunnel. *J. Fluids Struct.* **43**, 244–255.

BAIK, Y. S., BERNAL, L. P., GRANLUND, K. & OL, M. V. 2012 Unsteady force generation and vortex dynamics of pitching and plunging aerofoils. *J. Fluid Mech.* **709**, 37–68.

BARNES, C. J. & VISBAL, M. R. 2018 On the role of flow transition in laminar separation flutter. *J. Fluids Struct.* **77**, 213–230.

BEATUS, T. & COHEN, I. 2015 Wing-pitch modulation in maneuvering fruit flies is explained by an interplay between aerodynamics and a torsional spring. *Phys. Rev.* E **92** (2), 022712.

BERGOU, A. J., RISTROPH, L., GUCKENHEIMER, J., COHEN, I. & WANG, Z. J. 2010 Fruit flies modulate passive wing pitching to generate in-flight turns. *Phys. Rev. Lett.* **104** (14), 148101.

BERGOU, A. J., XU, S. & WANG, Z. J. 2007 Passive wing pitch reversal in insect flight. *J. Fluid Mech.* **591**, 321–337.

BHAT, S. S. & GOVARDHAN, R. N. 2013 Stall flutter of NACA 0012 airfoil at low Reynolds numbers. *J. Fluids Struct.* **41**, 166–174.

BOUDREAU, M., DUMAS, G., RAHIMPOUR, M. & OSHKAI, P. 2018 Experimental investigation of the energy extraction by a fully-passive flapping-foil hydrokinetic turbine prototype. *J. Fluids Struct.* **82**, 446–472.

DIMITRIADIS, G. & LI, J. 2009 Bifurcation behavior of airfoil undergoing stall flutter oscillations in low-speed wind tunnel. *AIAA J.* **47** (11), 2577–2596.

DOWELL, E., EDWARDS, J. & STRGANAC, T. 2003 Nonlinear aeroelasticity. *J. Aircraft* **40** (5), 857–874.

DOWELL, E. H., CURTISS, H. C., SCANLAN, R. H. & SISTO, F. 1989 *A Modern Course in Aeroelasticity*. Springer.

DOWELL, E. H. & HALL, K. C. 2001 Modeling of fluid-structure interaction. *Annu. Rev. Fluid Mech.* **33** (1), 445–490.

DUARTE, L., DELLINGER, N., DELLINGER, G., GHENAIM, A. & TERFOUS, A. 2019 Experimental investigation of the dynamic behaviour of a fully passive flapping foil hydrokinetic turbine. *J. Fluids Struct.* **88**, 1–12.

DUGUNDJI, J. 2008 Some aeroelastic and nonlinear vibration problems encountered on the journey to Ithaca. *AIAA J.* **46** (1), 21–35.

ELDREDGE, J. D. & JONES, A. R. 2019 Leading-edge vortices: mechanics and modeling. *Annu. Rev. Fluid Mech.* **51**, 75–104.

FAGLEY, C., SEIDEL, J. & MCLAUGHLIN, T. 2016 Cyber-physical flexible wing for aeroelastic investigations of stall and classical flutter. *J. Fluids Struct.* **67**, 34–47.

GARRICK, I. E. 1936 Propulsion of a flapping and oscillating airfoil. *NACA Tech. Rep.* 567.

Downloaded from https://www.cambridge.org/core. Brown University Library, on 30 Jul 2020 at 14:31:36, subject to the Cambridge Core terms of use, available at https://www.cambridge.org/core/terms. https://doi.org/10.1017/jfm.2020.481

GOVARDHAN, R. & WILLIAMSON, C. H. K. 2000 Modes of vortex formation and frequency response of a freely vibrating cylinder. *J. Fluid Mech.* **420**, 85–130.

GOVARDHAN, R. & WILLIAMSON, C. H. K. 2002 Resonance forever: existence of a critical mass and an infinite regime of resonance in vortex-induced vibration. *J. Fluid Mech.* **473**, 147–166.

GRANLUND, K. O., OL, M. V. & BERNAL, L. P. 2013 Unsteady pitching flat plates. *J. Fluid Mech.* **733**, R5.

HO, S., NASSEF, H., PORNSINSIRIRAK, N., TAI, Y.-C. & HO, C.-M. 2003 Unsteady aerodynamics and flow control for flapping wing flyers. *Prog. Aerosp. Sci.* **39** (8), 635–681.

HOVER, F. S., MILLER, S. N. & TRIANTAFYLLOU, M. S. 1997 Vortex-induced vibration of marine cables: experiments using force feedback. *J. Fluids Struct.* **11** (3), 307–326.

ISHIHARA, D., YAMASHITA, Y., HORIE, T., YOSHIDA, S. & NIHO, T. 2009 Passive maintenance of high angle of attack and its lift generation during flapping translation in crane fly wing. *J. Expl Biol.* **212** (23), 3882–3891.

JAFFERIS, N. T., HELBLING, E. F., KARPELSON, M. & WOOD, R. J. 2019 Untethered flight of an insect-sized flapping-wing microscale aerial vehicle. *Nature* **570** (7762), 491–495.

JANTZEN, R. T., TAIRA, K., GRANLUND, K. O. & OL, M. V. 2014 Vortex dynamics around pitching plates. *Phys. Fluids* **26** (5), 053606.

JIN, Y., KIM, J.-T., FU, S. & CHAMORRO, L. P. 2019 Flow-induced motions of flexible plates: fluttering, twisting and orbital modes. *J. Fluid Mech.* **864**, 273–285.

KHALAK, A. & WILLIAMSON, C. H. K. 1996 Dynamics of a hydroelastic cylinder with very low mass and damping. *J. Fluids Struct.* **10** (5), 455–472.

KIM, D., COSSÉ, J., CERDEIRA, C. H. & GHARIB, M. 2013 Flapping dynamics of an inverted flag. *J. Fluid Mech.* **736**, R1.

LEE, J. H., XIROS, N. & BERNITSAS, M. M. 2011 Virtual damper-spring system for VIV experiments and hydrokinetic energy conversion. *Ocean Engng* **38** (5–6), 732–747.

MACKOWSKI, A. W. & WILLIAMSON, C. H. K. 2011 Developing a cyber-physical fluid dynamics facility for fluid-structure interaction studies. *J. Fluids Struct.* **27** (5–6), 748–757.

MCCROSKEY, W. J. 1982 Unsteady airfoils. *Annu. Rev. Fluid Mech.* **14** (1), 285–311.

MENON, K. & MITTAL, R. 2019 Flow physics and dynamics of flow-induced pitch oscillations of an airfoil. *J. Fluid Mech.* **877**, 582–613.

MORSE, T. L. & WILLIAMSON, C. H. K. 2009 Prediction of vortex-induced vibration response by employing controlled motion. *J. Fluid Mech.* **634**, 5–39.

NAVROSE & MITTAL, S. 2017 The critical mass phenomenon in vortex-induced vibration at low *Re*. *J. Fluid Mech.* **820**, 159–186.

ONOUE, K. & BREUER, K. S. 2016 Vortex formation and shedding from a cyber-physical pitching plate. *J. Fluid Mech.* **793**, 229–247.

ONOUE, K. & BREUER, K. S. 2017 A scaling for vortex formation on swept and unswept pitching wings. *J. Fluid Mech.* **832**, 697–720.

ONOUE, K., SONG, A., STROM, B. & BREUER, K. S. 2015 Large amplitude flow-induced oscillations and energy harvesting using a cyber-physical pitching plate. *J. Fluids Struct.* **55**, 262–275.

PENG, Z. & ZHU, Q. 2009 Energy harvesting through flow-induced oscillations of a foil. *Phys. Fluids* **21** (12), 123602.

POIREL, D., HARRIS, Y. & BENAISSA, A. 2008 Self-sustained aeroelastic oscillations of a NACA0012 airfoil at low-to-moderate Reynolds numbers. *J. Fluids Struct.* **24** (5), 700–719.

POIREL, D., METIVIER, V. & DUMAS, G. 2011 Computational aeroelastic simulations of self-sustained pitch oscillations of a NACA0012 at transitional Reynolds numbers. *J. Fluids Struct.* **27** (8), 1262–1277.

POIREL, D. & YUAN, W. 2010 Aerodynamics of laminar separation flutter at a transitional Reynolds number. *J. Fluids Struct.* **26** (7–8), 1174–1194.

RAO, S. S. 1995 *Mechanical Vibrations*. Addison-Wesley.

RAZAK, N. A., ANDRIANNE, T. & DIMITRIADIS, G. 2011 Flutter and stall flutter of a rectangular wing in a wind tunnel. *AIAA J.* **49** (10), 2258–2271.

SHARMA, A. & VISBAL, M. 2019 Numerical investigation of the effect of airfoil thickness on onset of dynamic stall. *J. Fluid Mech.* **870**, 870–900.

Downloaded from https://www.cambridge.org/core. Brown University Library, on 30 Jul 2020 at 14:31:36, subject to the Cambridge Core terms of use, available at https://www.cambridge.org/core/terms. https://doi.org/10.1017/jfm.2020.481

SHYY, W., AONO, H., CHIMAKURTHI, S. K., TRIZILA, P., KANG, C.-K., CESNIK, C. E. S. & LIU, H. 2010 Recent progress in flapping wing aerodynamics and aeroelasticity. *Prog. Aerosp. Sci.* **46** (7), 284–327.

STRICKLAND, J. H. & GRAHAM, G. M. 1987 Force coefficients for a NACA-0015 airfoil undergoing constant pitch rate motions. *AIAA J.* **25** (4), 622–624.

STROGATZ, S. H. 1994 *Nonlinear Dynamics and Chaos: With Applications to Physics, Biology, Chemistry, and Engineering*. Perseus Books.

SU, Y & BREUER, K. S. 2019 Resonant response and optimal energy harvesting of an elastically mounted pitching and heaving hydrofoil. *Phys. Rev. Fluids* **4** (6), 064701.

THEODORSEN, T. 1935 General theory of aerodynamic instability and the mechanism of flutter. *NACA Tech. Rep.* 496.

TZEZANA, G. A. & BREUER, K. S. 2019 Thrust, drag and wake structure in flapping compliant membrane wings. *J. Fluid Mech.* **862**, 871–888.

VEILLEUX, J.-C. & DUMAS, G. 2017 Numerical optimization of a fully-passive flapping-airfoil turbine. *J. Fluids Struct.* **70**, 102–130.

WANG, Z., DU, L., ZHAO, J. & SUN, X. 2017 Structural response and energy extraction of a fully passive flapping foil. *J. Fluids Struct.* **72**, 96–113.

WANG, Z. J. 2005 Dissecting insect flight. *Annu. Rev. Fluid Mech.* **37**, 183–210.

WILLIAMSON, C. H. K. & GOVARDHAN, R. 2004 Vortex-induced vibrations. *Annu. Rev. Fluid Mech.* **36**, 413–455.

WU, K. S., NOWAK, J. & BREUER, K. S. 2019 Scaling of the performance of insect-inspired passive-pitching flapping wings. *J. R. Soc. Interface* **16** (161), 20190609.

XIAO, Q. & ZHU, Q. 2014 A review on flow energy harvesters based on flapping foils. *J. Fluids Struct.* **46**, 174–191.

YOUNG, J., ASHRAF, M. A., LAI, J. C. S. & PLATZER, M. F. 2013 Numerical simulation of fully passive flapping foil power generation. *AIAA J.* **51** (11), 2727–2739.

YOUNG, J., LAI, J. C. S. & PLATZER, M. F. 2014 A review of progress and challenges in flapping foil power generation. *Prog. Aerosp. Sci.* **67**, 2–28.

ZHU, Q. 2011 Optimal frequency for flow energy harvesting of a flapping foil. *J. Fluid Mech.* **675**, 495–517.

ZHU, Q. 2012 Energy harvesting by a purely passive flapping foil from shear flows. *J. Fluids Struct.* **34**, 157–169.

ZHU, Q., HAASE, M. & WU, C. H. 2009 Modeling the capacity of a novel flow-energy harvester. *Appl. Math. Model.* **33** (5), 2207–2217.

ZHU, Q. & PENG, Z. 2009 Mode coupling and flow energy harvesting by a flapping foil. *Phys. Fluids* **21** (3), 033601.

Downloaded from https://www.cambridge.org/core. Brown University Library, on 30 Jul 2020 at 14:31:36, subject to the Cambridge Core terms of use, available at https://www.cambridge.org/core/terms. https://doi.org/10.1017/jfm.2020.481

Aeroelastic Instability Boundaries of Pitching Swept Wings

Yuanhang Zhu * and Kenneth Breuer †
Center for Fluid Mechanics, School of Engineering, Brown University, Providence, RI 02912

We experimentally study the aeroelastic instability boundaries of pitching unswept and swept wings in a water tunnel at a Reynolds number of 50,000. The structural dynamics of the wings are simulated using a cyber-physical control system. We show that the Hopf point of flow-induced limit-cycle oscillations (LCOs) depends largely on the static characteristics of the wing. The saddle-node point of LCOs is found to change non-monotonically with the sweep angle, which we attribute to the non-monotonic power transfer between the ambient fluid and the elastic mount. An optimal sweep angle is observed to promote LCOs and thus enhance the power extraction performance. The frequency response of the system reveals a structural-hydrodynamic oscillation mode for wings with relatively high sweep angles. Lastly, three-dimensional flow structures measured by multi-layer stereoscopic particle image velocimetry are analyzed to explain the differences in power extraction for unswept and swept wings.

I. Nomenclature

W, D, L	=	width, depth, length of the water tunnel [m]
U_∞	=	free-stream velocity [m/s]
s, c	=	wing span, wing chord [m]
Λ	=	sweep angle [°]
$\theta, \dot{\theta}, \ddot{\theta}$	=	angular position [rad], velocity [rad/s], acceleration [rad/s^2]
τ_f	=	fluid torque [N·m]
I_p, I_v, I	=	physical inertia, virtual inertia, effective inertia [kg·m^2]
b_v, b	=	virtual structural damping, effective structural damping [kg·m^2/s]
k_v, k	=	virtual stiffness, effective stiffness [kg·m^2/s^2]
ρ, μ	=	water density [kg/m^3], water dynamic viscosity [kg/(m·s)]
ω_z	=	spanwise vorticity [1/s]
$\lvert A\rvert$	=	pitching amplitude [rad]
$\lvert\overline{A}\rvert$	=	static divergence angle [rad]
f_s, f_p	=	structural frequency, pitching frequency [Hz]
f_s^*, f_p^*	=	non-dimensional structural frequency, pitching frequency
Re, Ca	=	Reynolds number, Cauchy number
I^*, b^*, k^*, U^*	=	non-dimensional inertia, damping, stiffness, velocity
τ^*, τ_f^*	=	non-dimensional torque, fluid torque

II. Introduction

The fluid-structure interaction (FSI) of elastically mounted pitching wings finds application in many related fields. Under certain structural parameters, large-amplitude flow-induced oscillations may lead to catastrophic aeroelastic failure [1]. On the other hand, these oscillations can be beneficial if they are exploited for harvesting kinetic energy from tidal or river flows [2–4]. Moreover, understanding the instability boundaries of passively pitching wings is critical for studying animal flight [5–8] and developing flapping-wing micro air vehicles (MAVs) [9, 10]. The flow-induced oscillations of passively pitching wings originate from the two-way coupling between the structural dynamics of the elastic mount and the nonlinear fluid force experienced by the wing. The nonlinear fluid force is modulated by the formation, growth and shedding of a strong leading-edge vortex (LEV) [11, 12]. Therefore, the dynamics and stability

*Graduate Student, Center for Fluid Mechanics, School of Engineering, Brown University, Providence, RI 02912, AIAA Student Member.
†Professor of Engineering, Center for Fluid Mechanics, School of Engineering, Brown University, Providence, RI 02912, AIAA Associate Fellow.

of LEVs play an important role in shaping the flow-induced oscillations and thus determining the stability boundaries of passively pitching wings.

Swept wings are commonly seen for flapping-wing fliers and swimmers in nature [13–15]. It is believed that the wing sweep can stabilize leading-edge vortices through induced spanwise flows [13] and thus enhance lift generation. Wong and Rival [16] have shown both theoretically and experimentally that the wing sweep improves relative LEV stability by enhancing the spanwise vorticity transport. Moreover, it was shown that vortex stretching and the increase of reduced frequency also promote LEV stability. Onoue and Breuer [17] experimentally studied cyber-physically pitching unswept and swept wings and proposed a universal scaling for LEV formation time and circulation, which incorporated the effects of the pitching frequency, the pivot location and the sweep angle. The vortex circulation was demonstrated to be independent of the three-dimensional vortex dynamics. In addition, they concluded that the stability of LEVs can be improved by moderating the LEV circulation through vorticity annihilation, which is largely governed by the shape of the leading-edge sweep. Visbal and Garmann [18] numerically studied the effect of wing sweep on the dynamic stall of pitching three-dimensional wings and reported that the wing sweep can modify the the LEV structures and change the net aerodynamic damping of the wing.

These studies have characterized the relationship between the wing sweep and the LEV stability/structure, however, the effect of sweep angle on the stability characteristics of elastically mounted wings still remains elusive. In the present study, we aim to address this problem by extending the methodology developed in Zhu et al. [19] to swept wings and employing stereoscopic particle image velocimetry to quantify the three-dimensional flow fields. We use a cyber-physical system to simulate the elastic mount of the wings (§III). The static moment coefficients of the wings are measured (§IV.A) before we characterize the amplitude response (§IV.B) and the frequency response (§IV.C) of the system. We correlate the onset of flow-induced oscillations with the static characteristics of the wing (§IV.D) and use an energy approach to explain the nonlinear stability boundaries (§IV.E). Finally, we analyze the three-dimensional flow structures (§IV.F) to explain the difference in power extraction for unswept and swept wings. All the key findings are summarized in §V.

III. Experimental setup and non-dimensional parameters

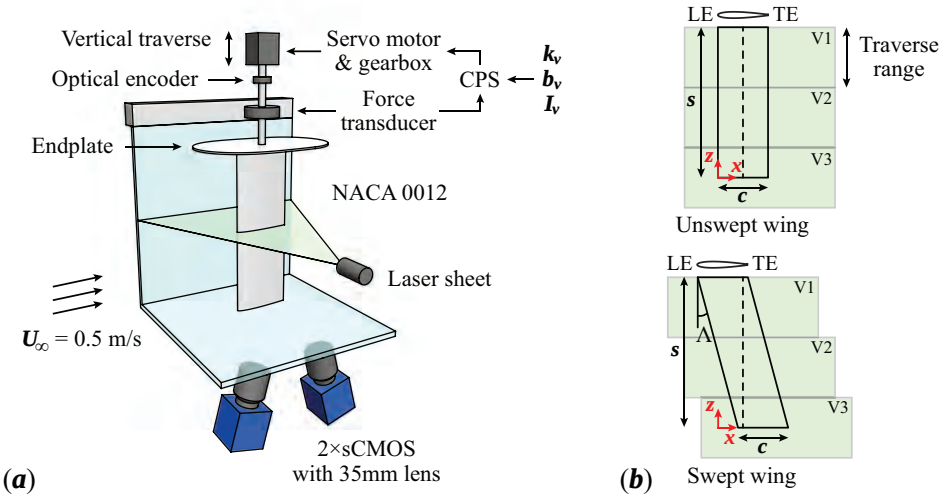


Fig. 1 (*a*) A schematic of the experimental setup. (*b*) Sketches of unswept and swept wings used in the experiments. The pivot axes are indicated by dashed lines. The green blocks represent volumes traversed by the laser sheet for 3D phase-averaged stereoscopic PIV measurements.

A. Cyber-physical system and wing geometry

We perform all the experiments in the Brown University free-surface water tunnel, which has a test section of $W \times D \times L = 0.8\text{ m} \times 0.6\text{ m} \times 4.0\text{ m}$. The free-stream velocity is fixed at $U_\infty = 0.5$ m/s throughout all the experiments.

Fig. 1(a) shows a schematic of the experimental setup. Unswept and swept NACA 0012 wings are mounted vertically in the tunnel, with an endplate on the top to skim surface waves and eliminate tip vortices at the root. The wing tip at the bottom does not have an endplate. The wings are connected to a six-axis force/torque transducer (ATI 9105-TIF-Delta-IP65) via a wing shaft. The shaft further connects the transducer to an optical encoder (US Digital E3-2500) and a servo motor (Parker SM233AE) coupled with a gearbox (Automation Direct PGCN23-0525). The force/torque transducer measures the fluid torque τ_f exerted on the wing and feed the value to the cyber-physical system (CPS) via a data acquisition (DAQ) board (National Instruments PCIe-6353). Based on the input virtual structural parameters (i.e. the torsional stiffness, k_v, damping, b_v, and inertia, I_v), the CPS calculates the desired pitching position of wing and output the signal to the servo motor via the same DAQ board. The optical encoder, which is independent of the CPS, is used to measure and verify the physical pitching position, θ. We operate the CPS at 4,000 Hz to minimize any phase delay between the input τ_f and the output θ. The detailed implementation of the CPS can be found in Zhu et al. [19].

The two types of wings (unswept and swept) used in the present study are sketched in Fig. 1(b). All the wings have a span of $s = 0.3$ m and a chord length of $c = 0.1$ m, which results in an aspect ratio of $AR = 3$ and a fixed chord-based Reynolds number at $Re \equiv \rho U_\infty c/\mu = 50,000$, where ρ and μ are water density and dynamic viscosity. For both unswept and swept wings, the leading edge (LE) and the trailing edge (TE) are parallel. Their pivot axes, represented by vertical dashed lines in the figure, pass through the mid chord point $x/c = 0.5$ of the mid span plane $z/s = 0.5$. The sweep angle Λ is defined as the angle between the leading edge and the vertical axis. Five wings with $\Lambda = 0°$ (unswept wing), $10°, 15°, 20°$ and $25°$ (swept wings) are used in the experiments.

B. Multi-layer stereoscopic particle image velocimetry

We use multi-layer phase-averaged stereoscopic particle image velocimetry (SPIV) to measure the three-dimensional (3D) velocity field around the pitching wings. The water flow is seeded using 50 μm silver-coated hollow ceramic spheres (Potters Industries) and illuminated using a horizontal laser sheet, generated by a double-pulse Nd:YAG laser (532 nm, Quantel EverGreen) with a LaVision laser guiding arm and sheet optics. Two sCMOS cameras (LaVision, 2560×2160 pixels) with 35mm lenses are used to capture image pairs of the flow field. These SPIV image pairs are fed into the LaVision DaVis software (v.10) for velocity vector calculation using multi-pass cross-correlations (two passes at 128×128 pixels, two passes at 64×64 pixels, both with 50% overlap).

To measure the two-dimensional-three-component (2D3C) velocity field at different spanwise layers, we use a motorized vertical traverse system (range: 120 mm) to raise and lower the testing rig (i.e. all the components connected by the shaft) in the z-axis [20]. Due to the limitation of the traversing range, three measuring volumes (V1, V2 and V3, see Fig. 1b) are needed to cover the entire wing span and the wing tip region. For each measuring volume, the laser sheet is fixed at the top layer and the rig is traversed upward with a step size of 5 mm. Note that the entire wing stays submerged, even at the highest traversing position. The bottom layer of V1 and the top layer of V2 overlap with each other. The velocity fields of these two layers are averaged to smooth the interface between the two volumes. The connection of V2 and V3 is also smoothed in the same way. We phase average 512 measured 2D3C velocity fields over 16 cycles (i.e. 32 measurements per cycle) to eliminate any instantaneous variations of the flow field while maintaining the key features across different layers. Finally, 70 layers of 2D3C velocity fields are stacked together to form a large volume of phase-averaged 3D3C velocity field ($\sim 3c \times 3c \times 3.6c$). The velocity fields of three wing models ($\Lambda = 0°$, $10°$ and $20°$) are measured. For the $\Lambda = 20°$ wing, the laser volumes are offset horizontally to compensate for the relatively large sweep angle (see the bottom subfigure of Fig. 1b).

C. Governing equations and non-dimensional parameters

The fluid-structure system has a governing equation

$$I\ddot{\theta} + b\dot{\theta} + k\theta = \tau_f\,, \tag{1}$$

where θ, $\dot{\theta}$, and $\ddot{\theta}$ are the angular position, velocity and acceleration, respectively. $I = I_p + I_v$ is the effective inertia, where I_p is the physical inertia of the wing and I_v is the virtual inertia that we prescribe with the CPS. Because the friction is negligible in our system, the effective structural damping, b, equals the virtual damping b_v in the CPS. k is the effective torsional stiffness and it is equivalent to the virtual stiffness k_v. Eq. 1 resembles a forced torsional mass-spring-damper system, where the nonlinear fluid torque, τ_f, acts as a nonlinear forcing term. Following Onoue et al. [21] and Zhu et al. [19], we normalize the effective inertia, damping, stiffness and the fluid torque using the fluid

inertia force to get the non-dimensional governing equation of the system:

$$I^*\ddot{\theta}^* + b^*\dot{\theta}^* + k^*\theta^* = \tau_f^*, \tag{2}$$

where

$$\theta^* = \theta,\ \dot{\theta}^* = \frac{\dot{\theta}c}{U_\infty},\ \ddot{\theta}^* = \frac{\ddot{\theta}c^2}{U_\infty^2},\ I^* = \frac{I}{0.5\rho c^4 s},\ b^* = \frac{b}{0.5\rho U_\infty c^3 s},\ k^* = \frac{k}{0.5\rho U_\infty^2 c^2 s},\ \tau_f^* = \frac{\tau_f}{0.5\rho U_\infty^2 c^2 s}. \tag{3}$$

We should note that the inverse of the non-dimensional stiffness is equivalent to the Cauchy number, $Ca = 1/k^*$, and the non-dimensional inertia, I^*, is analogous to the mass ratio between the wing and the surrounding fluid. The non-dimensional fluid torque, τ_f^*, is effectively the unsteady moment coefficient. We define the non-dimensional velocity as $U^* = U_\infty/(2\pi f_p c)$, where f_p is the *measured* pitching frequency.

IV. Results and discussion

A. Static characteristics of unswept and swept wings

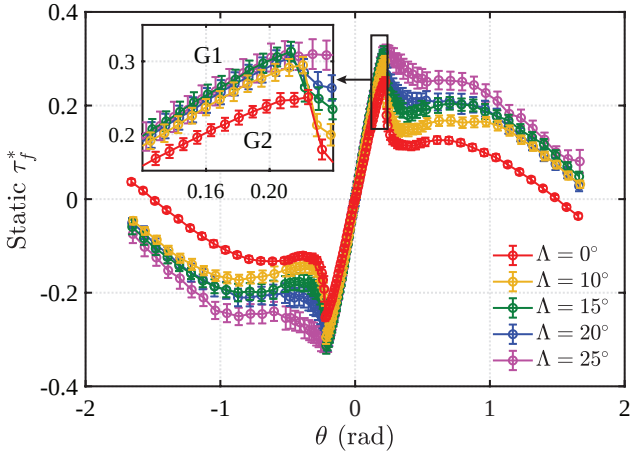


Fig. 2 Static moment coefficient of unswept and swept wings.

The static moment coefficient, τ_f^*, is measured for unswept ($\Lambda = 0°$) and swept wings ($\Lambda = 10° - 25°$) at $Re = 50,000$ and the results are plotted in Fig. 2. We see that at a fixed pitching position, θ, the static moment coefficient, τ_f^*, increases with the sweep angle, Λ. The inset shows a zoom-in view of the static τ_f^* for $\theta = 0.12 - 0.24$. It is seen that the τ_f^* curves cluster into two groups, with the unswept wing ($\Lambda = 0°$) being in G2 and all the other swept wings ($\Lambda = 10° - 25°$) being in G1. As we will show later, this grouping behavior is closely related to the onset of flow-induced oscillations (§IV.B & §IV.D) and it is important for understanding the system stability.

B. Subcritical bifurcations to flow-induced oscillations

We conduct bifurcation tests to evaluate the stability boundaries of elastically mounted pitching swept wings. Zhu et al. [19] have shown that for unswept wings, the onset of limit-cycle oscillations (LCOs) is independent of the wing inertia and the bifurcation type, and the extinction of LCOs for subcritical bifurcations at different wing inertias can be scaled by the non-dimensional velocity U^*. For these reasons, we choose to focus on one high-inertia case ($I^* = 10.6$) in the present study. In the experiments, we fix the structural damping of the system at a small value $b^* = 0.13$ and keep the initial angle of attack (AOA) at zero. To test for the onset boundary of LCOs, we first incrementally increase the Cauchy number, Ca, by decreasing the torsional stiffness, k^*. Then we reverse the operation to identify the extinction boundary of LCOs and to test for any hysteresis. The amplitude response of the system, $|A|$, is measured as the absolute peak pitching amplitude. The static divergence angle, $|\overline{A}|$, is defined as the absolute mean pitching angle.

Fig. 3 shows the amplitude response and the static divergence for swept wings with $\Lambda = 10°$ to $25°$. Data for the unswept wing ($\Lambda = 0°$) are also replotted from Zhu et al. [19] for comparison. It can be seen that as we increase

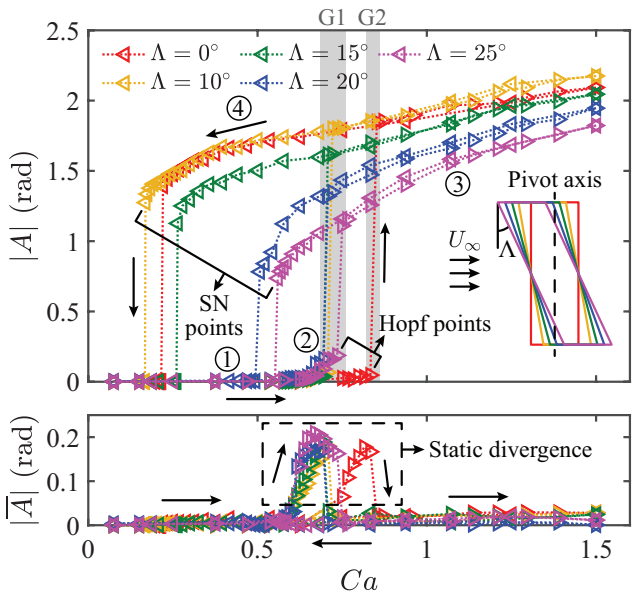


Fig. 3 Amplitude response and static divergence for unswept and swept wings. ▷: increasing Ca, ◁: decreasing Ca. The inset illustrates the wing geometry and the pivot axis. The colors of the wings correspond to the colors of the amplitude and the divergence curves in the figure.

Ca, the system first remains stable without any noticeable oscillations or divergence (regime ① in the figure). In this regime, the high stiffness of the system is able to pull the system back to a stable fixed point despite any small perturbations. As we further increase Ca, the system diverges into a small static angle, where the fluid torque is balanced by the virtual spring. Because of the existence of random flow disturbances and the decreasing spring stiffness, some small-amplitude oscillations around the static divergence angle also starts to emerge (regime ②). As Ca is further increased above a critical value (i.e. the Hopf point), the amplitude response of the system abruptly jumps into large-amplitude self-sustained LCOs and the static divergence angle drops back to zero. The large-amplitude LCOs are observed to be near-sinusoidal and have a dominant characteristic frequency. After the bifurcation, the amplitude response of the system continues to increase with Ca (regime ③). We then decrease Ca and find that the large-amplitude LCOs persist even when Ca is decreased below the Hopf point (regime ④). Finally, the system returns back to the stable fixed point regime via a saddle-node (SN) point. A hysteretic bistable region is created in between the Hopf point and the saddle-node point, which is a key feature of a subcritical Hopf bifurcation [22].

We observe that the Hopf points of unswept and swept wings can be roughly divided into two groups (Fig. 3, G1 & G2), with the unswept wing ($\Lambda = 0°$) being in G2 and all the other wings ($\Lambda = 10° - 25°$) being in G1, which agrees with the trend observed in Fig. 2 for static moment coefficients. The underlying physics behind this interconnection will be discussed in §IV.D. It is also seen that as the sweep angle increases, the LCO amplitude at the saddle-node point decreases monotonically. However, value of Ca at which the saddle-node point occurs first extends towards a lower value ($\Lambda = 0° \rightarrow 10°$) and then comes back towards a higher Ca ($\Lambda = 10° \rightarrow 25°$). This indicates that increasing the sweep angle first destabilizes the system from $\Lambda = 0°$ to $10°$ and then re-stabilizes it from $\Lambda = 10°$ to $25°$. This non-monotonic behavior of the saddle-node point will be discussed in §IV.E. The amplitude response, $|A|$, seems to follow a similar non-monotonic trend. Between $\Lambda = 0°$ and $10°$, $|A|$ becomes slightly higher at higher Ca. Whereas from $\Lambda = 10°$ to $25°$, $|A|$ decreases monotonically, indicating that higher Λ is not able to sustain LCOs at higher amplitudes.

C. Frequency response of the system

Fig. 4(a) shows the frequency response of the flow-induced large-amplitude LCOs observed in Fig. 3 as a function of the natural (structural) frequency and the sweep angle. In the figure, $f_p^* = f_p c/U_\infty$ and $f_s^* = f_s c/U_\infty$, where f_s is the structural frequency [23] calculated by

$$f_s = \frac{1}{2\pi}\sqrt{\frac{k}{I} - (\frac{b}{2I})^2}. \tag{4}$$

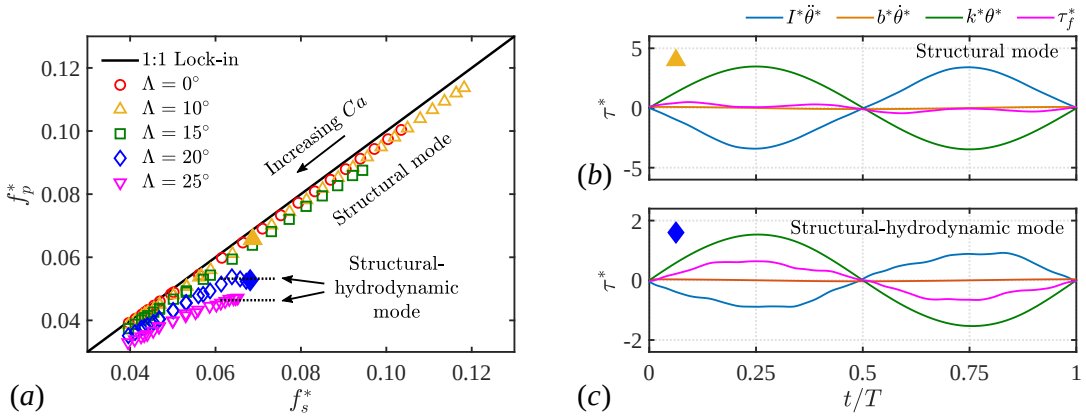


Fig. 4 (*a*) Frequency response of unswept and swept wings. (*b*, *c*) Force decomposition of the structural mode and the structural-hydrodynamic mode. (*b*) and (*c*) correspond to the filled yellow triangle and the filled blue diamond in (*a*), respectively.

We observe that for all the wings tested in the experiments, the measured pitching frequency, f_p^*, generally locks on to the calculated structural frequency, f_s^*, indicating that the oscillations are dominated by the balance between the structural stiffness and inertia. These oscillations thus correspond to a *structural* mode [19]. We decompose the torques experienced by the wing into the inertia torque, $I^*\ddot{\theta}^*$, the structural damping torque, $b^*\dot{\theta}^*$, the stiffness torque, $k^*\theta^*$, and the fluid torque, τ_f^*. For an example case at $\Lambda = 10°$, $f_s^* = 0.069$ (i.e. the filled yellow triangle in Fig. 4*a*), these torques are plotted in Fig. 4(*b*). We see that for the structural mode, the stiffness torque is mainly balanced by the inertia torque, while the structural damping torque and the fluid torque remain relatively small.

Apart from the structural mode, Zhu et al. [19] also observed a hydrodynamic mode, which corresponds to a low wing inertia. In the hydrodynamic mode, the oscillations are dominated by the fluid force, so that the measured pitching frequency, f_p^*, stays relatively constant for a changing Ca. In Fig. 4(*a*), we see that for $\Lambda = 20°$ and 25°, f_p^* flattens near the saddle-node boundary. This flattening trend shows an emerging dominating fluid time scale, resembling a hydrodynamic mode despite the high wing inertia. We take $\Lambda = 20°$, $f_s^* = 0.068$ (i.e. the filled blue diamond in Fig. 4*a*) as an example and decompose the torques in Fig. 4(*c*). It is observed that in this oscillation mode, the stiffness torque balances both the inertia torque and the fluid torque. For this reason, we define this hybrid oscillation mode as the *structural-hydrodynamic* mode.

For a fixed structural frequency, f_s^*, as the sweep angle increases, the measured pitching frequency, f_p^*, deviates from f_s^* moving to lower frequencies, suggesting an increasing added-mass effect. This is expected because of the way we pitch the wings in the experimental setup (see the inset of Fig. 3). As Λ increases, the accelerated fluid near the wing root and the wing tip produces more torque due to the increase of the moment arm, which amplifies the added-mass effect.

D. Onset of flow-induced oscillations

In Fig. 3, we have observed that the Hopf points of unswept and swept wings can be roughly divided into two groups (Fig. 3, G1 & G2) . In this section, we try to explain this phenomenon. Fig. 5(*a*) and (*b*) shows the temporal evolution of the pitching position, θ, the fluid torque, τ_f^* and the stiffness torque, $k^*\theta$, near the Hopf point for $\Lambda = 0°$. It can be seen that the wing undergoes small-amplitude oscillations around the divergence angle at the Hopf point. The divergence angle is below the static stall angle, θ_s, so that the flow stays mostly attached. The fluid torque, τ_f^*, is balanced by the stiffness torque, $k^*\theta$. When the Cauchy number, Ca, is changed to a value above the Hopf point (Fig. 4*a*, $t = 700$ s), $k^*\theta$ is not able to hold the pitching position below θ_s. Once the pitching position exceeds θ_s, stall occurs and the wing experiences a sudden drop in τ_f^*. $k^*\theta$ loses its counterpart and starts to accelerate the wing to pitch towards the opposite direction. This acceleration brings unsteadiness to the system and the quasi-steady small-amplitude oscillations gradually transition to large-amplitude LCOs. This transition process shows that the onset of large-amplitude LCOs depends largely on the static characteristics of the wing.

The triggering of flow-induced LCOs starts from θ exceeding the static stall angle after k^* is decreased below the Hopf point, causing τ_f^* to drop below $k^*\theta$. Therefore, the slope of the static stall point should be equal to the stiffness at

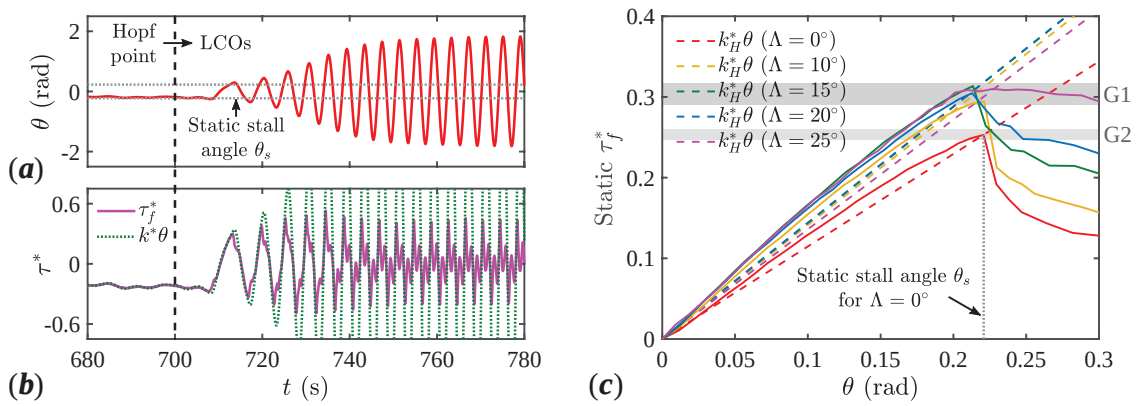


Fig. 5 Temporal evolution of (*a*) the pitching position θ, (*b*) the fluid torque τ_f^*, and the stiffness torque $k^*\theta$ near the Hopf point for $\Lambda = 0°$. (*c*) Static moment coefficients of unswept and swept wings.

the Hopf point, k_H^* (i.e. $\tau_{f,\,\text{stall}}^* = k_H^*\theta$). This is verified by Fig. 5(*c*), in which we replot the static moment coefficients of unswept and swept wings from Fig. 2 with error bars omitted for clarity. The corresponding $k_H^*\theta$ are also plotted. We see that the $k_H^*\theta$ lines all roughly pass through the static stall points (i.e. the maximum static τ_f^*) of the corresponding Λ. Note that $k_H^*\theta$ of $\Lambda = 15°$ and $20°$ overlap with each other. Similar to the trend observed for the Hopf point in Fig. 3 (or equivalently, the trend of $k_H^*\theta$), the static moment coefficient τ_f^* can also be divided into two groups, with the unswept wing ($\Lambda = 0°$) being in G2 and all the other wings ($\Lambda = 10° - 25°$) being in G1 (see also Fig. 2). This reinforces the argument that the onset of flow-induced LCOs is shaped by the static characteristics of the wing. Moreover, it is proven that this argument applies to both unswept and swept wings.

E. Power coefficient map and system stability

In this section, we analyze the stability of elastically mounted unswept and swept wings from the perspective of energy transfer. Menon and Mittal [24] and Zhu et al. [19] have shown numerically and experimentally that the flow-induced oscillations of elastically mounted 2D wings and unswept wings can only sustain when the net energy transfer between the ambient fluid and the elastic structure equals zero. To map out this energy transfer for a large range of pitching frequencies and amplitudes, we prescribe the pitching motion of the wing with

$$\theta = |A| \sin(2\pi f_p t), \tag{5}$$

where $0 \le |A| \le 2.5$ and $0.15\ \text{Hz} \le f_p \le 0.6\ \text{Hz}$. By integrating Eq. 2 over $n = 20$ cycles and averaging [21], we can get the power coefficient of the system

$$C_p = \frac{f_p^*}{n} \int_{t_0}^{t_0+nT} (\tau_f^* \dot{\theta}^* - b^* \dot{\theta}^{*2})\, dt^*. \tag{6}$$

In this equation, the $\tau_f^* \dot{\theta}^*$ term represents the power injected into the system by the ambient fluid, whereas the $b^* \dot{\theta}^{*2}$ term represents the power dissipated by the structural damping of the elastic mount. The power coefficient maps of unswept and swept wings are plotted in Fig. 6(*a*-*e*).

In these maps, red regions correspond to $C_p > 0$, where the power injected by the ambient fluid is higher than that dissipated by the structural damping. On the contrary, $C_p < 0$ in the blue regions. The colored dashed lines indicate the $C_p = 0$ contours, where the power injection balances the power dissipation. The $C_p = 0$ curve can be divided into three branches. Zhu et al. [19] have shown that for unswept wings, the top branch corresponds to stable LCO solutions for the structural mode, the middle branch represents stable LCO solutions for the hydrodynamic mode, and the bottom branch is the stable fixed point solution.

To correlate the power coefficient maps of prescribed oscillations with the stability boundaries of flow-induced oscillations, we overlay the amplitude response of the passive system from Fig. 3 onto Fig. 6(*a*-*e*). The measured pitching frequencies, f_p, are used to calculate the non-dimensional velocity, U^*, for large-amplitude LCOs (filled triangles). Because it is difficult to measure frequencies of stable fixed points and small-amplitude oscillations (hollow

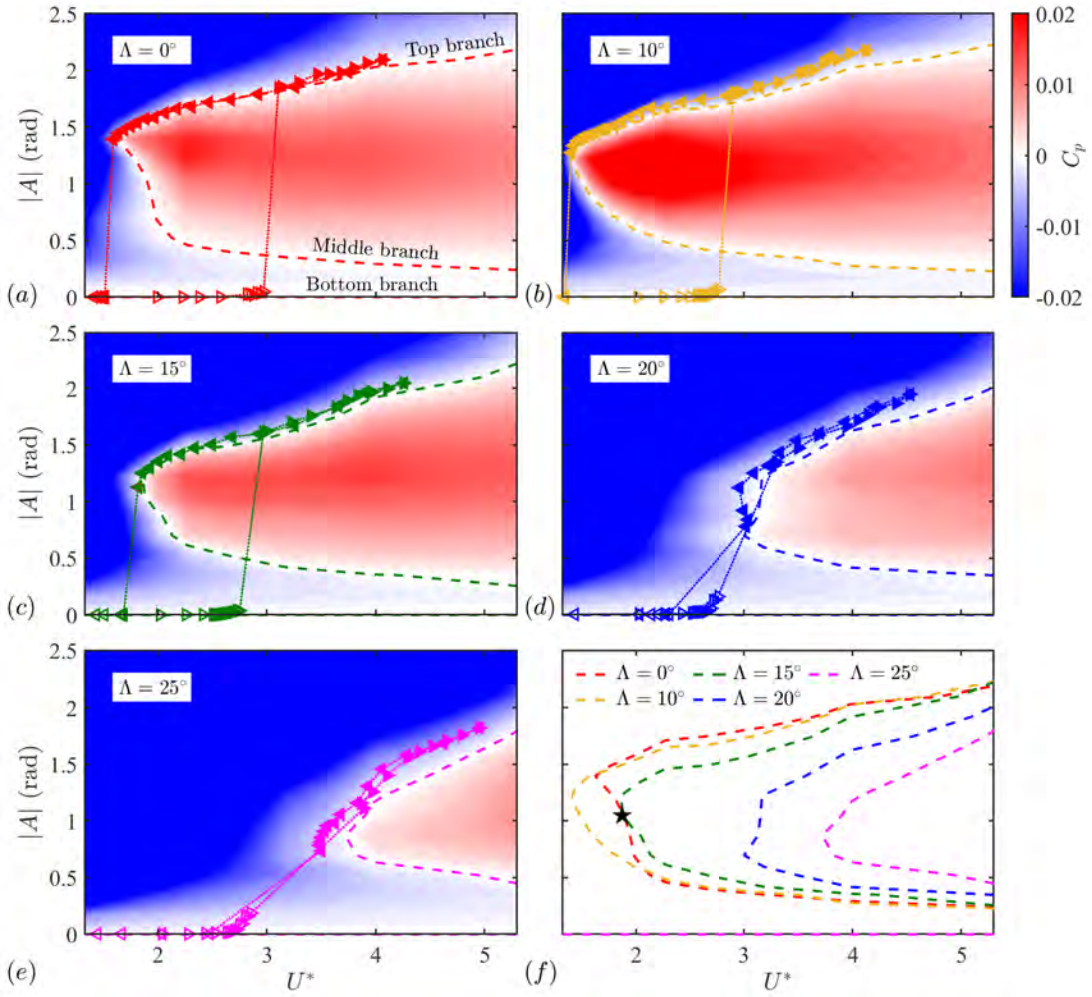


Fig. 6 (*a-e*) Power coefficient maps of prescribed sinusoidal oscillations overlaid by the bifurcation diagrams of elastically mounted unswept and swept wings. ▷: increasing Ca, ◁: decreasing Ca. (*f*) Neutral power transfer curves for unswept and swept wings.

triangles), we use the calculated structural frequency, f_s, to evaluate U^*. Fig. 6(*a-e*) show that for all the wings tested, the flow-induced large-amplitude LCOs agree remarkably well with the top branch of the $C_p = 0$ curve, indicating the broad applicability of the energy approach for both unswept and swept wings, a result that was observed by Menon and Mittal [24] and Zhu et al. [19] and is expected for instabilities that are well-described by sinusoidal motions (Eq. 5). The small discrepancies for large sweep angles can be attributed to the smooth C_p gradient near $C_p = 0$. The junction between the top and the middle $C_p = 0$ branches remains relative sharp for $\Lambda = 0° - 15°$ and becomes smoother for $\Lambda = 20° - 25°$. These smooth turnings result in a smooth transition in between the structural mode and the hydrodynamic mode, giving rise to the structural-hydrodynamic mode discussed in §IV.C.

The $C_p = 0$ curves for $\Lambda = 0° - 25°$ are summarized in Fig. 6(*f*). It is seen that the trend of the top branch is similar to that observed in Fig. 3 for large-amplitude LCOs. The location of the junction between the top branch and the middle branch changes non-monotonically with Λ, which accounts for the non-monotonic behavior of the saddle-node point. In addition, the maximum power extraction also shows a non-monotonic dependency on the sweep angle, which may inspire the future design of higher efficiency oscillating-foil energy harvesting devices.

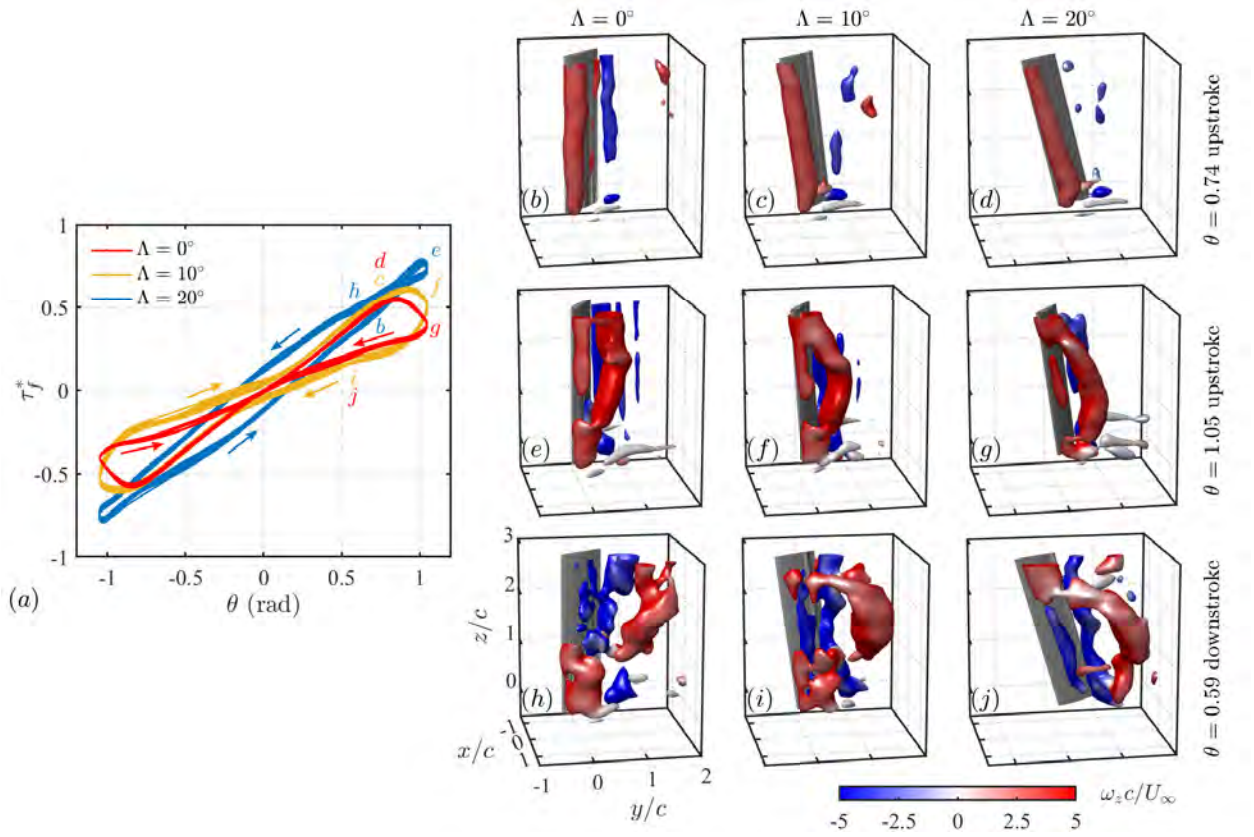


Fig. 7 (*a*) Force portraits for Λ = 0°, 10° and 20° at $|A| = 1.05$ and $f_p^* = 0.09$. (*b-j*) Phase-averaged 3D flow structures visualized with iso-Q surfaces ($Q = 50\ s^{-2}$) colored by the non-dimensional spanwise vorticity, $\omega_z c/U_\infty$.

F. Insights obtained from three-dimensional flow structures

In the previous section (§IV.E), we have established the interconnection between prescribed oscillations and flow-induced oscillations using the energy approach. In this section, we analyze the 3D flow structures obtained from phase-averaged stereo PIV experiments to get some insights for the differences in the power coefficient between unswept and swept wings. In the PIV experiments, three wings (Λ = 0°, 10° and 20°) are prescribed with sinusoidal pitching at $|A| = 1.05$ and $f_p^* = 0.085$, which corresponds to the black star shown in Fig. 6(*f*). This particular pitching kinematic is selected because it sits right on the $C_p = 0$ curve for Λ = 0° while leading to a positive C_p for Λ = 10° and a negative C_p for Λ = 20° (see Fig. 6*a,b,d,f*).

The τ_f^*-θ phase portraits for the three wings are plotted in Fig. 7(*a*) with arrows showing the temporal direction of the loops. For plotting purposes only, we apply a zero-phase sixth-order low-pass Butterworth filter (cutoff at $20 f_p$) to the raw torque data so as to smooth out small oscillations. It is important to note that this filter is only employed for post-processing of the data; no filter is used inside the real-time control loop. 3D velocity fields around the wings are measured using the technique described in §III.B and smoothed. Phase-averaged 3D flow structures visualized with iso-Q surfaces ($Q = 50\ s^{-2}$) at three pitching positions ($\theta = 0.74$ and 1.05, upstroke; $\theta = 0.59$, downstroke) are plotted in Fig. 7(*b-j*) for all the three wings. These 3D flow structures are colored by the non-dimensional spanwise vorticity, $\omega_z c/U_\infty$, with red being positive and blue being negative. The corresponding pitching positions of (*b-j*) are shown in Fig. 7(*a*).

The fluid torque, τ_f^*, shows a relatively linear growth (Fig. 7*a*) as the wings pitch up ($\theta = 0.74$, upstroke), which corresponds to the formation of a strong leading-edge vortex, as depicted by Fig. 7(*b-d*). At this time instant, the 3D flow structures for the three wings appear to be very similar. As the wings continue to pitch up, τ_f^* reaches its maximum. It is observed that τ_f^* peaks at higher values of θ as the sweep angle increases. At the maximum pitch angle ($\theta = 1.05$, upstroke), τ_f^* drops from the peak for Λ = 0° and 10° while reaching the maximum for Λ = 20°. The decrease of τ_f^* for

$\Lambda = 0°$ and $10°$ results from the shedding of the LEV as shown in Fig. 7(*e-f*). At this time instant, the LEV mostly detaches from the wing surface for $\Lambda = 0°$ (Fig. 7*e*) except for a small portion near the wing tip, which stays attached. A similar flow structure was observed by Yilmaz and Rockwell [25] for finite-span wings undergoing linear pitch-up motions. For $\Lambda = 10°$ (Fig. 7*f*), this small portion of the attached LEV shrinks. The top portion of the LEV near the wing root is also observed to stay closer to the wing surface as compared to the $\Lambda = 0°$ case. For $\Lambda = 20°$ (Fig. 7*g*), the attached portion of the LEV near the wing tip further shrinks and the top portion of the LEV also attaches to the wing surface, similar to that observed for $\Lambda = 10°$.

During the pitch reversal ($\theta = 0.59$, downstroke), as the LEV further detaches from the wing surface for $\Lambda = 0°$ and $10°$ (Fig. 7*h-i*), τ_f^* takes a lower path back to the equilibrium point ($\theta = 0$), resulting in a positive hysteresis loop. This positive loop corresponds to a positive $\tau_f^* \dot{\theta}^*$ term in Eq. 6, indicating a positive power injection by the ambient fluid. The loop area of $\Lambda = 10°$ is greater than that of $\Lambda = 0°$. For $\Lambda = 0°$, this power injection is balanced by the power dissipation of the structural damping, leading to $C_p = 0$ and self-sustained LCOs in the passive system (Fig. 6*a*). For $\Lambda = 10°$, this fluid power injection is greater than the structural power dissipation (note that all the three wings have the same structural power dissipation because they are prescribed with the same kinematics), resulting in a positive C_p. In the passive system, due to the power injection, the LCO amplitude increases and settles on the top branch of $C_p = 0$ (Fig. 6*b*). For $\Lambda = 20°$, however, τ_f^* takes an upper path back to $\theta = 0$, creating a negative hysteresis loop. This means that in addition to the structural damping, the ambient fluid also dissipates power from the system (i.e. positive fluid damping, see [26]). The combined effect of these two power dissipation mechanisms leads to a negative C_p and thus a decreasing LCO amplitude in the passive system, which further brings the system down to the bottom branch of the $C_p = 0$ curve (Fig. 6*c*). Fig. 7(*j*) shows that for $\Lambda = 20°$, the LEV largely detaches from the wing surface except for the top portion. As the top portion of the LEV is far from the pivot axis, the force generated by it has a long moment arm, which can result in a high fluid torque. This may account for the high τ_f^* observed for $\Lambda = 20°$ during the pitch reversal, as compared to $\Lambda = 0°$ and $10°$.

The change of LEV shapes as a function of the sweep angle observed in Fig. 7(*e-g*) can be associated with the arch vortices reported by Visbal and Garmann [18]. In their numerical study, it has been shown that for pitching unswept wings with free tips on both ends, an arch-type vortical structure began to form as the pitch reversal started (see their Fig. 6c). In our experiments, the wings have a free tip and an endplate (a wing-body junction, or symmetry plane). Therefore, the vortical structure shown in Fig. 7(*e*) is equivalently half of the arch vortex. If we mirror the flow structures about the wing root (i.e. the endplate), we can get a complete arch vortex similar to that observed by Visbal and Garmann [18]. For swept wings, we observe one complete arch vortex for both $\Lambda = 10°$ (Fig. 7*f*) and $20°$ (Fig. 7*g*). Again, if we mirror the flow structures about the wing root, there will be two arch vortices for each wing, which well agrees with the observation of Visbal and Garmann [18] (see their Fig. 10c and 13c). Moreover, Visbal and Garmann [18] reported that for swept wings, as Λ increases, the arch vortex moves towards the wing tip, which is also seen in our experiments.

V. Conclusions and future works

In this experimental study, we have investigated the nonlinear stability boundaries of elastically mounted pitching unswept and swept wings, with the elastic mount of the wings simulated using a cyber-physical control system. We have shown that the onset of flow-induced oscillations (i.e. the Hopf point) depends on the static characteristics of the wing. The non-monotonic trend of the saddle-node point as a function of the sweep angle has been attributed to the non-monotonic power transfer between the ambient fluid and the elastic mount. For swept wings with relatively high sweep angles ($\Lambda = 20°$ and $25°$), an hybrid oscillation mode, namely the structural-hydrodynamic mode, has been observed and characterized. Phase-averaged 3D flow structures measured by stereoscopic PIV have been analyzed to explain the differences in power extraction for unswept and swept wings. In addition, we have found that there exists an optimal sweep angle ($\Lambda = 10°$) for extracting power from fluid flows and thus promoting flow-induced oscillations. One may want to avoid this angle for MAV designs to stay away from aeroelastic instabilities. On the other hand, this angle may be employed for developing higher efficiency flapping-foil energy-harvesting devices.

In the present study, only qualitative analysis of 3D flow structures have been conducted and for a very limited set of sweep angles and flow parameters. In order to get a deeper understanding of the wing sweep effect on the dynamics and stability of the leading-edge vortex and thus the system stability boundaries, more quantitative analysis are needed, which will be the focus of a following work.

Acknowledgments

This work is funded by Air Force Office of Scientific Research, Grant FA9550-18-1-0322, managed by Dr. Gregg Abate.

References

[1] Dowell, E. H., Curtiss, H. C., Scanlan, R. H., and Sisto, F., *A modern course in aeroelasticity*, Springer, 1989.

[2] Xiao, Q., and Zhu, Q., "A review on flow energy harvesters based on flapping foils," *J. Fluids Struct.*, Vol. 46, 2014, pp. 174–191.

[3] Young, J., Lai, J. C. S., and Platzer, M. F., "A review of progress and challenges in flapping foil power generation," *Prog. Aerosp. Sci.*, Vol. 67, 2014, pp. 2–28.

[4] Su, Y., and Breuer, K. S., "Resonant response and optimal energy harvesting of an elastically mounted pitching and heaving hydrofoil," *Phys. Rev. Fluids*, Vol. 4, No. 6, 2019, p. 064701.

[5] Wang, Z. J., "Dissecting insect flight," *Annu. Rev. Fluid Mech.*, Vol. 37, 2005, pp. 183–210.

[6] Bergou, A. J., Xu, S., and Wang, Z. J., "Passive wing pitch reversal in insect flight," *J. Fluid Mech.*, Vol. 591, 2007, pp. 321–337.

[7] Beatus, T., and Cohen, I., "Wing-pitch modulation in maneuvering fruit flies is explained by an interplay between aerodynamics and a torsional spring," *Phys. Rev. E*, Vol. 92, No. 2, 2015, p. 022712.

[8] Wu, K. S., Nowak, J., and Breuer, K. S., "Scaling of the performance of insect-inspired passive-pitching flapping wings," *J. R. Soc. Interface*, Vol. 16, No. 161, 2019, p. 20190609.

[9] Ho, S., Nassef, H., Pornsinsirirak, N., Tai, Y.-C., and Ho, C.-M., "Unsteady aerodynamics and flow control for flapping wing flyers," *Prog. Aerosp. Sci.*, Vol. 39, No. 8, 2003, pp. 635–681.

[10] Shyy, W., Aono, H., Chimakurthi, S. K., Trizila, P., Kang, C.-K., Cesnik, C. E. S., and Liu, H., "Recent progress in flapping wing aerodynamics and aeroelasticity," *Prog. Aerosp. Sci.*, Vol. 46, No. 7, 2010, pp. 284–327.

[11] McCroskey, W. J., "Unsteady airfoils," *Annu. Rev. Fluid Mech.*, Vol. 14, No. 1, 1982, pp. 285–311.

[12] Dimitriadis, G., and Li, J., "Bifurcation behavior of airfoil undergoing stall flutter oscillations in low-speed wind tunnel," *AIAA J.*, Vol. 47, No. 11, 2009, pp. 2577–2596.

[13] Ellington, C. P., van den Berg, C., Willmott, A. P., and Thomas, A. L. R., "Leading-edge vortices in insect flight," *Nature*, Vol. 384, No. 6610, 1996, p. 626.

[14] Videler, J. J., Stamhuis, E. J., and Povel, G. D. E., "Leading-edge vortex lifts swifts," *Science*, Vol. 306, No. 5703, 2004, pp. 1960–1962.

[15] Lentink, D., Müller, U. K., Stamhuis, E. J., de Kat, R., van Gestel, W., Veldhuis, L. L. M., Henningsson, P., Hedenström, A., Videler, J. J., and van Leeuwen, J. L., "How swifts control their glide performance with morphing wings," *Nature*, Vol. 446, No. 7139, 2007, pp. 1082–1085.

[16] Wong, J. G., and Rival, D. E., "Determining the relative stability of leading-edge vortices on nominally two-dimensional flapping profiles," *J. Fluid Mech.*, Vol. 766, 2015, p. 611.

[17] Onoue, K., and Breuer, K. S., "A scaling for vortex formation on swept and unswept pitching wings," *J. Fluid Mech.*, Vol. 832, 2017, pp. 697–720.

[18] Visbal, M. R., and Garmann, D. J., "Effect of sweep on dynamic stall of a pitching finite-aspect-ratio wing," *AIAA J.*, Vol. 57, No. 8, 2019, pp. 3274–3289.

[19] Zhu, Y., Su, Y., and Breuer, K. S., "Nonlinear flow-induced instability of an elastically mounted pitching wing," *J. Fluid Mech.*, Vol. 899, 2020, p. A35.

[20] Zhong, Q., Han, T., Moored, K. W., and Quinn, D. B., "Aspect ratio affects the equilibrium altitude of near-ground swimmers," *J. Fluid Mech.*, Vol. 917, 2021.

[21] Onoue, K., Song, A., Strom, B., and Breuer, K. S., "Large amplitude flow-induced oscillations and energy harvesting using a cyber-physical pitching plate," *J. Fluids Struct.*, Vol. 55, 2015, pp. 262–275.

[22] Strogatz, S. H., *Nonlinear Dynamics and Chaos: With Applications to Physics, Biology, Chemistry, and Engineering*, Perseus Books, 1994.

[23] Rao, S. S., *Mechanical Vibrations*, Addison-Wesley, 1995.

[24] Menon, K., and Mittal, R., "Flow physics and dynamics of flow-induced pitch oscillations of an airfoil," *J. Fluid Mech.*, Vol. 877, 2019, pp. 582–613.

[25] Yilmaz, T. O., and Rockwell, D., "Flow structure on finite-span wings due to pitch-up motion," *J. Fluid Mech.*, Vol. 691, 2012, p. 518.

[26] Zhu, Y., Mathai, V., and Breuer, K., "Nonlinear fluid damping of elastically mounted pitching wings in quiescent water," *J. Fluid Mech.*, Vol. 923, 2021, p. R2.

Stability Boundaries and Fluid Damping of Elastically-Mounted Pitching Swept Wings

Yuanhang Zhu*, Yunxing Su, and Kenneth Breuer

School of Engineering, Brown University, Providence, RI 02912, USA

Summary We experimentally study the nonlinear stability characteristics and the role of fluid damping for elastically-mounted pitching swept wings using a cyber-physical system. We show that the onset of large-amplitude limit-cycle oscillations (LCOs) depends on the static characteristics of the wing. The non-monotonic variation of the stability boundary for different sweep angles is conjectured to be the competition between two mechanisms: (*a*) the stabilization of leading-edge vortices (LEVs) by wing sweep, which promotes LCOs and thus destabilizes the system, and (*b*) fluid damping, which damps out LCOs and thus stabilizes the system. We characterize the fluid damping by performing 'ring down' experiments in quiescent water and show that fluid damping increases with sweep angles.

INTRODUCTION AND EXPERIMENTAL SETUP

Fluid-structure interactions of elastically mounted pitching wings is central in many applications. Recent works explored the effect of different parameters on the dynamics and flow physics of such systems. Menon and Mittal [1] numerically investigated the effects of structural damping, initial angle of attach (AOA) and the location of pivot axis on the flow-induced oscillations of passively pitching two-dimensional wings. Zhu *et al.* [2] experimentally studied the effect of inertia and stiffness on the stability boundaries of a cyber-physical pitching two-dimensional wing and reported super- and sub-critical transitions to large-amplitude LCOs for low- and high-inertia wings respectively. However, the effect of wing sweep on the stability characteristics of elastically mounted pitching wings remains unclear. We address this problem in the present study.

A schematic of the experimental setup is shown in Figure 1(*a*). Five NACA 0012 wings with sweep angle $\Lambda = 0^\circ, 10^\circ, 15^\circ, 20^\circ, 25^\circ$ are tested in the present study. All the wings have a chord length of $c = 0.1$ m and a span of $s = 0.3$ m. The pivot (elastic) axis is a vertical line passing through the mid-chord point on the mid-span plane. A side view of the five wings is shown in Figure 1(*b*). The wing is mounted vertically in a water tunnel with a zero initial AOA. An endplate is added to the top of the wing to eliminate tip vortices at wing root. The structural properties of the wing are controlled by a cyber-physical system. The non-dimensional parameters used in the present study are inertia, I^*, damping, b^*, stiffness, k^*, and the fluid force (moment coefficient), τ_f^*. The inverse of k^* is the Cauchy number Ca, which defines the ratio between the fluid inertia force and the elastic restoring force. The Reynolds number, Re, is kept at 50,000 for all the stability boundary tests and static force measurements (Figure 1(*b*)(*c*)). For all the experiments testing the fluid damping (Figure 2), the water is quiescent. Detailed description and validation of the cyber-physical system and the definition of non-dimensional parameters can be found in [2].

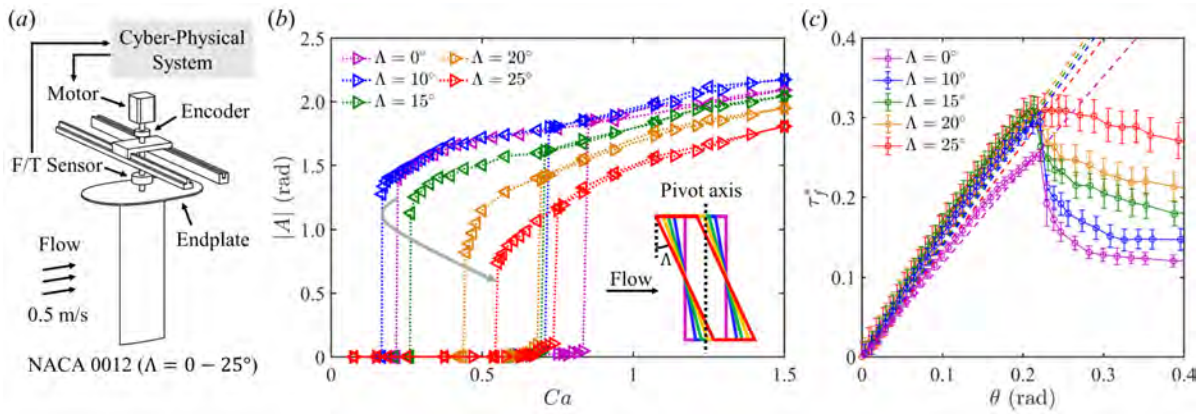


Figure 1: (*a*) A schematic of the experimental setup. (*b*) Bifurcation diagram at $I^* = 10.6$ and $b^* = 0.13$ for five wings ($\Lambda = 0^\circ, 10^\circ, 15^\circ, 20^\circ, 25^\circ$). $\triangleright$: increasing Ca, $\triangleleft$: decreasing Ca. (*c*) Static moment measurements.

RESULTS AND DISCUSSION

Stability boundaries of elastically mounted pitching swept wings

In the experiments, we fix $I^* = 10.6$ and $b^* = 0.13$, and incrementally vary Ca to define the stability boundaries of five wings with different sweep angles. Figure 1(*b*) shows the bifurcation diagram, in which the system response is represented by the pitching amplitude $|A|$. For all the wings, as Ca is increased, the system undergoes a subcritical bifurcation to large-amplitude LCOs, evidenced by an abrupt amplitude jump and a region of hysteretic bistability [2]. It is shown that both the onset and extinction of large-amplitude LCOs vary with the sweep angle. We attribute the difference in the onset point to the different static characteristics of the wings. Figure 1(*c*) shows that the static moment coefficient of the five wings can be divided into two groups, because the $\Lambda = 0^\circ$ wing experiences lower static fluid force compared to the other four wings. This grouping is also evident in the results presented in Figure 1(*b*), where large-amplitude LCOs

*Corresponding author. E-mail: yuanhang_zhu@brown.edu

are seen to occur at a higher critical Ca for the $\Lambda = 0°$ wing. The critical elastic restoring force, $k_c^*\theta$, where k_c^* is the critical wing stiffness, is plotted using dashed lines in Figure 1(c) for all the five wings. It can be observed that all of the dashed lines coincide with the static stall point, which further suggests that the onset of large-amplitude LCOs is related the static characteristics of the wing.

As shown by the gray arrow in Figure 1(b), the extinction point (i.e. the saddle-node (SN) point) of the large-amplitude LCOs changes non-monotonically with the sweep angle. We conjecture that this non-monotonic behavior is due to the competition between two mechanisms, the destabilizing effect brought by the wing sweep and the stabilizing effect caused by the fluid damping. For $\Lambda = 0° - 10°$, the SN point extends to lower Ca, indicating that the system becomes more unstable. Previous studies [1, 2] have shown that large-amplitude LCOs are associated with the formation and shedding of strong LEVs. The persistence of LCOs at lower Ca for $\Lambda = 10°$ indicates that LEVs become more stable as compared to $\Lambda = 0°$. This agrees with previous findings [3, 4] that the wing sweep has a stabilization effect on LEVs by strengthening spanwise vorticity transport. For higher sweep angles ($\Lambda = 10° - 25°$), the large-amplitude LCOs die down at higher Ca, suggesting that a stabilizing mechanism comes into play. We think this stabilizing mechanism is fluid damping, because under the same pitching amplitude, wings with a higher sweep angle move more fluid due to larger tip motion. Due to high fluid damping, the pitching amplitude also decreases with Λ.

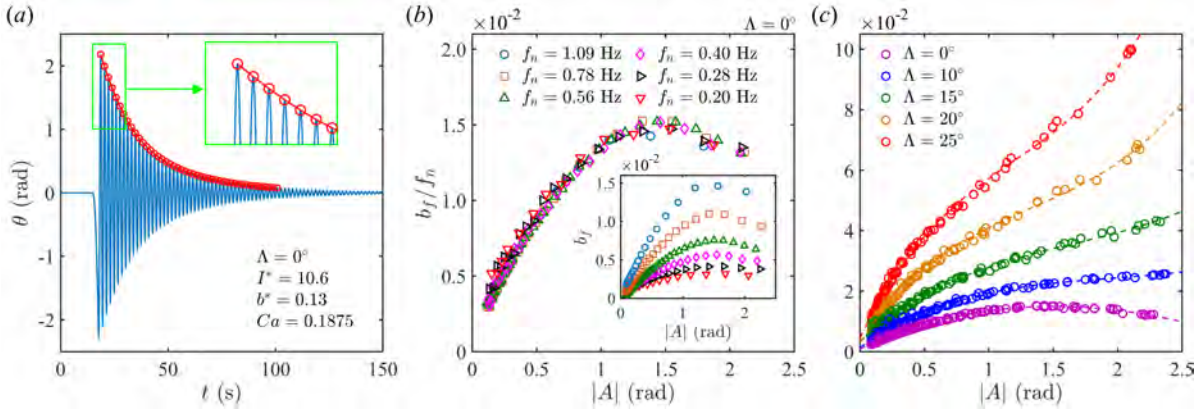


Figure 2: (a) An example of free damped oscillations. (b) Fluid damping scaling for the $\Lambda = 0°$ wing. Inset: Fluid damping versus pitching amplitude. (c) Fluid damping scaling for different wings. Note that (b) and (c) share the same y-axis label.

Fluid damping of swept wings in quiescent water

To characterize the fluid damping, we perform 'ring down' experiments in quiescent water, where we perturb the elastically mounted wing and analyze the amplitude evolution of the free oscillation. Figure 2(a) shows the result from a typical 'ring down' experiment. As shown in the zoom-in inset, for every two adjacent peaks (one cycle), we calculate the total cycle-averaged damping of the system by fitting an damped exponential to the two peaks. The structural damping is then subtracted from the total damping to get the cycle-averaged fluid damping, b_f. The corresponding pitching amplitude, $|A|$, is calculated to be the average amplitude of the two peaks. By changing the combination of I^* and k^*, we repeat the 'ring down' experiments for six different natural frequencies (f_n) and plot the result in the inset of Figure 2(b). It is seen that b_f increases non-monotonically with $|A|$ for a fixed f_n, and monotonically with f_n for a fixed $|A|$. When b_f is divided by f_n (Figure 2(b)), all the data points for different f_n collapse into one curve, indicating b_f/f_n is a good scaling parameter for the fluid damping. The 'ring down' experiments are repeated for the other four swept wings ($\Lambda = 10° - 25°$) and for each Λ, we are able to collapse the data points for different f_n using b_f/f_n, as shown in Figure 1(c). We observe that for a fixed $|A|$, b_f indeed increases with Λ. The b_f/f_n for each Λ can be accurately fit by a 3rd-order polynomial curve (dashed lines), and when Λ is high, b_f/f_n increases sharply, indicating the strengthening of nonlinear effects.

CONCLUSIONS AND FUTURE WORK

The onset of large-amplitude LCOs has been shown to depend on the static characteristics of the wing. The non-monotonic variation of the SN point has been attributed to the competition between a destabilizing mechanism brought by the stabilization of LEVs and a stabilizing mechanism caused by fluid damping. We have characterized the fluid damping for swept wings in quiescent water. A fluid damping scaling has been proposed and it has been shown that wings with higher sweep angles experience higher fluid damping. Our hypothesis that the system becomes more unstable because LEVs are stabilized by the wing sweep requires more experimental evidence and the next step is to characterize the effect of wing sweep on the LEV stability using 3D PIV experiments.

References

[1] Menon, K. and Mittal, R. Flow physics and dynamics of flow-induced pitch oscillations of an airfoil. *J. Fluid Mech.* **877**: 582–613, 2019.

[2] Zhu, Y., Su, Y. and Breuer, K. Non-Linear Stability Boundaries of an Elastically-Mounted Pitching Wing. *AIAA SciTech Forum*, AIAA 2020-1052, 2020.

[3] Onoue, K. and Breuer, K. A scaling for vortex formation on swept and unswept pitching wings. *J. Fluid Mech.* **832**: 697–720, 2017.

[4] Wong, J. G. and Rival, D. E. Determining the relative stability of leading-edge vortices on nominally two-dimensional flapping profiles. *J. Fluid Mech.* **766**: 611–625, 2015.

Downloaded from https://www.cambridge.org/core. Brown University Library, on 22 Jul 2021 at 17:10:36, subject to the Cambridge Core terms of use, available at https://www.cambridge.org/core/terms. https://doi.org/10.1017/jfm.2021.578

J. Fluid Mech. (2021), *vol*. 923, R2, doi:10.1017/jfm.2021.578



Nonlinear fluid damping of elastically mounted pitching wings in quiescent water

Yuanhang Zhu[1],†, **Varghese Mathai**[2] **and Kenneth Breuer**[1]

[1]Center for Fluid Mechanics, School of Engineering, Brown University, Providence, RI 02912, USA
[2]Department of Physics, University of Massachusetts, Amherst, MA 01003, USA

(Received 30 April 2021; revised 30 April 2021; accepted 21 June 2021)

We experimentally study the nonlinear fluid damping of a rigid but elastically mounted pitching wing in the absence of a free-stream flow. The dynamics of the elastic mount are simulated using a cyber-physical system. We perturb the wing and measure the fluid damping coefficient from damped oscillations over a large range of pitching frequencies, pitching amplitudes, pivot locations and sweep angles. A universal fluid damping scaling is proposed to incorporate all these parameters. Flow fields obtained using particle image velocimetry are analysed to explain the nonlinear behaviours of the fluid damping.

Key words: flow-structure interactions, vortex dynamics

1. Introduction

The interaction between elastically mounted pitching wings and unsteady flows is central to many applications. With a free-stream flow, this interaction can lead to self-sustained, flow-induced oscillations, which have been studied for understanding classic aeroelastic behaviour (Dowell *et al.* 1989; Dugundji 2008), as well as in developing oscillating foil energy harvesting devices (Xiao & Zhu 2014; Young, Lai & Platzer 2014). Without a free stream, but with prescribed heaving or flapping (i.e. hovering), the passive flow-induced pitching motions are used in modelling the thrust generation and manoeuvring in animal flight (Wang 2005; Bergou, Xu & Wang 2007; Shinde & Arakeri 2013; Kang & Shyy 2014; Beatus & Cohen 2015).

One of the critical parameters that govern the flow–structure interactions of passively pitching wings is the fluid damping. According to the semi-empirical Morison equation (Morison, Johnson & Schaaf 1950), the total fluid force exerted on a wing submerged in unsteady viscous fluid can be divided into two parts – the force associated with fluid inertia (i.e. the added mass force), which is in phase with acceleration (Brennen 1982; Corkery, Babinsky & Graham 2019), and the force induced by vortices in the flow (i.e. the fluid

† Email address for correspondence: yuanhang_zhu@brown.edu

© The Author(s), 2021. Published by Cambridge University Press

Downloaded from https://www.cambridge.org/core. Brown University Library, on 22 Jul 2021 at 17:10:36, subject to the Cambridge Core terms of use, available at https://www.cambridge.org/core/terms. https://doi.org/10.1017/jfm.2021.578

damping force), which is in phase with velocity (Shih & Buchanan 1971; Kang & Shyy 2014; Su & Breuer 2019). While the structural damping force is typically proportional to velocity because of the constant structural damping coefficient, the fluid damping force is expected to scale quadratically with velocity (Morison *et al.* 1950; Keulegan & Carpenter 1958), and owing to this nonlinearity, the fluid damping coefficient is usually obtained empirically as a function of the reduced frequency, the Reynolds number, the oscillation amplitude, etc. (Shih & Buchanan 1971). For pitching flexible wings (Alben 2008) and heaving membrane wings (Tzezana & Breuer 2019), the fluid damping coefficient is found to scale inversely with the oscillation frequency.

For elastically mounted pitching wings with a free stream, the interplay between the fluid damping and the structural damping governs the flow-induced oscillation. By mapping out the cycle-averaged energy transfer between the elastic system and the ambient fluid using prescribed kinematics, Menon & Mittal (2019) and Zhu, Su & Breuer (2020) showed that the energy injected by the negative fluid damping must be equal to the energy dissipated by the positive structural damping in order for the flow-induced oscillations to sustain. In other words, the total damping of the system must be zero (Dugundji 2008). The negative fluid damping arises primarily from the formation and shedding of dynamic stall vortices (McCroskey 1982; Corke & Thomas 2015). In the absence of a free stream, however, the fluid damping becomes positive and counteracts the pitching motion because of the drag effect. With both the fluid damping and the structural damping being positive, any perturbations to the system will be damped out. However, little is known about how the fluid damping shapes the damped oscillations, and understanding this is of critical importance for understanding the fluid–structure interactions of elastically mounted pitching wings under external perturbations such as gusts.

In the present study, we use laboratory experiments to characterise the fluid damping of elastically mounted pitching wings in quiescent water, with the elastic mount simulated using a cyber-physical system (§ 2). We perform 'ring down' experiments to extract the fluid damping (§ 3.1). The effects of many parameters are investigated, including the effects of the pitching frequency, the pitching amplitude, the pivot location and the sweep angle (§ 3.2). We propose a universal fluid damping scaling to incorporate these parameters (§ 3.3), and correlate the nonlinear behaviour of the fluid damping with the dynamics of the vortical structures measured using particle image velocimetry (§ 3.4). Finally, the key findings are summarised in § 4.

2. Experimental set-up

Figure 1(*a*) shows a schematic of the experimental set-up. We conduct all the experiments in the Brown University free-surface water tunnel (test section width $\times$ depth $\times$ length $=$ 0.8 m $\times$ 0.6 m $\times$ 4.0 m), with the flow speed kept at zero ($U_\infty = 0$ m s^{-1}). A NACA 0012 wing, made of clear acrylic, is mounted vertically in the tunnel, with an endplate on the top to skim surface waves and eliminate wingtip vortices at the root. The wing is connected to a six-axis force/torque transducer (ATI 9105-TIF-Delta-IP65), which measures the fluid torque τ_f exerted on the wing. This τ_f is then fed into the cyber-physical system (CPS). Depending on the input virtual structural parameters, specifically the torsional stiffness k_v, damping b_v and inertia I_v, the CPS calculates the pitching position of the wing and outputs the signal to the servo motor (Parker SM233AE). An optical encoder (US Digital E3-2500) which is independent of the CPS is used to measure the pitching position θ. The CPS is operated at 4000 Hz to minimise any phase delay between the input τ_f and the output θ. A detailed explanation of the CPS can be found in Zhu *et al.* (2020).

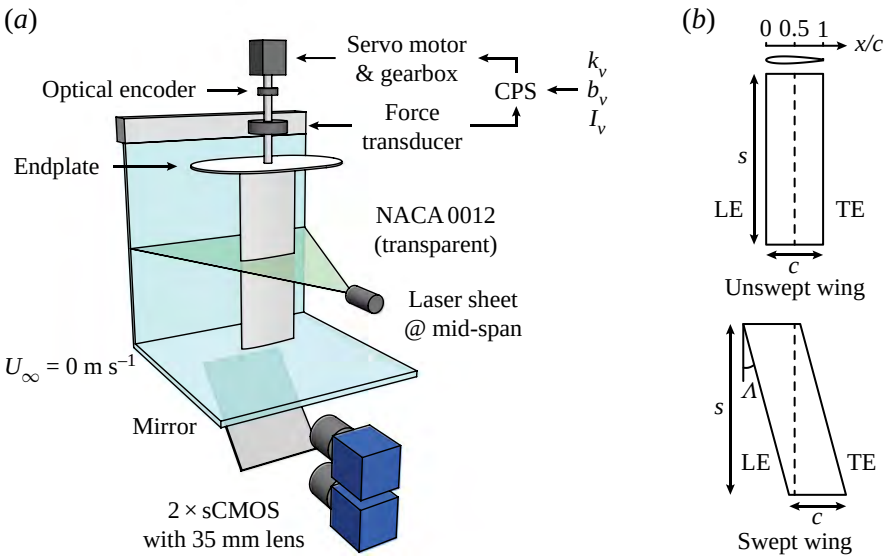


Figure 1. (*a*) A schematic of the experimental set-up. The structural dynamics of the wing is simulated by a CPS. (*b*) Sketches of unswept and swept wings. The leading edge (LE) and the trailing edge (TE) are parallel. Dashed lines represent the pivot axis.

We use two-dimensional particle image velocimetry (PIV) to measure the flow field around the wing. The flow is seeded using 50 μm diameter hollow ceramic spheres and illuminated by a laser sheet at the mid-span plane. The laser sheet is generated by a double-pulse Nd:YAG laser (532 nm, Quantel EverGreen) with LaVision sheet optics. The transparent wing enables flow field measurements on both sides of the wing. Due to the limitation of space beneath the tunnel, a 45° mirror is used to reflect the images into two co-planar sCMOS cameras (LaVision). We use the DaVis software (LaVision) to calculate (two passes at 64 × 64 pixels, two passes at 32 × 32 pixels, both with 50 % overlap) and stitch the velocity fields from the two cameras to form a field of view of $3.2c \times 3.2c$, where c is the chord length of the wing.

Figure 1(*b*) sketches the two types of wings we use in the present study. For the unswept wing, a wing holder mechanism (not shown) enables the pivot axis to be adjusted between $x/c = 0$ and $x/c = 1$ with a step size of 0.125. For the swept wings, the sweep angle Λ is defined as the angle between the leading edge and the vertical axis. Four swept wings with $\Lambda = 10°$, 15°, 20° and 25° are used. As shown in the figure, the pivot axis of swept wings is a vertical line passing through the mid-chord point ($x/c = 0.5$) of the mid-span plane. All the wings have a span of $s = 0.3$ m and a chord length of $c = 0.1$ m, which results in an aspect ratio of $AR = 3$.

The governing equation of the system is

$$I\ddot{\theta} + b\dot{\theta} + k\theta = \tau_f, \tag{2.1}$$

where θ, $\dot{\theta}$ and $\ddot{\theta}$ are the angular position, velocity and acceleration, respectively, while I, b and k are the effective inertia, damping and stiffness of the system. The effective inertia I is the sum of the virtual inertia I_v, which we prescribe with the CPS, and the physical inertia I_p of the wing (i.e. $I = I_v + I_p$). The effective damping b equals the virtual damping b_v (i.e. $b = b_v$) because the friction in the system is negligible. The effective stiffness k equals the virtual stiffness (i.e. $k = k_v$). The quantity τ_f is the nonlinear fluid torque experienced by the wing, which can be divided into the added mass torque, $\tau_a = -I_a\ddot{\theta}$, where I_a is the added fluid inertia, and the fluid damping torque, for simplicity $\tau_b = -b_f\dot{\theta}$, where b_f is the

Downloaded from https://www.cambridge.org/core. Brown University Library, on 22 Jul 2021 at 17:10:36, subject to the Cambridge Core terms of use, available at https://www.cambridge.org/core/terms. https://doi.org/10.1017/jfm.2021.578

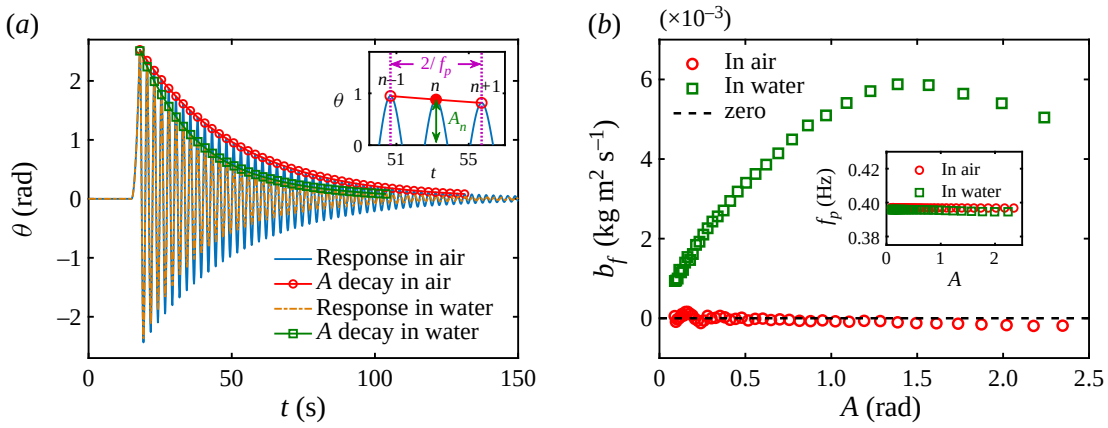


Figure 2. (*a*) System response and amplitude decay in a typical 'ring down' test, where an elastically mounted unswept wing ($\Lambda = 0^\circ$) pivots around the mid-chord ($x/c = 0.5$) at a frequency of $f_p = 0.40$ Hz. The inset shows the measurements of the pitching amplitude A_n and the pitching frequency f_p of the nth peak. The fluid damping b_f at A_n is extracted by fitting an exponential curve (i.e. the red solid line) to the three adjacent peaks. (*b*) Extracted b_f in air and in water. The zero value is indicated by the black dashed line. The inset compares the measured pitching frequency f_p in air and in water.

fluid damping coefficient (see § 1). Note that b_f is expected to be a function of $\dot{\theta}$ (Mathai *et al.* 2019). Equation (2.1) can thus be rearranged as

$$(I + I_a)\ddot{\theta} + (b + b_f)\dot{\theta} + k\theta = 0. \tag{2.2}$$

After a perturbation of amplitude A_0 is applied at time t_0, the damped oscillations of the system can be described as

$$\theta = A_0 \mathrm{e}^{-\gamma(t-t_0)} \cos\left[2\pi f_p (t - t_0)\right], \tag{2.3}$$

where

$$\gamma = \frac{b + b_f}{2(I + I_a)} \quad \text{and} \quad f_p = \frac{1}{2\pi}\sqrt{\frac{k}{I + I_a} - \gamma^2}. \tag{2.4a,b}$$

3. Results and discussion

3.1. *Extracting the fluid damping from 'ring down' experiments*

We conduct 'ring down' experiments to measure the fluid damping experienced by elastically mounted pitching wings. In the 'ring down' experiment, a short-time constant-torque impulse is applied to the CPS as the perturbation, after which the system response and the amplitude decay of the wing are recorded and analysed. Figure 2(*a*) shows the results from a typical 'ring down' experiment. In this specific case, we use an unswept wing ($\Lambda = 0^\circ$) which pivots around the mid-chord ($x/c = 0.5$) at a frequency of $f_p = 0.40$ Hz. We conduct the 'ring down' experiment twice – once in air and once in water. The pitching amplitude of the wing decays faster in water than in air, indicating a higher total damping in water.

To quantify this amplitude decay, the positive peaks of the system response are identified. As shown in the inset, the amplitude of the nth peak is denoted by A_n, and the corresponding pitching frequency is measured as $f_p = 2/(t_{n+1} - t_{n-1})$. To measure the total damping $b + b_f$ at amplitude A_n, we fit an exponential, $y = \alpha \mathrm{e}^{-\gamma t}$, to the three adjacent peaks, $n - 1$, n and $n + 1$, and extract the corresponding γ (see (2.3)). Now the

Downloaded from https://www.cambridge.org/core. Brown University Library, on 22 Jul 2021 at 17:10:36, subject to the Cambridge Core terms of use, available at https://www.cambridge.org/core/terms. https://doi.org/10.1017/jfm.2021.578

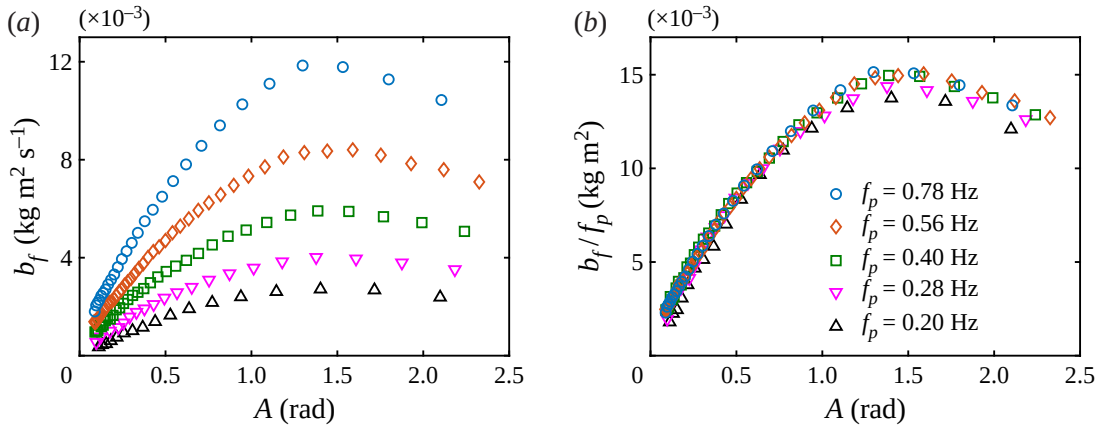


Figure 3. (*a*) Extracted fluid damping b_f at different pitching frequencies for $x/c = 0.5$. (*b*) A frequency scaling for the fluid damping which collapses b_f at different f_p into one curve. Note that panels (*a*) and (*b*) share the same legend.

only unknown in (2.4*b*) is the added mass, I_a. After obtaining I_a, we calculate the fluid damping, b_f, using (2.4*a*) (Rao 1995). Since f_p and γ are both measured, I_a and b_f are also measured quantities. Moreover, both I_a and b_f are cycle-averaged, meaning they cannot reflect the instantaneous variation of the fluid inertia and damping. The values of the measured fluid damping, b_f, in air and water are compared in figure 2(*b*). Since τ_f in (2.1) is negligible in air as compared to other forces in the equation, b_f stays near zero, which is indicated by the good agreement between the red circles and the black dashed line. As shown by the green squares, b_f in water is significant because of the existence of the fluid damping torque, τ_b. It is also observed that b_f in water increases non-monotonically with A. This nonlinear behaviour will be revisited later in § 3.4. The inset of figure 2(*b*) shows the measured pitching frequency, f_p, in both air and water. Because of the combined effect of the fluid inertia and damping, we see that f_p is slightly lower in water than in air.

3.2. *Frequency scaling of the fluid damping*

We repeat the 'ring down' experiment for the unswept wing ($\Lambda = 0°$) pivoting at the mid-chord, $x/c = 0.5$, and change the pitching frequency by tuning the virtual inertia, I_v, and the virtual stiffness, k_v, while keeping the virtual damping b_v constant (Onoue & Breuer 2016, 2017). Figure 3(*a*) shows the extracted fluid damping, b_f. (Note that figures 3(*a*) and 3(*b*) share the same legend.) We observe that b_f increases monotonically with the pitching frequency, f_p, and that the trend of b_f remains consistent for all frequencies. This agrees with the observations of Keulegan & Carpenter (1958) and Shih & Buchanan (1971) for heaving rigid plates, where the fluid damping coefficient scales inversely with the oscillation period. As we discussed earlier, b_f derives from the fluid damping torque τ_b, which depends strongly on the vortex-induced forces on the wing (Kang & Shyy 2014). Onoue & Breuer (2016, 2017) have shown that the circulation of leading-edge vortices scales with the strength of the feeding shear-layer velocity. In our case, without a free-stream flow, the feeding shear-layer velocity equals the leading-/trailing-edge velocity, which is proportional to f_p. Based on this, we divide b_f by f_p (figure 3*b*). It is seen that with this scaling, all of the fluid damping curves collapse nicely.

We extend this frequency scaling to unswept wings with different pivot axes (figure 4*a*) and to swept wings with different sweep angles (figure 4*b*). For comparison, in

Downloaded from https://www.cambridge.org/core. Brown University Library, on 22 Jul 2021 at 17:10:36, subject to the Cambridge Core terms of use, available at https://www.cambridge.org/core/terms. https://doi.org/10.1017/jfm.2021.578

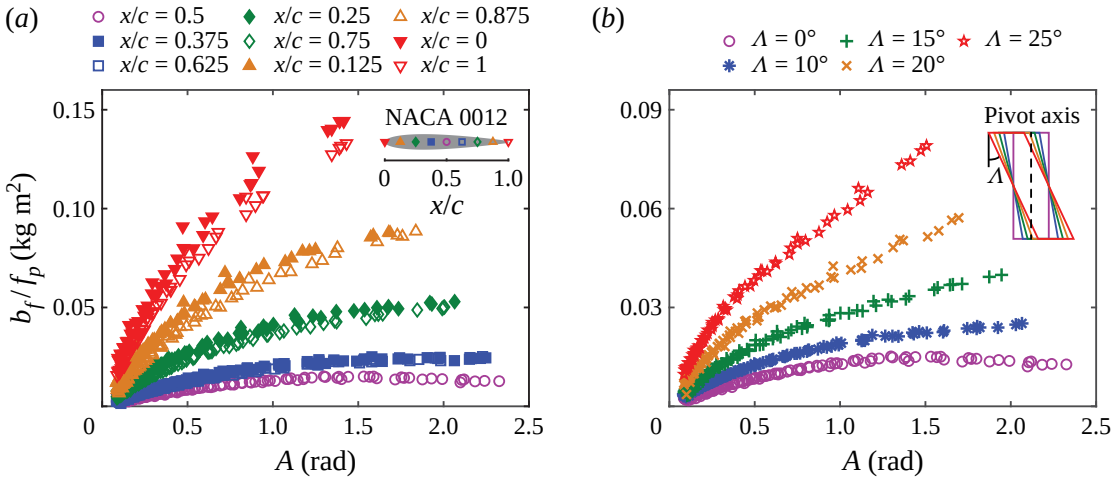


Figure 4. (*a*) Values of b_f/f_p for an unswept wing ($\Lambda = 0°$) pivoting at $x/c = 0$ to $x/c = 1$ with a step size of 0.125. The pivot location for each dataset is shown by the inset. (*b*) Values of b_f/f_p for swept wings with $\Lambda = 0°$, 10°, 15°, 20° and 25°. The inset shows side views of the five swept wings, and the dashed line indicates the pivot axis. The colours of the wings correspond to the colours of the b_f/f_p curves in the figure. The purple circles in (*a*,*b*) are replotted from figure 3(*b*). Note that each dataset in (*a*,*b*) includes five different f_p.

figure 4(*a*,*b*) we include the previous results (figure 3*b*) using purple circles. Note that each symbol shape in figure 4 contains five different pitching frequencies: $f_p = 0.20$, 0.28, 0.40, 0.56 and 0.78 Hz.

For the unswept wing ($\Lambda = 0°$), we change the pivot axis from $x/c = 0$ to $x/c = 1$ with a step size of 0.125 (see the inset of figure 4*a*). We observe that b_f/f_p increases as the pivot axis is moved away from the mid-chord, $x/c = 0.5$. For pivot axes that are symmetric with respect to the mid-chord (i.e. $x/c = 0.375$ & 0.625, 0.25 & 0.75, 0.125 & 0.875 and 0 & 1), the values of b_f/f_p roughly overlap. The slight inconsistency between the b_f/f_p values for $x/c > 0.5$ and $x/c < 0.5$ comes from the asymmetry of the NACA 0012 wing geometry with respect to the mid-chord; we see that the scaled damping, b_f/f_p, is always slightly higher for $x/c < 0.5$. In these cases, the damping at the trailing edge dominates because of the higher velocity and longer moment arm, and it is stronger than in the cases when $x/c > 0.5$, where the leading-edge damping dominates. We will show in § 3.4 that this is due to differences in the vortex structures generated by the sharp and rounded geometries.

This frequency scaling, b_f/f_p, also holds for three-dimensional swept wings (figure 4*b*). Again, each curve includes data from five pitching frequencies. Here, the pivot axes of swept wings are kept as a vertical line passing through the mid-chord of the mid-span plane (see the inset of figure 4*b*). As Λ increases, the average pivot axes of the top and the bottom portion of the swept wing move away from the mid-chord, leading to the increase of the scaled damping, b_f/f_p, in a manner similar to that observed for unswept wings with different pivot locations (figure 4*a*). This argument will be revisited in the next section.

3.3. *Universal fluid damping scaling for unswept and swept wings*

Figure 4(*a*) indicates that the pivot axis plays an important role in determining the fluid damping of unswept wings. We extend the frequency scaling of b_f to take into account this effect. First, we divide the wing into two parts, the fore part from LE to the pivot axis with a chord length of c_{LE}, and the aft part from the pivot axis to TE with a chord length of c_{TE} (see the inset of figure 5 for an example when the wing pivots at $x/c = 0.5$). The Morison equation (Morison *et al.* 1950) indicates that the fluid damping force F scales

Downloaded from https://www.cambridge.org/core. Brown University Library, on 22 Jul 2021 at 17:10:36, subject to the Cambridge Core terms of use, available at https://www.cambridge.org/core/terms. https://doi.org/10.1017/jfm.2021.578

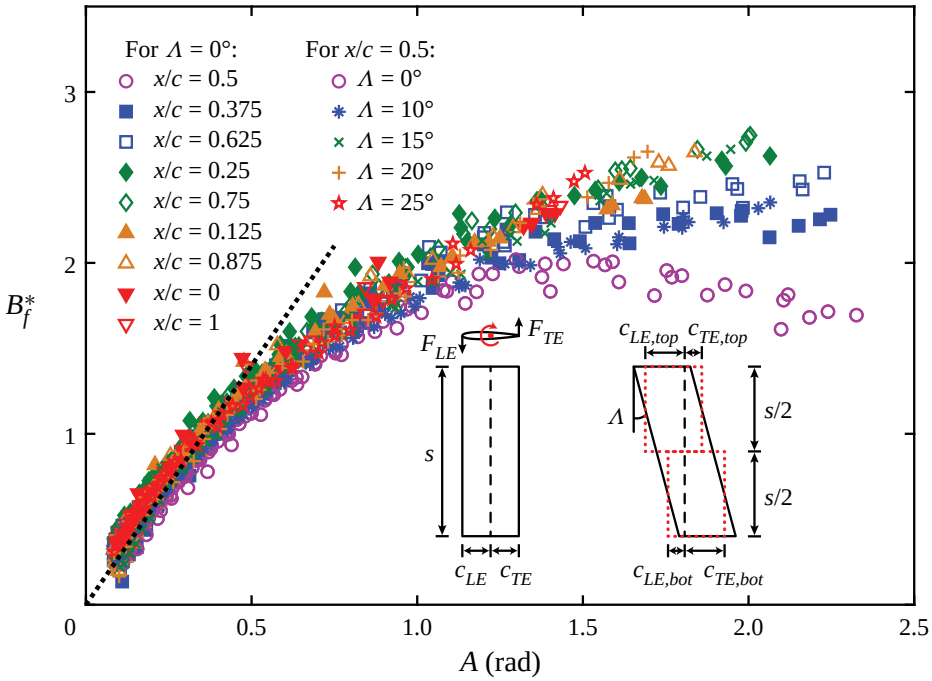


Figure 5. Non-dimensional fluid damping coefficient B_f^* versus pitching amplitude A for unswept wings pivoting at $x/c = 0$ to $x/c = 1$ and swept wings with sweep angles $\Lambda = 0^\circ$ to $\Lambda = 25^\circ$. The inset shows the definition of the leading-edge chord c_{LE} and the trailing-edge chord c_{TE}, with black dashed lines indicating the pivot axes. The black dotted line indicates the small-amplitude prediction for a drag coefficient of $C_D = 2.8$.

with $0.5\rho U^2 sc$, where ρ is the fluid density, $U \sim \dot{\theta} c$ is the characteristic velocity and sc is the wing area. We can express the total fluid damping torque as the sum of the torque exerted on the fore and aft portions of the wing,

$$\tau_b \sim K_{LE} F_{LE} c_{LE} + K_{TE} F_{TE} c_{TE}, \tag{3.1}$$

where the subscripts LE and TE refer to the leading- and trailing-edge contributions, and K_{LE} and K_{TE} are empirical factors that account for the subtle differences in the damping associated with the specific geometries of the leading and trailing edges (figure 4*a*). Since the differences are small, K_{LE} and K_{TE} should be close to one, and for consistency, their average value must equal one ($(K_{LE} + K_{TE})/2 = 1$).

Since the damped oscillations are observed to be near-sinusoidal (figure 2*a*), the average angular velocity is given by $4f_p A$. Simplifying, we arrive at an expression for the fluid damping:

$$b_f \sim 2\rho f_p A s (K_{LE} c_{LE}^4 + K_{TE} c_{TE}^4), \tag{3.2}$$

or, in non-dimensional form,

$$B_f^* \equiv \frac{b_f}{2\rho f_p s (K_{LE} c_{LE}^4 + K_{TE} c_{TE}^4)} \propto A. \tag{3.3}$$

For swept wings, because the pivot axis passes through $x/c = 0.5$ at the mid-span, the top half of the wing has an average pivot axis $x/c > 0.5$, while the bottom half has an average pivot axis $x/c < 0.5$. Ignoring three-dimensional effects, we approximate the swept wing by two 'equivalent' unswept wing segments. We choose not to divide the wing into a large number of narrow 'blade elements' (Glauert 1983), because the pivot axis of some elements near the wing root/tip for large sweep angles may lie outside the range

Downloaded from https://www.cambridge.org/core. Brown University Library, on 22 Jul 2021 at 17:10:36, subject to the Cambridge Core terms of use, available at https://www.cambridge.org/core/terms. https://doi.org/10.1017/jfm.2021.578

$x/c = [0, 1]$, where our scaling has not been tested. The inset of figure 5 shows how these two unswept wing segments are configured (rectangles with red dotted lines). Based on the wing geometry, we see that

$$\left.\begin{aligned} c_{LE,top} = c_{TE,bot} &= \frac{c}{2} + \frac{s}{4}\tan\Lambda, \\ c_{TE,top} = c_{LE,bot} &= \frac{c}{2} - \frac{s}{4}\tan\Lambda. \end{aligned}\right\} \tag{3.4}$$

Following the same analysis as for the unswept wing, and adding the fluid damping of the top and the bottom wing segments together, we find that the fluid damping for the full swept wing is given by

$$b_f \sim \rho f_p A s (K_{LE} c_{LE,top}^4 + K_{TE} c_{TE,top}^4 + K_{LE} c_{LE,bot}^4 + K_{TE} c_{TE,bot}^4). \tag{3.5}$$

If we define an effective leading-edge chord $c_{LE} = c_{LE,top} = c_{TE,bot}$ and an effective trailing-edge chord $c_{TE} = c_{TE,top} = c_{LE,bot}$, this scaling reduces to (3.2) with K_{LE} and K_{TE} cancelled out. This cancellation results because the effective pivot axes of the top and the bottom segments are symmetric about $x/c = 0.5$ at the mid-span, which averages out the slight differences in fluid damping experienced by the top and the bottom segments. For the same reason, K_{LE} and K_{TE} also cancel out in (3.3) for swept wings.

Figure 5 shows the non-dimensional fluid damping, B_f^*, as a function of the pitching amplitude, A, for unswept and swept wings. Here, we have used $K_{LE} = 0.95$ and $K_{TE} = 1.05$. We see that all of our measurements collapse remarkably well under the proposed scaling, especially for $A < 1.57$ (90°), despite the wide range of pitching frequencies ($f_p = 0.20$ Hz to $f_p = 0.78$ Hz), pivot axes ($x/c = 0$ to $x/c = 1$) and sweep angles ($\Lambda = 0°$ to $\Lambda = 25°$) tested in the experiments. In the small-amplitude limit ($A < 0.5$), B_f^* scales linearly with A, with a slope that corresponds to the drag coefficient, C_D. We note that $C_D \approx 2.8$, which is comparable to that of an accelerated normal flat plate (Ringuette, Milano & Gharib 2007). At higher pitching angles ($A > 0.5$), however, the linear approximation no longer holds and we see a decreasing slope of B_f^* as a function of A. This is presumably because the shed vortices no longer follow the rotating wing and the fluid force becomes non-perpendicular to the wing surface as A increases. For $A > 1.57$ (90°), the scaling works reasonably well except for the case $\Lambda = 0°$, $x/c = 0.5$, where a decreasing B_f^* is observed. In the next section, we will use insights from the velocity fields to explain this non-monotonic behaviour.

3.4. *Insights obtained from velocity fields*

To gain more insight regarding the nonlinear behaviour of B_f^*, we conduct two-dimensional PIV experiments to measure the surrounding flow fields of an unswept wing ($\Lambda = 0°$) with a prescribed pitching motion, $\theta = A\sin(2\pi f_p t)$. The results are shown in figure 6. The pitching frequency is kept at $f_p = 0.5$ Hz for all the cases, and the pitching amplitude is varied from $A = 0.52$ (30°) to $A = 2.09$ (120°) with a step size of 0.52 (30°). Two pivot axes are tested, $x/c = 0.5$ (figure 6*a–d*) and $x/c = 0.25$ (figure 6*e–h*). Note that the flow fields shown in figure 6 are not sequential. Instead, all the snapshots are taken right before $t/T = 0.25$ for different pitching amplitudes, where T is the pitching period. This specific time instant is chosen because it best reflects the difference in dynamics associated with the different pitching amplitudes and pivot axes.

For both pivot locations ($x/c = 0.5$ in figure 6(*a–d*) and $x/c = 0.25$ in figure 6(*e–h*)), the spanwise vorticity of the pitch-generated leading-edge vortex (LEV) and trailing-edge

Downloaded from https://www.cambridge.org/core. Brown University Library, on 22 Jul 2021 at 17:10:36, subject to the Cambridge Core terms of use, available at https://www.cambridge.org/core/terms. https://doi.org/10.1017/jfm.2021.578

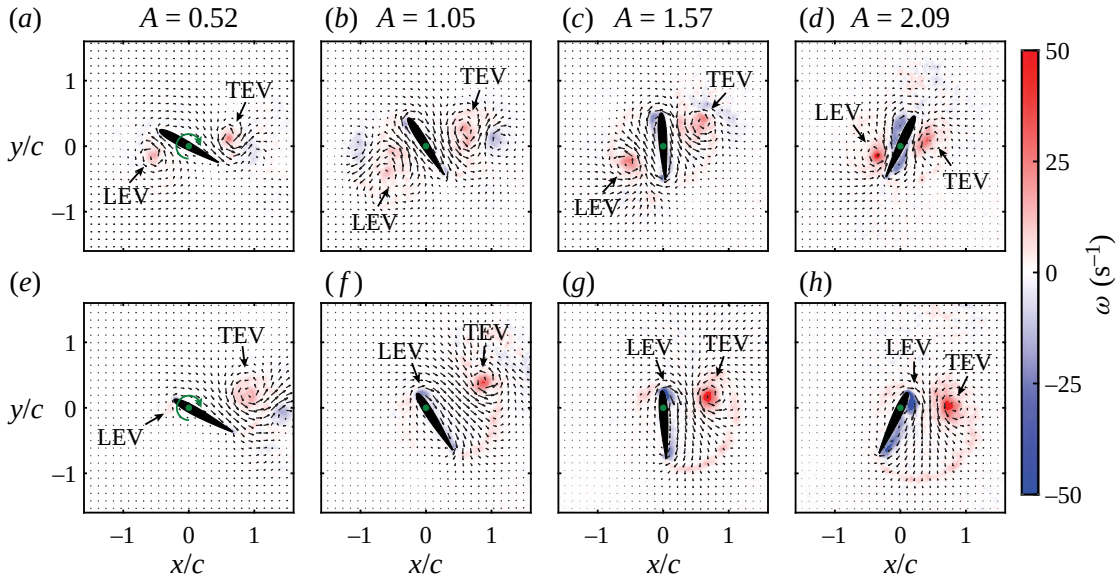


Figure 6. The PIV flow field measurements for an unswept wing undergoing prescribed sinusoidal pitching motions in quiescent water. (*a–d*) Pivot axis (shown by green dots) $x/c = 0.5$, pitching frequency $f_p = 0.5$ Hz, pitching amplitude $A = 0.52$ (30°), 1.05 (60°), 1.57 (90°) and 2.09 (120°). (*e–h*) Same as (*a–d*), except that the pivot axis is at $x/c = 0.25$. All the velocity fields are phase-averaged over 20 cycles. Only every fifth velocity vector is shown. Spanwise vorticity ω: positive (red), counterclockwise; negative (blue), clockwise. See supplementary material, available at https://doi.org/10.1017/jfm.2021.578, for the full movie.

vortex (TEV) increases with the pitching amplitude, A. This can be explained by the increase in the feeding shear-layer velocities associated with the higher pitching amplitudes (Onoue & Breuer 2016). The boundary vortices near the wing surface, which are related to the added mass effect (Corkery *et al.* 2019), also become more prominent because of the increase of the angular acceleration. When the wing pivots at $x/c = 0.5$ (figure 6*a–d*), the leading-edge velocity equals the trailing-edge velocity. As a result, the LEV and TEV are fairly symmetric about the pivot axis, with some subtle differences caused by the rounded and sharp edges, respectively. This confirms the arguments given earlier for the differences between the values of b_f/f_p for $x/c > 0.5$ and $x/c < 0.5$ (figure 4*a*). For $x/c = 0.25$ (figure 6*e–h*), however, the TEV is much more prominent than the LEV because of the higher trailing-edge velocity. Because of the low leading-edge velocity and the pitch-induced rotational flow, the sign of the LEV even reverses and becomes negative for $A = 1.05$ to $A = 2.09$ (figure 6*f–h*).

For both pivot locations, owing to the absence of a convective free stream and the existence of the pitch-induced rotational flow, the LEV and TEV (only the TEV for $x/c = 0.25$) are entrained closer to the wing surface as A increases. For $x/c = 0.5$, as shown in figure 6(*c*,*d*), the LEV moves towards the aft portion of the wing and the TEV moves towards the fore portion of the wing when $A \geqslant 1.57$ (90°). The torque generated by these two vortices, which counteracts the wing rotation for small A, now assists the rotation as the wing pitches up towards higher angular positions. This assist reduces the fluid drag experienced by the wing and thus lowers the fluid damping. This effect accounts for the non-monotonic behaviour of B_f^* for $x/c = 0.5$ (figure 5). For $x/c = 0.25$ (figure 6*g*,*h*), a similar scenario is observed, in which the TEV moves towards the fore portion of the wing and gets closer to the wing surface as A increases. However, because of the existence of a counter-rotating LEV, the TEV is not able to approach the wing surface as closely as in the $x/c = 0.5$ case. This explains why a flattening behaviour, rather than a non-monotonic

Downloaded from https://www.cambridge.org/core. Brown University Library, on 22 Jul 2021 at 17:10:36, subject to the Cambridge Core terms of use, available at https://www.cambridge.org/core/terms. https://doi.org/10.1017/jfm.2021.578

Downloaded from https://www.cambridge.org/core. Brown University Library, on 22 Jul 2021 at 17:10:36, subject to the Cambridge Core terms of use, available at https://www.cambridge.org/core/terms. https://doi.org/10.1017/jfm.2021.578

trend of B_f^*, is observed for $x/c = 0.25$ and presumably for other pivot locations at high pitching amplitudes.

4. Conclusions

By utilising a cyber-physical control system to create an elastically mounted pitching wing, we have experimentally measured the nonlinear fluid damping associated with vortices shed from a bluff body. A theoretical scaling has been proposed and validated, based on the Morison equation, which incorporates the frequency, amplitude, pivot location and sweep angle. The nonlinear behaviour of the scaled fluid damping has been correlated with the velocity fields measured using particle image velocimetry.

One should note that our scaling may not be applicable for instantaneous fluid damping, because the damping characterised in the present study is cycle-averaged over near-sinusoidal oscillations. In addition, we have not considered three-dimensional effects, which are present due to the wing tip flows. Incorporating these may further improve the collapse of the fluid damping coefficient, B_f^* (figure 5). Lastly, only qualitative analysis of the flow field has been performed thus far (in § 3.4). To get more accurate correspondence between the fluid damping and the flow dynamics, quantitative analysis of the vortex trajectory and circulation is needed, which will be the focus of future study.

Despite these limitations, the proposed scaling has been shown to collapse the data over a wide range of operating conditions ($f_p = 0.20$ Hz to $f_p = 0.78$ Hz and $A = 0$ to $A = 2.5$) for both unswept ($x/c = 0$ to $x/c = 1$) and swept wings ($\Lambda = 0^\circ$ to $\Lambda = 25^\circ$). It can be used to predict damping associated with shed vortices, and thus benefit the future modelling of a wide variety of flows, including unswept and swept wings in unsteady flows as well as other bluff body geometries. The universality of this scaling reinforces the underlying connection between swept wings and unswept wings with different pivot locations. In addition, the results presented in this study are of potential value as a source of experimental data for validation and comparison of future theoretical/computational models.

Supplementary movie. Supplementary movie is available at https://doi.org/10.1017/jfm.2021.578.

Funding. This work is funded by Air Force Office of Scientific Research, grant FA9550-18-1-0322, managed by Dr G. Abate. The authors thank members of the Breuer Lab for helpful discussions and insights.

Declaration of interests. The authors report no conflict of interest.

Author ORCIDs.
Yuanhang Zhu https://orcid.org/0000-0002-2080-1142;
Varghese Mathai https://orcid.org/0000-0001-7296-6056;
Kenneth Breuer https://orcid.org/0000-0002-5122-2231.

References

Alben, S. 2008 Optimal flexibility of a flapping appendage in an inviscid fluid. *J. Fluid Mech.* **614**, 355–380.
Beatus, T. & Cohen, I. 2015 Wing-pitch modulation in maneuvering fruit flies is explained by an interplay between aerodynamics and a torsional spring. *Phys. Rev.* E **92** (2), 022712.
Bergou, A.J., Xu, S. & Wang, Z.J. 2007 Passive wing pitch reversal in insect flight. *J. Fluid Mech.* **591**, 321–337.
Brennen, C.E. 1982 A review of added mass and fluid inertial forces. *Tech. Rep.* CR82.010. Naval Civil Engineering Laboratory.
Corke, T.C. & Thomas, F.O. 2015 Dynamic stall in pitching airfoils: aerodynamic damping and compressibility effects. *Annu. Rev. Fluid Mech.* **47**, 479–505.

CORKERY, S.J., BABINSKY, H. & GRAHAM, W.R. 2019 Quantification of added-mass effects using particle image velocimetry data for a translating and rotating flat plate. *J. Fluid Mech.* **870**, 492–518.

DOWELL, E.H., CURTISS, H.C., SCANLAN, R.H. & SISTO, F. 1989 *A Modern Course in Aeroelasticity*. Springer.

DUGUNDJI, J. 2008 Some aeroelastic and nonlinear vibration problems encountered on the journey to Ithaca. *AIAA J.* **46** (1), 21–35.

GLAUERT, H. 1983 *The Elements of Aerofoil and Airscrew Theory*. Cambridge University Press.

KANG, C.-K. & SHYY, W. 2014 Analytical model for instantaneous lift and shape deformation of an insect-scale flapping wing in hover. *J. R. Soc. Interface* **11** (101), 20140933.

KEULEGAN, G.H. & CARPENTER, L.H. 1958 Forces on cylinders and plates in an oscillating fluid. *J. Res. Natl Bur. Stand.* **60** (5), 423–440.

MATHAI, V., LOEFFEN, L.A.W.M., CHAN, T.T.K. & WILDEMAN, S. 2019 Dynamics of heavy and buoyant underwater pendulums. *J. Fluid Mech.* **862**, 348–363.

MCCROSKEY, W.J. 1982 Unsteady airfoils. *Annu. Rev. Fluid Mech.* **14** (1), 285–311.

MENON, K. & MITTAL, R. 2019 Flow physics and dynamics of flow-induced pitch oscillations of an airfoil. *J. Fluid Mech.* **877**, 582–613.

MORISON, J.R., JOHNSON, J.W. & SCHAAF, S.A. 1950 The force exerted by surface waves on piles. *J. Petrol. Tech.* **2** (05), 149–154.

ONOUE, K. & BREUER, K.S. 2016 Vortex formation and shedding from a cyber-physical pitching plate. *J. Fluid Mech.* **793**, 229–247.

ONOUE, K. & BREUER, K.S. 2017 A scaling for vortex formation on swept and unswept pitching wings. *J. Fluid Mech.* **832**, 697–720.

RAO, S.S. 1995 *Mechanical Vibrations*. Addison-Wesley.

RINGUETTE, M.J., MILANO, M. & GHARIB, M. 2007 Role of the tip vortex in the force generation of low-aspect-ratio normal flat plates. *J. Fluid Mech.* **581**, 453–468.

SHIH, C.C. & BUCHANAN, H.J. 1971 The drag on oscillating flat plates in liquids at low Reynolds numbers. *J. Fluid Mech.* **48** (2), 229–239.

SHINDE, S.Y. & ARAKERI, J.H. 2013 Jet meandering by a foil pitching in quiescent fluid. *Phys. Fluids* **25** (4), 041701.

SU, Y. & BREUER, K.S. 2019 Resonant response and optimal energy harvesting of an elastically mounted pitching and heaving hydrofoil. *Phys. Rev. Fluids* **4** (6), 064701.

TZEZANA, G.A. & BREUER, K.S. 2019 Thrust, drag and wake structure in flapping compliant membrane wings. *J. Fluid Mech.* **862**, 871–888.

WANG, Z.J. 2005 Dissecting insect flight. *Annu. Rev. Fluid Mech.* **37**, 183–210.

XIAO, Q. & ZHU, Q. 2014 A review on flow energy harvesters based on flapping foils. *J. Fluids Struct.* **46**, 174–191.

YOUNG, J., LAI, J.C.S. & PLATZER, M.F. 2014 A review of progress and challenges in flapping foil power generation. *Prog. Aerosp. Sci.* **67**, 2–28.

ZHU, Y., SU, Y. & BREUER, K.S. 2020 Nonlinear flow-induced instability of an elastically mounted pitching wing. *J. Fluid Mech.* **899**, A35.

Downloaded from https://www.cambridge.org/core. Brown University Library, on 22 Jul 2021 at 17:10:36, subject to the Cambridge Core terms of use, available at https://www.cambridge.org/core/terms. https://doi.org/10.1017/jfm.2021.578

AIAA SciTech Forum
January 3-7, 2022, San Diego, CA & Virtual
AIAA SCITECH 2022 Forum

10.2514/6.2022-2328

Check for updates

Aeroelastic Instability Boundaries of Pitching Swept Wings

Yuanhang Zhu * and Kenneth Breuer †
Center for Fluid Mechanics, School of Engineering, Brown University, Providence, RI 02912

We experimentally study the aeroelastic instability boundaries of pitching unswept and swept wings in a water tunnel at a Reynolds number of 50,000. The structural dynamics of the wings are simulated using a cyber-physical control system. We show that the Hopf point of flow-induced limit-cycle oscillations (LCOs) depends largely on the static characteristics of the wing. The saddle-node point of LCOs is found to change non-monotonically with the sweep angle, which we attribute to the non-monotonic power transfer between the ambient fluid and the elastic mount. An optimal sweep angle is observed to promote LCOs and thus enhance the power extraction performance. The frequency response of the system reveals a structural-hydrodynamic oscillation mode for wings with relatively high sweep angles. Lastly, three-dimensional flow structures measured by multi-layer stereoscopic particle image velocimetry are analyzed to explain the differences in power extraction for unswept and swept wings.

Downloaded by Kenny Breuer on January 2, 2022 | http://arc.aiaa.org | DOI: 10.2514/6.2022-2328

I. Nomenclature

W, D, L	=	width, depth, length of the water tunnel [m]
U_∞	=	free-stream velocity [m/s]
s, c	=	wing span, wing chord [m]
Λ	=	sweep angle [°]
$\theta, \dot{\theta}, \ddot{\theta}$	=	angular position [rad], velocity [rad/s], acceleration [rad/s^2]
τ_f	=	fluid torque [N·m]
I_p, I_v, I	=	physical inertia, virtual inertia, effective inertia [kg·m^2]
b_v, b	=	virtual structural damping, effective structural damping [kg·m^2/s]
k_v, k	=	virtual stiffness, effective stiffness [kg·m^2/s^2]
ρ, μ	=	water density [kg/m^3], water dynamic viscosity [kg/(m·s)]
ω_z	=	spanwise vorticity [1/s]
$\lvert A\rvert$	=	pitching amplitude [rad]
$\lvert\overline{A}\rvert$	=	static divergence angle [rad]
f_s, f_p	=	structural frequency, pitching frequency [Hz]
f_s^*, f_p^*	=	non-dimensional structural frequency, pitching frequency
Re, Ca	=	Reynolds number, Cauchy number
I^*, b^*, k^*, U^*	=	non-dimensional inertia, damping, stiffness, velocity
τ^*, τ_f^*	=	non-dimensional torque, fluid torque

II. Introduction

The fluid-structure interaction (FSI) of elastically mounted pitching wings finds application in many related fields. Under certain structural parameters, large-amplitude flow-induced oscillations may lead to catastrophic aeroelastic failure [1]. On the other hand, these oscillations can be beneficial if they are exploited for harvesting kinetic energy from tidal or river flows [2–4]. Moreover, understanding the instability boundaries of passively pitching wings is critical for studying animal flight [5–8] and developing flapping-wing micro air vehicles (MAVs) [9, 10]. The flow-induced oscillations of passively pitching wings originate from the two-way coupling between the structural dynamics of the elastic mount and the nonlinear fluid force experienced by the wing. The nonlinear fluid force is modulated by the formation, growth and shedding of a strong leading-edge vortex (LEV) [11, 12]. Therefore, the dynamics and stability

*Graduate Student, Center for Fluid Mechanics, School of Engineering, Brown University, Providence, RI 02912, AIAA Student Member.
†Professor of Engineering, Center for Fluid Mechanics, School of Engineering, Brown University, Providence, RI 02912, AIAA Associate Fellow.

Copyright © 2022 by Yuanhang Zhu, Kenneth Breuer. Published by the American Institute of Aeronautics and Astronautics, Inc., with permission.

of LEVs play an important role in shaping the flow-induced oscillations and thus determining the stability boundaries of passively pitching wings.

Swept wings are commonly seen for flapping-wing fliers and swimmers in nature [13–15]. It is believed that the wing sweep can stabilize leading-edge vortices through induced spanwise flows [13] and thus enhance lift generation. Wong and Rival [16] have shown both theoretically and experimentally that the wing sweep improves relative LEV stability by enhancing the spanwise vorticity transport. Moreover, it was shown that vortex stretching and the increase of reduced frequency also promote LEV stability. Onoue and Breuer [17] experimentally studied cyber-physically pitching unswept and swept wings and proposed a universal scaling for LEV formation time and circulation, which incorporated the effects of the pitching frequency, the pivot location and the sweep angle. The vortex circulation was demonstrated to be independent of the three-dimensional vortex dynamics. In addition, they concluded that the stability of LEVs can be improved by moderating the LEV circulation through vorticity annihilation, which is largely governed by the shape of the leading-edge sweep. Visbal and Garmann [18] numerically studied the effect of wing sweep on the dynamic stall of pitching three-dimensional wings and reported that the wing sweep can modify the the LEV structures and change the net aerodynamic damping of the wing.

These studies have characterized the relationship between the wing sweep and the LEV stability/structure, however, the effect of sweep angle on the stability characteristics of elastically mounted wings still remains elusive. In the present study, we aim to address this problem by extending the methodology developed in Zhu et al. [19] to swept wings and employing stereoscopic particle image velocimetry to quantify the three-dimensional flow fields. We use a cyber-physical system to simulate the elastic mount of the wings (§III). The static moment coefficients of the wings are measured (§IV.A) before we characterize the amplitude response (§IV.B) and the frequency response (§IV.C) of the system. We correlate the onset of flow-induced oscillations with the static characteristics of the wing (§IV.D) and use an energy approach to explain the nonlinear stability boundaries (§IV.E). Finally, we analyze the three-dimensional flow structures (§IV.F) to explain the difference in power extraction for unswept and swept wings. All the key findings are summarized in §V.

Downloaded by Kenny Breuer on January 2, 2022 | http://arc.aiaa.org | DOI: 10.2514/6.2022-2328

III. Experimental setup and non-dimensional parameters

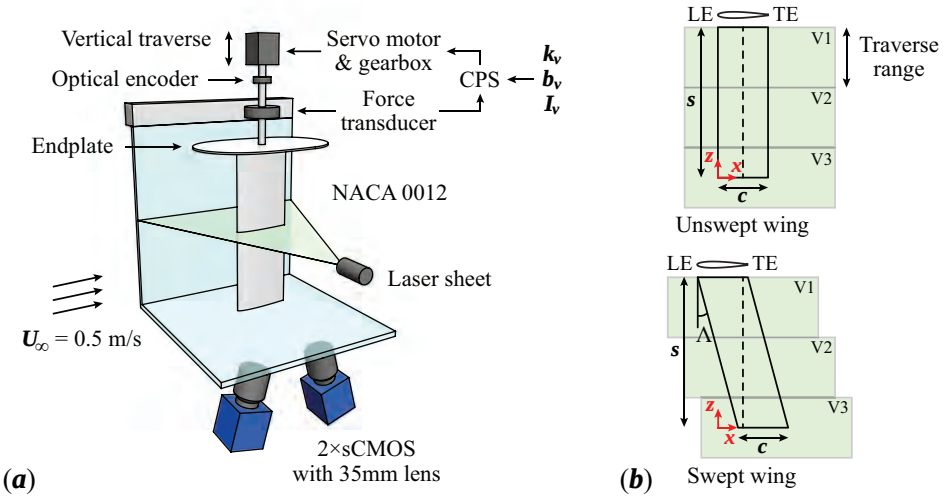


Fig. 1 (*a*) A schematic of the experimental setup. (*b*) Sketches of unswept and swept wings used in the experiments. The pivot axes are indicated by dashed lines. The green blocks represent volumes traversed by the laser sheet for 3D phase-averaged stereoscopic PIV measurements.

A. Cyber-physical system and wing geometry

We perform all the experiments in the Brown University free-surface water tunnel, which has a test section of $W \times D \times L = 0.8\text{ m} \times 0.6\text{ m} \times 0.4\text{ m}$. The free-stream velocity is fixed at $U_\infty = 0.5$ m/s throughout all the experiments.

Fig. 1(a) shows a schematic of the experimental setup. Unswept and swept NACA 0012 wings are mounted vertically in the tunnel, with an endplate on the top to skim surface waves and eliminate tip vortices at the root. The wing tip at the bottom does not have an endplate. The wings are connected to a six-axis force/torque transducer (ATI 9105-TIF-Delta-IP65) via a wing shaft. The shaft further connects the transducer to an optical encoder (US Digital E3-2500) and a servo motor (Parker SM233AE) coupled with a gearbox (Automation Direct PGCN23-0525). The force/torque transducer measures the fluid torque τ_f exerted on the wing and feed the value to the cyber-physical system (CPS) via a data acquisition (DAQ) board (National Instruments PCIe-6353). Based on the input virtual structural parameters (i.e. the torsional stiffness, k_v, damping, b_v, and inertia, I_v), the CPS calculates the desired pitching position of wing and output the signal to the servo motor via the same DAQ board. The optical encoder, which is independent of the CPS, is used to measure and verify the physical pitching position, θ. We operate the CPS at 4,000 Hz to minimize any phase delay between the input τ_f and the output θ. The detailed implementation of the CPS can be found in Zhu et al. [19].

The two types of wings (unswept and swept) used in the present study are sketched in Fig. 1(b). All the wings have a span of $s = 0.3$ m and a chord length of $c = 0.1$ m, which results in an aspect ratio of $AR = 3$ and a fixed chord-based Reynolds number at $Re \equiv \rho U_\infty c/\mu = 50,000$, where ρ and μ are water density and dynamic viscosity. For both unswept and swept wings, the leading edge (LE) and the trailing edge (TE) are parallel. Their pivot axes, represented by vertical dashed lines in the figure, pass through the mid chord point $x/c = 0.5$ of the mid span plane $z/s = 0.5$. The sweep angle Λ is defined as the angle between the leading edge and the vertical axis. Five wings with $\Lambda = 0°$ (unswept wing), $10°, 15°, 20°$ and $25°$ (swept wings) are used in the experiments.

B. Multi-layer stereoscopic particle image velocimetry

We use multi-layer phase-averaged stereoscopic particle image velocimetry (SPIV) to measure the three-dimensional (3D) velocity field around the pitching wings. The water flow is seeded using 50 μm silver-coated hollow ceramic spheres (Potters Industries) and illuminated using a horizontal laser sheet, generated by a double-pulse Nd:YAG laser (532 nm, Quantel EverGreen) with a LaVision laser guiding arm and sheet optics. Two sCMOS cameras (LaVision, 2560×2160 pixels) with 35mm lenses are used to capture image pairs of the flow field. These SPIV image pairs are fed into the LaVision DaVis software (v.10) for velocity vector calculation using multi-pass cross-correlations (two passes at 128×128 pixels, two passes at 64×64 pixels, both with 50% overlap).

To measure the two-dimensional-three-component (2D3C) velocity field at different spanwise layers, we use a motorized vertical traverse system (range: 120 mm) to raise and lower the testing rig (i.e. all the components connected by the shaft) in the z-axis [20]. Due to the limitation of the traversing range, three measuring volumes (V1, V2 and V3, see Fig. 1b) are needed to cover the entire wing span and the wing tip region. For each measuring volume, the laser sheet is fixed at the top layer and the rig is traversed upward with a step size of 5 mm. Note that the entire wing stays submerged, even at the highest traversing position. The bottom layer of V1 and the top layer of V2 overlap with each other. The velocity fields of these two layers are averaged to smooth the interface between the two volumes. The connection of V2 and V3 is also smoothed in the same way. We phase average 512 measured 2D3C velocity fields over 16 cycles (i.e. 32 measurements per cycle) to eliminate any instantaneous variations of the flow field while maintaining the key features across different layers. Finally, 70 layers of 2D3C velocity fields are stacked together to form a large volume of phase-averaged 3D3C velocity field ($\sim 3c \times 3c \times 3.6c$). The velocity fields of three wing models ($\Lambda = 0°$, $10°$ and $20°$) are measured. For the $\Lambda = 20°$ wing, the laser volumes are offset horizontally to compensate for the relatively large sweep angle (see the bottom subfigure of Fig. 1b).

C. Governing equations and non-dimensional parameters

The fluid-structure system has a governing equation

$$I\ddot{\theta} + b\dot{\theta} + k\theta = \tau_f\,, \tag{1}$$

where θ, $\dot{\theta}$, and $\ddot{\theta}$ are the angular position, velocity and acceleration, respectively. $I = I_p + I_v$ is the effective inertia, where I_p is the physical inertia of the wing and I_v is the virtual inertia that we prescribe with the CPS. Because the friction is negligible in our system, the effective structural damping, b, equals the virtual damping b_v in the CPS. k is the effective torsional stiffness and it is equivalent to the virtual stiffness k_v. Eq. 1 resembles a forced torsional mass-spring-damper system, where the nonlinear fluid torque, τ_f, acts as a nonlinear forcing term. Following Onoue et al. [21] and Zhu et al. [19], we normalize the effective inertia, damping, stiffness and the fluid torque using the fluid

Downloaded by Kenny Breuer on January 2, 2022 | http://arc.aiaa.org | DOI: 10.2514/6.2022-2328

inertia force to get the non-dimensional governing equation of the system:

$$I^*\ddot{\theta}^* + b^*\dot{\theta}^* + k^*\theta^* = \tau_f^*, \tag{2}$$

where

$$\theta^* = \theta,\ \dot{\theta}^* = \frac{\dot{\theta}c}{U_\infty},\ \ddot{\theta}^* = \frac{\ddot{\theta}c^2}{U_\infty^2},\ I^* = \frac{I}{0.5\rho c^4 s},\ b^* = \frac{b}{0.5\rho U_\infty c^3 s},\ k^* = \frac{k}{0.5\rho U_\infty^2 c^2 s},\ \tau_f^* = \frac{\tau_f}{0.5\rho U_\infty^2 c^2 s}. \tag{3}$$

We should note that the inverse of the non-dimensional stiffness is equivalent to the Cauchy number, $Ca = 1/k^*$, and the non-dimensional inertia, I^*, is analogous to the mass ratio between the wing and the surrounding fluid. The non-dimensional fluid torque, τ_f^*, is effectively the unsteady moment coefficient. We define the non-dimensional velocity as $U^* = U_\infty/(2\pi f_p c)$, where f_p is the *measured* pitching frequency.

IV. Results and discussion

A. Static characteristics of unswept and swept wings

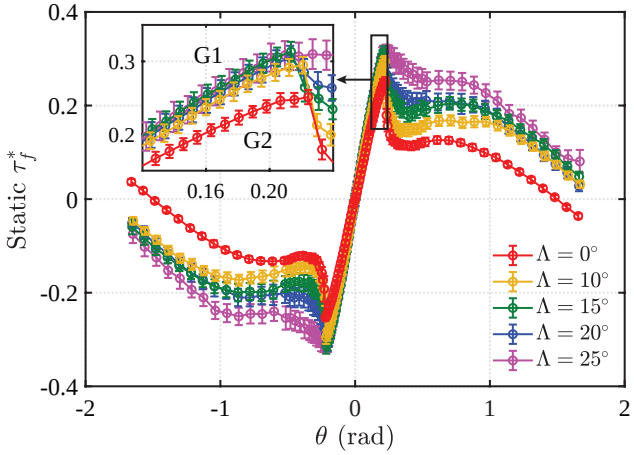


Fig. 2 Static moment coefficient of unswept and swept wings.

The static moment coefficient, τ_f^*, is measured for unswept ($\Lambda = 0°$) and swept wings ($\Lambda = 10° - 25°$) at $Re = 50,000$ and the results are plotted in Fig. 2. We see that at a fixed pitching position, θ, the static moment coefficient, τ_f^*, increases with the sweep angle, Λ. The inset shows a zoom-in view of the static τ_f^* for $\theta = 0.12 - 0.24$. It is seen that the τ_f^* curves cluster into two groups, with the unswept wing ($\Lambda = 0°$) being in G2 and all the other swept wings ($\Lambda = 10° - 25°$) being in G1. As we will show later, this grouping behavior is closely related to the onset of flow-induced oscillations (§IV.B & §IV.D) and it is important for understanding the system stability.

B. Subcritical bifurcations to flow-induced oscillations

We conduct bifurcation tests to evaluate the stability boundaries of elastically mounted pitching swept wings. Zhu et al. [19] have shown that for unswept wings, the onset of limit-cycle oscillations (LCOs) is independent of the wing inertia and the bifurcation type, and the extinction of LCOs for subcritical bifurcations at different wing inertias can be scaled by the non-dimensional velocity U^*. For these reasons, we choose to focus on one high-inertia case ($I^* = 10.6$) in the present study. In the experiments, we fix the structural damping of the system at a small value $b^* = 0.13$ and keep the initial angle of attack (AOA) at zero. To test for the onset boundary of LCOs, we first incrementally increase the Cauchy number, Ca, by decreasing the torsional stiffness, k^*. Then we reverse the operation to identify the extinction boundary of LCOs and to test for any hysteresis. The amplitude response of the system, $|A|$, is measured as the absolute peak pitching amplitude. The static divergence angle, $|\overline{A}|$, is defined as the absolute mean pitching angle.

Fig. 3 shows the amplitude response and the static divergence for swept wings with $\Lambda = 10°$ to $25°$. Data for the unswept wing ($\Lambda = 0°$) are also replotted from Zhu et al. [19] for comparison. It can be seen that as we increase

Downloaded by Kenny Breuer on January 2, 2022 | http://arc.aiaa.org | DOI: 10.2514/6.2022-2328

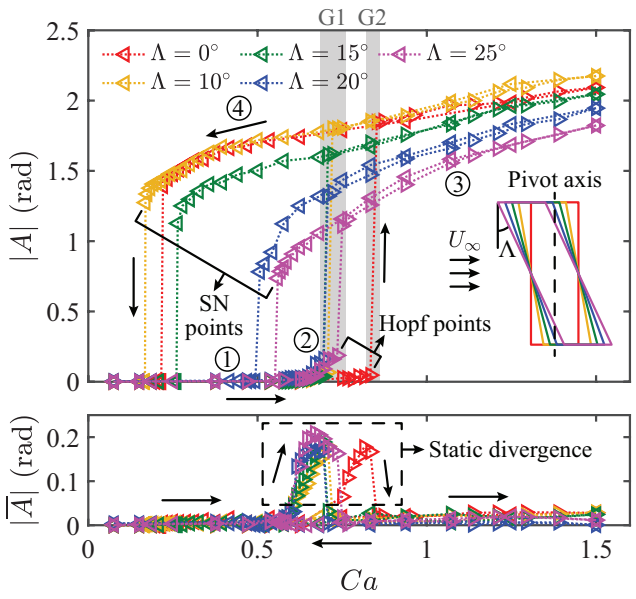


Fig. 3 Amplitude response and static divergence for unswept and swept wings. ▷: increasing Ca, ◁: decreasing Ca. The inset illustrates the wing geometry and the pivot axis. The colors of the wings correspond to the colors of the amplitude and the divergence curves in the figure.

Ca, the system first remains stable without any noticeable oscillations or divergence (regime ① in the figure). In this regime, the high stiffness of the system is able to pull the system back to a stable fixed point despite any small perturbations. As we further increase Ca, the system diverges into a small static angle, where the fluid torque is balanced by the virtual spring. Because of the existence of random flow disturbances and the decreasing spring stiffness, some small-amplitude oscillations around the static divergence angle also starts to emerge (regime ②). As Ca is further increased above a critical value (i.e. the Hopf point), the amplitude response of the system abruptly jumps into large-amplitude self-sustained LCOs and the static divergence angle drops back to zero. The large-amplitude LCOs are observed to be near-sinusoidal and have a dominant characteristic frequency. After the bifurcation, the amplitude response of the system continues to increase with Ca (regime ③). We then decrease Ca and find that the large-amplitude LCOs persist even when Ca is decreased below the Hopf point (regime ④). Finally, the system returns back to the stable fixed point regime via a saddle-node (SN) point. A hysteretic bistable region is created in between the Hopf point and the saddle-node point, which is a key feature of a subcritical Hopf bifurcation [22].

We observe that the Hopf points of unswept and swept wings can be roughly divided into two groups (Fig. 3, G1 & G2), with the unswept wing ($\Lambda = 0°$) being in G2 and all the other wings ($\Lambda = 10° - 25°$) being in G1, which agrees with the trend observed in Fig. 2 for static moment coefficients. The underlying physics behind this interconnection will be discussed in §IV.D. It is also seen that as the sweep angle increases, the LCO amplitude at the saddle-node point decreases monotonically. However, value of Ca at which the saddle-node point occurs first extends towards a lower value ($\Lambda = 0° \rightarrow 10°$) and then comes back towards a higher Ca ($\Lambda = 10° \rightarrow 25°$). This indicates that increasing the sweep angle first destabilizes the system from $\Lambda = 0°$ to $10°$ and then re-stabilizes it from $\Lambda = 10°$ to $25°$. This non-monotonic behavior of the saddle-node point will be discussed in §IV.E. The amplitude response, $|A|$, seems to follow a similar non-monotonic trend. Between $\Lambda = 0°$ and $10°$, $|A|$ becomes slightly higher at higher Ca. Whereas from $\Lambda = 10°$ to $25°$, $|A|$ decreases monotonically, indicating that higher Λ is not able to sustain LCOs at higher amplitudes.

C. Frequency response of the system

Fig. 4(a) shows the frequency response of the flow-induced large-amplitude LCOs observed in Fig. 3 as a function of the natural (structural) frequency and the sweep angle. In the figure, $f_p^* = f_p c/U_\infty$ and $f_s^* = f_s c/U_\infty$, where f_s is the structural frequency [23] calculated by

$$f_s = \frac{1}{2\pi}\sqrt{\frac{k}{I} - (\frac{b}{2I})^2}. \tag{4}$$

Downloaded by Kenny Breuer on January 2, 2022 | http://arc.aiaa.org | DOI: 10.2514/6.2022-2328

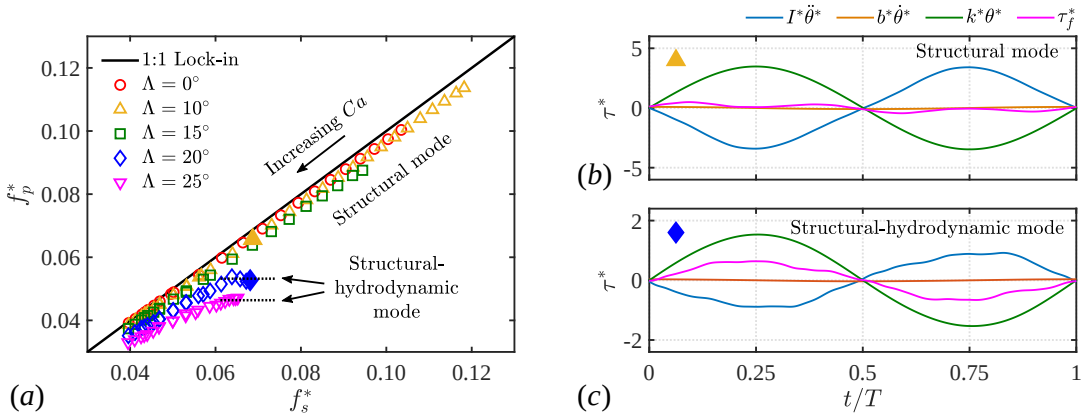


Fig. 4 (*a*) Frequency response of unswept and swept wings. (*b*, *c*) Force decomposition of the structural mode and the structural-hydrodynamic mode. (*b*) and (*c*) correspond to the filled yellow triangle and the filled blue diamond in (*a*), respectively.

We observe that for all the wings tested in the experiments, the measured pitching frequency, f_p^*, generally locks on to the calculated structural frequency, f_s^*, indicating that the oscillations are dominated by the balance between the structural stiffness and inertia. These oscillations thus correspond to a *structural* mode [19]. We decompose the torques experienced by the wing into the inertia torque, $I^*\ddot{\theta}^*$, the structural damping torque, $b^*\dot{\theta}^*$, the stiffness torque, $k^*\theta^*$, and the fluid torque, τ_f^*. For an example case at $\Lambda = 10°$, $f_s^* = 0.069$ (i.e. the filled yellow triangle in Fig. 4*a*), these torques are plotted in Fig. 4(*b*). We see that for the structural mode, the stiffness torque is mainly balanced by the inertia torque, while the structural damping torque and the fluid torque remain relatively small.

Apart from the structural mode, Zhu et al. [19] also observed a hydrodynamic mode, which corresponds to a low wing inertia. In the hydrodynamic mode, the oscillations are dominated by the fluid force, so that the measured pitching frequency, f_p^*, stays relatively constant for a changing Ca. In Fig. 4(*a*), we see that for $\Lambda = 20°$ and 25°, f_p^* flattens near the saddle-node boundary. This flattening trend shows an emerging dominating fluid time scale, resembling a hydrodynamic mode despite the high wing inertia. We take $\Lambda = 20°$, $f_s^* = 0.068$ (i.e. the filled blue diamond in Fig. 4*a*) as an example and decompose the torques in Fig. 4(*c*). It is observed that in this oscillation mode, the stiffness torque balances both the inertia torque and the fluid torque. For this reason, we define this hybrid oscillation mode as the *structural-hydrodynamic* mode.

For a fixed structural frequency, f_s^*, as the sweep angle increases, the measured pitching frequency, f_p^*, deviates from f_s^* moving to lower frequencies, suggesting an increasing added-mass effect. This is expected because of the way we pitch the wings in the experimental setup (see the inset of Fig. 3). As Λ increases, the accelerated fluid near the wing root and the wing tip produces more torque due to the increase of the moment arm, which amplifies the added-mass effect.

D. Onset of flow-induced oscillations

In Fig. 3, we have observed that the Hopf points of unswept and swept wings can be roughly divided into two groups (Fig. 3, G1 & G2) . In this section, we try to explain this phenomenon. Fig. 5(*a*) and (*b*) shows the temporal evolution of the pitching position, θ, the fluid torque, τ_f^* and the stiffness torque, $k^*\theta$, near the Hopf point for $\Lambda = 0°$. It can be seen that the wing undergoes small-amplitude oscillations around the divergence angle at the Hopf point. The divergence angle is below the static stall angle, θ_s, so that the flow stays mostly attached. The fluid torque, τ_f^*, is balanced by the stiffness torque, $k^*\theta$. When the Cauchy number, Ca, is changed to a value above the Hopf point (Fig. 4*a*, $t = 700$ s), $k^*\theta$ is not able to hold the pitching position below θ_s. Once the pitching position exceeds θ_s, stall occurs and the wing experiences a sudden drop in τ_f^*. $k^*\theta$ loses its counterpart and starts to accelerate the wing to pitch towards the opposite direction. This acceleration brings unsteadiness to the system and the quasi-steady small-amplitude oscillations gradually transition to large-amplitude LCOs. This transition process shows that the onset of large-amplitude LCOs depends largely on the static characteristics of the wing.

The triggering of flow-induced LCOs starts from θ exceeding the static stall angle after k^* is decreased below the Hopf point, causing τ_f^* to drop below $k^*\theta$. Therefore, the slope of the static stall point should be equal to the stiffness at

Downloaded by Kenny Breuer on January 2, 2022 | http://arc.aiaa.org | DOI: 10.2514/6.2022-2328

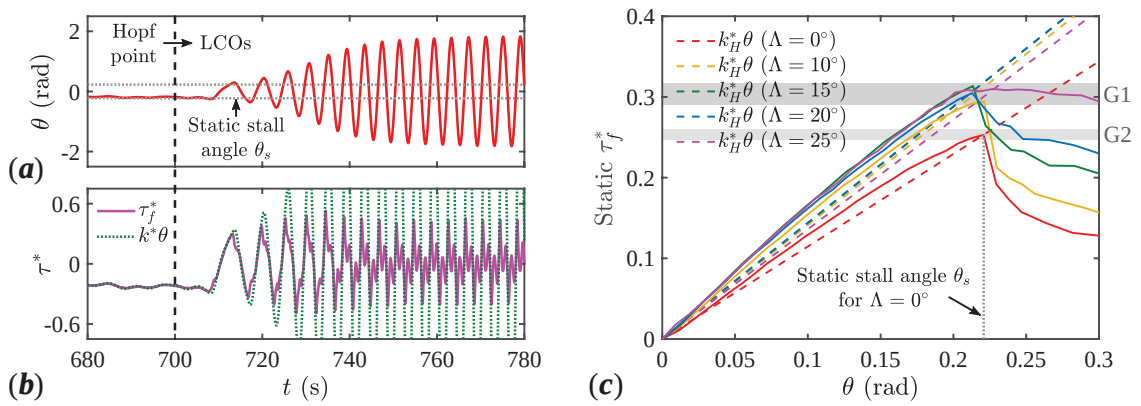


Fig. 5 Temporal evolution of (*a*) the pitching position θ, (*b*) the fluid torque τ_f^*, and the stiffness torque $k^*\theta$ near the Hopf point for $\Lambda = 0°$. (*c*) Static moment coefficients of unswept and swept wings.

the Hopf point, k_H^* (i.e. $\tau_{f,\,\text{stall}}^* = k_H^*\theta$). This is verified by Fig. 5(*c*), in which we replot the static moment coefficients of unswept and swept wings from Fig. 2 with error bars omitted for clarity. The corresponding $k_H^*\theta$ are also plotted. We see that the $k_H^*\theta$ lines all roughly pass through the static stall points (i.e. the maximum static τ_f^*) of the corresponding Λ. Note that $k_H^*\theta$ of $\Lambda = 15°$ and $20°$ overlap with each other. Similar to the trend observed for the Hopf point in Fig. 3 (or equivalently, the trend of $k_H^*\theta$), the static moment coefficient τ_f^* can also be divided into two groups, with the unswept wing ($\Lambda = 0°$) being in G2 and all the other wings ($\Lambda = 10° - 25°$) being in G1 (see also Fig. 2). This reinforces the argument that the onset of flow-induced LCOs is shaped by the static characteristics of the wing. Moreover, it is proven that this argument applies to both unswept and swept wings.

E. Power coefficient map and system stability

In this section, we analyze the stability of elastically mounted unswept and swept wings from the perspective of energy transfer. Menon and Mittal [24] and Zhu et al. [19] have shown numerically and experimentally that the flow-induced oscillations of elastically mounted 2D wings and unswept wings can only sustain when the net energy transfer between the ambient fluid and the elastic structure equals zero. To map out this energy transfer for a large range of pitching frequencies and amplitudes, we prescribe the pitching motion of the wing with

$$\theta = |A| \sin(2\pi f_p t), \tag{5}$$

where $0 \le |A| \le 2.5$ and $0.15\ \text{Hz} \le f_p \le 0.6\ \text{Hz}$. By integrating Eq. 2 over $n = 20$ cycles and averaging [21], we can get the power coefficient of the system

$$C_p = \frac{f_p^*}{n} \int_{t_0}^{t_0+nT} (\tau_f^* \dot{\theta}^* - b^* \dot{\theta}^{*2})\, dt^*. \tag{6}$$

In this equation, the $\tau_f^* \dot{\theta}^*$ term represents the power injected into the system by the ambient fluid, whereas the $b^* \dot{\theta}^{*2}$ term represents the power dissipated by the structural damping of the elastic mount. The power coefficient maps of unswept and swept wings are plotted in Fig. 6(*a-e*).

In these maps, red regions correspond to $C_p > 0$, where the power injected by the ambient fluid is higher than that dissipated by the structural damping. On the contrary, $C_p < 0$ in the blue regions. The colored dashed lines indicate the $C_p = 0$ contours, where the power injection balances the power dissipation. The $C_p = 0$ curve can be divided into three branches. Zhu et al. [19] have shown that for unswept wings, the top branch corresponds to stable LCO solutions for the structural mode, the middle branch represents stable LCO solutions for the hydrodynamic mode, and the bottom branch is the stable fixed point solution.

To correlate the power coefficient maps of prescribed oscillations with the stability boundaries of flow-induced oscillations, we overlay the amplitude response of the passive system from Fig. 3 onto Fig. 6(*a-e*). The measured pitching frequencies, f_p, are used to calculate the non-dimensional velocity, U^*, for large-amplitude LCOs (filled triangles). Because it is difficult to measure frequencies of stable fixed points and small-amplitude oscillations (hollow

Downloaded by Kenny Breuer on January 2, 2022 | http://arc.aiaa.org | DOI: 10.2514/6.2022-2328

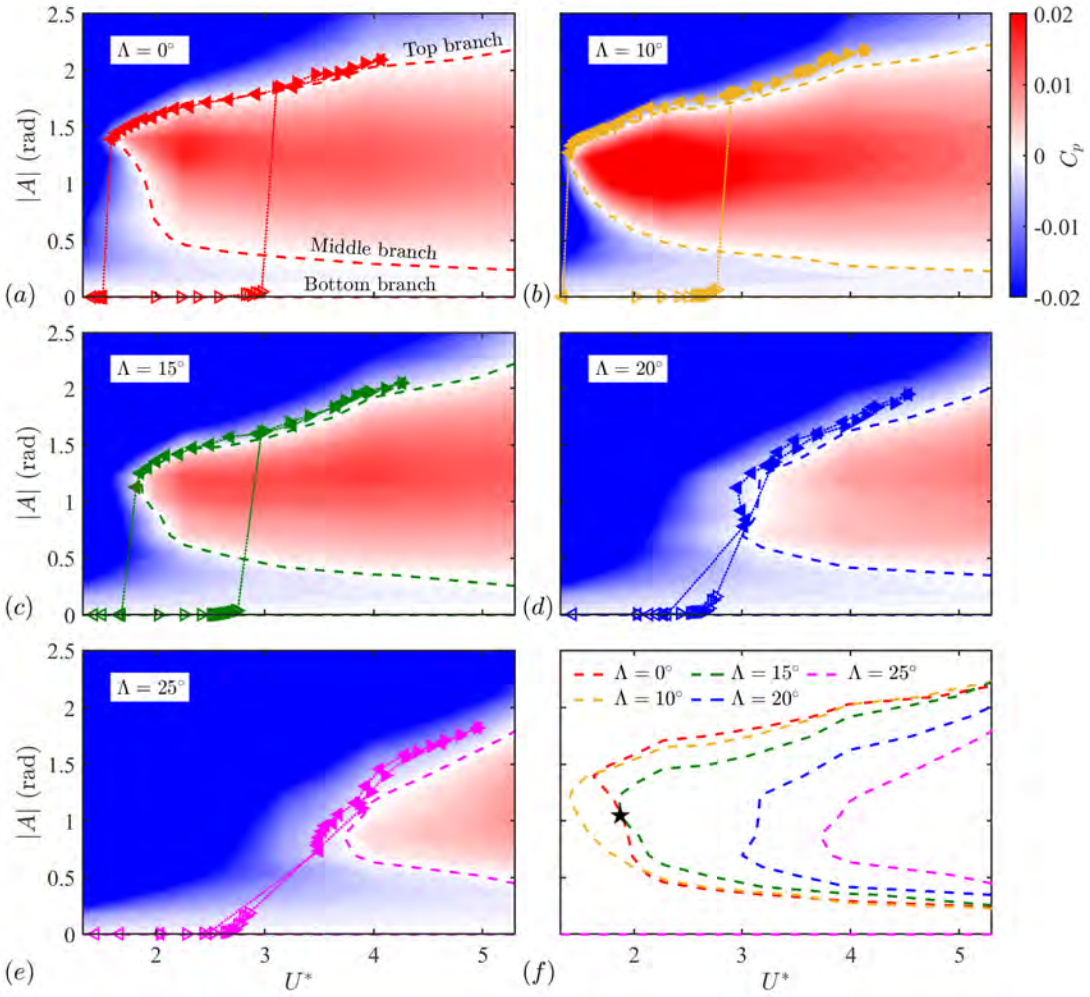


Fig. 6 (*a-e*) Power coefficient maps of prescribed sinusoidal oscillations overlaid by the bifurcation diagrams of elastically mounted unswept and swept wings. ▹: increasing Ca, ◃: decreasing Ca. (*f*) Neutral power transfer curves for unswept and swept wings.

triangles), we use the calculated structural frequency, f_s, to evaluate U^*. Fig. 6(*a-e*) show that for all the wings tested, the flow-induced large-amplitude LCOs agree remarkably well with the top branch of the $C_p = 0$ curve, indicating the broad applicability of the energy approach for both unswept and swept wings, a result that was observed by Menon and Mittal [24] and Zhu et al. [19] and is expected for instabilities that are well-described by sinusoidal motions (Eq. 5). The small discrepancies for large sweep angles can be attributed to the smooth C_p gradient near $C_p = 0$. The junction between the top and the middle $C_p = 0$ branches remains relative sharp for $\Lambda = 0° - 15°$ and becomes smoother for $\Lambda = 20° - 25°$. These smooth turnings result in a smooth transition in between the structural mode and the hydrodynamic mode, giving rise to the structural-hydrodynamic mode discussed in §IV.C.

The $C_p = 0$ curves for $\Lambda = 0° - 25°$ are summarized in Fig. 6(*f*). It is seen that the trend of the top branch is similar to that observed in Fig. 3 for large-amplitude LCOs. The location of the junction between the top branch and the middle branch changes non-monotonically with Λ, which accounts for the non-monotonic behavior of the saddle-node point. In addition, the maximum power extraction also shows a non-monotonic dependency on the sweep angle, which may inspire the future design of higher efficiency oscillating-foil energy harvesting devices.

Downloaded by Kenny Breuer on January 2, 2022 | http://arc.aiaa.org | DOI: 10.2514/6.2022-2328

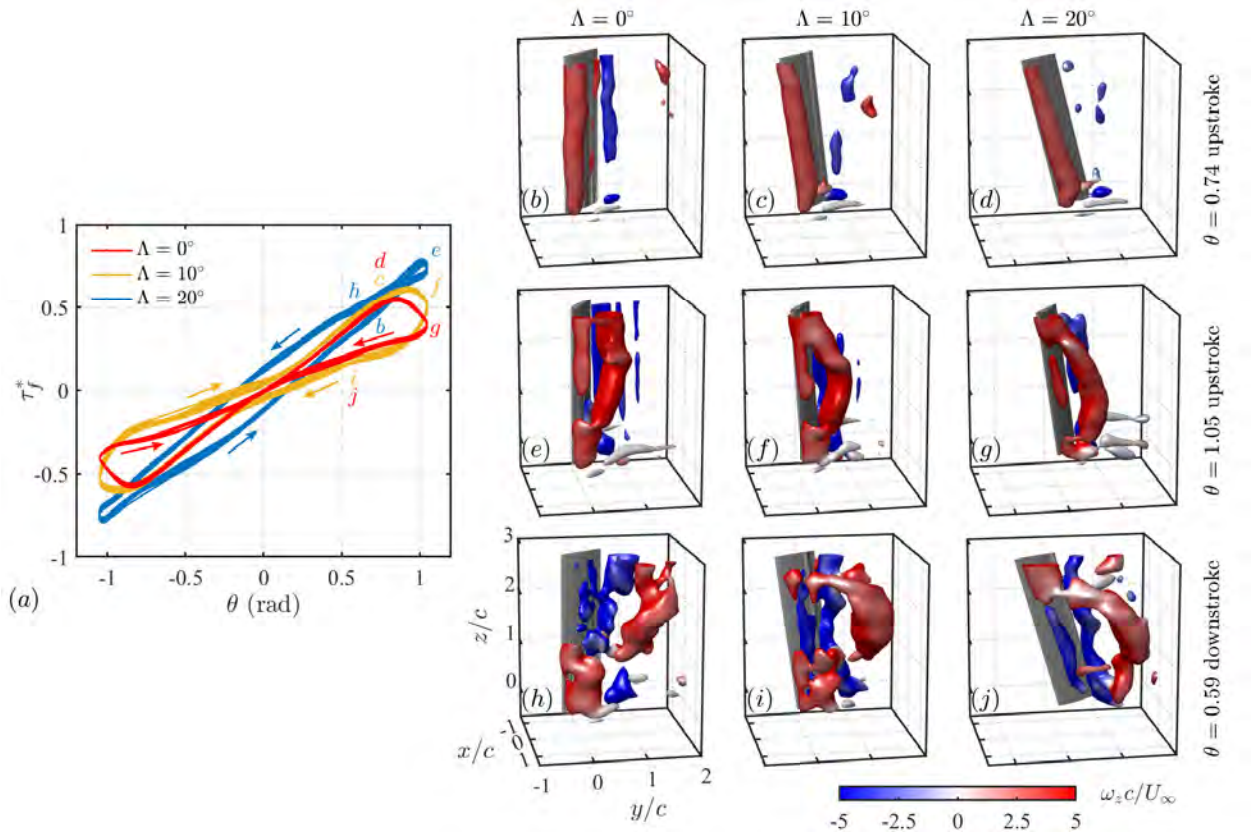


Fig. 7 (*a*) Force portraits for Λ = 0°, 10° and 20° at $|A|$ = 1.05 and f_p^* = 0.09. (*b-j*) Phase-averaged 3D flow structures visualized with iso-Q surfaces (Q = 50 s^{-2}) colored by the non-dimensional spanwise vorticity, $\omega_z c/U_\infty$.

F. Insights obtained from three-dimensional flow structures

In the previous section (§IV.E), we have established the interconnection between prescribed oscillations and flow-induced oscillations using the energy approach. In this section, we analyze the 3D flow structures obtained from phase-averaged stereo PIV experiments to get some insights for the differences in the power coefficient between unswept and swept wings. In the PIV experiments, three wings (Λ = 0°, 10° and 20°) are prescribed with sinusoidal pitching at $|A|$ = 1.05 and f_p^* = 0.085, which corresponds to the black star shown in Fig. 6(*f*). This particular pitching kinematic is selected because it sits right on the C_p = 0 curve for Λ = 0° while leading to a positive C_p for Λ = 10° and a negative C_p for Λ = 20° (see Fig. 6*a,b,d,f*).

The τ_f^*-θ phase portraits for the three wings are plotted in Fig. 7(*a*) with arrows showing the temporal direction of the loops. For plotting purposes only, we apply a zero-phase sixth-order low-pass Butterworth filter (cutoff at $20f_p$) to the raw torque data so as to smooth out small oscillations. It is important to note that this filter is only employed for post-processing of the data; no filter is used inside the real-time control loop. 3D velocity fields around the wings are measured using the technique described in §III.B and smoothed. Phase-averaged 3D flow structures visualized with iso-Q surfaces (Q = 50 s^{-2}) at three pitching positions (θ = 0.74 and 1.05, upstroke; θ = 0.59, downstroke) are plotted in Fig. 7(*b-j*) for all the three wings. These 3D flow structures are colored by the non-dimensional spanwise vorticity, $\omega_z c/U_\infty$, with red being positive and blue being negative. The corresponding pitching positions of (*b-j*) are shown in Fig. 7(*a*).

The fluid torque, τ_f^*, shows a relatively linear growth (Fig. 7*a*) as the wings pitch up (θ = 0.74, upstroke), which corresponds to the formation of a strong leading-edge vortex, as depicted by Fig. 7(*b-d*). At this time instant, the 3D flow structures for the three wings appear to be very similar. As the wings continue to pitch up, τ_f^* reaches its maximum. It is observed that τ_f^* peaks at higher values of θ as the sweep angle increases. At the maximum pitch angle (θ = 1.05, upstroke), τ_f^* drops from the peak for Λ = 0° and 10° while reaching the maximum for Λ = 20°. The decrease of τ_f^* for

Downloaded by Kenny Breuer on January 2, 2022 | http://arc.aiaa.org | DOI: 10.2514/6.2022-2328

$\Lambda = 0°$ and 10° results from the shedding of the LEV as shown in Fig. 7(*e-f*). At this time instant, the LEV mostly detaches from the wing surface for $\Lambda = 0°$ (Fig. 7*e*) except for a small portion near the wing tip, which stays attached. A similar flow structure was observed by Yilmaz and Rockwell [25] for finite-span wings undergoing linear pitch-up motions. For $\Lambda = 10°$ (Fig. 7*f*), this small portion of the attached LEV shrinks. The top portion of the LEV near the wing root is also observed to stay closer to the wing surface as compared to the $\Lambda = 0°$ case. For $\Lambda = 20°$ (Fig. 7*g*), the attached portion of the LEV near the wing tip further shrinks and the top portion of the LEV also attaches to the wing surface, similar to that observed for $\Lambda = 10°$.

During the pitch reversal ($\theta = 0.59$, downstroke), as the LEV further detaches from the wing surface for $\Lambda = 0°$ and 10° (Fig. 7*h-i*), τ_f^* takes a lower path back to the equilibrium point ($\theta = 0$), resulting in a positive hysteresis loop. This positive loop corresponds to a positive $\tau_f^* \dot{\theta}^*$ term in Eq. 6, indicating a positive power injection by the ambient fluid. The loop area of $\Lambda = 10°$ is greater than that of $\Lambda = 0°$. For $\Lambda = 0°$, this power injection is balanced by the power dissipation of the structural damping, leading to $C_p = 0$ and self-sustained LCOs in the passive system (Fig. 6*a*). For $\Lambda = 10°$, this fluid power injection is greater than the structural power dissipation (note that all the three wings have the same structural power dissipation because they are prescribed with the same kinematics), resulting in a positive C_p. In the passive system, due to the power injection, the LCO amplitude increases and settles on the top branch of $C_p = 0$ (Fig. 6*b*). For $\Lambda = 20°$, however, τ_f^* takes an upper path back to $\theta = 0$, creating a negative hysteresis loop. This means that in addition to the structural damping, the ambient fluid also dissipates power from the system (i.e. positive fluid damping, see [26]). The combined effect of these two power dissipation mechanisms leads to a negative C_p and thus a decreasing LCO amplitude in the passive system, which further brings the system down to the bottom branch of the $C_p = 0$ curve (Fig. 6*c*). Fig. 7(*j*) shows that for $\Lambda = 20°$, the LEV largely detaches from the wing surface except for the top portion. As the top portion of the LEV is far from the pivot axis, the force generated by it has a long moment arm, which can result in a high fluid torque. This may account for the high τ_f^* observed for $\Lambda = 20°$ during the pitch reversal, as compared to $\Lambda = 0°$ and 10°.

The change of LEV shapes as a function of the sweep angle observed in Fig. 7(*e-g*) can be associated with the arch vortices reported by Visbal and Garmann [18]. In their numerical study, it has been shown that for pitching unswept wings with free tips on both ends, an arch-type vortical structure began to form as the pitch reversal started (see their Fig. 6c). In our experiments, the wings have a free tip and an endplate (a wing-body junction, or symmetry plane). Therefore, the vortical structure shown in Fig. 7(*e*) is equivalently half of the arch vortex. If we mirror the flow structures about the wing root (i.e. the endplate), we can get a complete arch vortex similar to that observed by Visbal and Garmann [18]. For swept wings, we observe one complete arch vortex for both $\Lambda = 10°$ (Fig. 7*f*) and 20° (Fig. 7*g*). Again, if we mirror the flow structures about the wing root, there will be two arch vortices for each wing, which well agrees with the observation of Visbal and Garmann [18] (see their Fig. 10c and 13c). Moreover, Visbal and Garmann [18] reported that for swept wings, as Λ increases, the arch vortex moves towards the wing tip, which is also seen in our experiments.

V. Conclusions and future works

In this experimental study, we have investigated the nonlinear stability boundaries of elastically mounted pitching unswept and swept wings, with the elastic mount of the wings simulated using a cyber-physical control system. We have shown that the onset of flow-induced oscillations (i.e. the Hopf point) depends on the static characteristics of the wing. The non-monotonic trend of the saddle-node point as a function of the sweep angle has been attributed to the non-monotonic power transfer between the ambient fluid and the elastic mount. For swept wings with relatively high sweep angles ($\Lambda = 20°$ and 25°), an hybrid oscillation mode, namely the structural-hydrodynamic mode, has been observed and characterized. Phase-averaged 3D flow structures measured by stereoscopic PIV have been analyzed to explain the differences in power extraction for unswept and swept wings. In addition, we have found that there exists an optimal sweep angle ($\Lambda = 10°$) for extracting power from fluid flows and thus promoting flow-induced oscillations. One may want to avoid this angle for MAV designs to stay away from aeroelastic instabilities. On the other hand, this angle may be employed for developing higher efficiency flapping-foil energy-harvesting devices.

In the present study, only qualitative analysis of 3D flow structures have been conducted and for a very limited set of sweep angles and flow parameters. In order to get a deeper understanding of the wing sweep effect on the dynamics and stability of the leading-edge vortex and thus the system stability boundaries, more quantitative analysis are needed, which will be the focus of a following work.

Downloaded by Kenny Breuer on January 2, 2022 | http://arc.aiaa.org | DOI: 10.2514/6.2022-2328

Acknowledgments

This work is funded by Air Force Office of Scientific Research, Grant FA9550-18-1-0322, managed by Dr. Gregg Abate.

References

[1] Dowell, E. H., Curtiss, H. C., Scanlan, R. H., and Sisto, F., *A modern course in aeroelasticity*, Springer, 1989.

[2] Xiao, Q., and Zhu, Q., "A review on flow energy harvesters based on flapping foils," *J. Fluids Struct.*, Vol. 46, 2014, pp. 174–191.

[3] Young, J., Lai, J. C. S., and Platzer, M. F., "A review of progress and challenges in flapping foil power generation," *Prog. Aerosp. Sci.*, Vol. 67, 2014, pp. 2–28.

[4] Su, Y., and Breuer, K. S., "Resonant response and optimal energy harvesting of an elastically mounted pitching and heaving hydrofoil," *Phys. Rev. Fluids*, Vol. 4, No. 6, 2019, p. 064701.

[5] Wang, Z. J., "Dissecting insect flight," *Annu. Rev. Fluid Mech.*, Vol. 37, 2005, pp. 183–210.

[6] Bergou, A. J., Xu, S., and Wang, Z. J., "Passive wing pitch reversal in insect flight," *J. Fluid Mech.*, Vol. 591, 2007, pp. 321–337.

[7] Beatus, T., and Cohen, I., "Wing-pitch modulation in maneuvering fruit flies is explained by an interplay between aerodynamics and a torsional spring," *Phys. Rev. E*, Vol. 92, No. 2, 2015, p. 022712.

[8] Wu, K. S., Nowak, J., and Breuer, K. S., "Scaling of the performance of insect-inspired passive-pitching flapping wings," *J. R. Soc. Interface*, Vol. 16, No. 161, 2019, p. 20190609.

[9] Ho, S., Nassef, H., Pornsinsirirak, N., Tai, Y.-C., and Ho, C.-M., "Unsteady aerodynamics and flow control for flapping wing flyers," *Prog. Aerosp. Sci.*, Vol. 39, No. 8, 2003, pp. 635–681.

[10] Shyy, W., Aono, H., Chimakurthi, S. K., Trizila, P., Kang, C.-K., Cesnik, C. E. S., and Liu, H., "Recent progress in flapping wing aerodynamics and aeroelasticity," *Prog. Aerosp. Sci.*, Vol. 46, No. 7, 2010, pp. 284–327.

[11] McCroskey, W. J., "Unsteady airfoils," *Annu. Rev. Fluid Mech.*, Vol. 14, No. 1, 1982, pp. 285–311.

[12] Dimitriadis, G., and Li, J., "Bifurcation behavior of airfoil undergoing stall flutter oscillations in low-speed wind tunnel," *AIAA J.*, Vol. 47, No. 11, 2009, pp. 2577–2596.

[13] Ellington, C. P., van den Berg, C., Willmott, A. P., and Thomas, A. L. R., "Leading-edge vortices in insect flight," *Nature*, Vol. 384, No. 6610, 1996, p. 626.

[14] Videler, J. J., Stamhuis, E. J., and Povel, G. D. E., "Leading-edge vortex lifts swifts," *Science*, Vol. 306, No. 5703, 2004, pp. 1960–1962.

[15] Lentink, D., Müller, U. K., Stamhuis, E. J., de Kat, R., van Gestel, W., Veldhuis, L. L. M., Henningsson, P., Hedenström, A., Videler, J. J., and van Leeuwen, J. L., "How swifts control their glide performance with morphing wings," *Nature*, Vol. 446, No. 7139, 2007, pp. 1082–1085.

[16] Wong, J. G., and Rival, D. E., "Determining the relative stability of leading-edge vortices on nominally two-dimensional flapping profiles," *J. Fluid Mech.*, Vol. 766, 2015, p. 611.

[17] Onoue, K., and Breuer, K. S., "A scaling for vortex formation on swept and unswept pitching wings," *J. Fluid Mech.*, Vol. 832, 2017, pp. 697–720.

[18] Visbal, M. R., and Garmann, D. J., "Effect of sweep on dynamic stall of a pitching finite-aspect-ratio wing," *AIAA J.*, Vol. 57, No. 8, 2019, pp. 3274–3289.

[19] Zhu, Y., Su, Y., and Breuer, K. S., "Nonlinear flow-induced instability of an elastically mounted pitching wing," *J. Fluid Mech.*, Vol. 899, 2020, p. A35.

[20] Zhong, Q., Han, T., Moored, K. W., and Quinn, D. B., "Aspect ratio affects the equilibrium altitude of near-ground swimmers," *J. Fluid Mech.*, Vol. 917, 2021.

[21] Onoue, K., Song, A., Strom, B., and Breuer, K. S., "Large amplitude flow-induced oscillations and energy harvesting using a cyber-physical pitching plate," *J. Fluids Struct.*, Vol. 55, 2015, pp. 262–275.

Downloaded by Kenny Breuer on January 2, 2022 | http://arc.aiaa.org | DOI: 10.2514/6.2022-2328

[22] Strogatz, S. H., *Nonlinear Dynamics and Chaos: With Applications to Physics, Biology, Chemistry, and Engineering*, Perseus Books, 1994.

[23] Rao, S. S., *Mechanical Vibrations*, Addison-Wesley, 1995.

[24] Menon, K., and Mittal, R., "Flow physics and dynamics of flow-induced pitch oscillations of an airfoil," *J. Fluid Mech.*, Vol. 877, 2019, pp. 582–613.

[25] Yilmaz, T. O., and Rockwell, D., "Flow structure on finite-span wings due to pitch-up motion," *J. Fluid Mech.*, Vol. 691, 2012, p. 518.

[26] Zhu, Y., Mathai, V., and Breuer, K., "Nonlinear fluid damping of elastically mounted pitching wings in quiescent water," *J. Fluid Mech.*, Vol. 923, 2021, p. R2.

Downloaded by Kenny Breuer on January 2, 2022 | http://arc.aiaa.org | DOI: 10.2514/6.2022-2328

Leading edge vortex formation and wake trajectory: Synthesizing measurements, analysis, and machine learning

Howon Lee,* Nicholas Simone, Yunxing Su, and Yuanhang Zhu
Center for Fluid Mechanics, School of Engineering, Brown University, Providence, Rhode Island

Bernardo Luiz R. Ribeiro and Jennifer A. Franck
Department of Engineering Physics, University of Wisconsin-Madison, Madison, Wisconsin

Kenneth Breuer
Center for Fluid Mechanics, School of Engineering, Brown University, Providence, Rhode Island

(Received 11 August 2021; accepted 1 July 2022; published 21 July 2022)

The strength and trajectory of a leading edge vortex (LEV) formed by a pitching-heaving hydrofoil (chord c) is studied. The LEV is identified using the Q-criterion method, which is calculated from the 2D velocity field obtained from particle image velocimetry measurements. The relative angle of attack at midstroke, $\alpha_{T/4}$, proves to be an effective method of combining heave amplitude (h_0/c), pitch amplitude (θ_0), and reduced frequency (f^*) into a single variable that predicts the maximum value of Q over a wide range of operating conditions. Once the LEV separates from the foil, it travels downstream and rapidly weakens and diffuses. The downstream trajectory of the LEV has two characteristic shapes. At low values of $\alpha_{T/4}$, it travels straight downstream after separating from the foil, while at higher values of $\alpha_{T/4}$, an accompanying trailing edge vortex (TEV) forms and the induced velocity generates a cross-stream component to the vortex trajectories. This behavior is accurately predicted using a potential flow model for the LEV and TEV. Supervised machine learning algorithms, namely support vector regression and Gaussian process regression, are used to create regression models that predicts the vortex strength, shape, and trajectory during growth and after separation. The regression model successfully captures the features of two vortex regimes observed at different values of $\alpha_{T/4}$. However, the predicted LEV trajectories are somewhat smoother than observed in the experiments. The strengths of the vortex is often under-predicted. Both of these shortcomings may be attributed to the relatively small size of the training data set.

DOI: 10.1103/PhysRevFluids.7.074704

I. INTRODUCTION

The oscillating hydrofoil offers an appealing alternative to conventional rotary turbine hydrokinetic energy converters (HEC), with lower blade speeds, a low cut-in velocity, and a geometry favorable for shallow waters such as rivers and tidal estuaries [1]. A typical configuration of the oscillating hydrofoil is shown in Fig. 1. The hydrofoil heaves upward with a high angle of attack inducing leading edge stall and the formation of a strong leading-edge vortex (LEV). The vortex core has an associated low pressure region acting on the upper surface of the foil which generates a large heaving force. Once the LEV separates from the leading edge and begins to convect downstream,

*Present address: Department of Aerospace Engineering, Georgia Tech, Atlanta, GA.

 ©2022 American Physical Society

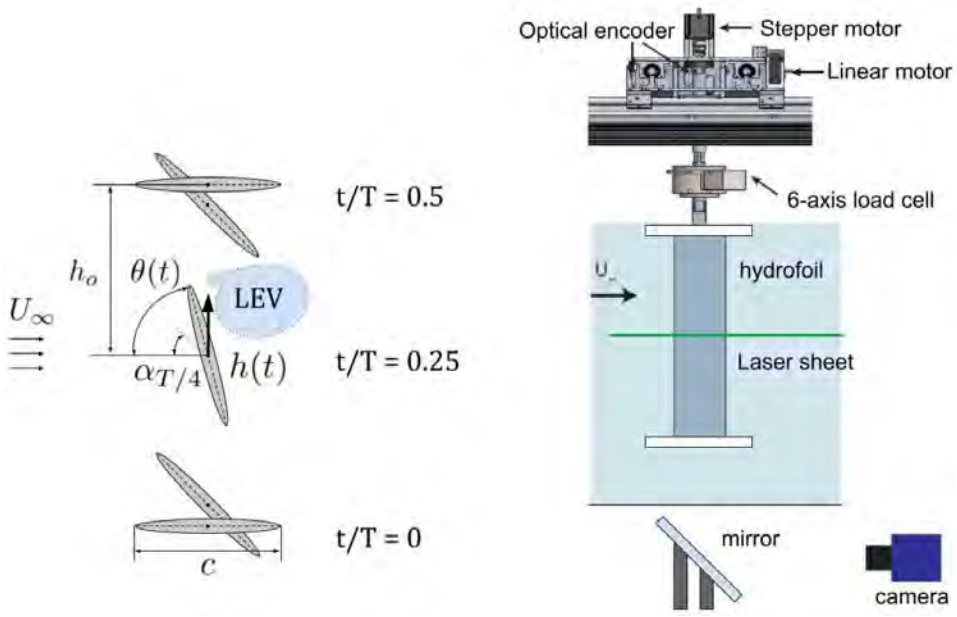


FIG. 1. Left: The motion of a single oscillating hydrofoil for a half-cycle from a top-down view. At the start of the cycle, $t/T = 0$, the foil is positioned at the negative peak amplitude and is angled at 0°. The foil follows a sinusoidal heaving and pitching motion with a phase difference of $\pi/2$. Right: The PIV experimental set up in the flume used for verification PIV data.

the lift quickly deteriorates and the hydrofoil must rotate and heave in the other direction, repeating the energy harvesting cycle.

The first investigation of power extraction by a flapping foil was carried out by McKinney and DeLaurier [2], demonstrating the potential to generate power from a steady flowing fluid. A numerical study by Kinsey and Dumas [3] found that for a heaving amplitude of one chord length, efficiencies as high as 35% could be obtained at a reduced frequency, $f^* = fc/U_\infty$, of 0.15 and maximum heaving amplitude of 0.75 chord length. Kim *et al.* [4] divided the power generated by the foil into heave and pitch components which had different behaviors. The heave component of energy harvesting efficiency increased with reduced frequency. In contrast, the pitch component of efficiency decreased, with the efficiency even changing signs from positive to negative at times [4]. Numerous field tests have also successfully demonstrated the energy harvesting capabilities in realistic environments [5–7].

Various studies have investigated methods to increase the energy harvesting efficiency of oscillating hydrofoils. Simpson *et al.* [8], for example, showed experimentally that increasing the aspect ratio improves the efficiency of the foil. This agrees with the airfoil theory where the detrimental effect of the tip vortices on the lift generation capabilities of a foil weakens with greater aspect ratio. Kim *et al.* [4] found that a similar relationship can be applied to the hydrofoil in heaving motion and observed that the change in efficiency is due to the power by heaving motion being significantly affected by the aspect ratio. It has been reported that efficiency increased when a trapezoidal pitching motion with a sinusoidal heaving motion was used rather than a sinusoidal motion for both heaving and pitching [9–11]. Kinsey and Dumas have also found that when end plates are mounted, the total efficiency is improved by reducing the 3D hydrodynamic losses [12]. In a similar effect to that of increasing the aspect ratio, the benefits of end plates are usually thought to be the suppression of the tip vortex effects [4]. However, with the increase in size of the end plate, the additional skin friction and flow structure interaction may work against this benefit, reducing the hydrodynamic force on the hydrofoil [4]. Many studies have also explored another approach to improving energy

harvesting efficiency by taking advantage of the wall confinement effect, operating the foil close to a wall inside a channel [13,14].

Another practical means to improve the overall power production of an oscillating foil installation is to pack the foils into closely spaced arrays. In the case of vertical-axis wind turbine arrays (VAWTs), arranging two counter-rotating VAWTs together can prove advantageous [15] due to the "constructive interference" of the structured vortex wake shed by the leading turbine, which can improve the efficiency of the trailing turbine. For oscillating hydrofoils, numerous experimental and computational studies have been conducted analyzing the performance of oscillating hydrofoils in tandem configuration. A 2D unsteady Reynolds-averaged Navier-Stokes (URANS) study by Kinsey and Dumas showed that having a counterclockwise vortex above the trailing foil or a clockwise vortex slightly below the trailing foil has a favorable impact on power extraction [16]. Simeski and Franck [17] explored various combinations of vertical and horizontal separation between the foils and found that staggered configurations result in the efficiency of the trailing foil exceeding that of the leading hydrofoil. Ribeiro *et al.* [18] investigated the power extraction and LEV trajectory of an oscillating hydrofoil from large-eddy simulations (LES) and direct numerical simulations (DNS), where they identified two regimes of efficiency in terms of the relative angle of attack at midupstroke, or $\alpha_{T/4}$. They found that for $\alpha_{T/4} < 22^\circ$, the boundary layer remains attached to the foil with minimal separation and no distinct LEV while for $\alpha_{T/4} > 22^\circ$, the LEV becomes more prominent and contributes to high efficiency [18].

However, a taxonomy of the trajectory and strength of the LEV shed by the leading turbine in an array has not been completed over any range of operating parameters (frequency, pitch angle, and heave amplitude), and the lack of this knowledge, coupled with the difficulty in conducting experiments and computations of multifoil configurations has inhibited progress in designing oscillating foil farms. We aim to fill this this gap in our knowledge in this work.

This manuscript combines experimental measurements of oscillating foil turbine wakes with simple theory and machine learning tools to report on the strength, size, shape and trajectory of the LEV formed behind an oscillating hydrofoil. Particle image velocimetry (PIV) experiments are performed to obtain the LEV characteristics and position over a wide range of pitch and heave amplitudes and oscillating frequencies. Qualitative and quantitative analysis is used to explain the trends observed in the characteristics of the LEV and its wake trajectory after it is shed from the foil.

The PIV measurements generate vast quantities of data—unsteady velocity fields—and to take advantage of these fields in ways that we cannot intuitively guess, we also report on the use of machine learning tools to predict the strength, shape and trajectory of the LEV wakes. These tools, if accurate (and we will demonstrate that they are promising), provide a unique ability to predict LEV behavior for parameter combinations that we have not tested and still do not have complete modeling capability. The ML tools, once trained, will be cheap to use in guiding future design of oscillating flow turbine arrays.

The paper is organized as follows. In the following section we describe the techniques used in the measurements and review the methods used for vortex identification and machine learning (ML) training. In Sec. III, we discuss the experimental results, including the scaling of the vortex characteristics, as well as the success of a simple potential flow model used to predict the vortex trajectory after separation. The accuracy and limitations of the ML modeling is presented and discussed in Sec. II C. Some concluding remarks complete the paper in Sec. IV.

II. EXPERIMENTAL METHODS

A. Experimental setup

The experiments were conducted in the free-surface water flume at Brown University, with a 0.8 m wide and 0.6 m deep test section. The testing configuration is largely the same as that of Su *et al.* [19,20] and Ribeiro *et al.* [21], and consists of a single vertically mounted hydrofoil with

TABLE I. The kinematic parameters of an oscillating hydrofoil explored in this study, the corresponding number of velocity field frames used for machine learning training matrix, and whether they were phase-averaged data. The kinematics are arranged in ascending order of $\alpha_{T/4}$, the relative angle of attack at midstroke.

f^*	θ_0 (deg)	h_0/c	$\alpha_{T/4}$	# Frames	Phase avg.
0.12	55	1	0.31	187	O
0.12	65	1.25	0.38	20	X
0.15	65	1	0.38	20	X
0.12	65	1	0.49	187	O
0.12	65	0.75	0.62	22	X
0.12	75	1	0.66	185	O
0.08	65	1	0.67	13	X
0.12	65	0.5	0.77	186	O
0.12	85	1	0.84	24	X

an elliptical cross section, with a chord length of 10 cm, and an aspect ratio of 3.5. End plates are mounted at each end of the foil to minimize effects from tip vortices.

PIV was performed to obtain the flow field around the hydrofoil and in the wake. The PIV setup is similar to that described by Su [19,20]. The laser sheet was generated by a double-pulse laser (200 mJ Nd:YAG, EverGreen, Quantel USA, MT) with a wavelength (λ) of 532 nm. The flow was seeded with silver-coated hollow ceramic spheres (diameter: 100 μm, Potter Industries). Four Imager sCMOS cameras with 35 mm lenses were used to record the flow images at 15 Hz and the flow fields were calculated using Davis (v10, LaVision). A slightly modified experimental set up was used to obtain a second set of PIV data, used to verify the machine learning predictions. Figure 1 shows the camera configuration for these experiments, which used a single sCMOS camera (4 MegaPixels), capturing the flow field with the aid of a mirror positioned below the water flume, angled at 45°.

The hydrofoil can execute computer-controlled heaving and pitching motions. A linear servo motors (AeroTech) is used for the heaving motion and a stepper motor (Applied Motion Products) for the pitching motion. The pitch axis of the foil is located at the midchord. The pitching and heaving motions are described by

$$\theta(t) = \theta_0 \sin(2\pi f t + \phi), \tag{1}$$

$$h(t) = h_0 \sin(2\pi f t), \tag{2}$$

where θ_0 and h_0 are maximum pitching and heaving amplitudes, respectively, f is the oscillation frequency, and ϕ is the phase difference between the two motions. A phase difference of $\phi = \pi/2$ was used for all experiments, the value for the optimal energy harvesting performance [2]. The effective angle-of-attack of the foil at midstroke ($t/T = 0.25$), $\alpha_{T/4}$ is defined as

$$\alpha_{T/4} = \tan^{-1}(-2\pi\ h_0/c\ fc/U_\infty) + \theta_0, \tag{3}$$

and has been shown [4,21] to be a useful parameter to describe the overall energy-harvesting efficiency of the hydrofoil.

Table I shows the range of foil kinematics measured with the PIV experiments. They were conducted at three different reduced frequencies, $f^* = fc/U_\infty = 0.08$, 0.12, and 0.15. Pitching and heaving amplitudes were varied when f^* was fixed at 0.12. The pitching amplitude, θ_0, was varied from 55° to 85° in increments of 10°, while the heaving amplitude, h_0/c, was varied from 0.5 to 1.25 in increments of 0.25. At other frequencies, the pitching and heaving amplitudes were fixed at 65° and 1.0, respectively. These parameter combinations resulted in a variation of $\alpha_{T/4}$ ranging from 0.31 to 0.84.

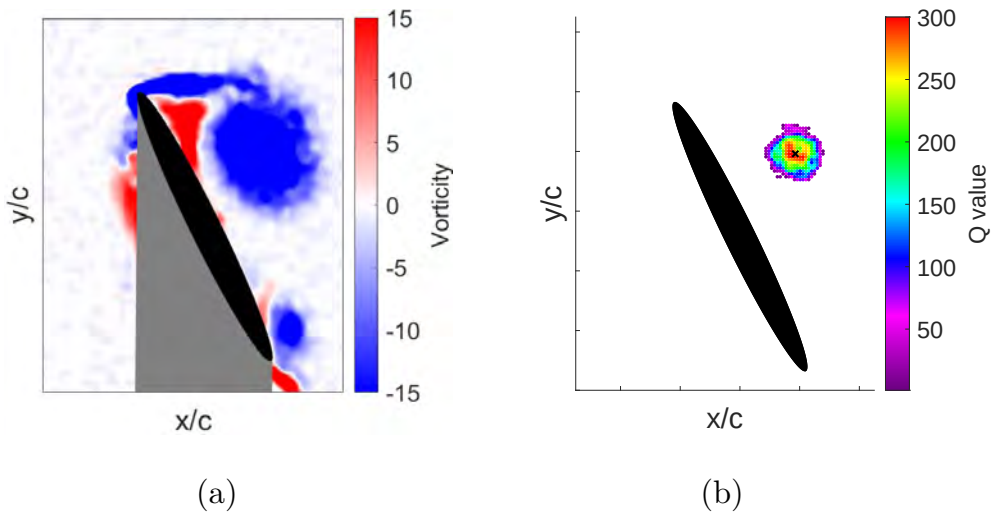


FIG. 2. An example of Q criterion used to detect and track LEV from the velocity field and its corresponding vorticity field. The foil's operating kinematics are: $f^* = 0.12$, $\theta_0 = 65^\circ$, $h_0/c = 0.5$ at $t/T = 0.30$. (a) Nondimensionalized vorticity field for a typical case during midstroke from the PIV measurements. (b) The corresponding "cloud" of Q values of the flow field. The black marker indicates the location of the LEV centroid.

B. Vortex tracking

The oscillating flow turbine is characterized by the formation, growth, separation, and advection of a strong leading-edge vortex (LEV) [3,4]. A typical velocity field, obtained from PIV measurements is shown in Fig. 2(a). The LEV was detected and tracked using the Q criterion [22]. The gradient of the velocity field, $\nabla\mathbf{v}(\boldsymbol{x}, t)$, can be decomposed into the sum of the rate of vorticity tensor and the rate of strain tensor: $\nabla\mathbf{v} = \boldsymbol{\Omega} + \boldsymbol{S}$, where

$$\boldsymbol{\Omega} = \tfrac{1}{2}[\nabla\mathbf{v} + (\nabla\mathbf{v})^T], \tag{4}$$

and

$$\boldsymbol{S} = \tfrac{1}{2}[\nabla\mathbf{v} - (\nabla\mathbf{v})^T]. \tag{5}$$

Here, T denotes the transpose of a matrix.

The Q value is defined as

$$Q = \tfrac{1}{2}[|\boldsymbol{\Omega}|^2 - |\boldsymbol{S}|^2], \tag{6}$$

and a "vortex" is identified as regions where the norm of the rate of vorticity tensor is greater than that of the rate of strain tensor, $Q > 0$. For this study, an interrogation window was drawn manually around the vortex observed from the PIV field data to fully capture the LEV in each frame. The size of the window is dependent on the kinematics of the foil which affects the size of the LEV. It, however, does not exceed beyond a chord length. This agrees with the findings of Rival *et al.* [23], where they discovered that the critical LEV diameter is one chord length. Q values were then calculated from the velocity field [Eq. (6)]. The centroid of the maximum 300 Q values was then used to define the position of the LEV core [Fig. 2(b)]. For each vortex, an ellipse with the same image moment (i.e., the equivalent moment ellipse) was fitted. The lengths of the two semi-axes of the ellipse was used to define the vortex size, shape, and orientation.

C. Machine learning

The Machine Learning Toolbox (MATLAB, Mathworks, Natick, MA) was used to train machine learning regression models that predict vortex characteristics and behavior. Several machine learning algorithms were evaluated before settling on Gaussian process regression (GPR) and support

vector machines (SVM) for use in this work. These were chosen for their robustness against outliers and overall flexibility [24]. GPR models are nonparametric kernel-based probabilistic models [25]. Gaussian processes (GPs) develop these kernels adaptively based on the available data, and provide probability distributions for the respective model parameters. GPs have been used extensively in time-dependent problems, which makes them appealing for our study of LEV behavior over time. Furthermore, with a proper choice of kernel function, the prediction capabilities of a GPR model can be enhanced. As we have observed exponential behavior in the physics of an LEV (such as vortex strength decay), the exponential kernel function was chosen. However, it should be noted that GPR can be computationally expensive which could be problematic with increasing data size [26].

While the exponential GPR is proved to perform well for many of our parameters, it does not handle discontinuities very well [27]. This is problematic for the vortex trajectory predictions which exhibit rapid changes in direction when they separate from the hydrofoil (as discussed in later sections). For this reason, support vector regression (SVR) was used to predict the x and y position of the LEV. SVR is an extension of SVM—a popular machine learning algorithm used for classification [28]. In the field of fluid mechanics, SVR has been successfully applied to turbulence modeling and reduced-order modeling [29]. The implementation employed in the current work is the linear epsilon-insensitive SVM (ϵ-SVM) regression. Here, the value of ϵ defines a margin of tolerance where no penalty is given to errors. In ϵ-SVM regression, the set of training data includes the velocity fields as well as several predictor variables and the observed response values. The training goal is to find a function that deviates from the ground truth, by a value no greater than a specified tolerance ϵ for each training point x, and at the same time is as flat as possible and thus less sensitive to perturbations in the features [25]. The user can tune ϵ against noise through a "loss function," which balances the various learning objectives (e.g., accuracy, simplicity, smoothness, etc.) [26]. SVM algorithms use a set kernel function, which in this case we choose a third-order polynomial ("cubic"). SVM has the advantage that it is capable of maintaining higher precision in the case of nonlinearity and small samples [30], thus amenable to the small data set of non-phase-averaged velocity fields. It is also computationally inexpensive in comparison to the GPR.

1. Training process

A separate training was performed for each of five different response values: the x and y position of the vortex, its size (defined by the the lengths of the semi-axes of its equivalent moment ellispe), orientation, and Q value. For each training performed, a total of 844 experimentally measured velocity fields, each with two components of velocity (u, v), were used as the basis of the training data, sampled from the range of parameters identified in Table I and at different times, t/T, during the pitch-heave cycle. A mix of phase-averaged and instantaneous flow fields were used depending on data availability (see Table I). Each velocity field in the training set also included the appropriate response value as well as several other predictor values: the relative angle of attack at midstroke, $\alpha_{T/4}$, the nondimensional frequency, f^*, the heaving and pitching positions, $h(t)$, $\theta(t)$, and the nondimensional cycle time, t/T. All values were appropriately normalized by freestream velocity, chord, frequency. The Q value was normalized by its maximum value for that specific set of kinematics.

A good supervised machine learning model should be generalizable, providing good predictions from previously unseen data. In this respect, cross-validating the model prevents overfitting and prevents the model to fit the training data perfectly at the cost of its generalizability and real life applications [26]. In this study, the selected scheme of cross-validation was tenfold cross-validation. The training data was partitioned so that 30% of the data was also used for validation.

The prime metric for assessing the performance of the trained model in predicting a generic quantity, a, is the root-mean-square error (RMSE):

$$\mathrm{RMSE}_a = \sqrt{\sum_{i=1}^{n} \frac{(\hat{a}_i - a_i)^2}{n}}, \tag{7}$$

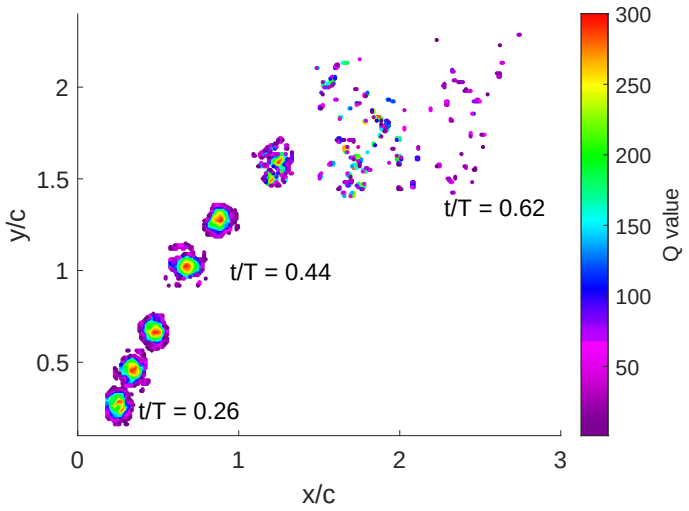


FIG. 3. An example of the evolution of the leading-edge vortex (LEV), as a function of time as indicated by the movement of clouds of Q values. The largest 300 Q values for each time are plotted. The tracking begins at $t/T = 0.26$ and ends at $t/T = 0.64$, while the clouds of Q values are captured every 0.06 t/T. The growth, separation and advection of the LEV is typical over almost all parameter combinations. In this case, the kinematics are: $f^* = 0.12,\ \theta_0 = 85^\circ,\ h_0/c = 1, \alpha_{T/4} = 0.84$.

where n is the size of the training data set (in this study, 844 fields). $\hat{a}_i$ are the predicted values of the variable a generated by the machine learning process—for example, the x location of the LEV, its normalized Q strength, etc. In contrast, a_i are the ground-truth data.

III. RESULTS AND DISCUSSION

A. LEV behavior

A qualitative view of the vortex core, represented by the Q-value "cloud" (Fig. 3), clearly shows the LEV growing in strength, as the increase in the red area of the LEV from $t/T = 0.26$ to $t/T = 0.44$ indicates. The LEV then separates from the foil and dissipates in the wake as it travels downstream. The evolution of the vortex strength was quantified by taking the average of the highest 50 Q values from the 300 points within the cloud for each frame in time (Fig. 4). The top 50 Q values rather than just one maximum point were chosen because it reduced some of the frame-to-frame fluctuations among the maximum average Q values; increasing the quantity beyond 50 did not yield any noticeable improvement. The LEV is formed early in the cycle, and retains its high strength, as vorticity is continuously fed into the vortex from the feeding shear layer that connects the LEV to the leading edge of the hydrofoil.

At about $t/T = 0.44$, as the foil nears the pitch reversal point ($t/T = 0.5$), the LEV separates (indicated by the red marker in Fig. 4), and advects downstream. After separation, the vortex begins to decay exponentially in strength (Fig. 4). For the example shown, $\bar{Q}_{\max} \sim \exp(-18.8t/T)$.

The evolution of the size of the LEV also follows a characteristic pattern. From the cloud of Q points, ellipses that have the same position and image moments [31,32] are fitted. A typical example of the evolution of the LEV size is shown in Fig. 4. Confirming our qualitative assessment (Fig. 3) we see that the vortex remains as a stronger and compact structure until the point of separation (marked in red). After LEV separates from the foil, new vorticity is no longer being fed into the vortex and the vortex strength starts to decay. At the same time, we see a rapid increase in the area of the equivalent moment ellipse. Both the amplitude decay and area increase are due to a combination of turbulent dissipation and 3D mixing by the tip vortex.

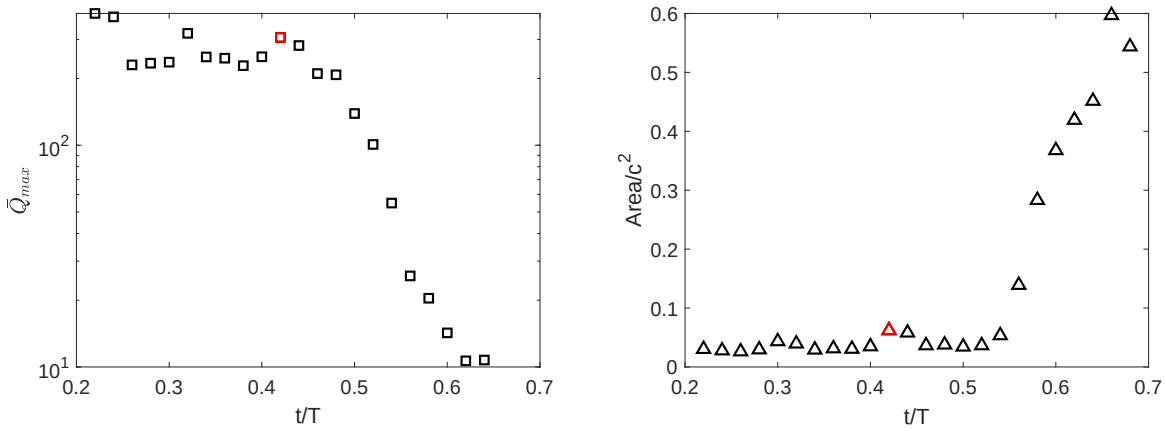


FIG. 4. An example of the evolution of the vortex strength, $\bar{Q}_{\max}$ (left), and area (right), as a function of time. The red marker indicates the point of separation of the LEV from the leading edge, determined by a visual assessment of the vorticity plot. The foil's operating kinematics are: $f^* = 0.12,\ \theta_0 = 85^\circ,\ h_0/c = 1, \alpha_{T/4} = 0.84$.

Although the kinematics are defined by three parameters: the nondimensional frequency of oscillation, f^*, heaving amplitude, h_0/c, and pitching amplitude, θ_0, the maximum strength of the LEV, as measured by the highest $\bar{Q}_{\max}$ throughout the cycle [i.e., $\max(\bar{Q}_{\max})$], is well predicted by the relative angle of attack at midupstroke, $\alpha_{T/4}$ [Eq. (3)], and shows a monotonic rise over the range of $\alpha_{T/4}$ considered (Fig. 5). A purely empirical fit of this behavior is given by: $\max(\bar{Q}_{\max}) = 377.51 \log(\alpha_{T/4}) + 584.29$. Similar results were found by Ribeiro *et al.* [21], who found from both PIV measurements and DNS simulations that, with few exceptions, the strength of the primary leading-edge vortex increases with increasing relative angle of attack.

B. Behavior of the LEV trajectory in the wake

1. Experimental observations

Using the Q-criterion method of vortex detection, we identify the trajectory that the LEV follows in the PIV field of view—approximately 2 to 2.5 chord lengths downstream from the foil. Two

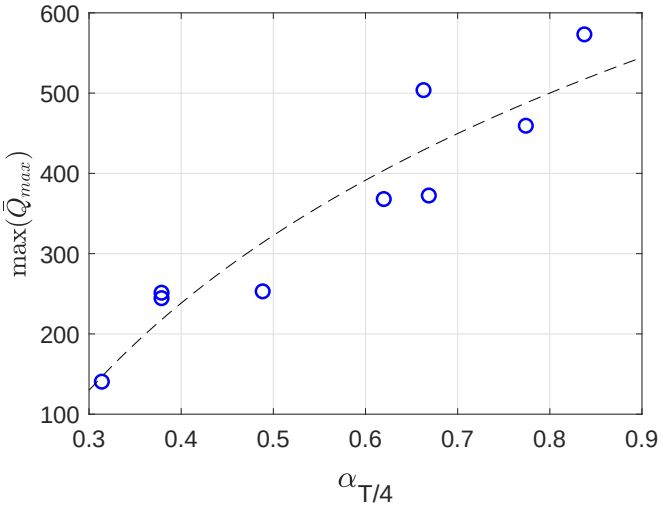


FIG. 5. Strength of the highest $\bar{Q}_{\max}$ throughout the cycle, or $\max(\bar{Q}_{\max})$, for various values of $\alpha_{T/4}$. The best fit line follows the equation $377.51 \log(\alpha_{T/4}) + 584.29$.

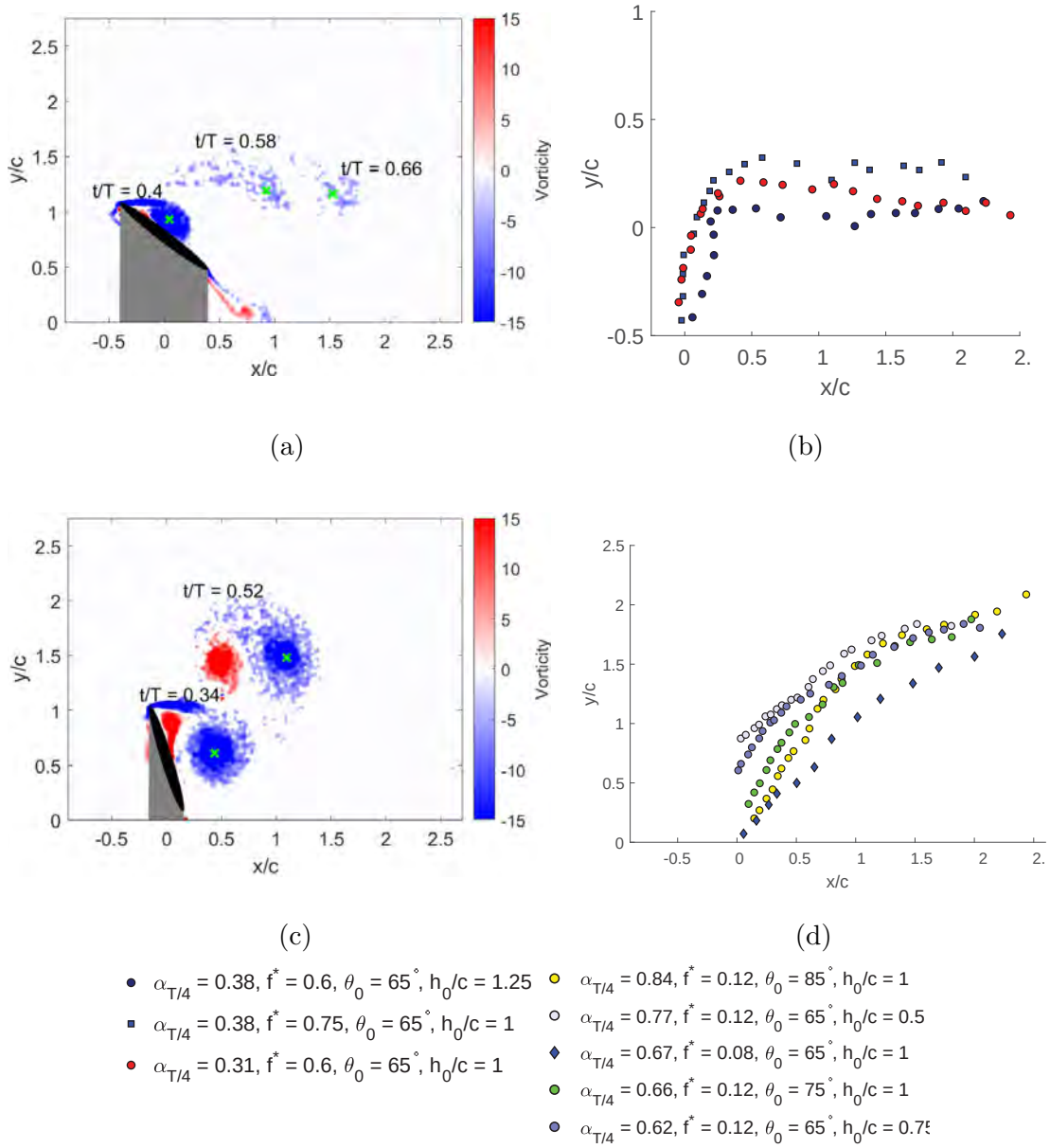


FIG. 6. (a) Snapshots at different points in time of a typical PIV vorticity plot of a LEV developing under the LEV regime. The tracked positions of the LEV centroid are indicated by green crosses. The foil kinematics for this example are: $f^* = 0.12$, $\theta_0 = 55°$, $h_0/c = 1$. (b) Trajectories of 4 different kinematics in LEV regime. The vortices follow a steep upwards motion early in the trajectory. After separation, LEVs convect downstream with relatively small y displacements. (c) Snapshots at different points in time of a typical PIV vorticity plot of a vortex pair developing under the LEV+TEV regime. Only the LEV is tracked. The foil kinematics for this example are $f^* = 0.12$, $\theta_0 = 85°$, $h_0/c = 1$. (d) Trajectories of five different kinematics in the LEV+TEV regime. The initial steep upwards motion is still seen. After separation, however, LEVs continue to retain positive y velocity.

regimes of trajectories were identified. The LEV trajectories for values of $\alpha_{T/4}$ below ∼0.5 can be seen in Fig. 6(b) and will be denoted as the "LEV regime" following the nomenclature by Ribeiro *et al.* [21]. In this regime, the LEV initially remains attached to leading edge as the foil heaves upwards and follows its motion. It detaches from the foil soon after the foil reaches its maximum

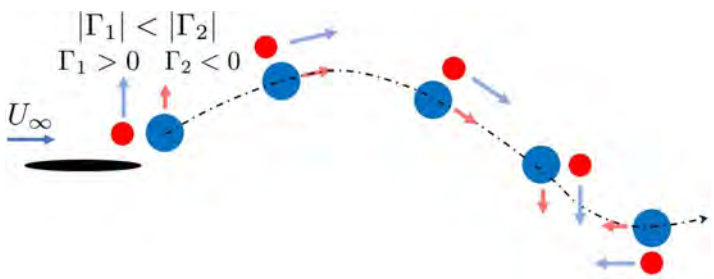


FIG. 7. The interaction between the LEV and the TEV and the resultant trajectory characteristic to LEV+TEV regime. The circles represent the two vortices with the colors indicating the sign of circulation. The arrow indicates the direction of induced velocity.

heave amplitude, subsequently advecting downstream with minimal y displacement, which results in this regime's characteristic "hockey stick" trajectory.

At higher values of $\alpha_{T/4}$ greater than 0.49, the trend in trajectory changes [Fig. 6(d)]. This regime is denoted as "LEV+TEV regime" [21], and is characterized by the presence of an additional vortex, of opposite sign, in the flow field. Depending on the foil kinematics, this new vortex is formed either due to separation at the trailing edge which creates a trailing-edge vortex (TEV), or by the vorticity sheet that forms below the LEV on the upper surface of the foil consolidating into a vortex at the trailing edge and shed into the wake. In the LEV+TEV regime, the LEVs share a similar initial trajectory when the foil remains attached to the leading edge. After separation, however, the vortex exhibits a positive y velocity and forms a curved trajectory as it travels downstream.

The straight downstream trajectory of the separated LEV for low values of $\alpha_{T/4}$ are simply due to the fact that the vortices travel with the local flow, and the local flow is predominantly in the x direction. In contrast, the cause of the positive y velocity in the LEV+TEV regime is likely a consequence of the presence of the additional vortex which interacts with the LEV. The counterclockwise vortex's counterclockwise rotation induces the upwards motion of the LEV, while the clockwise rotation of the clockwise vortex induces the same effect on the TEV. The LEV trajectory resultant from this interaction is illustrated schematically in Fig. 7.

2. Potential flow model

To verify this explanation of the vortex trajectories observed in the LEV+TEV regime, a simple model based on potential flow theory was tested. The LEV and TEV each induce a velocity on the other: $u_i = \frac{\Gamma_j}{4\pi d}$ where Γ_j is the circulation and $2d$ is the distance between the vortex cores. The circulation is obtained by taking a contour integral of the velocity field from the PIV measurements.

The circulation of the LEV and TEV were assumed to be constant, established at the time the vortices separated from the hydrofoil. The position of each vortex, the vortex separation and the respective induced velocity vectors were updated in time using a MATLAB script to generate a predicted trajectory for the vortex pair. To incorporate the sensitivity of the trajectory predictions to uncertainties in the initial vortex positions and strengths, a Monte Carlo method was used, where the position of the contour integral and the vortex location was varied by up to 0.1c, and a total of 100 trajectories were generated and averaged to obtain a mean trajectory and uncertainty limit. Viscous decay was ignored in this model.

An example of the result from this simulation is shown in Fig. 8. The predictions based on potential flow theory agree well with the experimental data, capturing the upward motion of the LEV that is characteristic of LEV+TEV regime. It should be noted, however, that the three dimensional effects from tip vortex contribute to the experimental vortex trajectory which results a decrease in accuracy of the two-vortex potential flow model. However, the potential flow model was also applied to CFD data of oscillating foils' vortex wake [18] for which longer downstream evolutions were

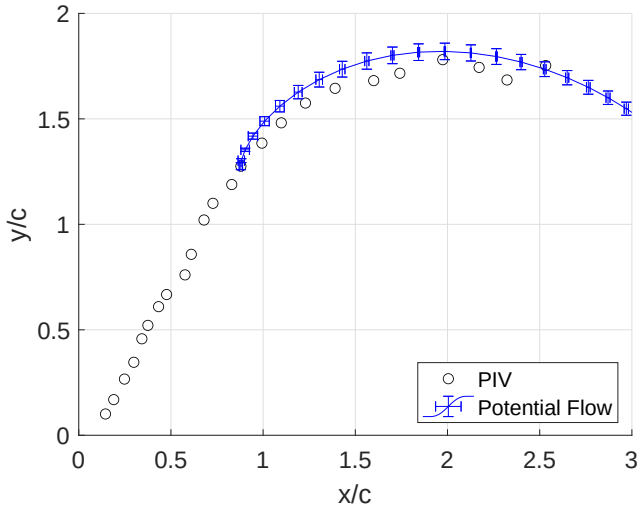


FIG. 8. An example of the comparison between a trajectory predicted from the potential flow model and a trajectory obtained experimentally. The error bars represent the standard deviation of Monte Carlo simulation of the potential flow model. The kinematics of the foil (a) $f^* = 0.12$, $\theta_0 = 85^\circ$, $h_0/c = 1$.

available. The model also demonstrated excellent agreement over a range of operating conditions (Fig. 9).

In cases where the model prediction was less faithful to the observations, largely two types of deviations can be observed. The first is when the predicted initial slope of the upwards motion was not as steep as the CFD data indicated [e.g., Fig. 9(d)]. This error can be attributed to the sensitivity of the model to the vortex circulation. The second deviation between the model and the observations were increasing errors as the LEV traveled downstream [e.g., Fig. 9(c)] shows that the predicted trajectory begins to flatten at $x/c = 3$ while the vortex predicted by the CFD data travels further down in y direction. The CFD data shows additional vortex formations that occur which the potential flow model does not take into account. The resultant interactions between numerous vortices likely causes these differences.

In summary, the LEV trajectory characteristics of the LEV+TEV regime is due to the introduction of a vortex of opposite sign. The direction of the velocity induced by the new vortex depends on the position of the TEV with respect to the LEV. When the vortex pair is initially shed from the foil, there is a net positive y velocity. Because the circulation of the LEV is greater than that of the TEV, the TEV moves faster and orbits about the LEV. When the TEV has rotated more than 90 degrees, a net negative velocity is induced. Therefore, a downward concave curve is observed in the experiments. After the TEV rotates 270 degrees about the LEV, the induced velocity is in the positive y direction once again which flattens out the trajectory. This occurs at approximately $x/c \sim 3$–4. Beyond that point, the same interaction will eventually cause a change in direction within the trajectory.

C. Machine learning

After the training process outlined in Sec. II, the models that provided the optimal results are outlined in Table II which includes the quantitative errors. The training times were attained using Intel Core i7-6700HQ CPU and GeForce GTX 960M GPU.

A qualitative assessment of the success of the machine learning process is the "predicted-versus-actual" plot [25,33], the results of which are shown in Fig. 10 for each of the quantities tested. A high performance model should have points clustered along the 1:1 diagonal, with small deviations. If any clear patterns, different from the perfect prediction diagonal, are observed in the plot, it is

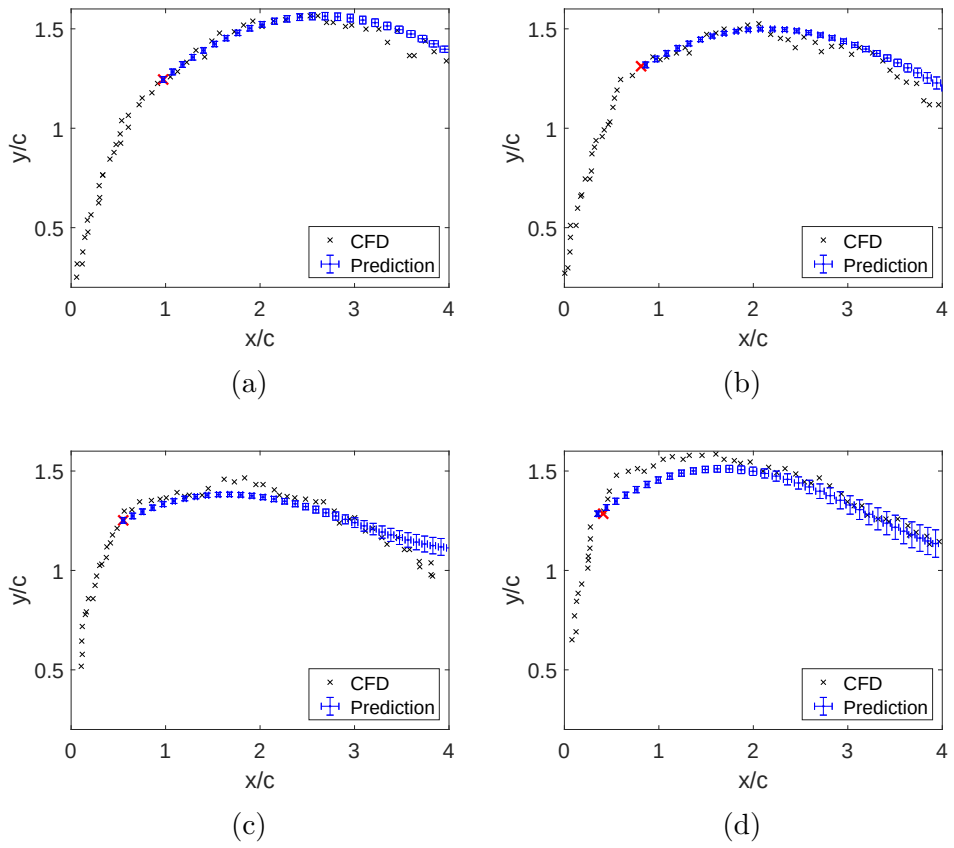


FIG. 9. Four examples of the comparison between a trajectory predicted from the potential flow model and a trajectory obtained from the vortex formations in the CFD data. The error bars represent the standard deviation of Monte Carlo simulation. Red cross indicates the point of separation of the LEV from the leading edge. The kinematics of the foil are: (a) $f^* = 0.10$, $\theta_0 = 65^\circ$, $h_0/c = 1$. (b) $f^* = 0.11$, $\theta_0 = 65^\circ$, $h_0/c = 1$. (c) $f^* = 0.12$, $\theta_0 = 65^\circ$, $h_0/c = 1$. (d) $f^* = 0.15$, $\theta_0 = 75^\circ$, $h_0/c = 1$.

likely that the model can be improved and different types of models can be explored to ensure the most optimal results.

Overall, it can be seen that the regression model predictions of the LEV positions [Figs. 10(a) and 10(b)] agree very well with training data, as demonstrated by the points being clustered around the 1:1 line. Note that the horizontal bands in each of the predicted-versus-actual plot reflect the fact that at each value of t/T, the model predicts a single value for the (x, y) position of the LEV, but uses multiple individual realizations as part of the training data.

TABLE II. Summary of models used for each feature predicting algorithm with their training times and root-mean-square errors [Eq. (7)].

Predicted feature	Model	Time (s)	RMSE
X position	Cubic SVM	12.50	0.11
Y position	Cubic SVM	17.49	0.072
$\bar{Q}_{\max}/\max(\bar{Q}_{\max})$	Exponential GPR	29.19	0.16
Ellipse major axis	Exponential GPR	23.52	0.058
Ellipse minor axis	Exponential GPR	46.14	0.038

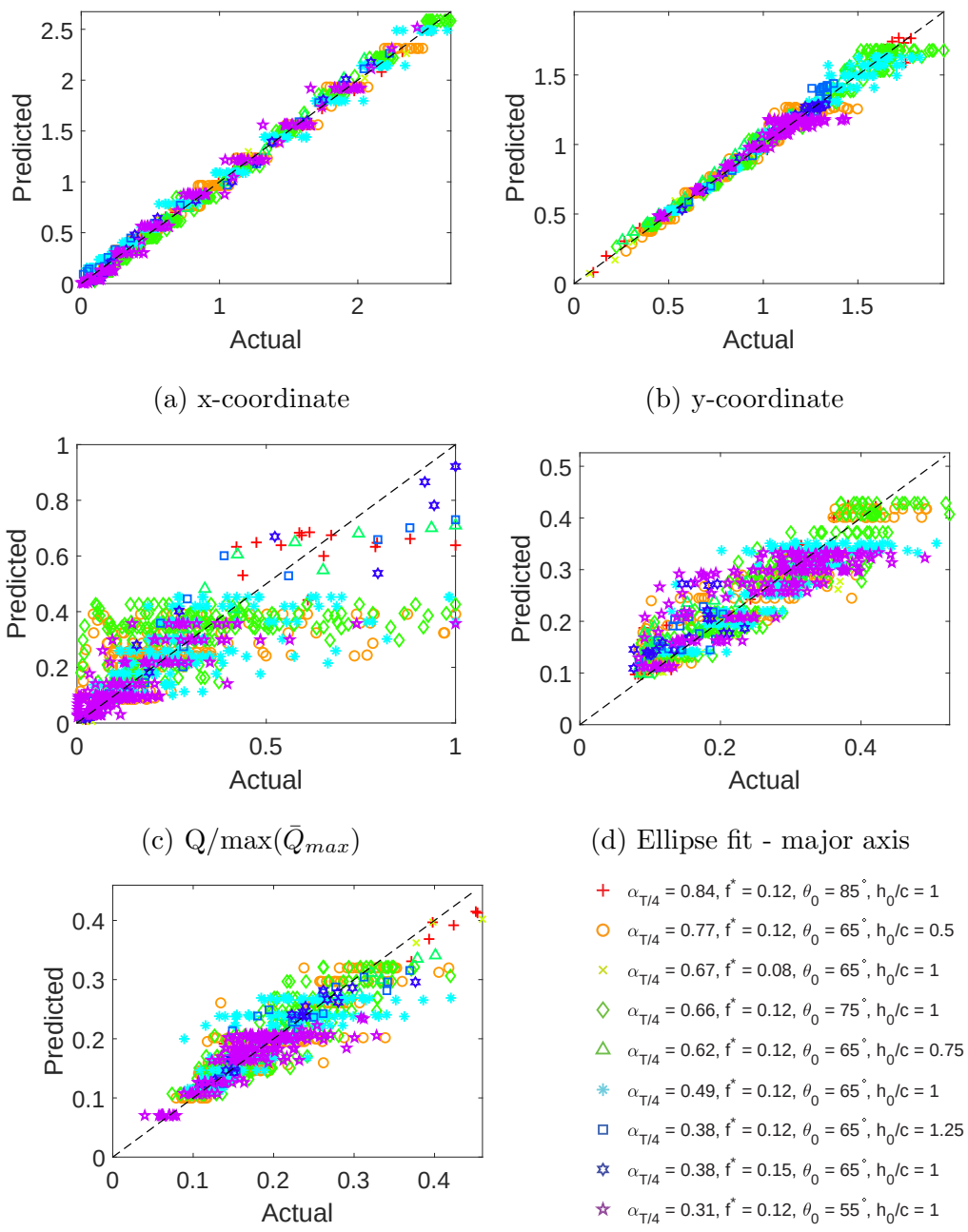
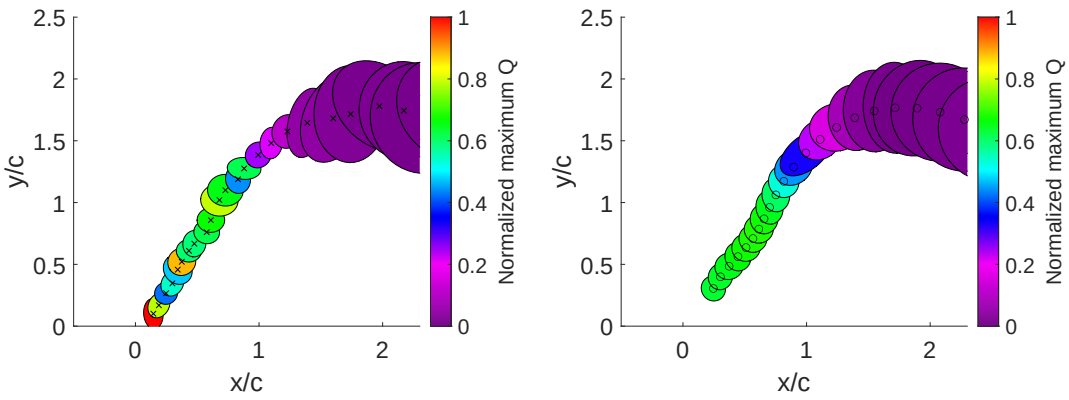


FIG. 10. The ML performance per predicted variable as demonstrated by the "predicted vs actual" plot. The black diagonal line represents a perfect prediction, while the plot markers represent the actual true response of the ML algorithm for each PIV frame used in the training. Due to the non-phase-averaged nature of the training data, multiple actual values exist for each kinematics resulting in a horizontal "line" in the plots. The length of this line represents the range of the actual value within the training data. The predicted values are: (a) centroid x coordinate, (b) centroid y coordinate, (c) $Q/\max(\bar{Q}_{\max})$, (d) major axis of equivalent ellipse, (e) minor axis of equivalent ellipse.



(a) Measured (b) Predicted

FIG. 11. A comparison between the measured LEV trajectory (a) and the equivalent predicted trajectory (b) at foil kinematics $f^* = 0.12,\ \theta_0 = 85^\circ,\ h_0/c = 1$. Dark crosses and circles represent the centroids of the LEV. The ellipse represents the LEV's equivalent moment ellipses while their colors represent the maximum value of Q that occurs within the vortex. The maximum Q values are normalized by the highest value that occurs in the cycle.

The shape of the best-fit ellipse [Figs. 10(d) and 10(e)], is also well predicted by the regression, although not as successfully as the position prediction. The "rounder" appearance of the point cluster indicates that the predictions are less accurate when the LEV is midsized, and more accurate at the early and late stages of its evolution.

The prediction of the Q value [Fig. 10(c)] exhibits the worst performance, particularly for high values of Q where the ML consistently underpredicts Q, particularly for the midrange values of $\alpha_{T/4}$. This weakness corresponds to early in the vortex shedding cycle where the Q value is high, but interestingly, the prediction is much better as the vortex weakens, corresponding to the later times in the cycle. From the perspective of developing a tool to predict the location and strength of shed vortices for tandem foil vortex interactions, this is encouraging performance. Although the maximum Q value of the vortex is useful, it is more important to accurately estimate the position and strength of the shed vortex further downstream at the point where it will interact with a second foil, or downstream object.

As long as the parameters remain similar to the range of the parameters used in the training data (Table I), we should be able to use the machine learning results to predict the trajectory of an LEV formed from a oscillating hydrofoil. To reassure model's performance, a test parameter combination within the training data is used and a similar vortex tracking is observed between measured and predicted (Fig. 11).

However, the power of any machine learning utility is to compare predicted and observed LEV trajectories for parameter combinations that are not part of the training data. Qualitatively, a high performance model should accurately capture the (i) the sharp increase in the y-position early in the cycle, reflective of the movement of the foil, (ii) the development of a high Q value during this early stage where the LEV is still attached to the foil, (iii) a change in behavior after separation, determined by the trajectory regime which is dependent on $\alpha_{T/4}$, (iv) an increase in vortex size during this stage, reflective of the diffusion of the vortex, and lastly, (v) a decrease in the Q value after separation from the foil, reflecting the vortex decay. Four parameter combinations, detailed in Table III, were used to test the accuracy of the ML regression. Two cases are at the nondimensional frequency $f^* = 0.12$, which was a common frequency in the training data, while the other two cases lie well outside the training range.

Figure 12 shows a side-by-side comparison between the measured trajectory obtained from PIV data analysis (left) and the corresponding machine learning prediction (right). At first glance, it can

TABLE III. The kinematic parameters of an oscillating hydrofoil used for machine learning verification.

Case	f^*	θ_0 (deg)	h_0/c	$\alpha_{T/4}$
i	0.12	80	1	0.75
ii	0.10	75	1	0.75
iii	0.12	70	1	0.58
iv	0.10	55	1	0.40

be seen that the predicted and true vortex characteristics agree with each other. The time-dependent traits, such as a decrease in vortex strength, represented by the colors of the vortices, and the increase in the size of the vortices, represented by the size of the equivalent ellipses, are accurately captured. The change in the y velocity of the vortex between the LEV and the LEV+TEV regime is also reasonably well captured.

The differences between the observed and predicted behavior is instructive. The regression machine learning models tend to predict trajectories that are smoother, and the abrupt changes in direction—the "hockey-stick" trajectories observed at low $\alpha_{T/4}$ are less pronounced in the predictions, replaced by smoother paths. An example of this is the trajectory of the LEVs shown in Figs. 12(e) and 12(f). In the PIV data, at approximately $x/c = 0.3$, the LEV abruptly changes course once separation from the foil occurs. The machine learning model's interpretation of this behavior qualitatively agrees, but is much more gradual, resulting in a smoother trajectory.

A point to concern when selecting training parameters is the possible coupling between different input variables which, if present, may reduce the accuracy of the predictions if not taken into account. For example, in a limited study, a single model was trained to simultaneously predict both the x and y positions of the LEV. This model yielded similar, but at times, poorer, predictions compared to those generated by the independent models. The lack of improvement may come from the fact the change in the x position is dominated by the freestream velocity, which is significantly greater than the induced velocity in the x direction from the vortex pair interaction. In contrast, the y trajectory is strongly affected by the induced velocity of the second vortex.

Another distinct shortcoming in the machine learning performance is in the prediction of the LEV amplitude. This is already reflected in the predicted-actual data [Fig. 10(c)], and is confirmed here. Observing the development of the maximum normalized Q value through time in the experimental data in Fig. 12, we see that the LEV strength decays relatively slowly, retaining a high Q value greater than 0.5 early in the cycle, until the vortex convects to approximately $x/c = 1$. The higher normalized Q values are indicative of the LEV remaining attached to the leading edge of the foil. It is only after separation that the LEV begins to decay at significantly higher rate [e.g., Fig. 12(e)]. This behavior is not captured with the same accuracy by the machine learning predictions, which observe a more gradual decrease in the Q value [Fig. 12(f)] after separation. The consequence of this is that more frames are required to achieve the same change in the rapid change in Q. In some cases, the overall decay of the vortex seems delayed, retaining Q values near 1 until the point of separation. This issue can likely be resolved with a greater number of training data.

Despite these differences, the machine learning predictions for the LEV trajectories are remarkably accurate, and a quantitative analysis of the errors is shown in Fig. 13. Most of the time, the absolute position error (the distance between the actual and predicted LEV centroid positions) remains below 0.15c. As the trajectory evolves, the error accumulates, resulting in the highest overall errors at the larger times. The smoothing of the trajectory, mentioned above, also contributes to the error. In particular, between $t/T \sim 0.3$–0.4, and the LEV separates from the foil, the experimental trajectory experiences a sharp change in direction. As the machine learning equivalent smooths out the abrupt shift, the errors during this time period are larger, confirmed by the bumps observed for all four validation cases in Fig. 13.

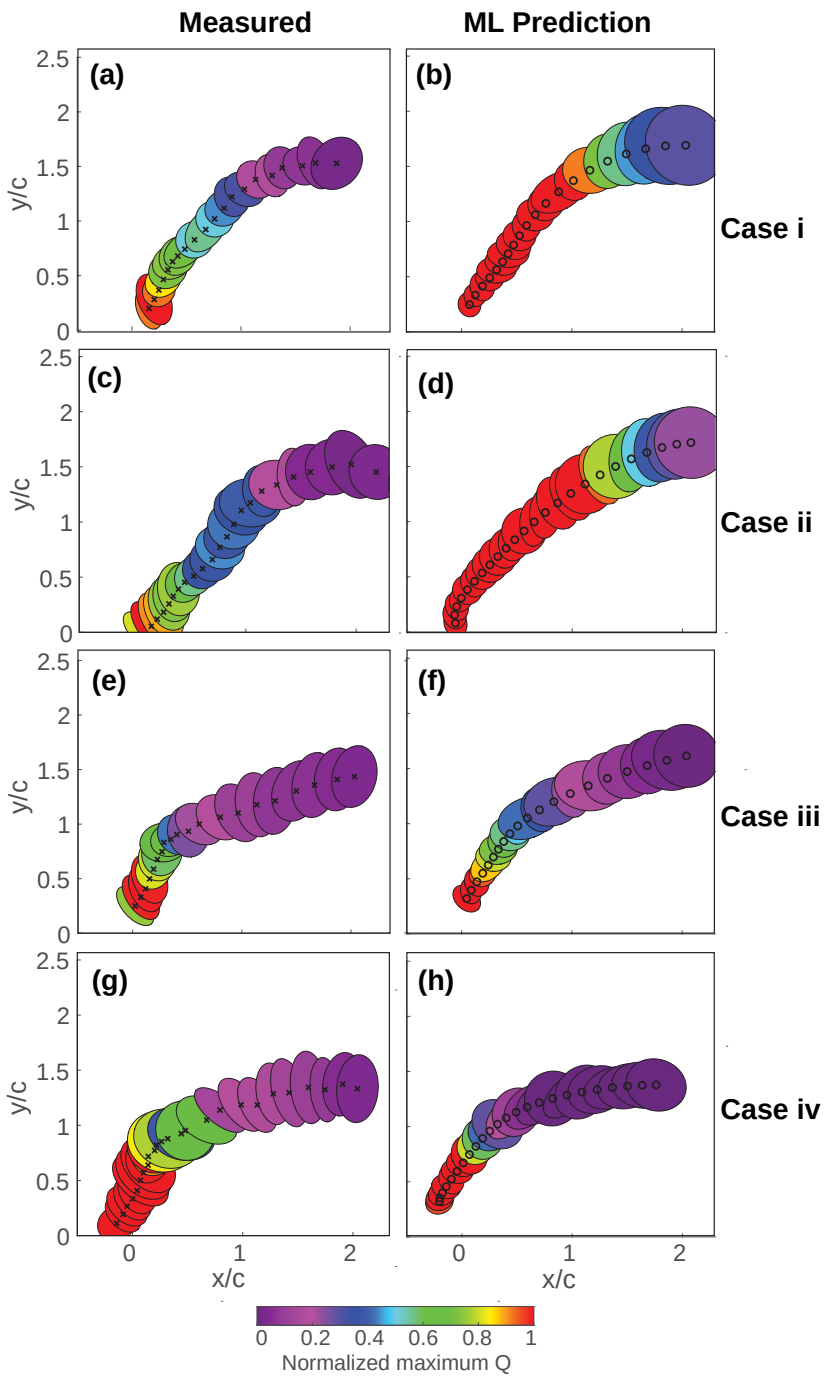
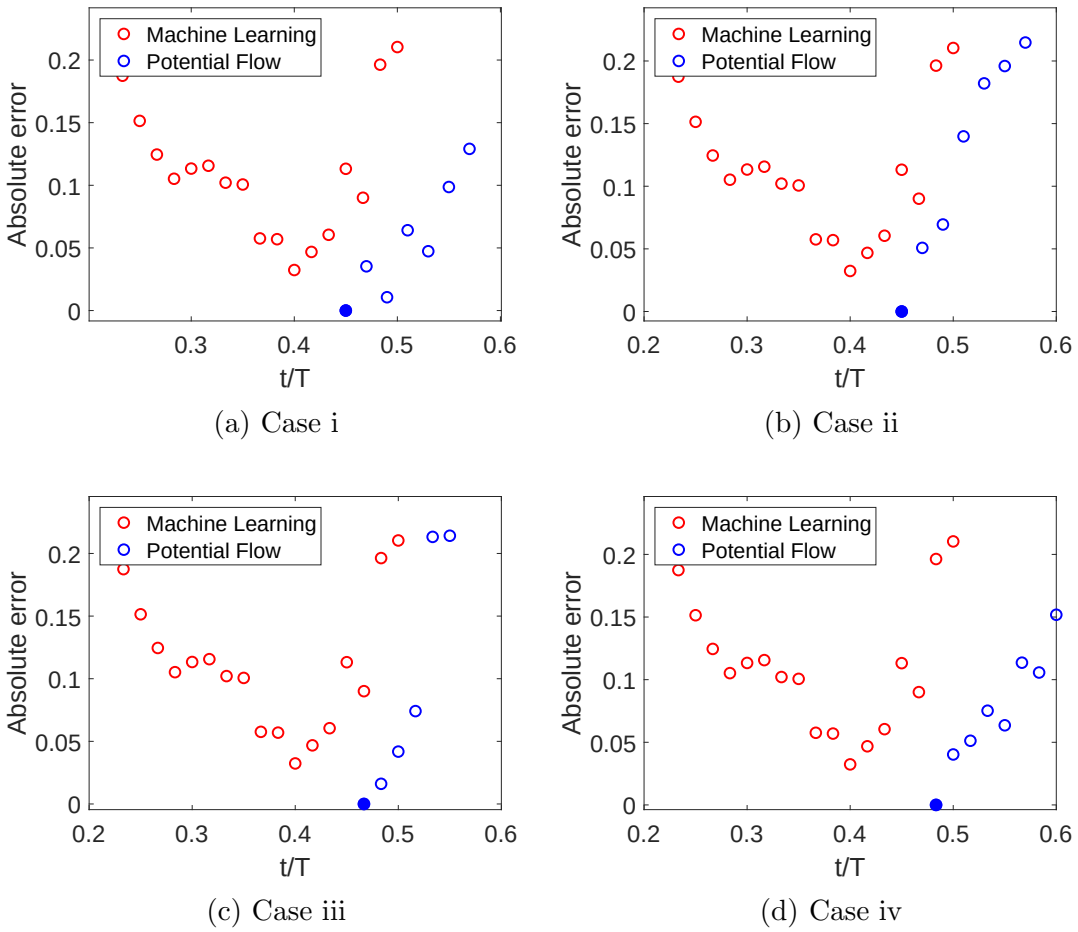


FIG. 12. Comparison between predicted and actual LEV trajectory. Left: PIV data; right: ML prediction. Dark crosses/circles represent the centroids of LEVs for PIV and ML, respectively. The color of the equivalent moment ellipse is based on the maximum Q value in the field, normalized by the maximum Q value over the entire cycle. Refer to Table III for foil kinematics.

Despite promising performance of the machine learning predictions, it can be seen in Fig. 13 that the ML prediction errors are higher than those of the potential flow model predictions, which are based on a physical analysis of the experimental data. However, it should be noted that the potential flow model is initiated at the point of separation with the inputs of the LEV-TEV vortex pair's respective positions and circulations. As such, it starts with the positional error of 0 at a much later



(a) Case i (b) Case ii

(c) Case iii (d) Case iv

FIG. 13. The position error, defined by the equation $\sqrt{(x_0 - x)^2 + (y_0 - y)^2}$, of the LEV trajectory predicted by machine learning and potential flow models compared to the measured trajectory. The solid blue marker indicates the time at which the potential flow model is initiated, and the error is thus zero. x_0, y_0 are the predicted x,y positions of the LEV centroids while x, y are the measured x, y positions. Refer to Table III for foil kinematics.

point in the cycle and an accurate measure of the key vortex circulation. Yet, we see that the rate of increase in the error is roughly similar to that of the machine learning model, indicating that the ML model performs as well as the potential flow model with regards to the propagation of the error. This, in addition to the fact that machine learning model is capable of generating a prediction from just the foil kinematic, means that the machine learning model could be an attractive alternative. Furthermore, once it is trained, the machine learning model produces its predictions in a much shorter time than the potential flow tool for forecasting the wake vortex topology without extensive measurements or further calculations.

IV. CONCLUDING REMARKS

The ability to accurately predict the formation, separation, and downstream trajectory of LEVs over a range of operating parameters is of fundamental interest, as well as of practical utility. Several physical systems rely on an accurate prediction of the strength and location of LEVs, including understanding the dynamics of fish schooling [34], as well as optimal placement within arrays of vertical axes wind turbines [15] or oscillating hydrofoils [21].

Here, a heaving-pitching hydrofoil is used to generate LEVs of varying strength, and in analyzing PIV measurements over a wide range of parameters, we have found that, although there are three

parameters needed to fully describe its motion—pitching, heaving amplitude, and frequency—the effective angle of attack at midstroke, $\alpha_{T/4}$, is a convenient quantity that collapses all three parameters and serves as an accurate predictor of subsequent LEV characteristics.

The strength of the LEV, measured by the maximum Q value, increases with $\alpha_{T/4}$. In agreement with other results [18], the trajectory that the LEV follows after separation can be loosely divided into two regimes: LEV and LEV+TEV regimes, where the transition occurs at approximately $\alpha_{T/4} = 0.49$. In both cases, the LEV follows the motion of the hydrofoil until separation. For the LEV regime, the LEV simply convects downstream with minimal y displacement. In contrast, in the LEV+TEV regime, an additional vortex with an opposite-signed strength is formed near the trailing edge. The presence of a vortex-pair results in a self-induced motion in the positive y direction—a motion very well described by a simple potential flow model that relies only on the knowledge of the vortex strengths and positions as they separate from the hydrofoil.

After gaining an understanding of the physics behind LEV trajectory, a machine learning approach was used to create a reduced-order modeling tool to capture trends that were found. Supervised regression machine learning was found to accurately predict numerous LEV characteristics over a wide range of foil kinematic parameters. The trained model was successful in capturing the two vortex trajectory regimes, as well as the progression of the vortex size and strength, particularly after the initial phase of vortex separation. Verification of the regression model, using additional PIV data, indicates that the error in the predicted trajectory is small, usually limited to 0.15 chord lengths.

Although there is no substitute for a detailed understanding the physics of LEV formation, separation, and advection, the machine learning (ML) tools provide the capability to generate useful predictions of the wake structure from just the foil kinematics without the need for time-consuming experiments or high-fidelity numerical simulations. The efficiency of the ML prediction is ideal for exploring a large parameter space required in optimization problems, and has the potential to be an attractive tool to rapidly reduce the size of the search space required to design arrays of oscillating hydrofoils that can harvest the energy from the LEV shed from upstream devices [15,18]. Of course, the ML results have clear limitations. In the present study we have trained the predictions at a single Reynolds number, and with a limited set of kinematics that only considers sinusoidal motion. Reynolds number effects on single foil performance have been shown to be very modest [18], although there is no data on Re effects on the wake behavior. In addition, extrapolation of the model for parameters that stray far from the training data would be of questionable reliability. As such, more complex kinematics may well prove attractive [35,36] but at this stage, it is not yet clear whether $\alpha_{T/4}$ will remain a good predictor of the leading foil performance [21] and how the ML predictions will fare as the kinematic space grows. These are clearly subjects for future study. Lastly, although these results show excellent promise, other deep learning techniques, such as convolutional neural networks [37] may prove to be an attractive alternative that might demonstrate better performance than is observed in this initial study.

ACKNOWLEDGMENTS

This research was funded by the U.S. National Science Foundation (CBET Award No. 1921594 to J.F. and B.R.; CBET Award No. 1921359 to K.B.), and the U.S. Air Force Office of Scientific Research (Grant No. FA9550-18-1-0322 to K.B., N.S., Y.S., and Y.Z.). H.L. was supported by the Karen T. Romer Undergraduate Teaching and Research Award from Brown University.

[1] N. D. Laws and B. P. Epps, Hydrokinetic energy conversion: Technology, research, and outlook, Renewable Sustain. Energy Rev. **57**, 1245 (2016).

[2] W. McKinney and J. DeLaurier, Wingmill: An oscillating-wing windmill, J. Energy **5**, 109 (1981).

[3] T. Kinsey and G. Dumas, Parametric study of an oscillating airfoil in a power-extraction regime, AIAA J. **46**, 1318 (2008).
[4] D. Kim, B. Strom, S. Mandre, and K. Breuer, Energy harvesting performance and flow structure of an oscillating hydrofoil with finite span, J. Fluids Struct. **70**, 314 (2017).
[5] T. Kinsey, G. Dumas, G. Lalande, J. Ruel, A. Méhut, P. Viarouge, J. Lemay, and Y. Jean, Prototype testing of a hydrokinetic turbine based on oscillating hydrofoils, Renew. Energy **36**, 1710 (2011).
[6] J. L. Cardona, M. J. Miller, T. Derecktor, S. Winckler, K. Volkmann, A. Medina, S. Cowles, R. Lorick, K. S. Breuer, and S. Mandre, Field-testing of a 1 kW oscillating hydrofoil energy harvesting system, in *Proceedings of the 4th Marine Energy Technology Symposium* (2016), Vol. 560, p. 5.
[7] S. Mandre, J. Franck, K. Breuer, A. Fawzi, J. Cardona, M. J. Miller, Y. Su, A. Medina, C. Loera Loera, E. Junquera, F. Simeski, K. Volkmann, R. Lorick, S. Cowles, B. Luiz Rocha Ribeiro, S. Winckler, and T. Derecktor, Oscillating hydrofoils for tidal energy extraction: Experiments, simulations and salt water field tests, in *AGU Fall Meeting Abstracts* (2015), Vol. 2015, pp. GC53C–1216.
[8] B. Simpson, S. Licht, F. Hover, and M. Triantafyllou, Energy extraction through flapping foils, in *Proceedings of the 27th International Conference on Offshore Mechanics and Arctic Engineering (OMAE)* (2008), Vol. 6, pp. 389–395.
[9] M. Ashraf, J. Young, J. Lai, and M. Platzer, Numerical analysis of an oscillating-wing wind and hydropower generator, AIAA J. **49**, 1374 (2011).
[10] J. Young, J. Lai, and M. Platzer, A review of progress and challenges in flapping foil power generation, Prog. Aerosp. Sci. **67**, 2 (2014).
[11] Y. Su and K. Breuer, Resonant response and optimal energy harvesting of an elastically mounted pitching and heaving hydrofoil, Phys. Rev. Fluids **4**, 064701 (2019).
[12] T. Kinsey and G. Dumas, Three-dimensional effects on an oscillating-foil hydrokinetic turbine, J. Fluids Eng. **134**, 071105 (2012).
[13] C. Garrett and P. Cummins, The efficiency of a turbine in a tidal channel, J. Fluid Mech. **588**, 243 (2007).
[14] Y. Su, M. Miller, S. Mandre, and K. Breuer, Confinement effects on energy harvesting by a heaving and pitching hydrofoil, J. Fluids Struct. **84**, 233 (2019).
[15] J. O. Dabiri, Potential order-of-magnitude enhancement of wind farm power density via counter-rotating vertical-axis wind turbine arrays, J. Renew. Sustain. Energy **3**, 043104 (2011).
[16] T. Kinsey and G. Dumas, Optimal tandem configuration for oscillating-foils hydrokinetic turbine, J. Fluids Eng. **134**, 031103 (2012).
[17] F. Simeski and J. Franck, Simulations of constructive interaction in oscillating hydrofoil arrays, in *Proceedings of the 5th Marine Energy Technology Symposium* (2017).
[18] B. L. R. Ribeiro, S. L. Frank, and J. A. Franck, Vortex dynamics and reynolds number effects of an oscillating hydrofoil in energy harvesting mode, J. Fluids Struct. **94**, 102888 (2020).
[19] Y. Su, Energy Harvesting and Aeroelastic Instabilities Using Prescribed and Elastically Mounted Pitching and Heaving Hydrofoils, Ph.D. thesis, Brown University (2019).
[20] Y. Zhu, Y. Su, and K. Breuer, Nonlinear flow-induced instability of an elastically mounted pitching wing, J. Fluid Mech. **899**, A35 (2020).
[21] B. L. R. Ribeiro, Y. Su, Q. Guillaumin, K. S. Breuer, and J. A. Franck, Wake-foil interactions and energy harvesting efficiency in tandem oscillating foils, Phys. Rev. Fluids **6**, 074703 (2021).
[22] J. Jeong and F. Hussain, On the identification of a vortex, J. Fluid Mech. **285**, 69 (1995).
[23] D. E. Rival, J. Kriegseis, P. Schaub, A. Widmann, and C. Tropea, Characteristic length scales for vortex detachment on plunging profiles with varying leading-edge geometry, Exp. Fluids **55**, 1660 (2014).
[24] M. Awad and R. Khanna, Support vector regression, in *Efficient Learning Machines: Theories, Concepts, and Applications for Engineers and System Designers* (Apress, Berkeley, CA, 2015), pp. 67–80.
[25] *Statistics and Machine Learning Toolbox User's Guide* (The MathWorks, Natick, MA, 2021).
[26] S. L. Brunton, B. R. Noack, and P. Koumoutsakos, Machine learning for fluid mechanics, Annu. Rev. Fluid Mech. **52**, 477 (2020).
[27] N. Zhang, J. Xiong, J. Zhong, and K. Leatham, Gaussian process regression method for classification for high-dimensional data with limited samples, in *Proceedings of the 8th International Conference on Information Science and Technology (ICIST)* (IEEE, 2018), pp. 358–363.

[28] V. Vapnik, *The Nature of Statistical Learning Theory* (Springer, New York, 2000).
[29] K. Fukami, K. Fukagata, and K. Taira, Assessment of supervised machine learning methods for fluid flows, Theor. Comput. Fluid Dyn. **34**, 497 (2020).
[30] J. Liu, G. Shi, and K. Zhu, Online multiple outputs least-squares support vector regression model of ship trajectory prediction based on automatic information system data and selection mechanism, IEEE Access **8**, 154727 (2020).
[31] L. Rocha, L. Velho, and P. C. P. Carvalho, Image moments-based structuring and tracking of objects, in *Proceedings of the XV Brazilian Symposium on Computer Graphics and Image Processing* (2002), pp. 99–105.
[32] R. Candelier, Tracking object orientation with image moments (2016), http://raphael.candelier.fr/?blog=Image%20Moments.
[33] H. Brink, J. W. Richards, and M. Fetherolf, *Real-World Machine Learning* (Manning, Shelter Island, NY, 2017).
[34] R. Whittlesey, S. Liska, and J. Dabiri, Fish schooling as a basis for vertical axis wind turbine farm design, Bioinspir. Biomimet. **5**, 035005 (2010).
[35] J. Young, M. A. Ashraf, J. C. S. Lai, and M. F. Platzer, Numerical simulation of fully passive flapping foil power generation, AIAA J. **51**, 2727 (2013).
[36] I. Fenercioglu, B. Zaloglu, J. Young, M. A. Ashraf, J. C. S. Lai, and M. F. Platzer, Flow structures around an oscillating-wing power generator, AIAA J. **53**, 3316 (2015).
[37] M. Raissi, P. Perdikaris, and G. Karniadakis, Physics-informed neural networks: A deep learning framework for solving forward and inverse problems involving nonlinear partial differential equations, J. Comput. Phys. **378**, 686 (2019).

Leading Edge Vortex Dynamics on Finite Aspect Ratio Swept Wings Exhibiting Large Amplitude Oscillations

Casey Fagley*, Adam Jirasek†, Jürgen Seidel‡
Department of Aeronautics, U.S. Air Force Academy, CO 80840, USA

The fluid-structural interaction present with stall flutter is driven by the dynamic stall process which is typically presented as primarily a two-dimensional flow phenomenon. Because of this, studies to date have predominantly focused on rectangular wing sections where 3D flow features are not prevalent. Recent investigations indicate that the influence of wing sweep (i.e. spanwise flow and cross-flow instability) influence the size and strength of the leading edge vortex formation for prescribed motions. This paper assesses the aeroelastic instabilities associated with stall flutter with and without sweep indicating the influence of LEV formation, progression and separation. Analyses are also conducted on prescribed versus responding motions and the effects of wing sweep on the flutter dynamics of a NACA0012 wing.

Nomenclature

b	Span	Re	Reynolds number
c	Chord	S	Planform area
C_L	Lift coefficient	s	Laplace variable
C_M	Pitch moment coefficient	U_∞	Freestream velocity
J_{cp}	Cyber-physical torsional inertia	α	Angle of attack
J	Overall torsional inertia	η_{cp}	Cyber-physical torsional damping
J_w	Wing torsional inertia	η	Overall torsional damping
k_{cp}	Cyber-physical torsional stiffness	η^*	Non-dimensional torsional damping
k	Overall torsional stiffness	η_w	Wing torsional damping
k^*	Non-dimensional torsional stiffness	Λ	Sweep angle
k_w	Wing torsional stiffness	τ_a	Aerodynamic torque
M	Mach number	τ_{cp}	Cyber-physical torque
q	Dynamic pressure		

I. Introduction

Aeroelasticity is a very well studied field investigating the interaction of structural dynamics and aerodynamics. These aeroelastic interactions can be represented by Collar's triangle of forces; the transfer of energy between inertial, elastic, and aerodynamic forces produces aeroelastic phenomena. Fluid-structure interactions are prominent design considerations for current air vehicles; for instance, at certain operating conditions (i.e. Mach, altitude, weight, fuel levels, etc.) aeroelastic instabilities may be detrimental to the integrity of the aircraft structure. Such instabilities are typically identified as flutter, or in the situation of a marginally stable system, a limit cycle oscillation.

Two modes of aeroelastic instabilities are commonly identified, classical flutter and stall flutter. In classical flutter, at least two elastic modes of the structure merge or couple together and create an exponentially increasing deformation. This aeroelastic instability is present at small angles of attack and grows from small amplitudes; therefore, it is well represented by linear models. [1]. Further extensions have been made to improve the prediction of the critical velocity at which the instability occurs.[2, 3] While this instability is linear in nature and is characterized by the coupling of two or more elastic structural modes, non-linearities in the flow field and structure may bound the limit cycle oscillation at large angles of attack and displacements. In fact, the post-critical, classical flutter behavior of a flat plate free to pitch

*Research Associate, Department of Aeronautics, Senior Member
†Research Associate, Department of Aeronautics, Senior Member
‡Director, High Performance Computing Research Center, Department of Aeronautics, Associate Fellow

and plunge showed that aerodynamic non-linearities, as opposed to cubic structural non-linearities, contributed most to bounding the instability.[4]

A more recently identified aeroelastic instability is stall flutter. This mode of instability requires only a single structural mode (typically pitch or torsion) which couples with the non-linearities and unsteadiness of the fluid dynamics rather than another elastic structural mode. The flow separates and reattaches during the cyclic structural motion and is largely driven by the well-identified dynamic stall process.[5] Because this flutter mode is only encountered at large angles of attack, only a limited number of aeroelastic systems may encounter this type of flutter. For instance, applications in which high angles of attack are reached with torsionally weak structures, such as helicopter rotors [6], wind turbine blades [7], high aspect ratio wings [8], flapping wings [9], turbomachinery blades, power transmission lines, and even bridge decks [10] may experience stall flutter.

Typically, large base angles of attack (where stall is present) are necessary to initiate the associated LCO.[11] It has also been shown that stall flutter can occur at low angles of attack beyond the static divergence limit for pitching flat plates or thin airfoils. [12] At these low angles of attack it is the interaction of static divergence with non-linearities in the structure or flow such as flow separation, dynamic stall, and fluidic hysteresis that creates the oscillatory behavior of stall flutter. At large angles of attack, stall flutter may occur for speeds below the divergence velocity [11, 13] which is commensurate with results shown in this study.

The fluid-structural interaction present with stall flutter is driven by the dynamic stall process which is typically presented as primarily a two-dimensional flow phenomenon. Because of this, studies to date have predominantly focused on rectangular wing sections where 3D flow features are not prevalent. Experimental investigations of a torsionally flexible, rectangular planform wing indicated that the variation of angle of attack along the span and spanwise pressure gradient reduced the tendency of stall flutter to occur. [14] Additionally, the influence of wing sweep, which causes a spanwise flow toward the wing tip and instability in the boundary layer, has been shown to influence the size and strength of the leading edge vortex formation for prescribed motions.[15] This paper explores the effects of wing sweep on the flutter dynamics of a NACA0012 wing.

II. Setup

The model under investigation is a finite span wing aligned with the flown aspect ratio of 3 and a chord length of 15 cm. Four configurations of wing sweep were tested, $\Lambda = 0°$, $10°$, $20°$, and $30°$. The models were swept such that the airfoil chord line remained aligned with the flow and the axis of rotation was canted backward such that the axis of rotation was held parallel to the leading edge of the foil. This axis of rotation intersected the wing at the mid chord position in the mid span plane, irrespective of sweep angle. To thoroughly investigate the influence of wing sweep on the flutter dynamics both experimental and computational tools have been employed. The setup is shown for both experimental and computational investigations in the following sections.

A. Experimental Setup

1. Facility

Experiments were conducted in the Subsonic Wind Tunnel in the Aeronautics Laboratory at the United States Air Force Academy, as shown in Fig. 1. The wind tunnel is a recirculating tunnel, designed and built by FluiDyne Engineering. It has a 0.91 m by 0.91 m by 1.83 m test section and a maximum achievable velocity of M = 0.6. The tunnel is instrumented with a variety of measurement equipment, including but not limited to a 6-Dof external force balance, pressure measurements, shear stress measurements, optical access to perform stereo particle velocimetry and measure structural displacement using digital image correlation (DIC). The tunnel velocity measurement is based on total temperature and pressure and the dynamic pressure measured between a static ring at the entrance of the test section and the total pressure in the stilling chamber.

A rod is mounted through the ceiling of the tunnel through bearing blocks. Beneath the tunnel sits a motor for position, velocity or torque controlled modes. Additionally, a torque cell is connected to the main shaft to measure the total moment on the system. The experimental setup and components are described in more detail later in the Setup.

A stereoscopic particle velocimetry (SPIV) campaign was conducted to measure the unsteady velocity components to elucidate key flow features which may play a role the development of the LEV or interaction with cross-flow. The optical setup consisted of two image pro-X cameras, both above the test section, and an Evergreen EVG00200 nd-Yag dual pulsed laser which were all rigidly mounted on a 3-DoF traverse. The traverse was used to translate all of the optical equipment in the span-wise direction to illuminate specific span-wise planes on the airfoil section. The data reduction

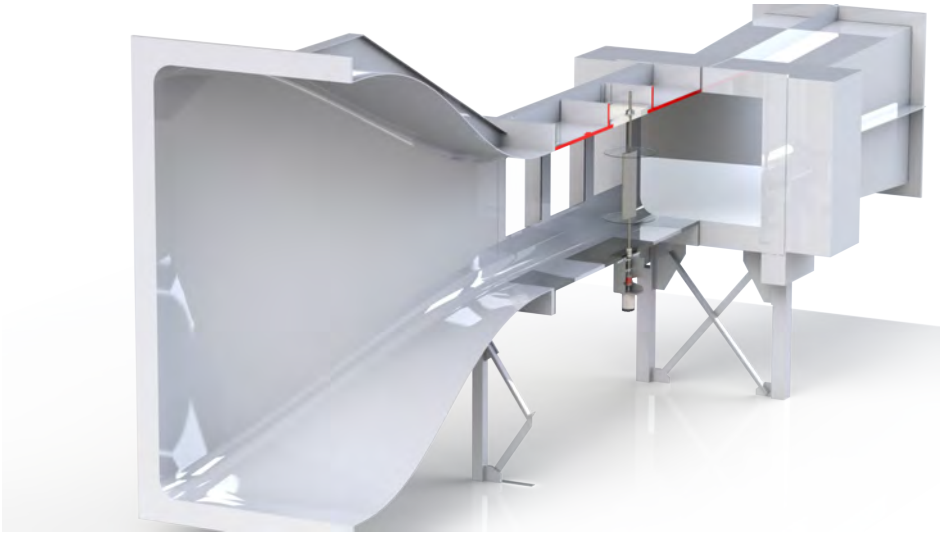


Fig. 1 USAFA Subsonic Wind Tunnel experimental test setup

was carried out on DaVis software which also was used to control the optical configuration. The SPIV datasets were phase-locked at specific angles in which an encoder measuring the angular position of the fluttering would trigger the SPIV accordingly at the desired location. Matlab was used to post process the SPIV data which included calculation of Γ_1 [16] criteria and bounded circulation.

2. Models

The four models are shown in Figure 2. An unswept NACA0012 is tested to understand the leading edge vortex behavior and flutter characteristics. The chord length was 15 cm and the aspect ratio was 3 for all geometries. The wing consisted of an end plate at the root and a rounded wing tip at the end of the wing. The end plate serves as a symmetry plane and effectively increased the aspect ratio by a factor of 2. Furthermore, the sweep of the wing was tested by fabricating 3 additional wings with $\Lambda = 10°$, $20°$, and $30°$. Note that the axis of rotation was at the mid-chord position and parallel to the leading edge of the swept wing, i.e. the axis of rotation is always aligned with the leading edge of the wing. The flutter boundaries were evaluated to understand differences of the leading edge vortex behavior in the presence of a span-wise flow due to the sweep of the model. The wind tunnel models were 3D printed using stereo lithography. To minimize inertial forces relative to aerodynamic forces, the wings were hollow.

3. Cyber-Physical Dynamics

The cyber-physical dynamics are implemented with a National Instruments^{TM} CompactRIO, a reconfigurable, modular embedded control system. The CompactRIO embedded architecture makes use of two processers to segregate time deterministic tasks from lower priority tasks, a field programmable gate array (FPGA) and real-time digital signal processor. Three modules were used in the CompactRIO, specifically, a high speed digital I/O, multichannel analog input and multichannel analog output modules. A Copley controls Accelnet motion controller was used to as the power electronics, to stabilize the current loop, and commutate the motor signal. Thus, an analog voltage prescribed by the control system was directly related into shaft torque through the motion controller.

The embedded control system, data logging and communication protocols were completely designed in National Instruments^{TM} LabView real-time language. The angle of attack is measured via an incremental differential rotary encoder with 16,000 counts per revolution at the base of the motor. The digital I/O module with FPGA software performed the quadrature decoding to record both direction and number of digital counts produced by the optical encoder. This digital signal is then converted into an analog representation of the angular position. Subsequently, the angular velocity and angular acceleration (first and second order derivatives) were numerically computed on the FPGA. The derivatives were computed in the Laplace domain where an n^{th} order filter with a prescribed frequency response and phase delay can be specified in real time. The virtual dynamics were chosen to be a second order mass-spring-damper



(a) NACA0012 (b) Swept Models

Fig. 2 Swept/unswept NACA0012 wind tunnel models

system of the form

$$I_{cp}\ddot{\alpha} + b_{cp}\dot{\alpha} + k_{cp}\alpha = \tau_{cp}. \tag{1}$$

All coefficients of the second order system, i.e. torsional inertia (I_{cp}), damping (b_{cp}) and stiffness (k_{cp}), are specified, and the torque (τ_{cp}) is then computed according to eqn. 1. The subscript cp denotes the cyber-physical portion of the overall wing dynamics. A low pass filter is employed to reduce the effects of numerical noise. Also, a deadzone non-linearity to reduce the influence of Coulomb friction (both in the DC motor and wing itself) was used. Finally, saturation limits were placed to bound the amount of current draw to the motor to ensure safety and reliability of the cyber-physical wing. A validation of the cyber-physical setup for aeroelastic investigations is given in [14] and [17].

To determine the inertia, damping and stiffness added by the physical wing model to the prescribed cyber-physical parameters, the wing dynamics must be characterized. The equation of motion for torsion of the cyber-physical wing is

$$I\ddot{\alpha} + b\dot{\alpha} + k\alpha = \tau_s, \tag{2}$$

where the terms are intertial, damping and stiffness from left to right and τ_s is the overall shaft torque. These overall structural characteristics are combinations of the inherent wing dynamics and the prescribed cyber physical settings, i.e $I = I_w + I_{cp}$, where the overall inertial properties of the wing is a combination of the inherent wing inertia and the prescribed virtual inertia. Because the torque cell directly measures the overall shaft torque given by eqn. (2), the aerodynamic torque, τ_{aero}, must be isolated. The pitching moment coefficient, C_m, about the mid chord reference location can then be non-dimensionally defined by

$$C_M = I^*\ddot{\alpha} + b^*\dot{\alpha} + k^*\alpha \tag{3}$$

where the non-dimensional structural terms are denoted by * and given by $I^* = 2I/\rho c^2 b$, $b^* = 2b/\rho U_\infty cb$ and $k^* = 2k/\rho U_\infty^2 cb$. As shown by Eq. 3, values of the wing structural dynamics are needed to isolate the aerodynamic torque from the resulting shaft torque measurement. The process employed here is very similar to the one described in Onoue and Breuer [18] who extracted the aerodynamic torque from a cyber-physical system. Additionally, a similar method for non-dimensionalization is taken from Zhu et al. [19] and Menon and Mittal [20].

B. Computational setup

Kestrel is the fixed-wing product of the CREATE^{TM} -AV program funded by the DoD High Performance Computing Modernization Program (HPCMP). The objective of the CREATE^{TM} program is to improve the Department of Defense acquisition time, cost, and performance using state-of-art computational tools for design and analysis of ships, aircraft and antenna. Kestrel is specifically developed for multidisciplinary fixed-wing aircraft simulations incorporating components for aerodynamics, jet propulsion integration, structural dynamics, kinematics, and kinetics [21]. The code has a Python-based infrastructure that integrates Python, C, C++, or Fortran-written components [22]. Kestrel 10.4.1 is used in this work. The code has been extensively tested and a variety of validation documents have been reported.

Kestrel CFD solvers include KCFD [23], COFFE [24], and KCFD/SAMAir [25]. The KCFD flow solver is used in this study. KCFD uses a second-order accurate cell-centered finite-volume discretization, however, SAMAir utilizes a fifth-order finite-volume discretization on Cartesian meshes [26]. In more detail, the KCFD flow solver discretizes the Reynolds–Averaged Navier Stokes (RANS) equations into a second-order cell-centered finite-volume form. The code then solves the unsteady, three-dimensional, compressible RANS equations on hybrid unstructured grids [27]. The KCFD flow solver uses the Method of Lines (MOL) to separate temporal and spatial integration schemes from each other [23]. The spatial residual is computed via a Godunov type scheme [28]. Second-order spatial accuracy is obtained through a least squares reconstruction. The numerical fluxes at each element face are computed using various exact and approximate Riemann schemes with a default method based on HLLE++ scheme [29]. In addition, the code uses a subiterative, point-implicit method (a typical Gauss-Seidel technique) to improve the temporal accuracy. Some of the turbulence models available within Kestrel include Spalart–Allmaras (SA) [30], Spalart–Allmaras with rotational/curvature correction (SARC) [31], Menter's SST [32], and Delayed Detached Eddy Simulation (DDES) with SARC [33].

The motion is updated every subiteration so the coupling of the CFD and structural solver is considered a strong coupling. The time stepping scheme on the CFD side is a second order accurate scheme where the solution is marched to the next time step using a five Newton subiterations. The time stepping scheme of the structural solver is third order accurate forward finite difference scheme.

The structural model for comparison with the experiments is a simple torsional spring, modeled as

$$I\ddot{\alpha} + C\dot{\alpha} + K\alpha = M \tag{4}$$

where I is moment of inertia, C is damping coefficient and K is stiffness coefficient. M is the external loading, in this case the aerodynamic torque. The values of I, C and K were provided by the experiments. This equation is solved with the third order in time integration scheme. Because of the low speeds utilized in the experiments, Loci/CHEM was used with a low-speed preconditioner. The coupling between the CFD solver and the structural solver is performed at every sub-iteration.

The computational meshes were created in Pointwise. Two meshes were made, a medium and a fine mesh. The medium mesh has 400 cells along the airfoil chord and 200 cells along the span. The surface mesh is a quadrilateral structured mesh for the whole wing except on the wing tip. The fine mesh has 600 cells along the airfoil chord and 350 along the span. The mesh layout is the same as for the medium mesh. The mesh count for the medium mesh is approx. 5M cells and for the fine mesh about 15M cells. The thickness of the first prism cells is $y_1 = 0.000015m$ and there are nominally 70 prism layers spaced with a growth rate of 1.25.

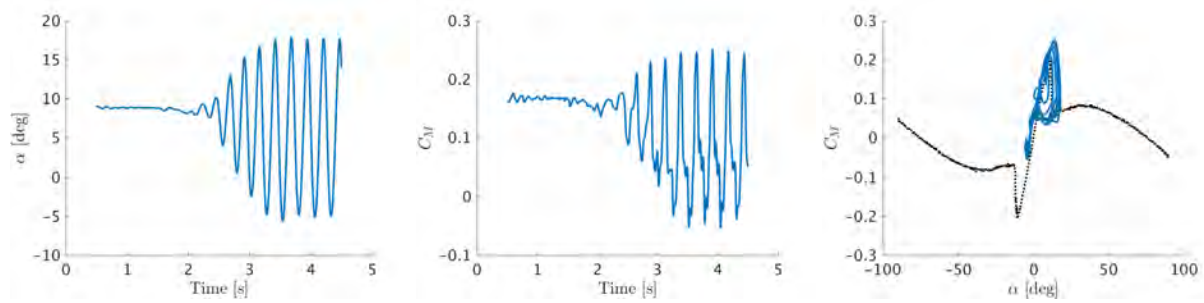
III. Results and Discussion

A. Aero-Elastic Stability Behavior for the Unswept Wing

The tests were conducted at a constant wind tunnel velocity of Mach 0.05. Initially, a large stiffness was chosen such that the wing was stationary. The stiffness was decremented slowly until flutter oscillations were observed. An example of this is shown in Figure 3 which shows the growth of the angle of attack and pitch moment coefficient over time as wellas pitch moment coefficient versus angle of attack. As shown in Figure 3(c) as the wing approaches the static stall angle (static data shown in black), the dynamic stall process starts to interact with wing and causes flutter oscillations to occur.

The flutter envelope or stability characteristics were then observed throughout a range of stiffnesses. These tests were conducted by incrementally decreasing stiffness. The system was perturbed with a controlled impulsive torque and the system response was measured. If the system returned to the zero amplitude equilibrium branch, the time history of oscillation would damp out; if the system sustained a limit cycle oscillation (LCO), the resulting instability branch amplitude was measured. The results of the unswept wing are shown in Figure 4 which shows the amplitude of the limit cycle oscillation plotted against the inverse of non-dimensional stiffness. As shown, as the stiffness decreases the instability occurs by an observation of a stationary LCO indicated by a non-zero amplitude in the figure. This amplitude grows when the stiffness is further reduced. The stiffness is then increased again and a bifurcation is observed as stable LCOs are shown for stiffness less than the onset of the instability.

To further understand the instability behavior for these symmetric LCOs, prescribed motion is commonly used to characterize the instability branches and further explore the aero-elastic dynamics[19, 20, 34]. Forced sinusoidal oscillations in which $\alpha(t) = \alpha_0 + \alpha_1 \sin(\omega t)$ were prescribed in which the frequency and amplitude of the oscillation was



(a) (b) (c)

Fig. 3 Initiation of flutter showing the growth of the angle of attack (a), the resulting aerodynamic pitch moment (b) and the resulting angle of attack versus pitch moment relative to the static measurements.

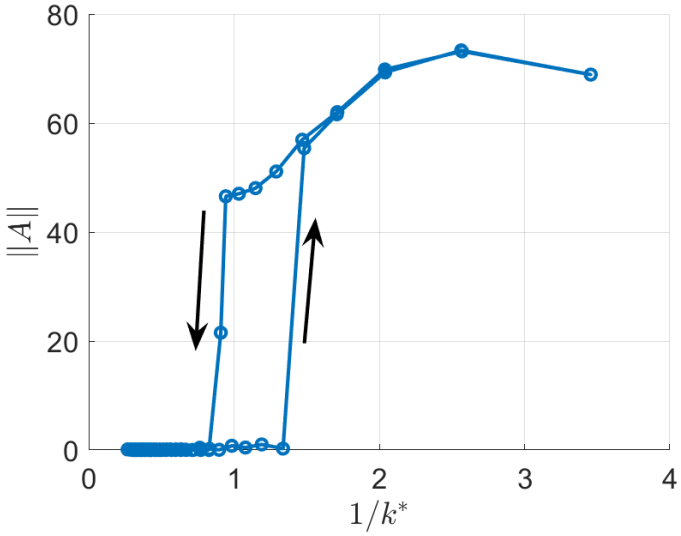
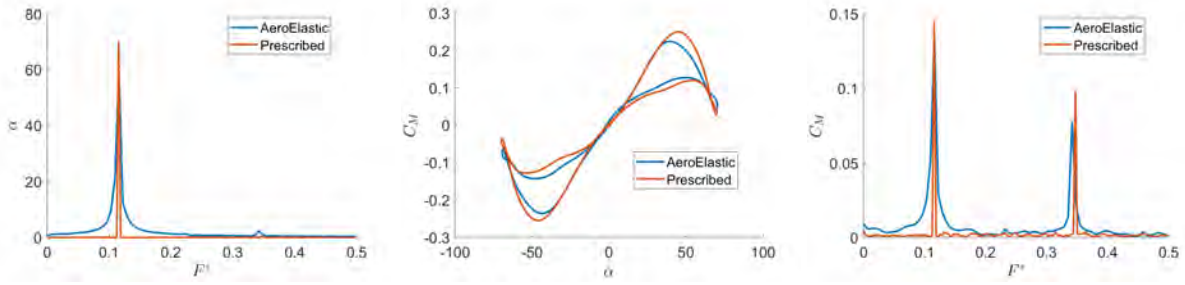


Fig. 4 LCO Stability behavior indicated by LCO amplitude for the unswept wings with variation non-dimensional stiffness.

varied over the range in which the aeroelastic instabilities were observed. A specific case shown for a non-dimensional frequency of 0.11 is shown in Fig. 5. The non-dimensional frequency is defined by $F^* = fc/U_\infty$ where f is the observed pitching frequency of the aero-elastically coupled motion, not the resonant frequency of the wing $\sqrt{k/I}/2\pi$. Figure 5 compares the matched aero-elastic motion with the prescribed sinusoidal motion. As shown, slight differences between the two datasets are observed. The frequency spectrum (Fig 5(a)) of the aero-elastic case has a larger bandwidth at the fundamental frequency than that of the prescribed motion. This is expected as the observed frequency of oscillating for the aero-elastically coupled case may wander slightly due to uncontrolled experimental factors. Secondly, the presence of a third harmonic is observed in the coupled motion which was not modeled for the prescribed motion. As shown the resulting pitching moment coefficient for both motions has some slight differences. The prescribed motion attains a slightly larger pitching moment and a more abrupt/deeper stalled condition.

While slight differences were observed between the prescribed and responding motions, particularly the amplification of the third harmonic arising from the development of secondary and tertiary LEV structures, the prescribed motion provides a powerful and systematic way to traverse through large-dimensional parameter spaces. Interestingly, the energy flux throughout the oscillatory period can be related to the aero-elastic instability locations. The energy flux, as described by the power coefficient,

$$C_p = \frac{1}{qU_\infty bc^2} \int_0^t (\tau_f \dot{\alpha} - b\dot{\alpha}^2) dt, \tag{5}$$



(a) (b) (c)

Fig. 5 Comparison of prescribed vs aero-elastic coupled motion for a particular non-dimensional frequency. a) shows the frequency content for the motion trajectories, b) resulting pitch moment coefficient vs angle of attack and c) resulting frequency content of the pitch moment coefficient.

indicates the average power difference between the aerodynamic energy flux, $\int_0^t \tau_f \dot{\alpha} dt$, and the dissipated structural energy, $\int_0^t b\dot{\alpha}^2 dt$. The derivation of this relationship can be found in Menon and Mittal [20]. The instability branches of the aero-elastic motions align with a net energy flux of zero; that is, the resulting motion balances the aerodynamic and structural dynamic energy fluxes.

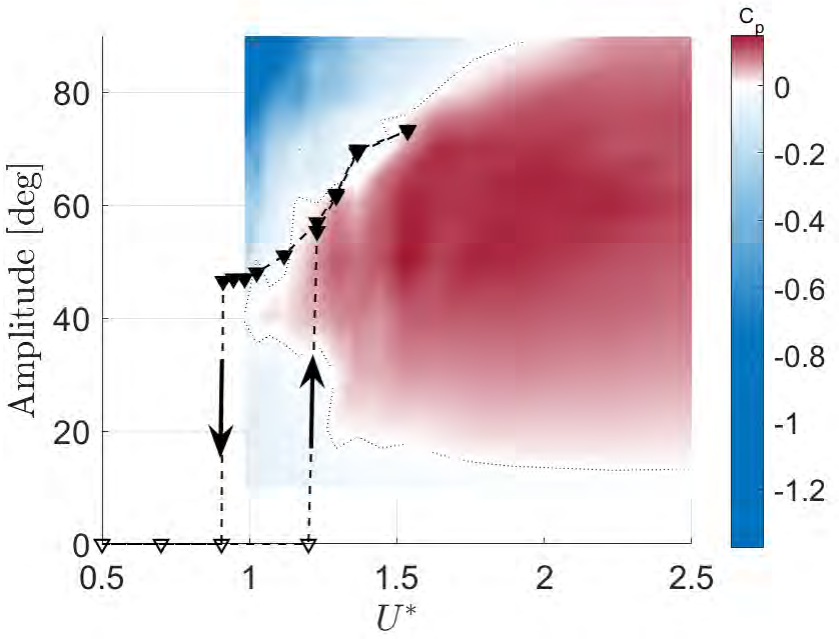


Fig. 6 Surface of the power coefficient or energy map of prescribed motion plotted with the aero-elastic cases in black triangles.

The resulting energy flux and power coefficient was computed and Figure 6 shows the power coefficient surface for the frequency and amplitude space. Positive power coefficients indicate that the energy flux is from the flow to the structure and negative coefficients indicate that the flux is from the structure to the flow. Interestingly, the aeroelastic cases from Fig. 4 lie directly on the zero power coefficient contour line which indicates the balanced exchange of energy between the fluid and structural coupled systems.

B. Flow Physics of Large Amplitude LCOs on Unswept Wing

To understand and decouple the physics of the fluid and structural interactions, two specific cases were chosen which both exhibited a net zero power coefficient, i.e. an aeroelastic case. The first selected case has a non-dimensional velocity, $U^* = 1.22$ and an amplitude $\|A\| = 55^o$; the second case had a non-dimensional velocity of $U^* = 1.65$ and an amplitude, $\alpha_1 = 76^o$. In essence, Case I was a torsionally stiffer wing which exhibited a higher frequency and smaller amplitude LCO in comparison to Case II. The maximum angular velocity for both cases was $\alpha_1/U^* = \alpha_1 F^* = 0.25$. Interestingly, all aero-elastic conditions for this inertial range of models preferred this maximum angular velocity which will be discussed later.

Figure 7 shows a pitching moment coefficient comparison between Case I and Case II relative to the static pitching moment coefficient. Even though these cases exhibited differing angular frequencies and amplitudes, the resulting trends of the pitch moment are comparable. Case I (stiffer) tends to have a stronger LEV, by the enhanced magnitude of C_M, whereas Case II has a weaker LEV, but it appears the LEV has an influence over a broader range of angle of attack. Secondly, Case II reaches a deeper stall due to the high angle of attack and large pitch moment deficit which may indicate that the trailing edge vortex becomes a predominant flow feature.

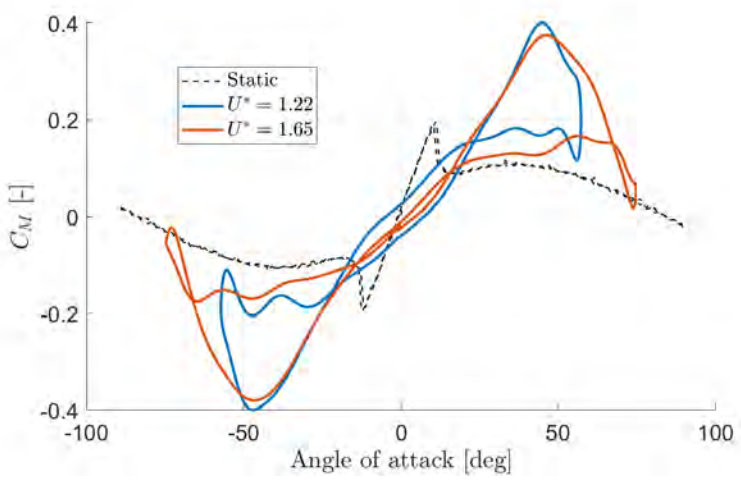


Fig. 7 Comparison of pitching moments for Case I (U^* of 1.22 and amplitude, α_1 of 55 degrees) and Case II U^* of 1.65 and amplitude, α_1 of 76 degrees

A stereo particle velocimetry campaign was conducted on each of these cases. The SPIV system was aligned to the mid-span location and triggered at prescribed angles to capture an image pair on each camera. A total of 500 images were acquired at each angle, and the data was averaged. Figure 8 shows the velocity and vorticity fields for each case at specific angles throughout the pitch up cycle. The initiation of the LEV begins around 30^o in which the boundary layer on the suction side of the wing begins to advect toward the leading edge of the wing. The cross stream vorticity accumulates toward the leading edge and the LEV forms (Fig. 8(b)). As the LEV grows in size and strength, the presence of secondary shear is observed on the upper surface of the wing due to the reverse flow (Figs. 8(c)-8(d)). After the LEV is fully developed, the evolution of the LEV is clearly seen. Once the wing begins to decelerate in the LCO, the LEV is pinched off from the wing surface and advects downstream. During this process strong leading and trailing edge shear layers are observed; however, the leading edge shear decouples from the LEV at large enough angle of attack (Fig. 8(e)).

Upon scrutinizing the differences of flow physics between Case I and Case II, the hypothesis from the force transducer data is confirmed. The LEV size, strength, and location throughout the pitch up cycle is comparable for both aero-elastic cases. Case I shows an abrupt pinching and convection of the LEV whereas the LEV persists to higher angle of attack in Case II. The trailing edge vortex in Case II is much stronger at the maximum angle of attack (compare Figs. 8(f) and 8(l)).

To further analyze the vortex dynamics, the Γ_1 criterium was used to identify the vortex core location. Γ_1 which was initially introduced by Graftieaux et al. [16] is a common method for vortex identification on two-dimensional velocity fields. The identified vortex locations are plotted on the quiver plots (Fig. 8) as red dots. On successful identification of a vortex (which did not happen at all angles), the bounded circulation was computed as $\Gamma = \oint_S \vec{V} d\vec{S}$ where the path was chosen as a circle centered at the identified vortex location. The radius of the circle was varied until the circulation value

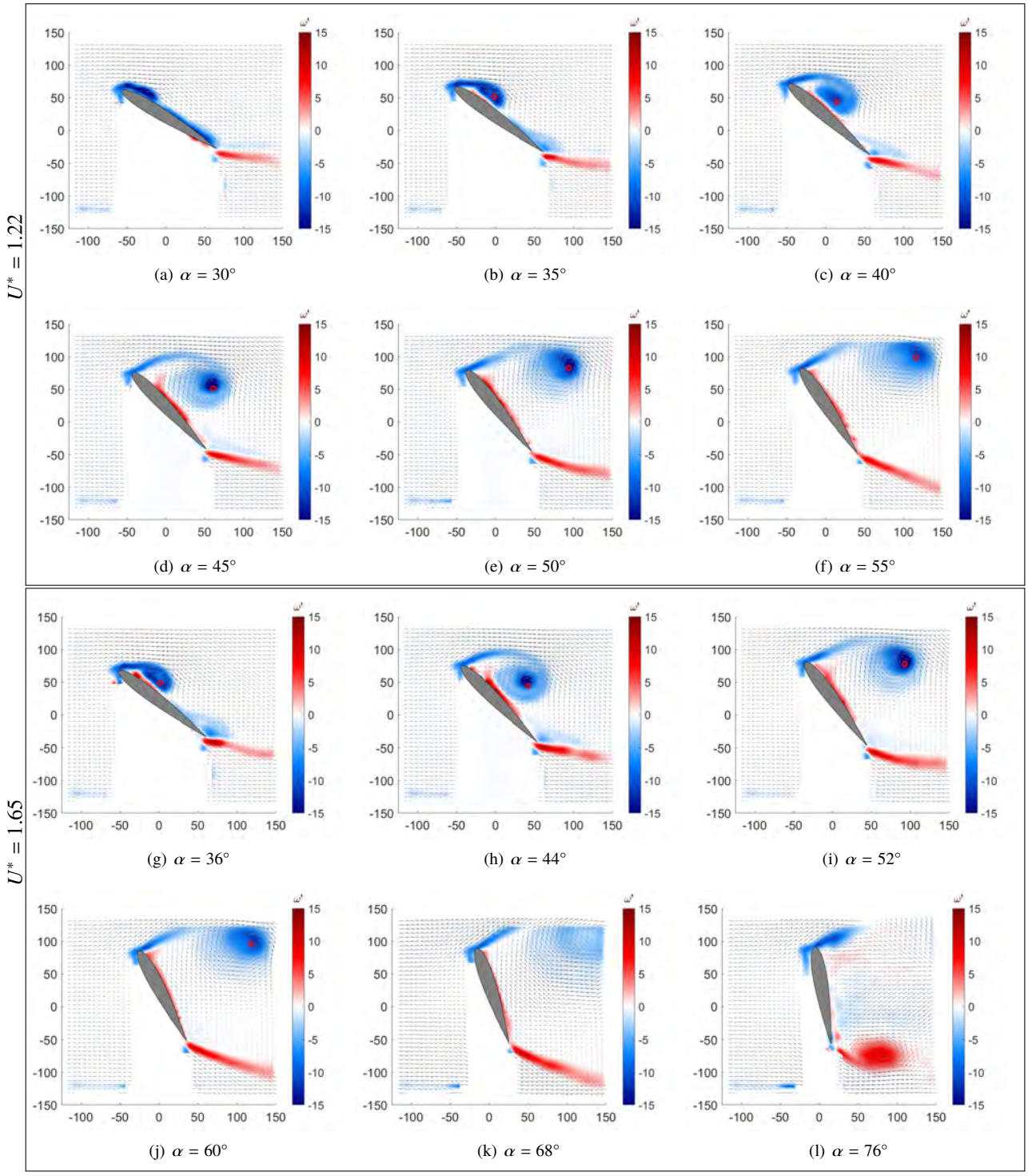
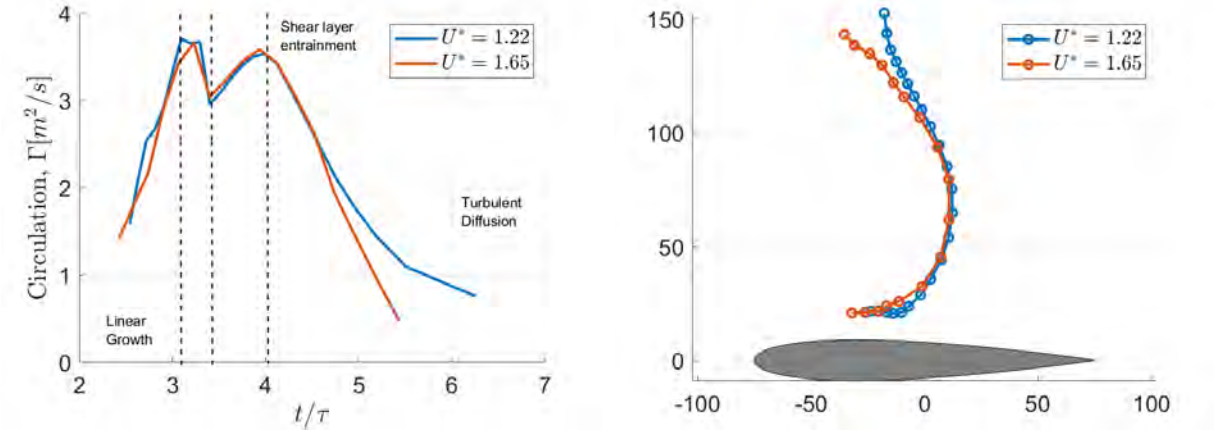


Fig. 8 PIV meausuremens of CASE I and CASE II at particular angles of attack during the upstroke. Quiver plots are colored by vorticity, ω_z



(a) Vortex Strength

(b) Vortex Position

Fig. 9 Vortex strength and position for Case I and Case II from SPIV data

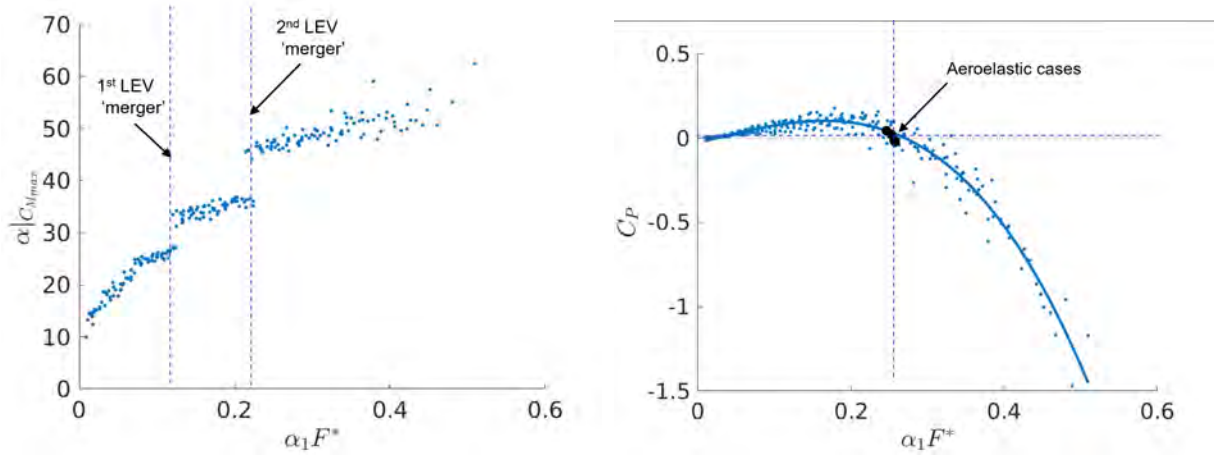
converged. The results are shown in Figure 9 which shows circulation as a function of phase angle, non-dimensionalized by the convective time scale, $\tau = c/U_\infty$, throughout the pitch up motion. Interestingly, the convective time and phase angle scales the vortex strengths throughout these two cycles. Initially, the LEV grows linearly in strength until a point at which the LEV saturates and begins ingesting the opposite signed secondary shear layer vorticity as shown by a reduction of circulation. The vortex then begins advecting away from the surface, lessening the interaction with the secondary shear, but it is still being fed by the primary shear layer which allows the LEV to grow in strength again, until finally the vortex advects away from the surface and diffuses into the wake flow.

The investigation of these two aero-elastic cases provided insight on the scaling properties of the flow physics by maximum angular velocity, $\alpha_1/U^* = \alpha_1 F^*$. For this range of Reynolds number and inertial scales, the flow naturally prefers a maximum angular velocity of $\dot{\alpha}_{max} = 0.25$ which corresponds to a power coefficient of zero. To understand assertion, all of the data presented in the energy map in Fig. 6 is collapsed to a single parameter, $\alpha_1 F^*$. With this scaling, certain figures of merit can be plotted to understand the the influence of angular rate on the flow physics. For instance, Figure 10(a) shows the angle of attack at maximum pitch moment coefficient. This shows three distinct bins in which LEV merging is observed. At small angular rates, the LEV sheds relatively quickly as the flow-structure interaction approaches a quasi-steady nature. As the angular velocity is increased, a primary and secondary LEV merge into a stronger LEV which occurs at larger maximum angle of attack. At the largest angular rates, a second merger is observed. The aeroelastic cases for this particular Reynolds number and inertial scale exist in this 3rd bin. Finally, the coefficient of power can be plotted as a function of the non-dimensional angular rate, Fig. 10(b). At small rates, the power coefficient is negative, indicating that the flow is an energy sink. As the angular rate increases, the flow begins to do work on the structure until Cp crosses zero again around $\dot{\alpha}_{max} = 0.25$, which encompasses the aero-elastic cases.

C. Aero-Elastic Stability Behavior for Swept Wings

To investigate the effect of spanwise flow on the LEV development, three wing models were fabricated with sweep angles of $\Lambda = 0°, 10°, 20°$ and $30°$. The axis of rotation for each wing was parallel to the leading edge. A hinged mechanism was integrated onto the motor mount to skew the cantilevered bar backwards to a desired angle. Initially, the static pitch moment was measured. Figure 11(a) shows the resulting $C_M - \alpha$ curve for all wings. As shown, $\Lambda = 0°$ and $10°$ show a similar static stall angle and moment coefficient magnitude, indicating that the spanwise flow does not significantly influence the development of the separation characteristics. However, at larger sweep angles, it is apparent that both the lift curve slope and maximum lift are significantly reduced.

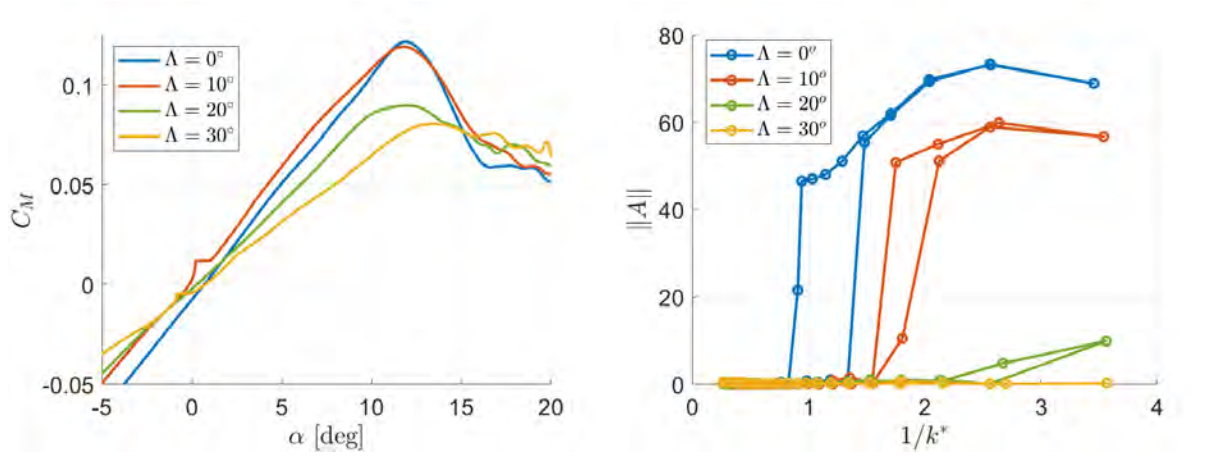
Beyond static information, the dynamic aero-elastic effects were also assessed in the same why as described above for the unswept wing. Figure 11(b) shows the instability branches. The unswept wing is shown as well for comparison purposes. As the sweep in increased to $10°$ the instability bifurcation is delayed to lower torsional stiffness, and the resulting amplitude of LCO is reduced as well. The instability behavior is similar to the unswept case, as a hysteresis is also observed for wing stiffening. Finally, the higher swept wings of $20°$ and $30°$ never attained a fully developed LCO.



(a) (b)

Fig. 10 Non-dimensional angular velocity at maximal pitch moment coefficient and power coefficient versus.

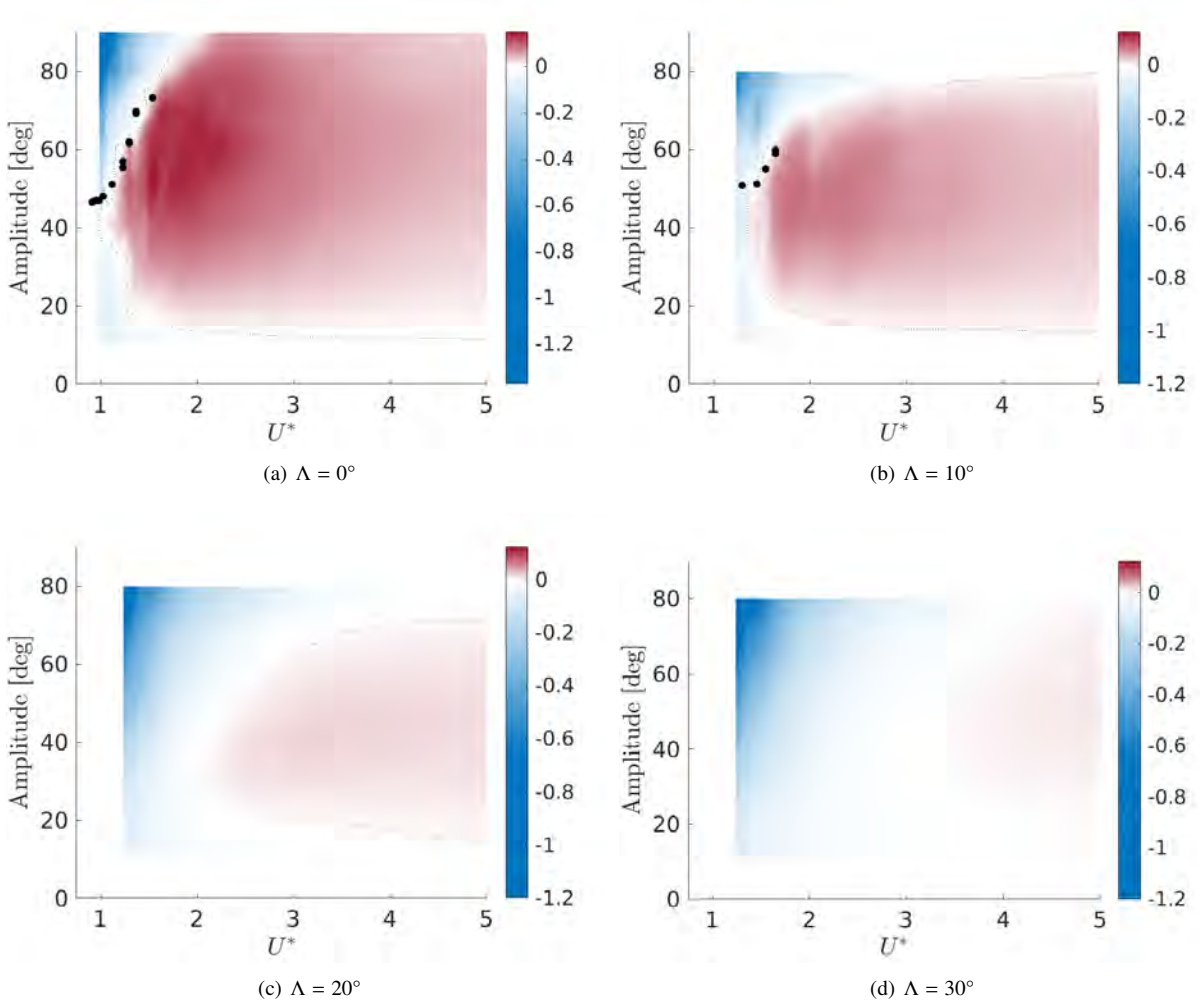
The 20° wing exhibited some aperiodic oscillations at the smallest stiffness, but this motion was not comparable to a stall flutter LCO and thus discarded. Ultimately, the presence of the spanwise flow diminished the aeroelastic instability from a stall flutter perspective; that is, the LEV becomes weaker and less significant with increasing wing sweep.



(a) (b)

Fig. 11 Static pitching moment for swept wings (left), and aero-elastic instability branches for variations of wing sweep($\Lambda = 0°, 10°, 20°, 30°$)

A similar study comparing prescribed motion to responding motion was carried out with the swept wings. In particular, the same amplitude and frequency parameter study was conducted and the results are shown in Fig. 12. The resulting energy maps copmuted from the power coefficient (5) are shown for each frequency and amplitude combination. The aeroelastic instability branches are also provided and align nicely with the $C_p = 0$ contour. Interestingly, as the sweep angle increases, the maximum power coefficient reduces, which shows that the size and strength and therefore the overall significance of the LEV is diminishing. Also, the $C_p = 0$ contour is pushed further to the right (i.e., toward torsionally weaker wings). Because a $C_p = 0$ contour was observed for each wing, it is postulated that aeroelastic instabilities would be possible for higher swept wings. However, at this range of non-dimensional inertia, the aeroelastic instability was not sustained for $\Lambda = 20°$ or 30°. This is similar to the results observed in Zhu et al. [19] in which the non-dimensional inertia plays an important role in determining where along this instability branch the system will equilibrate.



(a) $\Lambda = 0°$ (b) $\Lambda = 10°$

(c) $\Lambda = 20°$ (d) $\Lambda = 30°$

Fig. 12 Energy maps showing instability branches for the unswept and swept wings

D. Three Dimensional Flow Structure

To understand the three dimensional flow structure, both unsteady computations and phase-averaged SPIV across the wing planform were conducted. Prescribed motion given the parameters of Case I ($U^* = 1.22$ and $\alpha_1 = 57°$) was selected for the investigation of the spanwise flow effects. The SPIV system was traversed along the span of the wing and triggered at 1° increments along the upstroke of the wing. The results are shown in Figs. 13(a)-13(f) for prescribed angles of attack. The visualization shows isosurfaces of total vorticity colored by the cross-stream vorticity component. Initially, at $\alpha = 20°$ a shear layer along the suction side of the surface is shown with a opposite signed shear layer in the wake. As the angle progresses upward, the shear layer contracts toward the leading edge of the wing, accumulating into the LEV which is also fed from the primary shear layer at the leading edge. At an angle of $\alpha = 30°$, the LEV has detached from the surface and is beginning to entrain the secondary shear layer. The vortex begins to form an arch shape as the LEV is bounded by both tip vortices. Finally, the LEV pinches off and a stall-type cell is observed on the surface.

Figures 13(g)-13(l) show the companion computational flow fields at the same prescribed motion and angles of attack. Note that here the view is in the downstream direction. As shown, good agreement of flow structure size and arrangement with the SPIV measurements is observed. However, because the CFD simulations are time accurate, small scale structures are present in the data whereas the SPIV data shows the mean flow at the particular angle of attack due to the phase averaging over multiple cycles. Nonetheless, a nice agreement exists between the large coherent features. Specifically, the development of the LEV, bounding effects of the tip vortices and the separation arch vortex structure at larger angles of attack are clearly observed in both experiments and simulations.

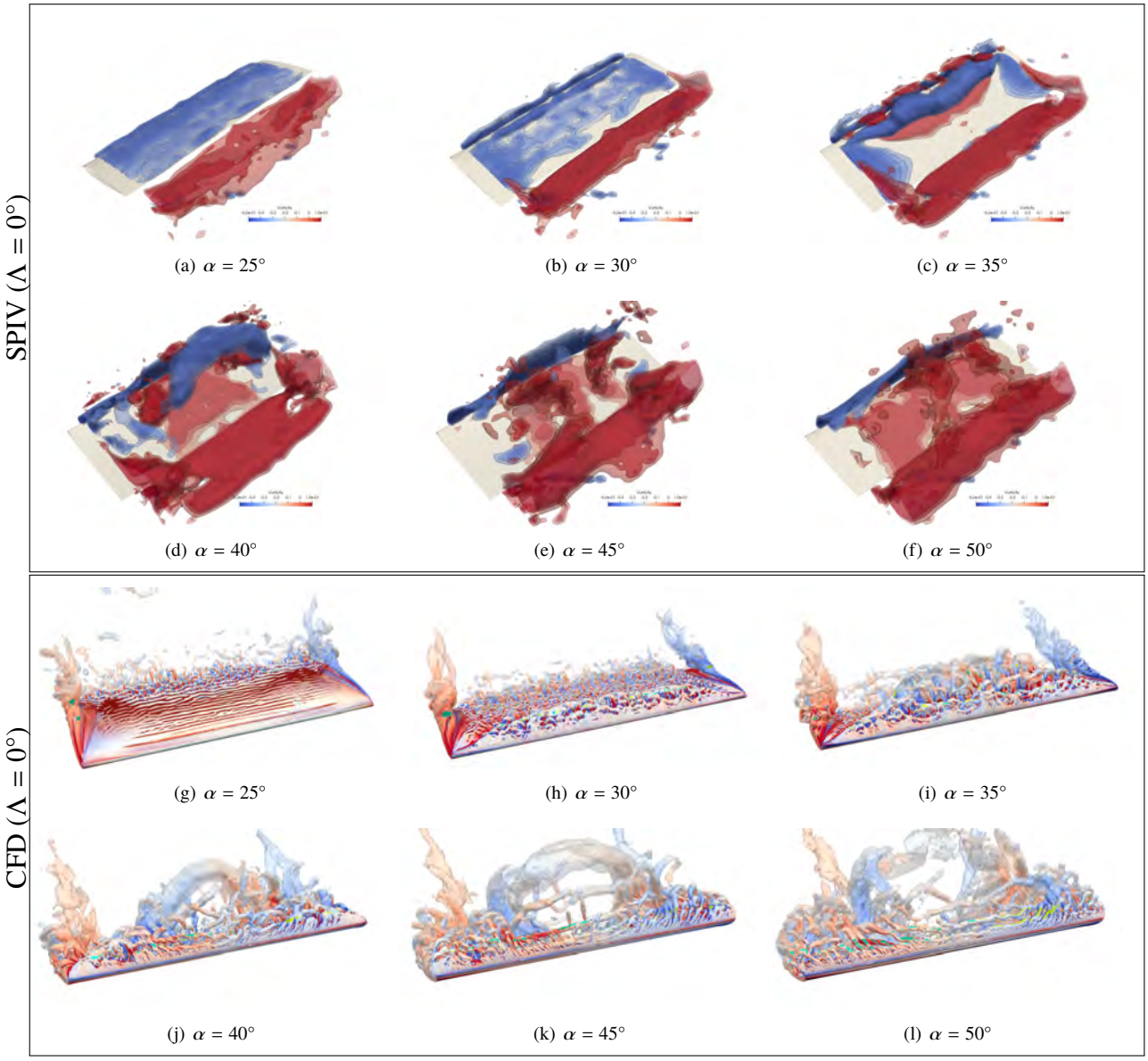


Fig. 13 Top row: isometric view of SPIV isosurfaces of constant total vorticity colored by the magnitude of vorticity. Bottom row: Unsteady CFD simulation results, isosurfaces of Q-criterion colored by streamwise vorticity

Figure 14 shows the CFD simulations of the three swept wings ($\Lambda = 10°, 20°$ and $30°$). Each wing had the same angular frequency and amplitude as the unswept wing above, so that comparisons can be made at specific angles of attack. The arrangement of the figure is $\Lambda = 10°$ in the upper block, $\Lambda = 20°$ in the middle block, $\Lambda = 30°$ in the lower block of images. At an angle of attack of 25°, the influence of the spanwise flow is already apparent. Here, the flow remains attached on the inboard section, and as the cross flow instability develops, a separated shear layer structure is observed along the outboard section. This phenomenon is enhanced at higher degrees of sweep angle. As the angle of attack continues to progress upward, the development of the LEV is shown. At a sweep angle of $\Lambda = 10°$, the formation of a coherent LEV and subsequent arch vortex is observed; however, the shape of the larger scale features is no longer symmetric. The arch vortex is now pushed outboard due to the spanwise flow, but it is still bounded by the wing tip vortex, so the LEV becomes squished toward the outboard tip vortex. At higher degrees of sweep the presence of the arch vortex becomes washed out as highly unsteady small scale flow structures dominate the separation process. At a sweep angle of $\Lambda = 20°$, the arch vortex structure is observed, but at the largest sweep angle this vortex structure is no longer coherent.

IV. Conclusions

A study was conducted on a wing exhibiting increased degrees of sweep. The aeroelastic instability was characterized through a cyber-physical system in which the torsional stiffness produced varying height and frequency limit cycle oscillations. Similarities were developed between the forced oscillation or prescribed motion with that of the responding structure. PIV measurements along with computational simulations were employed to characterize the flow behavior, primary LEV development and convection. Results indicate that sweep causes a discernible difference in the flutter amplitude. As simulations and PIV showed, the presence of spanwise flow caused a weaker LEV leading to a stabilizing dynamic effect.

Acknowledgments

The authors would like to acknowledge funding from Drs. Douglas Smith and Gregg Abate through the Air Force Office of Scientific Research Unsteady Aerodynamics&Turbulence portfolio.

This material is in part based on research sponsored by the US Air Force Academy under agreements number FA7000-13-2-0002 and FA7000-13-2-0009. The U.S. Government is authorized to reproduce and distribute reprints for Governmental purposes notwithstanding any copyright notation thereon.

The views and conclusions contained herein are those of the authors and should not be interpreted as necessarily representing the official policies or endorsements, either expressed or implied, of the US Air Force Academy or the U.S. Government.

References

[1] Theodorsen, T., "General theory of aerodynamic instability and the mechanism of flutter," *NACA Report No. 496*, 1934.

[2] Peters, D. A., Karunamoorthy, S., and Cao, W.-M., "Finite state induced flow models. I-Two-dimensional thin airfoil," *J. Aircraft*, Vol. 32, No. 2, 1995, pp. 313–322.

[3] Dowell, E. H., and Hall, K. C., "Modeling of Fluid-Structure Interaction," *Ann. Rev. Fluid Mech.*, Vol. 33, 2001, pp. 445–490.

[4] Amandolese, X., Michelin, S., and Choquel, M., "Low speed flutter and limit cycle oscillations of a two-degree-of-freedom flat plate in a wind tunnel," *Journal of Fluids and Structures*, Vol. 43, 2013, pp. 244–255.

[5] Ericsson, L. E., "Dynamic Airfoil Flow Separation and Reattachment," *J. Aircraft*, Vol. 32, No. 6, 1995, pp. 1191–1197.

[6] Tang, D., and Dowell, E., "Comparison of theory and experiment for non-linear flutter and stall response of a helicopter blade," *Journal of Sound and Vibration*, Vol. 165, No. 2, 1993, pp. 251–276.

[7] Sarkar, S., and Bijl, H., "Nonlinear aeroelastic behavior of an oscillating airfoil during stall-induced vibration," *Journal of Fluids and Structures*, Vol. 24, No. 6, 2008, pp. 757–777.

[8] Patil, M. J., Hodges, D. H., and Cesnik, C. E., "Limit-cycle oscillations in high-aspect-ratio wings," *J. Fluids and Structures*, Vol. 15, No. 1, 2001, pp. 107–132.

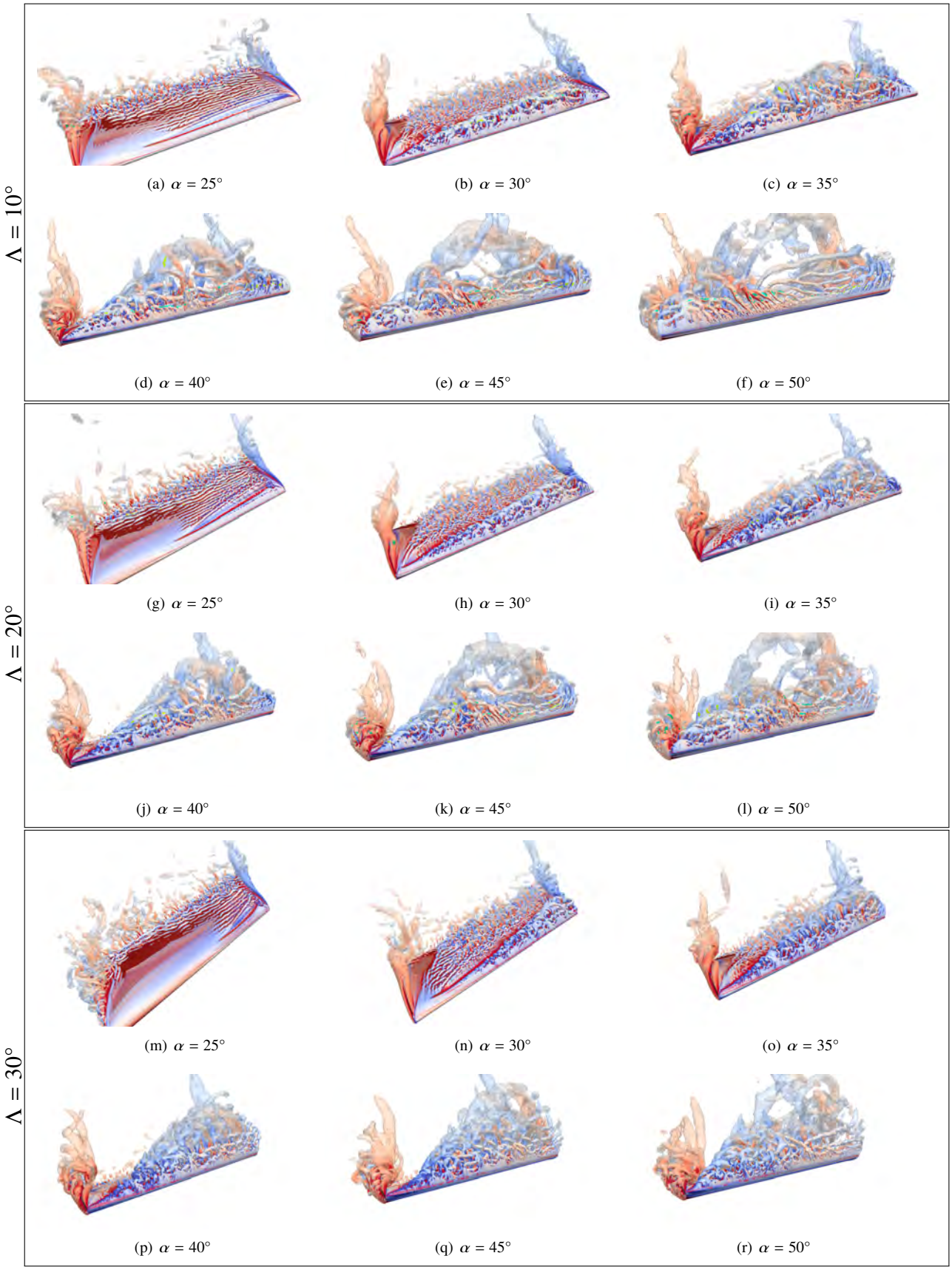


Fig. 14 Unsteady CFD simulation results for swept wings, isosurfaces of Q-criterion colored by streamwise vorticity

[9] Ol, M., and Granlund, K., "Abstraction of Aerodynamics of Flapping-Wings: Is it Quasi-Steady?" *AIAA Paper 2012-0587*, 2012.

[10] Nakamura, Y., "On the aerodynamic mechanism of torsional flutter of bluff structures," *Journal of Sound and Vibration*, Vol. 67, No. 2, 1979, pp. 163–177.

[11] Razak, N. A., Andrianne, T., and Dimitriadis, G., "Flutter and stall flutter of a rectangular wing in a wind tunnel," *AIAA J.*, Vol. 49, No. 10, 2011, pp. 2258–2271.

[12] Onoue, K., and Breuer, K. S., "Vortex formation and shedding from a cyber-physical pitching plate," *J. Fluid Mech.*, Vol. 793, 2016, pp. 229–247.

[13] Dimitriadis, G., and Li, J., "Bifurcation behavior of airfoil undergoing stall flutter oscillations in low-speed wind tunnel," *AIAA J.*, Vol. 47, No. 11, 2009, pp. 2577–2596.

[14] Fagley, C., Seidel, J., and McLaughlin, T., "Cyber-physical flexible wing for aeroelastic investigation of stall and classical flutter," *J. Fluid Struc.*, Vol. 67, 2016, pp. 34–47. doi:https://doi.org/10.1016/j.jfluidstructs.2016.07.021.

[15] Visbal, M. R., and Garmann, D. J., "Computational Investigation of the Effect of Sweep on a Pitching Finite-Aspect-Ratio Wing," *AIAA Paper 2018-0357*, 2018.

[16] Graftieaux, L., Michard, M., and Grosjean, N., "Combining PIV, POD and vortex identification algorithms for the study of unsteady turbulent swirling flows," *Measurement Science and Technology*, Vol. 12, No. 9, 2001, p. 1422.

[17] Fagley, C., Seidel, J., and McLaughlin, T., "Experimental Investigation of the Aeroelastic Behavior a NACA0018 Cyber-Physical FlexibleWing," *AIAA Paper 2015-2251*, 2015.

[18] Onoue, K., and Breuer, K., "Vortex Formation, Shedding and Energy Harvesting from a Cyber-Physical Pitching Flat Plate," *Bulletin of the American Physical Society*, Vol. 59, 2014.

[19] Zhu, Y., Su, Y., and Breuer, K., "Nonlinear flow-induced instability of an elastically mounted pitching wing," *Journal of Fluid Mechanics*, Vol. 899, 2020.

[20] Menon, K., and Mittal, R., "Flow physics and dynamics of flow-induced pitch oscillations of an airfoil," *Journal of Fluid Mechanics*, Vol. 877, 2019, pp. 582–613.

[21] Roth, G., Morton, S., and Brooks, G., "Integrating CREATE-AV products DaVinci and Kestrel: experiences and lessons learned," *AIAA Paper 2012–1063*, January 2012. doi:10.2514/6.2012-1063.

[22] Morton, S. A., and Meakin, R. L., "HPCMP CREATE-AV Kestrel Architecture, Capabilities, and Long Term Plan for Fixed-Wing Aircraft Simulations," *AIAA Paper 2016-0565*, 2016.

[23] McDaniel, D. R., Nichols, R. H., Eymann, T. A., Starr, R. E., and Morton, S. A., "Accuracy and Performance Improvements to Kestrel's Near-Body Flow Solver," *AIAA Paper 2016–1051*, January 2016. doi:10.2514/6.2016-1051.

[24] Glasby, R. S., and Erwin, J. T., "Introduction to COFFE: The Next-Generation HPCMP CREATETM-AV CFD Solver," *AIAA Paper 2016–0567*, January 2016. doi:10.2514/6.2016-0567.

[25] Eymann, T. A., Nichols, R. H., McDaniel, D. R., and Tuckey, T. R., "Cartesian Adaptive Mesh Refinement with the HPCMP CREATETM-AV Kestrel Solver," *AIAA Paper 2015–0040*, January 2015. doi:10.2514/6.2015-0040.

[26] Glasby, R., Erwin, J., Eymann, T., Nichols, R., McDaniel, D., Karman Jr, S., Stefanski, D., and Holst, K., "Results from DoD HPCMP CREATETM-AV Kestrel for the 3rd AIAA High Lift Prediction Workshop," *AIAA Paper 2018–1256*, January 2018. doi:10.2514/6.2018-1256.

[27] Morton, S. A., Tillman, B., McDaniel, D. R., Sears, D. R., and Tuckey, T. R., "Kestrel–A Fixed Wing Virtual Aircraft Product of the CREATE Program," *AIAA Paper 2009–0338*, January 2009. doi:10.2514/6.2009-0338.

[28] Godnov, S., "A difference scheme for numerical computation of discontinuous solution of hydrodynamic equations, Math Sbornik, Vol 47, 271-306 (in Russian) translated US Joint Publ," *Res. Service, JPRS*, Vol. 7226, 1969.

[29] Tramel, R., Nichols, R., and Buning, P., "Addition of improved shock-capturing schemes to OVERFLOW 2.1," *AIAA Paper 2009–3988*, June 2009. doi:10.2514/6.2009-3988.

[30] Spalart, P., and Allmaras, S., "A one-equation turbulence model for aerodynamic flows," *AIAA Paper 1992–0439*, January 1992. doi:10.2514/6.1992-439.

[31] Spalart, P., and Shur, M., "On the sensitization of turbulence models to rotation and curvature," *Aerospace Science and Technology*, Vol. 1, No. 5, 1997, pp. 297–302. doi:10.1016/S1270-9638(97)90051-1.

[32] Menter, F. R., "Eddy viscosity transport equations and their relation to the k-ε model," *ASME Journal of Fluids Engineering*, Vol. 119, No. 4, 1997, pp. 876–884. doi:10.1115/1.2819511.

[33] Spalart, P. R., "Comments on the feasibility of LES for wings, and on a hybrid RANS/LES approach," *Proceedings of first AFOSR international conference on DNS/LES*, Greyden Press, 1997.

[34] Lee, H., Simone, N., Su, Y., Zhu, Y., Ribeiro, B. L. R., Franck, J. A., and Breuer, K., "Leading edge vortex formation and wake trajectory: Synthesizing measurements, analysis, and machine learning," *arXiv preprint arXiv:2205.12658*, 2022.